Anodic Titanium Dioxide Nanotubes for Greywater Reclamation

BY

CLAYTON FARRUGIA

BSC (HONS) MSC MRSC

DEPARTMENT OF METALLURGY AND MATERIALS
ENGINEERING FACULTY OF ENGINEERING
UNIVERSITY OF MALTA

A dissertation submitted in partial fulfilment of the requirements for the research-based degree of Doctor of Philosophy of The University of Malta

May 2023

L-Università ta' Malta

FACULTY/INSTITUTE/CENTRE/SCHOOL - Engineering

DECLARATION OF AUTHENTICITY FOR DOCTORAL STUDENTS

(a) Authenticity of Thesis/Dissertation

I hereby declare that I am the legitimate author of this Thesis/Dissertation and that it is my original work.

No portion of this work has been submitted in support of an application for another degree or qualification of this or any other university or institution of higher education.

I hold the University of Malta harmless against any third party claims with regard to copyright violation, breach of confidentiality, defamation and any other third party right infringement.

(b) Research Code of Practice and Ethics Review Procedure

I declare that I have abided by the University's Research Ethics Review Procedures.
Research Ethics & Data Protection form code 5022_19042019_Clayton Farrugia.

☒ As a Ph.D. student, as per Regulation 66 of the Doctor of Philosophy Regulations, I accept that my thesis be made publicly available on the University of Malta Institutional Repository.

□ As a Doctor of Sacred Theology student, as per Regulation 17 (3) of the Doctor of Sacred Theology Regulations, I accept that my thesis be made publicly available on the University of Malta Institutional Repository.

□ As a Doctor of Music student, as per Regulation 26 (2) of the Doctor of Music Regulations, I accept that my dissertation be made publicly available on the University of Malta Institutional Repository.

□ As a Professional Doctorate student, as per Regulation 55 of the Professional Doctorate Regulations, I accept that my dissertation be made publicly available on the University of Malta

This research work was carried out in partnership with the consortium of the Micro Wastewater Treatment Systems using Photocatalytic Surfaces (Micro WatTS) Project. Work carried out by other members of the consortium will be marked accordingly.

Journal Publications

Lia, F.; **Farrugia, C**.; Buccheri, M.A.; Rappazzo, G.; Zammit, E.; Rizzo, A.; Grech, M.; Refalo, P.; Abela, S. Effect of the Surface Morphology of TiO_2 Nanotubes on Photocatalytic Efficacy Using Electron-Transfer-Based Assays and Antimicrobial Tests. *Appl. Sci.* 2020, *10*, 5243.

Farrugia, C., Di Mauro, A., Lia, F., Zammit, E., Rizzo, A., Privitera, V., Impellizzeri, G., Buccheri, M. A., Rappazzo, G., Grech, M., Refalo, P., & Abela, S. (2021). **Suitability of Different Titanium Dioxide Nanotube Morphologies for Photocatalytic Water Treatment**. Nanomaterials. 2021

Farrugia C, Lia F, Zammit E, Rizzo A, Privitera V, Impellizzeri G, Di Mauro A , Buccheri MA, Rapazzo G, Grech M, Refalo P, Abela S, (2021) **Aging of anodic titanium dioxide nanotubes in synthetic greywater: Assessment of stability and retention of photocatalytic activity.** Materials Chemistry and Physics

Abela S, Farrugia C, Xuereb R, Lia F, Zammit E, Rizzo A, Refalo P, Grech M. **Photocatalytic Activity of Titanium Dioxide Nanotubes Following Long-Term Aging**. Nanomaterials. 2021.

Abstract

Photocatalysis has been seen by many as an invaluable eco-friendly tool for environment remediation. Of special interest has been the use of photocatalysis for wastewater treatment. Titanium dioxide (TiO_2) has been the photocatalyst of choice for the last few decades. The combination of chemical stability, low-cost, non-toxicity and excellent optical properties have put it at the forefront of wastewater treatment research. Whilst other oxides, such as tungsten trioxide (WO_3) and iron oxide (Fe_2O_3) possess lower band gaps and can thus be activated by visible light, their resistance towards photocorrosion is lower than that of TiO_2. The inherent limitation of TiO_2 is its wide band gap which means that it can only be activated by UV light. Interest in the material has been consistently growing with strategies being devised to extend its activity into the visible region of the spectrum. Similarly,the advent of LED lights with low power consumption has helped overcome this limitation.

In this work TiO_2 nanotubes were produced via anodic oxidation. Anodic oxidation or anodising, is a facile way by which nanotube array can be grown. The process also provides a high level of control on the morphology of the produced nanotubes. The effect of different process variables on the photocatalytic activity of the produced was assessed. The process parameters used were dependent on the type of electrolyte being used. In one instance, a solution of 0.5 wt% sodium fluoride in 1 M sodium sulfate was employed. The anodising was carried out at 20 V for 6 hours. An acidic electrolyte consisting of 0.5% wt% sodium fluoride solution in 1 M phosphoric acid was used with a potential of 20 V applied for 3 hours. A non-aqueous solution containing 0.5 wt% ammonium fluoride, 3 wt% water and ethylene glycol as the balance was used for a process at 70 V for 1 hour. One set of surfaces produced in glycol was decorated with silver nanoparticles. The different electrolytes and associated process parameters produced nanotube layers with different morphologies. All materials when irradiated with UVA light showed a high activity towards the degradation of both chemical and bacterial contaminants. The chemical contaminants were the dye methylene blue, the analgesic paracetamol and the surfactant sodium dodecyl sulfate. The ubiquitous *E.Coli* was used as the bacterial contaminant. All pollutants can be found in all wastewater streams including greywater. The materials produced in glycol had the highest photocatalytic activity towards all pollutants. This is attributable to the increased

thickness, tube diameters and high anatase contents. These properties were the result of the high potential used (70 V) and the electrolyte which could support the high potential.

The mechanical and chemical stability of the materials was tested using two different aging regimes. A lab-based reactor was constructed to expose the photocatalysts to flowing synthetic greywater and a light source similar in composition to that of the solar spectrum for 12 weeks. The second aging exercise aimed to better replicate the conditions encountered during field use. A second reactor was built where synthetic greywater was circulated over the nanotube array irradiated with solar light and exposed to the different climatic conditions encountered. The morphology of the surface governed the resistance of the materials against fouling. The arrays produced in the ethylene glycol were devoid of spaces between the tubes and this delayed the accumulation of debris and the resulting occlusion of the tube tops. Despite the surfaces showing extensive fouling in both aging exercises, a significant level of activity towards the degradation of both the dye methylene blue and the bacterium *E.Coli* were retained. The photocatalysts were also free from chemical dissolution and mechanical damage with the crystalline structure being similarly unaltered. A cleaning regime was implemented to determine the ability of the materials to recover their reactivity. Recovery rates were high for all materials with respect to the degradation of the dye and only marginal for the antibacterial activity.

The material synthesised in the glycol without the silver decoration, was selected for upscaling. This material retained the highest activity after aging. The nanotube arrays were synthesised on 15 cm X 15 cm plates. These plates were installed in two different prototype flat plate photocatalytic reactors. The first reactor used UVA LED strips to activate the photocatalytic reaction. The effect of changing pollutant concentration, flowrate and the volume of solution were assessed in order to find the maximum productivity of the unit. A synthetic greywater mixture without *E.Coli*, paracetamol and methylene blue solutions were used as the water matrices to be treated. Another pilot reactor was installed on a rooftop to study the possibility of disinfecting greywater using sunlight. In this case the synthetic greywater mixture was seeded with *E.coli.* A noticeable level of degradation of the contaminants used was recorded in the UVA unit. The solar disinfection efficiency was only marginal. The efficiency of the reactors was hampered by an unfavourable ratio of photocatalyst surface area to solution volume.

The nanotube arrays installed in flat plate reactor show potential for greywater treatment however further work is required before successful commercialisation of the units.

Dedication

In memoriam

Josephine Farrugia (1945 - 2020)

Mother, fighter and indomitable Spirit

Malcolm Farrugia (1979 - 2022)

The companion of many a childhood adventure

Dedicated to my parents Josephine (RIP) and Angelo for their constant support. Both went out of their way to ensure that I could get opportunities that they did not have growing up.

Acknowledgements

This research work has not been a solo effort. A great number of people went out of their way to assist me throughout this endeavour.

My thanks go to my supervisors Prof Ing Stephen Abela and Dr Paul Refalo for their continuous support, technical expertise and for their unwavering belief in my abilities. I would like to thank Prof Ing Maurice Grech who apart from being an excellent researcher has thought me much, directly and indirectly, about project management.

I also wish to thank the members of the DMME technical and administrative staff team. Mr Andrew Agius, Mr Noel 'AP' Tonna, Mr Daniel 'TK' Dimech, Ing James Camilleri and Mr Nicholas Gingell whose technical contributions made this work proceed more smoothly. I am also extremely privileged to be able to call them friends. Lab work would also have been less cheerful without my post grad lab buddies. Ms Christabelle 'THB' Tonna, Dr Antonino Mazzonello, Dr Jeanelle Arpa and Dr Eleanor Saliba made life at the lab so much better.

The Micro WatTs project was also invaluable for meeting some great researchers who are now my friends. Dr Alessandro Di Mauro, great researcher and even greater friend/human being. Dr Maria Cantarella and Dr Maria Antonietta Buccheri have also thought me so much and were extremely kind when I was working at their facilities.

Lastly, but not in order of importance, my outmost gratitude goes to my family. My parents' support, not only throughout my doctoral studies, was the foundation on which many experiences were built. My in-laws John and Miriam for taking me in as their son. Their support through some very tough times kept me going. Miriam's excellent cooking also fuelled many a busy day. To my partner Cher, whose grit rubbed off on me, helping me persevere during periods of hardship. Her support was also unwavering even when she was busy with her doctoral studies and her myriad other academic and professional endeavours.

Table of Contents

List of Figures

List of Tables

List of Abbreviations and Acronyms

ANTA	Anodic Nanotube Arrays
IPA	Isopropyl Alcohol
CB	Conduction Band
VB	Valence Band
Eg	Band Gap
h^+	Electron Hole
TiO_2	Titanium dioxide
ZnO	Zinc oxide
MB	Methylene Blue
PZc	Point of Zero Charge
PVD	Physical Vapour Deposition
CVD	Chemical Vapour Deposition
ALD	Atomic Layer Deposition
SDS	Sodium Dodecyl Sulfate
XRD	X-Ray Diffraction
FESEM	Field Emission Scanning Electron Microscope
EDX	Energy Dispersive X-Ray Spectroscopy
LB	Luria Bertani
PBS	Phosphate Buffered Saline
PP	Polypropylene
AC	Activated Carbon
MF	Microfiltration
UF	Ultrafiltration

NF	Nanofiltration
BOD	Biological Oxygen Deman
TOC	Total Organic Carbon
RBC	Rotating Biological Contactor
MMBR	Moving Bed Biofilm Reactor

Chapter 1: Introduction

1.1 The Why?

Global water shortage is a terrible reality which is unlikely to improve unless ways to address it are found and implemented quickly. Water shortage is a complex problem with many a contributing factor. Population growth and economic development come with an increased water consumption for domestic, agricultural and industrial applications. Aridity due to climate change is also putting a major stress on the available water resources. Water shortage has been described as either moderate or chronic. Moderate water shortage refers to an availability of around 1000 m^3 – 1700 m^3 / capita/ year. Chronic water shortage is further divided into high (500 m^3 /capita/year) and extreme (< 500 m^3). In the early 2000s, 2.3 billion people lived under conditions of chronic water shortage. [1, 2].

The available resources must be governed by a sustainable management plan. This will not only curb water wastage but also provide strategies for water reuse where this is possible. Greywater can be gainfully reused if successfully treated in applications where potable water is not required. Treated greywater could replace potable water for use in toilet flushing, irrigation, car and floor washing. Separation of greywater sources from other wastewater streams and treating the water at the point of source also lessens the load on the local infrastructure [3, 4]. This greywater re-use not only aids water scarcity but also can translate to financial savings for the end-user [5].

1.2 The how?

Photocatalysis has shown great promise for the degradation of wastewater. Photocatalytic reactions produce reactive oxygen species with high oxidative power and low selectivity, thus being able to degrade a vast majority of pollutants found in wastewater. Both chemical and microbial contaminants can be successfully treated including recalcitrant molecules [6, 7]. Photocatalysis can be an eco-friendly alternative to other more commonly used treatment technologies. Photocatalysis only requires the photocatalyst, the wastewater and a light source [8].

Titanium dioxide is a ubiquitous material with a low toxicity, high chemical stability and low cost. Nanometric titanium dioxide serves as an excellent photocatalyst with high oxidative ability under UV light. Titanium dioxide nanotubes are one such photocatalyst which can be obtained through a facile synthetic process. This work will investigate the use of titanium dioxide nanotubes for greywater treatment.

1.3 Thesis Structure

This dissertation will follow a layout which is composed of four main sections. Chapter 2 is a literature survey which will provide the reader with the required theory on photocatalysis and photocatalytic materials. The remaining sections will be in a journal article style. The first of these chapters (chapter 3) will discuss the synthesis and activity of the anodic titanium nanotube arrays (ANTA). The stability of the ANTA after different aging cycles is assessed in chapter 4. The upscaling and use of ANTA in greywater treatment reactors will be studied in chapter 5.

Research Questions tackled in this work

Chapter 3

Research Question 1: Can ANTA degrade contaminants found in greywater?

Hypothesis 1: Given the non-selectivity and high oxidising power of the ROS produced by the photocatalysts, common contaminants should be degraded.

Methods 1: Different anodic oxidation methods will be used to produce ANTA. The photocatalytic activity of the single materials will be determined. The changes in absorbance and total organic carbon (TOC) of three model pollutants and the antibacterial activity towards *Escherichia Coli* (*E.Coli*) will be used to quantify the activity.

Research Question 2: Does a specific morphology or morphological feature promote higher photocatalytic activities?

Hypothesis 2: Better contact between pollutant and photocatalyst promotes higher degradation rates. The structure of the photocatalyst can thus be used to optimise the effective contact area.

Methods 2: The morphology of the ANTA is studied in detail using scanning electron microscopy (SEM) and the dimensions of different morphological features are measured by image analysis. The photocatalytic activity of the individual materials will be compared to their morphology to check for correlation between the two.

Chapter 4

Research Question 1: Can ANTA be used for long term treatment of greywater?

Hypothesis 1: Titanium dioxide photocatalysts have high oxidising power and have a high chemical stability. Photocatalysts can serve as self-cleaning materials. Thus, ANTA should provide a long-term solution for greywater treatment.

Methods 1: The different ANTA produced in chapter 3 will be aged using aging regimes under different sources of irradiation and different exposure durations. The changes in morphology will be assessed by image analysis of SEM images and X-Ray Diffraction (XRD). The photocatalytic activity after aging will be quantified using the degradation of methylene blue (MB) and the inactivation of *E.Coli*.

Research Question 2: Can deactivated ANTA be regenerated after long term use?

Hypothesis 2: Catalysts can be regenerated and re-used for repeated cycles. Photocatalysts should with suitable treatment be reactivated and re-used.

Methods 2: A selection of reactivation methods will be studied. The recovery in photocatalytic activity after these methods are employed will be determined using the degradation of MB and inactivation of *E.Coli*.

Chapter 5

Research Question 1: ANTA can be upscaled for use in greywater treatment reactors?

Hypothesis 1: Anodising of metals which can be passivated has been used for around a century and large-scale components have been produced. Anodic oxidation for the production of titanium dioxide nanotubes should, by determining proper process parameters, be upscaled.

Methods 1: The anodising process will be adapted and modified to be able to produce large scale photocatalytic surfaces. Strategies to maintain suitable temperatures and current densities will be determined.

Research Question 2: Can ANTA be used fruitfully for greywater reclamation?

Hypothesis 2: The high oxidising ability of titanium dioxide can be harnessed to degrade pollutants in greywater. The facile anodic oxidation process should be able to provide a cost-effective and eco-friendly way to treat greywater.

Methods 3: Pilot units will be constructed and the difference in productivity of the units when UV and solar irradiation are used will be assessed. Operational parameters of the units will be optimised to maximise the amount of treated effluent produced.

1.3 References

[1] M. Kummu, P. J. Ward, H. de Moel, and O. Varis, "Is physical water scarcity a new phenomenon? Global assessment of water shortage over the last two millennia," Environmental Research Letters, vol. 5, p. 034006, 2010/08/16 2010.

[2] A. Van de Walle, M. Kim, M. K. Alam, X. Wang, D. Wu, S. R. Dash, *et al.*, "Greywater reuse as a key enabler for improving urban wastewater management," Environmental Science and Ecotechnology, vol. 16, p. 100277, 2023/10/01/ 2023.

[3] T. Larsen, K. Udert, and J. Lienert, Source separation and decentralization for wastewater management: Iwa Publishing, 2013.

[4] C. Noutsopoulos, A. Andreadakis, N. Kouris, D. Charchousi, P. Mendrinou, A. Galani, *et al.*, "Greywater characterization and loadings–physicochemical treatment to promote onsite reuse," Journal of environmental management, vol. 216, pp. 337-346, 2018.

[5] A. Dixon, D. Butler, and A. Fewkes, "Water saving potential of domestic water reuse systems using greywater and rainwater in combination," Water Science and Technology, vol. 39, pp. 25-32, 1999/01/01/ 1999.

[6] J. Kou, C. Lu, J. Wang, Y. Chen, Z. Xu, and R. S. Varma, "Selectivity Enhancement in Heterogeneous Photocatalytic Transformations," Chemical Reviews, vol. 117, pp. 1445-1514, 2017/02/08 2017.

[7] D. Chen, Y. Cheng, N. Zhou, P. Chen, Y. Wang, K. Li, *et al.*, "Photocatalytic degradation of organic pollutants using TiO_2

-based photocatalysts: A review," Journal of Cleaner Production, vol. 268, p. 121725, 2020/09/20/ 2020.

[8] A. Charanpahari, N. Gupta, V. Devthade, S. Ghugal, and J. Bhatt, "Ecofriendly Nanomaterials for Sustainable Photocatalytic Decontamination of Organics and Bacteria," in Handbook of Ecomaterials, L. M. T. Martínez, O. V. Kharissova, and B. I. Kharisov, Eds., ed Cham: Springer International Publishing, 2018, pp. 1-29.

Chapter 2. Literature Review

This literature search has been compiled in such a way to provide the required background for the topics discussed in chapters 3,4 and 5 of this thesis. This review will introduce the problem being tackled, the technology required together with its benefits and limitations and the work carried out in this work which will contribute to the state of the art.

2.1 Water as a resource – The current situation

Water is essential for life to be sustained as it is required for all the biological processes of animals and plants. Water is ubiquitous as it covers around 70% of the earth's surface but the availability of easily accessible freshwater is low. Around 96.5% of this water is contained within the oceans and out of the remaining 3.5%, only 2.5% is freshwater. Around 68.6% of this freshwater is found in the ice caps, 30.1% in the aquifer and 1.3% as surface water [1].

Freshwater is used extensively for human consumption, sanitation, agriculture and industrial activities. The increase in the world's population and the continuous economic growth have contributed to the decline of both the quantity and quality of the available freshwater. It is predicted that the world's population will exceed 9 billion by 2050, further increasing the demand for this already scarce resource [2]. Water scarcity is defined using two terms, water shortage and water stress. Water shortage is population dependent and describes the consequences of having low water quantities per person. Water stress on the other hand refers to the inability of the available freshwater supply to meet the demand [3].

Malta is an island state with very limited natural resources and a very high population density. The island can only provide 40 m^3 of fresh water per capita, and is thus one of the world's driest countries [4]. With consumption far exceeding the supply of naturally available fresh, water must be obtained by desalination which is an energy intensive process. The problem is further exuberated by the current wasteful practices by the domestic sector where high-quality potable water is used for all household requirements. Malta has suffered and will continue to suffer from both water shortage and stress. In Malta the only considerable natural freshwater source is groundwater. The low levels of

precipitation, combined with the time taken for the water to reach the aquifer make replenishment extremely difficult. Groundwater sources can also be over extracted leading to a decline in the water quality due to saltwater intrusion.

2.2 Greywater to the rescue?

Given that climatic conditions cannot be controlled and the water producing infrastructure increased at leisure, curbing water wastage might be the only viable way to ensure an adequate water supply is available. If the use of potable water could only be relegated to uses where water of the outmost quality is required such as drinking, cooking and bathing, this would further help safeguard the water supply.

Greywater is one of the wastewater streams generated during household activities, the other being blackwater. Blackwater is toilet wastewater and greywater is that generated from bathing, dishwashing and laundering clothes. Since human excreta are absent from greywater, the bacterial load is significantly lower than that of blackwater. Despite the lower bacterial load, it can still be unsafe for reuse without prior treatment [5]. Greywater can be divided roughly in low strength (light) or high strength (dark) and the type is determined by the concentration of organic compounds [6]. Low strength greywater is derived from baths/showers and wash hand basins. Its components include personal care products, lint, hairs, skin oils and trace amounts of urine and faeces. High strength greywater is derived from kitchen sinks and laundry. Typical components include fats and oils, food particles, dish washing detergents, clothing fibres, laundry detergents and bleaches [7]. Low strength greywater is much more easily treated that high strength greywater.

Should greywater be treated and rendered safe for reuse, this would limit the use of potable water in applications where other waters of lower qualities are adequate. Treated greywater could be used for irrigation, car washing and toilet flushing. In essence, the re-use of greywater doubles the lifetime of potable water as this is used for a second application. If treatment could be performed at the point of use, the load on the municipal wastewater infrastructure would also be eased, as lower volumes of water would reach the sewer network.

2.3 Challenges in the reuse of greywater

Whilst the positive environmental impact of greywater reuse is undeniable, its treatment and reuse are not without their complications. In this section some of the current challenges will be discussed.

2.3.1 Defining the Treatment Process Required

Whilst greywater, especially low strength greywater is more amenable to being treated than say black water, a universal treatment solution does not exist. As will be discussed in section 2.4 there are numerous treatment processes and all of these require knowing the physico-chemical and biological properties of the greywater in detail for the selection of a viable treatment route.

The term greywater captures a myriad of possible greywater types. Household greywater already provides an idea of the variability of the composition of greywater. Laundry greywater does not have the same composition as that obtained from wash hand basins. The quality of the greywater depends on the lifestyle, number of inhabitants and the type of products used. The complexity of the contaminants also governs the process selection. Thus, the process selected must also be able to deal with some variability as a consistent chemical composition on a daily basis cannot be assured.

2.3.2 Legal Considerations and Compliance

A robust legal framework for greywater reuse is required. In many countries, including Malta, no legislation is in place which governs greywater treatment and its reuse. Strict guidelines are required as the effluent quality which must be reached for different reuse scenarios. Reuse activities which generate aerosols would undoubtedly require more stringent quality requirements. Also, legislation regarding commissioning of greywater treatment systems and certification of the units for fitness of purpose over time is required.

2.3.3 The perspective of the end-user

The psychological aspect of greywater reuse cannot be overlooked. People might be reluctant to reuse a wastewater stream irrespective of its quality. This has been termed the 'yuck factor' and is most prominent when greywater reuse for drinking is discussed [8, 9]. This reluctancy towards greywater reuse is more relevant when a greywater treatment unit would serve several dwellings such as an apartment building. Users of a particular dwelling might be reluctant to reuse water which in part originated from other households.

The cost of the unit and its maintenance vis a vis the savings obtained by using recycled greywater needs to be assessed. In the case of a domestic greywater treatment systems all the associated costs will be incurred by the user. Depending on the technology being used, the complexity of the system can increase quickly. This not only increases the initial investment cost but also possible recurring maintenance costs. Another consideration is the separation and catchment of the greywater streams. Unless already catered for during the planning stages, the greywater streams need to be separate from those carrying blackwater. This not only facilitates the treatment but also safeguards the health of the users. If alterations to the plumbing system are required, this is an extra cost placed on the user.

2.3.4 Environmental Concerns

The main environmental concerns are related to the use of recycled greywater for irrigation. Insufficiently treated greywater can introduce pollutants in the soil which might affect adversely the flora and fauna present. There can also be bacterial contamination, introducing new species not typically found in the soil ecosystem. If crops watered with greywater are to be consumed, the need for proper legislation is even more crucial.

2.4 Greywater Treatment Strategies

In this section some of the main and most commonly reported greywater treatment strategies are discussed. This section does not, however, aim to provide an exhaustive review of all the available technologies and processes.

2.4.1 Physico-Chemical Treatments

Adsorption is the process by which a solute is transferred from a bulk fluid to a solid (adsorbent), usually porous, solid. The process involves the formation of either physical forces (Van Der Waal's) or chemical bonds between the solute and the adsorbent [10]. Activated carbon (AC) is one suitable adsorbent for greywater treatment. Sharaf *et al.* reported an 80% removal of total organic carbon (TOC) following filtration through a biologically derived AC. The authors report that apart from sorption of the contaminants, the AC granules in the filter were also able to support biological degradation. Hess *et al.* reported similar findings to those obtained by Sharaf, when a biologically derived AC was used for post treatment of greywater following biological treatment [11].

Membrane processes filter the greywater through a porous membrane by applying pressure on the influent side of the membrane. The pore size used determines the species which are removed. A microfilter (MF) rejects particles and molecules larger than 100 nm. In ultrafiltration (UF) particles and molecules smaller than 100 nm and larger than 2 nm are rejected. Nanofiltration (NF) particles and molecules smaller than 2 nm are rejected [12]. Hourlier *et al.* reported that nanofiltration was able to remove all faecal coliforms and *Enteroccus* together with a 95% reduction in TOC [13]. Guilbaud *et al.* using the same membrane as Hourlier reported a 93% reduction in chemical oxygen demand (COD) [14]. The species filtered according to pore diameter are given in figure 2.1.

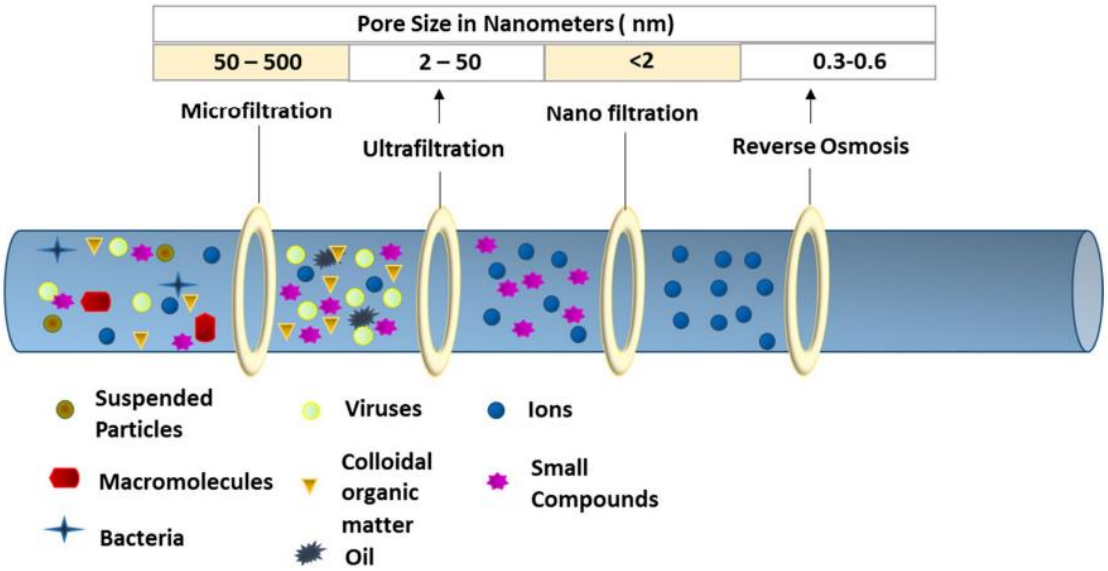

Figure 2. 1 Schematic showing the species filtered by membranes having different pore sizes. Reproduced from [15]

2.4.2 Biological Treatment

In biological treatment, the organic species present in greywater are consumed as food by bacteria. The organic content is quantified as biochemical oxygen demand (BOD). The term refers to the amount of oxygen required by the bacteria to breakdown the organic species present in water [16]. The soluble species are converted into solids as biomass when bacteria grow and reproduce. The BOD determination is typically conducted over 5 days and thus BOD is commonly known as BOD5.

One methodology for biological treatment involves the use of a rotating biological contactor (RBC). The RBC uses rotating discs on which bacteria already present in the greywater proliferate and form biofilm layers which are essentially a ‘slime’ which coats the discs. These discs are partially submerged in greywater where the bacteria, the rotation alternates the exposure of the biofilm to the greywater and to the oxygen in the atmosphere. This rotation allows for aerobic bacteria to grow and also for aeration of the greywater, thereby replenishing the dissolved oxygen levels [17]. Nolde installed a pilot RBC for the treatment of greywater for use in toilet flushing and monitored the performance over a period of 10 years [18]. The author reported the biodegradation of TOC in 90 L of laundry greywater over a period of 12 hours. The bacterial content of the effluent was also very low, on occasion even being below the detection limit of the

experimental procedure used for quantification. Two different RBC layouts are shown in figure 2.2.

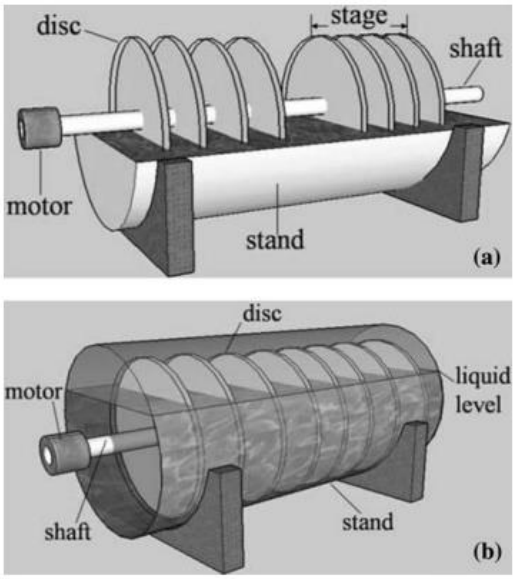

Figure 2. 2 Different RBC layouts: a) two-stage b) single stage Adapted from [17]

Another methodology used is the moving bed biofilm reactor (MMBR). The biofilm in this reactor is formed on plastic carriers which are mixed with the greywater. The term moving bed refers to the fact that the carriers supporting the biofilm are continuously being mixed with the water using an air supply. This method has the advantage of exposing a high surface area of biofilm to the water being treated whilst keeping the size of the reactor low. Chrispim *et al.* constructed and MMBR which treated a homogenised stream of laundry, shower and wash hand basin greywater. The authors reported a reduction of 75% in turbidity, 78% in COD, 75% in TOC and 97% in total coliforms. The quality of the treated effluent was such that the water could be used for irrigation of crops [19].

A combination of biological and physical treatment is used in membrane bioreactor (MBR). In this configuration, the bacteria are suspended with the greywater and are not supported on a medium. After biological treatment, the water is filtered through a membrane, such as an ultrafiltration membrane. The effluent is of exceedingly high quality but a considerable drawback is the fouling of the membrane. Reductions of 96% in total COD (dissolved and insoluble) and 97% BOD in a low strength greywater were reported by Friedler *et al* [20]. Bani-Melham *et al.* used a MBR reactor for the treatment of mixed household greywater. The authors reported a reduction of 88% in COD, 88%

in ammonia nitrogen (NH_3-N), 73% in anionic surfactants and 56% in total phosphorus [21]. A combined MBBR and MBR layout is shown in figure 2.3.

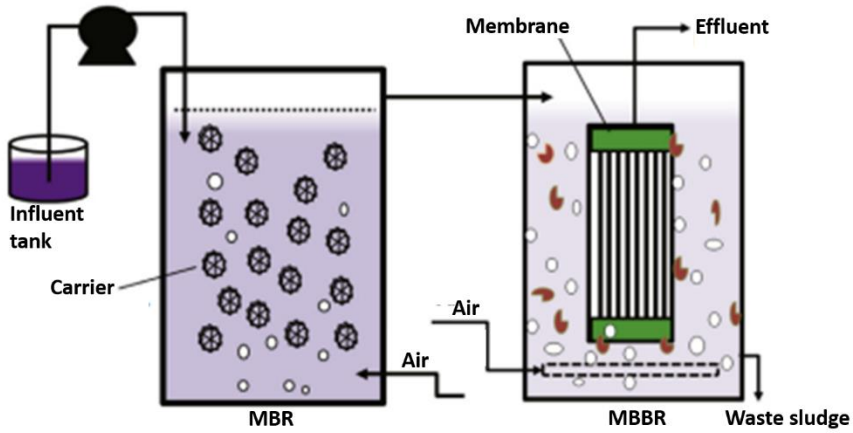

Figure 2. 3 Combined MBBR and MBR Processes Adapted from [22]

2.4.3 Chemical Treatments

Coagulation and flocculation are methods by which the totals suspended solids of water can be drastically reduced. In coagulation, the addition of a coagulant causes the de-stabilisation of colloidal suspensions of solids. Flocculation involves the addition of a flocculant to aid the adhesion of the de-stabilised solids to form larger particles called flocs. Flocs can either be allowed to settle and the supernatant re-used or floated to the surface and removed[22, 23]. Pidou *et al.* reported excellent removal of solids and organics by using alum ($Al_2(SO_4)_3$ but this required careful adjustment of the pH. By using ferric chloride ($FeCl_3$) and polyaluminium chloride as coagulants (PAC) Ghaitidak *et al.* reported the complete removal of faecal coliforms and *E.Coli* from greywater derived from showers, baths and wash hand basins. Their use of PAC made pH adjustment less critical [24].

Electrocoagulation (EC) is a process where the coagulant species are produced in situ. In the process a direct current is applied sacrificial electrodes submerged in the solution to be treated. The sacrificial electrodes (anodes) are typically made of aluminium or iron. Oxidation at the anode causes the release of metal ions. These ions, for example Fe^{2+}, Fe^{3+} and Al^{3+}, hydrolyse in water to produce hydroxides. The hydroxides produced act as coagulants. The process offers a low-cost solution without the need to dose with

chemicals[25, 26]. Barışçı *et al.* used an EC process using both iron and aluminium as electrode materials concurrently. The authors reported a nearly 100% reduction in COD in a blend of low and high strength greywater after a 30-minute cycle at a current density of 1 mA/cm^2. Patel *et al.* reported a removal in of 70% in COD, 87.5% in BOD, 82.7% in nitrate and 84.7% in phosphate using a current density of 0.5 mA/cm^2 for 100 minutes for a higher strength greywater than that used by Barışçı [27]. A schematic describing the electrocoagulation process including the formation of flocs is presented in figure 2.4.

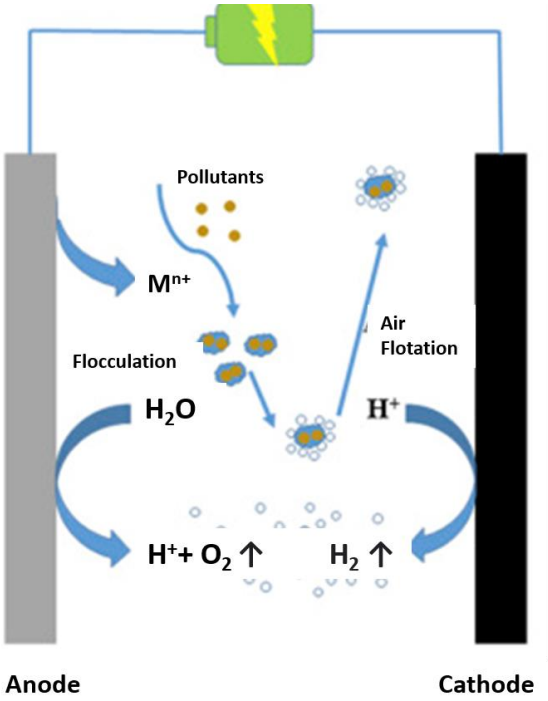

Figure 2. 4 Schematic of electrocoagulation process. Adapted from [29]

2.4.4 Advanced Oxidation Processes

The methods discussed thus far, perhaps with the exception of EC, are described as the classic methods for wastewater treatment. Whilst highly effective for the removal of several pollutant types, the classic methods, generally fail in treating more persistent pollutants such as pesticides and pharmaceuticals. Given the abundance and variety of chemical species entering the different wastewater streams a more complete solution for their degradation is required.

Advanced oxidation processes (AOPs) provide a way in which recalcitrant species can be degraded. An optimised AOP system can mineralise complex molecules to carbon

dioxide (CO_2), water and simple inorganic species. Non-biodegradable molecules can also be broken down to biodegradable species which can then by treated with one of the classic biological methods. There are different AOPs but their commonality lies in that they all degrade pollutants by generating reactive oxygen species (ROSs) such as hydroxyl (OH•) and superoxide ($•O_2^-$) radicals. These ROSs are extremely strong oxidisers, with the most common OH◦ radical having a reduction potential (2.8 V) close to that of fluorine (2.87 V). The different processes can generally be divided in two, homogenous and heterogenous AOPs. Heterogenous processes require the use of a solid catalyst, whereas for homogenous ones the chemicals required are dissolved in the water [28, 29]. Whilst the AOPs offer high oxidising power, it is unlikely that one process will completely degrade all the pollutants. The capabilities and limitations of some AOPs are tabulated in table 2.1.

2.4.4.1 Ozonation

Ozone is a strong oxidising agent with reduction potential of 2.07 V and can react with the majority of the organic and inorganic species in wastewater without requiring any specific conditions of pH. Degradation by ozonation occurs via two pathways namely indirect and direct reaction. In direct ozonation, the ozone molecule (O_3) reacts with the pollutants. This method is extremely selective and mainly targets organic compounds with double bonds. In the indirect reaction the ozone decomposes in water to form OH• radicals. The hydroxyl radicals are not selective reagents and will oxidise most organic species. The overall reaction for the production of OH• is given in equation 2.1. The two reaction pathways take place simultaneously in solution[30, 31]. Alrousan *et al*. reported a reduction in TOC of around 15% and of about 3% for BOD at an ozone flowrate of 45 mg/min applied for 3 hours. The authors however reported higher degradation rates when ozonation was carried under solar irradiance [32].

Equation 2.1 $3O_3 + H_2O \rightarrow 2\ OH• + 4\ O_2$

2.4.4.2 Fenton Reaction

The Fenton reaction produces OH◦ radicals by the decomposition of hydrogen peroxide by using the ferrous ion (Fe^{3+}) as a catalyst in acidic conditions. The OH◦ radical is non-selective and can degrade refractory compounds. A generalised mechanism for the Fenton reaction is presented in equations 2.2 and 2.3 [33].

Equation 2.2 $Fe^{2+} + H^{+} + H_2O_2 \rightarrow Fe^{3+} + H_2O + OH\bullet$

Equation 2.3 $Fe^{3+} + H_2O_2 \rightarrow Fe^{2+} + HO_2\bullet + H^{+}$

Chin reported the use of the Fenton reaction for the treatment of greywater with a starting COD concentration of ≈ 230 mg/L using 1mM Fe^{2+}/ 5mM H_2O_2 over a period of 3 hours. The author reported a reduction of around 100 mg/L with the concentrations and process durations used. Peroxide concentrations higher than 5mM resulted in a lower rate of reaction due to the scavenging of OH• by the peroxide. On increasing the peroxide concentration 12.5 mM and a UVC dose of 54,000 $mJ.cm^{-2}$ over 3 hours, a reduction of around 200 ppm COD was obtained [34].

2.4.4.2 Electrochemical Oxidation

Electrochemical oxidation degrades pollutants by producing ROS by reactions occurring at the surfaces of electrodes. The process involves passing a current between two electrodes (anode & cathode) whereby OH• and other oxidising species are generated at the anode.This process is an example of heterogenous AOPs. The process can be described as having a direct and indirect degradation pathway. The direct pathway involves the OH• generated at the anode reacting with organic species adsorped on the same electrode. The process is summarised in equations 2.4 to 2.6. In equation 2.4 water is oxidised at the anode to form surface adsorped OH•. The OH• adsorped on the surface reacts with organic compounds adsorped on the surface in equation 2.5. Equation 2.6 represents the formation of oxygen at the anode.

Equation 2.4 $M + H_2O \rightarrow M[OH\bullet] + H^{+} + e^{-}$

Equation 2.5 $M[OH\bullet] + R \rightarrow M + RO + H^{+} + e^{-}$

Equation 2.6 $M[OH\bullet] + H_2O \rightarrow M + O_2 + 3H^{+} + 3e^{-}$

Where: M is the anode

M[OH•] is the surface adsorped OH• radical,

R is a generic organic compound

and RO is the oxidised organic compound.

Indirect reaction refers to the formation of oxidising species such as OH• and $•O_2^-$. Depending of the water matrix chlorine and sulfate-based oxidisers can also form.

2.4.4.3 Photocatalysis

In photocatalysis, light is used to activate the reduction-oxidation properties of a semiconductor. Photocatalysis can be used to degrade a variety of contaminants in wastewater. The photocatalyst brings about the degradation of the contaminant either via direct reaction with the surface or through the generation of ROSs. Photocatalysis is often seen as the future of AOPs and as such will be discussed in greater detail in the section 2.5.

Table 2. 1 Advantages and disadvantages of different AOPs. Adapted Reproduced from [37]

AOP	Advantages	Disadvantages
Fenton's Reaction	• Able to degrade soluble and insoluble dyes in industrial effluent. • No potential formation of bromated byproducts.	• Iron sludge generation due to combined flocculation of the reagent and organic compounds. • Low pH (<2.5) is required to keep iron in solution • pH adjustment will increase operating cost
TiO_2 Catalysed UV Oxidation	• No potential formation of bromated byproducts. • Recycling of the catalysts. • Performance also at higher wavelengths and under solar irradiation.	• No full-scale application exists • If the catalyst is added as a slurry, a separation step is required. • Adaptation and optimum concentration of catalyst requires rigorous study.
H_2O_2 / O_3	• Formation of strong, non-selective hydroxyl radicals that are able to breakdown the conjugated double bond. • Ozone can be used in its gaseous state and consequently does not raise the volume of the wastewater. • No sludge generation.	• Low rate of degradation when compared to other AOP due to a lower reduction of hydroxyl radicals. • Ozone may form toxic byproducts. • High cost. • Requires the addition of excess H_2O_2 due to potential for microbial growth.
O_3 / UV	• More efficient than O_3 and UV alone. • Disinfection • For equal oxidant concentration, more efficient at generating hydroxyl radical than H_2O_2 / UV.	• Potential formation of bromated byproducts. • UV light penetration can be disrupted by turbidity • Species such as nitrate can interfere with the absorbance of UV light
Sonication	• Less heat transfer relative to UV systems • No formation of bromated compounds if O_3 is not used.	• No full-scale application exists. • Oxidant may be needed to improve the efficiency of the treatment, thereby increasing cost

2.5 Photocatalysis – A new hope for wastewater treatment?

2.5.1 Definitions and Mechanisms

The International Union of Pure and Applied Chemistry (IUPAC) defines photo catalysis as the 'Change in the rate of a chemical reaction or its initiation under the action of ultraviolet, visible or infrared radiation in the presence of a substance—the photocatalyst—that absorbs light and is involved in the chemical transformation of the reaction partners'[35].

Photocatalysis as with other AOPs can be grossly divided in two, homogenous and heterogenous photocatalysis. In homogenous photocatalysis, catalyst and substrate are in the same physical state. The components required for the reaction, the photosensitiser or light absorbing system and the catalytic sites which support the reduction-oxidation reactions form part of a single solution. The use of near UV and visible light to enhance the Fenton process, called photo-Fenton is an example of homogenous catalysis [36]. In heterogenous photocatalysis catalyst and substrate are in different physical states. Heterogenous photocatalysis has been brought to the forefront by Honda and Fujishima's 1972 seminal work. The duo reported the splitting of water on a titanium dioxide (TiO_2) photoanode under UV light [37]. Heterogenous photocatalysis using semiconductors has since then been touted as an eco-friendly solution for remediation of water. This work will focus on heterogenous photocatalysis using TiO_2 as the semiconductor. The remainder of this literature survey will thus deal solely on semiconductor photocatalysis.

For semiconductor photocatalysis the transfer of electrons from the valence band (VB) of the semiconductor to its conduction band (CB). The energy required to promote an electron to the conduction band is called the band gap (Eg). Whether a material is considered an insulator, a conductor or a semiconductor is based on the value of the band gap. In general, conductors have an Eg lower than 1 eV, insulators an Eg greater than 5 eV and the Eg for semiconductors lies between 1.5 and 3 eV. A graphical distinction between the three types of materials is shown in figure 2.5. A band gap lower than 3 eV shifts the activity of the photocatalyst into the visible region, which can exploit the solar spectrum more fully [38].

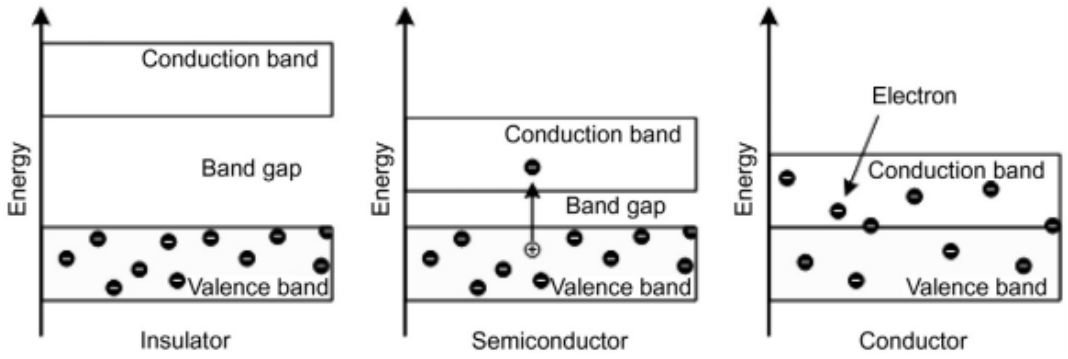

Figure 2. 5 Definition of insulator, semiconductor and conductor based on valence and conduction band positions. Adapted from [42]

In order for the photocatalyst to be activated, it must be exposed to light having a specific wavelength. Lower wavelengths, which are more energetic, are also suitable for activation. Once the correct amount of energy is supplied, this is absorbed by an electron (e^-) in the VB which is then promoted to the CB. This promotion leaves a positive charge in the location previously occupied by the electron in the valence band. This positive charge is called an electron hole (h^+). The e^- and h^+ are termed charge carriers.

The photogenerated e^- and h^+ can either recombine anywhere between 10 and 100 nanoseconds from their generation to give off heat [39]. This charge carrier recombination reduces the efficiency of the photocatalytic reaction and generally occurs in the bulk of the catalyst. Charge carriers which do not recombine migrate to the surface where they can take part in charge transfer processes with chemical species adsorbed on the surface. The h^+ possessing a redox potential that makes them essentially able to degrade any contaminant. Reactions involving h^+ can be divided in direct and indirect processes. The h^+ itself can react with species adsorbed to the photocatalyst surface. The indirect mechanism, involves the generation of surface adsorbed OH• radicals by reaction with surface adsorbed water and hydroxide groups. The overall mechanism is summarised in equations 2.7 and 2.8

Equation 2.7 $h^+ + H_2O_{ads} \rightarrow OH\bullet_{ads} + h^+$

Equation 2.8 $h^+ + HO^- \rightarrow OH\bullet_{ads}$

The negative charges arising from the photogenerated electrons need to neutralised. The electrons react with dissolved oxygen to produce different oxidising agents as per the pathways given in equations 2.9 to 2.14.

Equation 2.9 $O_2 + e^- \rightarrow O_2^{\bullet-}$

Equation 2.10 $O_2\bullet^- + H^+ \rightarrow HO_2^\bullet$

Equation 2.11 $2\ HO^\bullet \rightarrow H_2O_2$

Equation 2.12 $H_2O_2 + h\nu \rightarrow 2OH\bullet$

Equation 2.13 $H_2O_2 + O_2^- \rightarrow OH\bullet + HO^- + O_2$

Equation 2.14 $H_2O_2 + e^- \rightarrow OH\bullet + HO$

The OH• radicals are the main oxidisers and offer a non-selective degradation pathway which can mineralise many organic species. The reactions occurring as TiO_2 is irradiated with UV light are shown in figure 2.6.

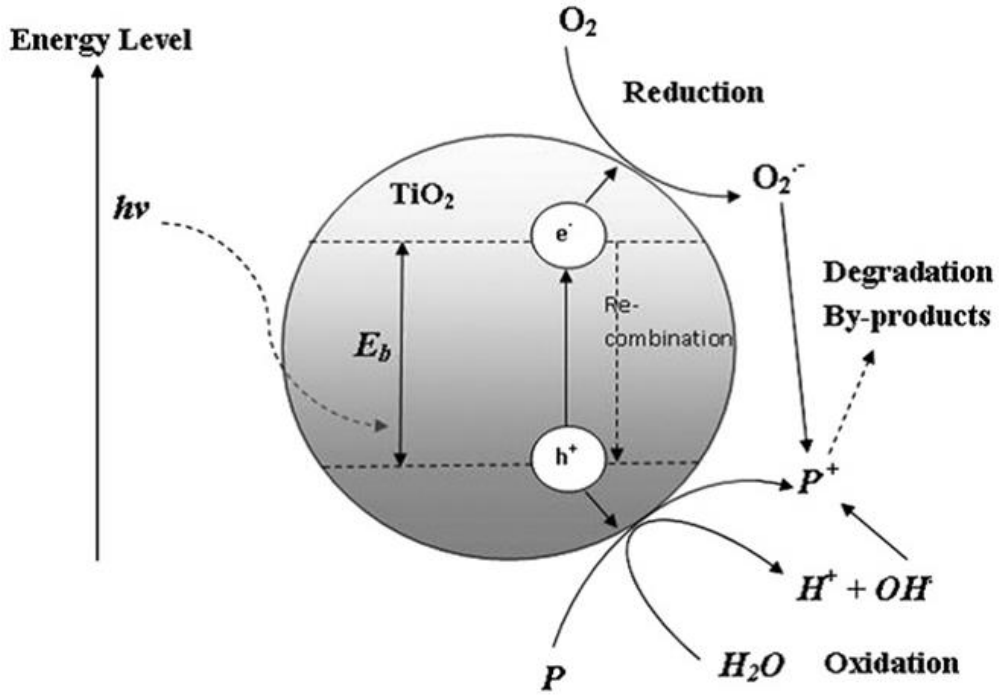

Figure 2. 6 Schematic showing charge carrier and ROS generation. Adapted from [44]

2.5.2 Viable Photocatalysts

The research in the past few decades has identified several photocatalytic materials. A simple classification system has been adopted by Chan *et al* [40]. The photocatalysts are divided in titanium dioxide, zinc oxide and other metal oxides such as tungsten oxide, cerium oxide and molybdenum oxide. A selection of photocatalysts and their respective band gaps is presented in figure 2.7.

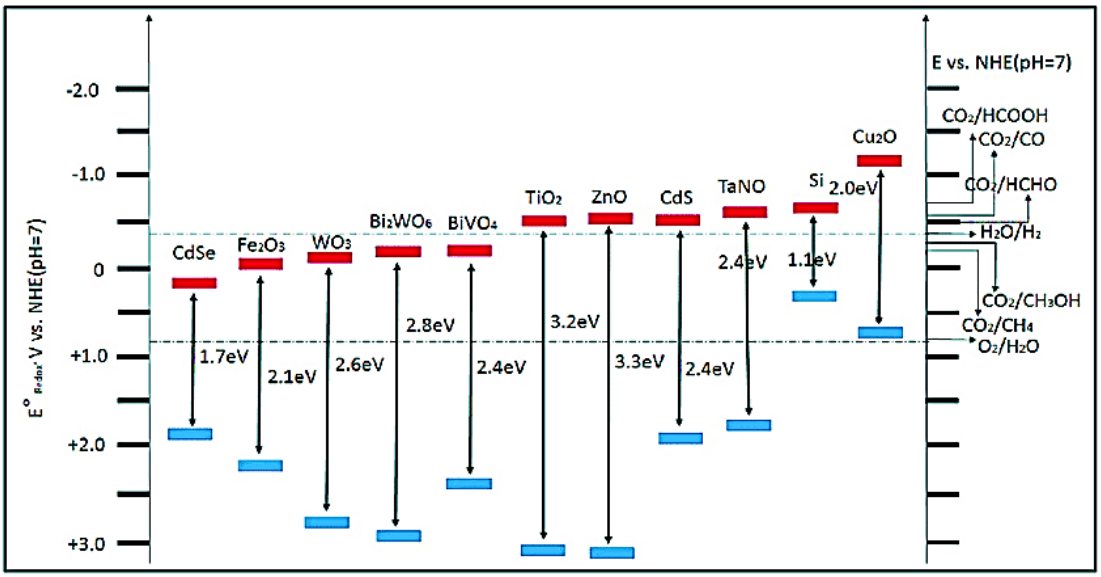

Figure 2. 7 Schematic showing charge carrier and ROS generation. Adapted from [46]

Despite the variety of available materials titanium dioxide (TiO_2) and zinc oxide (ZnO) nanostructured semiconductors are considered to be the gold standard photocatalysts. Their photocatalytic properties have been investigated both at the laboratory scale and in pilot photocatalytic reactors. Both are low-cost, non-toxic, are stable towards photo induced degradation and can be synthesised in several ways. Nanometric particles are also available commercially in different sizes.

Both TiO_2 and ZnO are wide bandgap semiconductors, with a typical bandgap value of 3.2eV and 3.34eV respectively, meaning that they require UV activation. Three different polymorphs of ZnO exist, wurzite, zinc blende and rocksalt. The wurzite polymorph has the highest thermodynamic stability and is thus the form most commonly encountered [41]. Similarly, three polymorphs exist for TiO_2, anatase, rutile and brookite. Brookite is metastable whereas rutile is the thermodynamically stable phase [42]. Anatase is overall highly stable but can be converted to rutile if it is heated above 600°C [43]. Anatase has a larger band gap than rutile at 3.2 eV and 3.0 eV respectively. Rutile can thus absorb a portion of the visible spectrum, whereas anatase require UV light. Anatase is however considered to be the better catalyst of the two polymorphs. The larger band gap of anatase could raise the VB maximum at higher levels than the reduction potentials of the molecules adsorbed on the surface. This furnishes the electrons with a greater oxidising power and makes transfer of electrons to the molecules adsorbed more efficient. Anatase has an indirect band gap which is smaller than the direct one. That of rutile is possibly direct or its indirect band gap is very close in energy to its direct one.

Semiconductors with indirect band gaps tend to have longer lived charge carriers. The longer electron-hole pair lifetime in anatase increase the probability of the charge carriers migrating to the surface to take part in surface reactions [44]. The effect of an indirect band gap on the energy required to promote an electron to the conduction band is shown in figure 2.8.

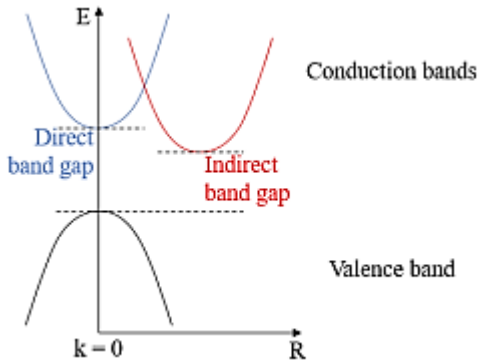

Figure 2. 8 Schematic showing differing energy levels for direct and indirect band gap. Adapted from [51]

2.5.3 Photocatalytic Activity of ZnO and TiO_2

2.5.3.1 Degradation of Organic Compounds

A facile procedure to determine the photocatalyst's ability to degrade pollutants is to conduct dye degradation experiments. Dyes are complex molecules with strong absorption maxima in the visible range. The change in absorbance of the solution with exposure to the photocatalyst and UV light is measured on a UV-Visible spectrophotometer. The lower the absorbance value after exposure, the higher the activity of the photocatalyst. Methylene blue, methyl orange and rhodamine B are commonly used dyes. Barnes *et al.* compared the efficiency of both TiO_2 and ZnO in the degradation of methylene blue (MB). A 1g/L suspension of TiO_2 nanoparticles, reduced the concentration of methylene blue by 74% after 1 hour of UVA exposure at 365 nm. The same concentration of ZnO resulted in a lowering of only 18% [45]. The authors attributed the incomplete degradation of the dye to the shadowing effect of the suspension. When a high concentration of particles is in suspension, the particles closest to the light source block light from reaching the particles in the bulk of the solution. The low degradation rate of ZnO was attributed to shadowing and photocorrosion [45]. Neppolian *et al.* reported that lower concentrations of TiO_2 nanoparticles than ZnO

nanoparticles were required for the complete degradation of the dye reactive red 2. This difference in efficiency has been attributed to photocorrosion and the authors recorded an increase in Zn^{2+} in the solution [46]. The photocorrosion mechanism for ZnO is given in equation 2.15 [47].

Equation 2.15 $ZnO + 2h^{+} (vb) \rightarrow Zn^{2+} + ½ O_2$

Akyol *et al.* on the other hand did not report any loss of activity due to photocorrosion despite the materials being exposed to several working cycles. Li and Haneda described the effect of morphology and crystallinity on photocorrosion susceptibility of the materials [48]. Thus, the same metal oxide semiconductor can be both susceptible and resistant towards photocorrosion. In general, it has been agreed that TiO_2 can tolerate UV irradiation cycles well. Some authors have argued that during photo induced events such as water splitting, AOPs and superhydrophilicity, the surface undergoes changes in crystallinity. These changes have been found to be reversible when the irradiation is terminated. Salvador has reported that n-rutile single crystal electrons were susceptible to selective etching along the < 001> direction when exposed to UV radiation [49]. Nakajima *et al.* reported that changes in structure attributed to photocorrosion, result in superhydrophilicity. This effect is desirable and is reversible when UV radiation is removed [50]. As previously discussed, certain morphologies tend to be more susceptible towards photocorrosion. Thus, whilst perhaps TiO_2 is more photostable, sometimes also considered immune, photocorrosion might still be a reality. This is especially so, when rutile is one of the phases in the semiconductor structure. Suppression of photocorrosion is however reported in anatase due to the presence of {101} and {001} facets which are highly resistant to photo-induced etching. The {001} facet is of particular interest since it the more highly photoactive of the two [51].

2.5.3.2 Antibacterial Activity

Matsunaga *et al.* first reported the antimicrobial activity of the TiO_2 photocatalytic oxidation in 1985 [52]. Since then, the effect photocatalytic oxidation has been studied on a wide variety of microorganisms, including several bacterial species, fungi and viruses. The antimicrobial properties have been attributed to the •OH species and other ROSs. The photogenerated species damage the cell membrane by causing lipid peroxidation. Uncontrolled lipid peroxidation can result in structural damage to the cell

membrane, causing leaking of cellular contents and ingress of ROSs which oxidise the cellular contents. Vohra *et al.* attributed cell death to the photooxidation of coenzyme A which leads to the inhibition of cellular respiration [53].

Li *et al.* managed to successfully correlate the concentration of generated ROS species with bactericidal activity on E. coli, a gram-negative strain [54]. Furthermore, they reported that nanometric TiO_2 generated ROS concentrations exceeding those of ZnO twofold. The same order of efficiency (TiO_2 > ZnO) was reported for the antibacterial action [54]. Barnes *et al.* reported a positive correlation between the rate of degradation of methylene blue and antibacterial action. This confirms the role of ROSs in the degradation mechanism of both organic and bacterial contaminants [45].

2.5.5 Photocatalytic Greywater Treatment

The photocatalytic efficiency testing methodologies discussed above are somewhat limited when it comes to the analysis of greywater. Greywater is a complex water matrix, with thousands of chemical species and several bacterial strains. Analysing the single components, especially the chemical species, for evaluation of the photocatalytic efficiency is thus unfeasible. Testing at the bench scale will also provide inconclusive results as to the efficiency of a photocatalytic reaction in the field.

Boyjoo *et al.* measured the change in TOCto measure the efficiency of the reactor in purifying shower water. The TOC load came primarily from the surfactants present in personal care products such as shower gels, shampoos and conditioners. TOC is a better indicator of photocatalytic performance since it is not limited to measuring the concentration of coloured compounds. The reactor used a slurry of Aeromax P25 TiO_2 nanoparticles as the photocatalyst. The slurry was recirculated under UV irradiation for 6 hours. The authors reported a reduction in TOC of 57%, which could possibly be reduced further with a longer exposure time [55]. On the other hand, Tsoumachidou reported negligible photocatalytic activity when similar experiments were carried out. The author reported a TOC degradation of 72% was only achieved through the addition of hydrogen peroxide [56]. Saran *et al.* reported a decrease of 32% of organic species when TiO_2 nanoparticles were circulated in a photoreactor in sunlight. The near complete removal of dissolved carbon species was reported to occur only after the addition of hydrogen peroxide [57].

2.5.6 Extending the Activity Towards Visible Light Activity

Whilst TiO_2 possess a high photocatalytic activity when it absorbs UV light, its wide band gap limits its ability to exploit the more abundant visible portion of the solar spectrum. In this section possible strategies to extend the activity of photocatalysts will be discussed.

2.5.6.1 Dye-sensitization

A dye molecule on irradiation with visible light it injects its photoexcited electrons from the dye to the conduction band of the photocatalyst. The electron transfer to the conduction band of TiO_2 has often resulted in a high photocatalytic reaction. Photocatalytic degradation of the dye itself reduces the efficiency of the dye-sensitisation process, and this requires the addition of sacrificial species [149]. The main advantage of dye-sensitisation over other strategies is the fast injection of electrons in the conduction band and the much slower reverse reaction. A schematic representation of the dye sensitisation mechanism is presented in figure 2.9.

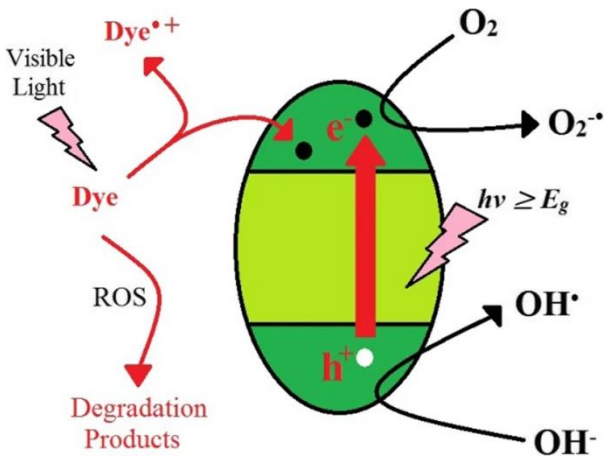

Figure 2. 9 Schematic showing electron injection from excited dye molecule to conduction band together with the generation of ROSs from electron holes and electrons. Adapted from [58]

2.5.6.2 Doping

Doping is a process by which the energy required for the electrons in the valence band to be promoted into the conduction band i.e. the band gaps. The process requires the introduction of impurities within the crystal structure of the photocatalyst. Both metals and non-metals can be used as dopants. The dopants introduce new energy levels (bands)

between the valence and conduction bands. These levels reduce the band gap by promoting electrons within these new levels to the conduction band. Metal dopants such as cobalt, copper, manganese and iron introduce a new energy band below the conduction band of the photocatalyst [59-61]. Non-metal dopants such as nitrogen and phosphorus introduce a new band above the valence band [62, 63]. The effect on non-metal and metal doping on the energy bands of the photocatalysts is presented in figures 2.10 and 2.11.

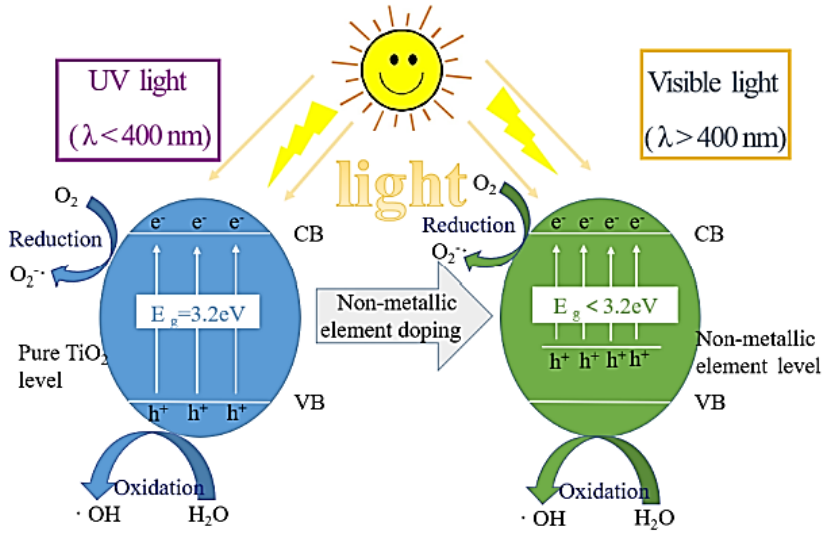

Figure 2. 10 Effect of non-metal doping on band gap. Adapted from [71]

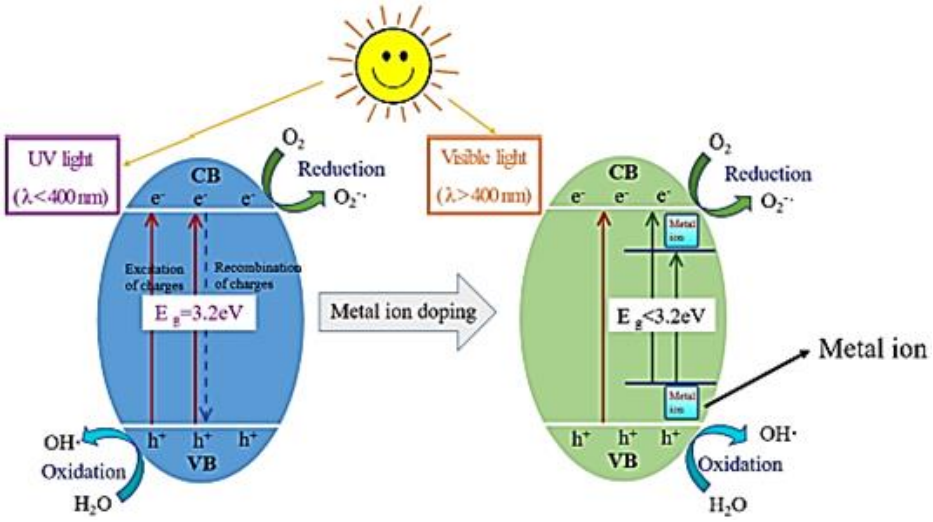

Figure 2.11 Effect of metal doping on band gap. Adapted from [64]

2.5.6.3 Noble Metal Deposition

The deposition of noble metals such as silver, gold and enhance visible light activity by reducing the charge carrier recombination rate. The Fermi level of the metals lies between the conduction and valence band and this provides a path for the transfer of electrons from the conduction band to the metal particles [65]. The electron capture pathway is shown in figure 2.12.

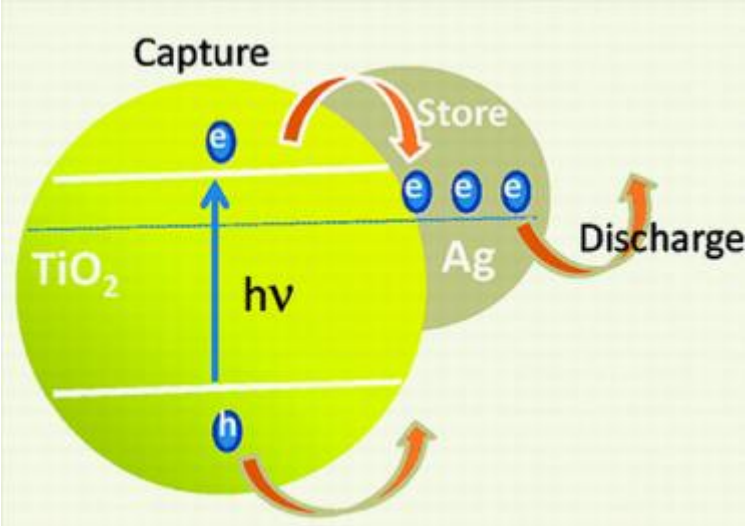

Figure 2. 12 Electron capture by deposited silver particles. Adapted from [65]

Wang *et al.* reported that oxides of silver also exhibit photocatalytic activity both under UV and visible light. The authors also reported that the oxides are stable and retain a significant activity after re-use [66]. Jiang *et al*. reported similar findings together with the material being active when exposed to infrared light [67]. Kohtani reported that this enhanced activity was due to the better separation of the photogenerated holes and electrons [68].

2.5.7 Factors Affecting Photocatalytic Degradation

Several parameters can affect the rate of the photocatalytic activity. Apart from the photocatalyst itself, factors such as solution pH, pollutant concentration, light wavelength, intensity and catalyst loading all have a role to play.

2.5.7.1 Temperature

The overall reaction rate is mainly unaffected if minor changes in temperature occur during photocatalytic degradation. Excessive solution temperature can reduce the amount of dissolved oxygen in the solution. As discussed previously, oxygen is used to produce other different oxidising agents and also scavenges surface electrons, avoiding charge build on the surface. An increase in temperature generally results in a rise in reaction rate. On exceeding 80°C, however, the charge carrier recombination rate increases along with the desorption of surface adsorbed pollutant molecules [69]. Temperatures lower than 80°C favour the adsorption of molecules. The optimum temperature lies between 20 and 50°C [70].

2.5.7.2 Catalyst Loading

Catalyst loading refers to the concentration of the photocatalyst available for reaction with the pollutants. The concentration required for complete degradation, ideally mineralisation, depends on both the solution volume and concentration. The higher the catalyst loading, the higher the generation of ROSs and thus the higher the photocatalytic reaction rate. Catalyst loading is also applicable for supported or deposited catalysts. Proper substrate coverage enhances the catalyst load. Lim *et al.* reported that thicker layers contributed to higher MB degradation rates [71]. This is so as thicker layers are a way of increasing the catalyst load in the photocatalytic system. An optimum ratio of catalyst concentration to pollutant concentration thus exists and must be determined experimentally.

2.5.7.3 Solution pH

The solution pH alters the ability of the organic pollutants to adsorb to the surface. The pH can alter the charge of the surface and also the charge of the molecule itself. The point of zero charge (pzc) is the pH at which the surface charge is neutral and the knowledge of its value is important for the determination of the adsorption efficiency at different pHs. The effect on pH on the surface charge of TiO_2 is summarised in equations 2.16 and 2.17.

Equation 2.16 Acidic Solution pH $Ti\text{-}OH + H^+ \rightleftharpoons Ti\text{-}OH_2^+$

Equation 2.17 Basic Solution pH $Ti\text{-}OH + OH^- \rightleftharpoons Ti\text{-}O^- + H_2O$

Acidic solution pHs favour the adsorption of negatively charged organic compounds and conversely basic solutions favour the adsorption of positively charged species. The optimum pHs for the degradation of a series of pollutants by different photocatalysts is given in table 2.2.

Table 2. 2 Optimum solution pH for different photocatalyst-contaminant systems

Pollutant Type	Light source	Photocatalyst	pH range	Optimum pH
Phenol	UV	TiO_2	4.1-12.7	7.4
Chrysoidine Y	UV	TiO_2	3.0-9.0	9.0
m-Nitrophenol	UV	TiO_2	4.1-12.7	8.9
Reactive Blue 4	UV	Nd- ZnO	3.0-13.0	11.0
BPA	Solar	TiO_2	2.0-10.0	6.0
Methylene Blue	Visible	La^{3+}- TiO_2	2.0-10.0	10.0
Supra Blue BRL	Visible	K^+ - TiO_2	4.5-11.8	7.2
Reactive Orange 4	UV	F - TiO_2	1.0-9.0	3.0
Acid Red 88	Visible	Ag - TiO_2	0.2-1.8	1.8
Remazol Brilliant Blue R	Solar	TiO_2	3.0-11.0	3.0
Disperse Blue 1	UV	TiO_2	3.0-11.0	3.0
Methyl Orange	UV	Pt - TiO_2	2.5-11.0	2.5
Amaranth	UV	TiO_2	3.45-9.31	7.73
Bismarck	UV	TiO_2	3.25-7.85	3.25
Acid Orange 8	UV	TiO_2	3.0-11.0	9.0
Acid Blue 45	UV	TiO_2	2.05-10.05	5.8
Acridine Orange	Visible	ZnO	2.9-7.1	7.1
Bromothymol	UV	TiO_2	2.2-9.0	4.35
Fast Green FCF	UV	TiO_2	3.0-11.0	4.4
Methyl Red	UV	Ag - TiO_2	3.0-13.0	3.0-10.0
Acid Blue 80	Solar	TiO_2	2.0-10.0	10.0
Acid Red 29	UV	TiO_2	3.0-10.5	10.5

2.5.7.4 Wavelength and Intensity of Light

The wavelength required for the activation of the photocatalyst is dictated by its bandgap. Ideally photocatalysts have band gaps lower than 3 eV to use the visible portion of the solar spectrum. UV light whilst more energetic than visible light, it only makes up around 5% of the solar spectrum [72]. Matthews *et al.* reported that degradation of phenol and salicylic acid was higher at 254 nm (UVC) than at 350 nm (UVA). This is due to the higher energy of the photons at 254 nm. The atmosphere filters out UVC and thus research in UV photocatalysis is mainly carried out using UVA sources. The intensity of the light source has an effect on the number of photons absorbed by the photocatalysis, generally higher intensities translate to higher photon absorbance. Li *et al.* reported that the rate of degradation of rhodamine b increased with an increase in UV intensity. The authors however found the increase in reaction rate was also governed by the concentration of the dye and the catalyst content [73]. In essence,

higher irradiances do not necessarily make up for unfavourable photocatalyst to pollutant ratios.

2.5.7.5 Pollutant Concentration

A high concentration can increase the number of molecules adsorped to the photocatalyst surface, this facilitates the degradation of the pollutants. Venkatachalam *et al.* reported the increase in the degradation rate of 4-chlorophenol as the initial concentration was increased up to 0.194 mM [74]. The authors reported a decrease when the concentration was increased to 0.233 mM. This reduction has been attributed to the UV screening properties of the molecules at high concentrations. High enough concentrations can result in the occupation of all available absorption sites. These require a similarly higher generation rate of ROSs. The rate of ROS generation is however constant unless the irradiance or catalyst concentration are increased. Thus, the degradation rate decreases with increasing pollutant concentration [75].

2.5.7.6 Inhibiting Species

The presence of species other than the target contaminant can affect the rate of reaction. Anions in the solution can scavenge ROSs reducing the concentration available for reaction with the target contaminant. Their reaction with the hydroxyl radical is summarised in equations 2.18 to 2.22 [76]. Devi *et al.* reported the following order in the inhibitive ability of anions: $SO_4^{2-} > Cl^- > HCO_3^- > NO_3^- > C_2O_4^{2-}$ [77]. Rincon *et al.* reported the inhibitive effect of anions on the inactivation of *E.Coli* [78]. The authors ranked the inhibitive effect of the anions as: $Cl^- > NO_3^- > SO_4^{2-} >> HCO_3^- > HPO_4^{2-}$.

Equation 2.18 $CO_3^{2-} + OH\bullet \rightarrow CO_3^{\bullet-} + OH^{\bullet-}$

Equation 2.19 $HCO_3^- + OH\bullet \rightarrow CO_3\bullet + H_2O$

Equation 2.20 $Cl^- + OH\bullet \rightarrow Cl\bullet + OH^-$

Equation 2.21 $SO_4^{2-} + OH\bullet \rightarrow SO_4^{\bullet-} + OH^-$

Equation 2.22 $SO_4^{\bullet-} + H_2O \rightarrow SO_4^{2-} + OH\bullet + H^+$

Afwa *et al.* reported the inhibitive effect of natural organic matter on the photocatalytic degradation of carbamazepine. The authors reported that molecules with a large molecular weight and those possessing extended aromaticity tend to inhibit the

photocatalytic reaction. They also reported that proteins found in wastewater had a deleterious effect on photocatalytic activity [79].

2.6 Synthetic Methods for Viable Photocatalysts

This section will serve as an introduction to the synthetic methods available to produce immobilised photocatalysts. The current treaty will concentrate on the synthesis of TiO_2 based catalysts. This is mainly due to the much-reported photostability and high activity of TiO_2, making it an ideal candidate for prolonged and repeated photocatalytic cycles. This is regarded an essential feature required to provide the necessary reliability for the production of a long-lasting treatment unit. The efficiency of the catalysts will also be discussed with examples from literature.

2.6.1 Sol-Gel Method

The sol-gel method starts with the formation of a colloidal suspension obtained by hydrolysis and polymerisation of precursor compounds. With further polymerisation and loss of solvents a solid gel is produced which can be deposed on solid substrates by spin, dip or spray coating. TiO_2 structures with high crystallinity and specific geometries can be obtained on a variety of substrate materials such as metals, glass and polymeric. Dip coating also allows the formation of thin films on substrates with a complex geometry. The fluidity of the sol-gel allows for the templating of desired structures. Nanotubes or nanorods can be produced by dip-coating templates such as anodic alumina membranes.

Yu *et al.* prepared nanoporous anatase thin films by addition of polyethylene glycol (PEG) to the precursor mix. Pore size could be directly modified by varying the amount of PEG added. A dye degradation test using methyl orange and UV light revealed that the nanoporous coating had photocatalytic properties [80]. Blanco *et al.* reported a similar nanoporous anatase film with a lower electron-hole recombination rate [81]. Photocatalytic degradation of gaseous compounds was reported by Nam and his colleagues [82]. Thin sol-gel films were used successfully by thermally decomposing trichloroethylene. Sol-gel TiO_2 also found use in pilot photocatalytic reactors. Gelover *et al.* reported that TiO_2 immobilised on glass tubes was as effective in breaking down 4-chlorophenol as effectively as suspended TiO_2 nanoparticles [83]. One way of making

TiO_2 more active in the visible region is the inclusion of non-metal dopants. Li *et al.* reported that TiO_2 sol-gels could be nitrogen doped using ethylenediamine as the nitrogen source. The nitrogen doped TiO_2 was found to be extremely efficient in visible light, with a methyl orange degradation rate of 96.6% in 90 minutes. The same efficiency was reported after 8 degradation cycles [84]. A Co-doped boron-nitrogen sol-gel was described by Gombac *et al.* as a viable synthetic route to highly photoactive coatings. They reported that efficiency in terms of the reaction rate for degradation of methyl orange, where the reaction rate increased with time rather than decreased [85]. Another doping strategy involves doping with transition metals. Seery *et al.* produced silver doped TiO_2 sol-gels with enhanced visible light activity due to enhanced absorption by the silver species. They also reported lower electron-hole recombination rates [86].

Despite the flexibility afforded by the ability to coat objects with varied geometries and the ability to dope the photocatalyst in-situ, the method is not without its drawbacks. The process duration is typically long and the metal alkoxides required as feedstocks are expensive. Sol-gel coatings tend to be brittle and tend to delaminate due to the distinct coating-substrate interface. Shrinkage and cracking also occur during the evaporation of the organic solvents used during the drying process. Coating large surfaces can also introduce inhomogeneity in the composition of the material. Heinrichs *et al.* managed to overcome some of the limitations of the process. The authors reported a process which can produce 21 cm X 15 cm using water as a solvent [87, 88]. These findings, whilst promising required several layers to be deposited which required several steps between each deposition, making this a lengthy process.

2.6.2 Physical Vapour Deposition and Chemical Vapour Deposition

In a vapour deposition process a material in vapour form is condensed on a substrate to form a solid material. In the absence of a chemical reaction on the substrate surface, the process is called physical vapour deposition (PVD). In general, the material to be deposited is either in solid or molten form. In a chemical vapour deposition (CVD) process, the material to be deposited is in the form of a gaseous precursor. The precursor reacts either in the atmosphere of the chamber or on the substrate surface to deposit a solid material. Unreacted precursor molecules or reaction by products are then evacuated from the chamber. A variation of CVD is atomic layer deposition (ALD). ALD consists of sequential pulses of gaseous precursors which react with the substrate.

Each precursor-substrate interaction is termed a half-reaction. This process is a self-limiting process and only allows for the formation of a monolayer. Excess precursor is purged out of the system and a second precursor which activates the deposited layer towards further growth is introduced. After re-purging the system, the starting precursor is re-introduced resulting in the deposition of a second monolayer. The process is repeated for a number of cycles until the desired film thickness is achieved [89]. There are various other PVD and CVD technologies, however discussing them in detail is beyond the scope of this review.

Michalcik *et al.* reported the deposition of nano-structured TiO_2 anatase/rutile thin films by PVD. The substrate was mounted on a holder which could be rotated to adjusted the angle of deposition. This resulted in the formation of columnar TiO_2 films amongst other geometries. They reported the successful photocatalytic degradation of the dye acid orange 7 by the PVD produced columnar films. Their efficiency was also reported to be 70% that of the commercially available Degussa P25 [90]. Horakova deposited silver doped TiO, where the deposited silver particles act as charge carrier traps, reducing the frequency of electron-hole recombination [91]. Zhu *et al.* deposited TiN by DC magnetron sputtering which were then oxidised and annealed to produce TiO_2. The resulting layer had a nodular morphology and contained less than 1 at% nitrogen. Crystallinity in the form of anatase was obtained, with a complete conversion of TiN to TiO_2 being recorded. The authors reported the presence of an O-Ti-N bond with nitrogen substituting oxygen in the TiO lattice [92]. They also reported an increase in photocurrent density when the films were exposed to visible light which was attributed to band gap narrowing [93]. Bessergenev deposited anatase on the inside of a quartz tube using a CVD process and installed the tube in a pilot photocatalytic reactor. Under UV irradiation, the solid TiO_2 was just as efficient as commercial nanoparticles in degrading several types of pharmaceuticals and pesticides. They also reported a photocatalyst longevity in excess of two years after periodically flushing the tube with water whilst under UV light [94]. Quesada Gonzalez produced boron doped TiO_2 by CVD where the boron rather than substituting the oxygen was incorporated interstitially. The crystallite size was found to increase with the addition of boron, resulting in lower electron-hole recombination frequencies. An increase in photocatalytic activity compared with undoped CVD anatase was also recorded, where the doped photocatalyst was more efficient in degradation of stearic acid [92].

The high capital investment required for both PVD and CVD somewhat tarnishes the attractiveness of the techniques. The difficulty of PVD in coating substrates with complex shapes can limit the inclusion of materials synthesised via this route to reactors having specific layouts. The process itself is inherently complex, limiting its use for the large-scale production of photocatalysts. The reagents and byproducts involved in the CVD process make the process less than ecofriendly. The rates of deposition of CVD are also low and long process durations are required to deposit thick layers.

2.6.3 Electrochemical oxidation (Anodising)

A nanotubular TiO_2 arrangement has been deemed to favour the photocatalytic processes due to it possessing a high surface area. The tubular nanostructures are reported to possess lower electron-hole recombination frequencies and to have an excellent photocurrent conversion efficiency. Nanotubular TiO_2 structures directly connected to the unoxidized metal allow for facile transport of the photogenerated electrons. In general, anodising is carried out in a two-electrode set-up at constant voltage with the anode being oxidised and the cathode sustaining a gas producing reaction. The anodised surface is modified during the process by a dissolution reaction initiated and supported by the fluoride (F^-) anion. The competition between oxidation and dissolution gives rise to the nanotubular arrangement. The morphology and dimensions of the nanostructures are mainly dependent on the nature of the electrolyte composition, process voltage, electrolyte temperature, and duration [95]. Table 2.3 provides an overview of the evolution of the electrolyte and the morphologies obtained [96].

Table 2. 3 Evolution of anodising processes – effect of electrolytes and potentials on morphology

Generation	Electrolyte Type	Potential	Anodisation Time	Morphology	Main Factor
First generation: Inorganic aqueous electrolytes (HF based electrolyte)	0.5 wt% HF	10-23 V	≥20 min	Short nanotubes. • Length: 200-500 nm • Diameter: 10-100 nm • Wall thickness: 13-27 nm	Potential, Electrolyte
		1-25 V		• Length: 20-1000 nm • Diameter: 15-120 nm • Wall thickness: 20 nm	
	0.3-0.5 wt% HF + 1M H_3PO_4		2 h		
Second generation: Buffered electrolytes (F^- based electrolytes)	1M Na_2SO_4 + 0.1-1.0 wt% NaF	20V	10 min-6 h	Rough wall with rings. • Length: 0.5-2.4 µm • Diameter: 100 nm • Wall thickness: 12 ± 2 nm	Potential, pH, time
	1M $(NH_4)_2SO_4$ + 0.5 wt% NH_4F	20V	15-30 min	• Length: 0.5-1.0 µm • Diameter: 90-110 nm	
Third generation: Organic electrolyte containing F^- ions)	0.5 wt% NH_4F + 0-5 wt% H_2O in glycerol	20 V	13 h	Smooth tube. • Length: 70 µm • Diameter: ≈ 40 nm • Wall thickness: 12 ± 2 nm	Potential, water content, time
	0.1-0.7 wt% NH_4F + 2-3.5 wt% H_2O in ethylene glycol	60 V	216 h	Ultra-long tube • Length: 1000 µm • Diameter: 120 ± 10 nm	
Fourth generation: Fluoride free electrolytes	0.01-3M $HClO_4$	15-60 V	1 min	Disordered tubes. • Length: 30 µm • Diameter: 20-40 nm • Wall thickness: 10 nm	Electrolyte, time

Whilst some degree of crystallinity is achieved during the anodization process itself, the as formed nanotubes must be annealed in order to obtain anatase. Temperature ranges between 400 and 500°C have been successfully been used. Higher temperatures commonly result in the breakdown of the nanotubular structure. Macak *et al.* reported the successful degradation of both acid orange 7 and methylene blue after UV exposure. Complete degradation was obtained for nanotubes with a length of 4.5µm. The authors also compared the photocatalytic efficiency of the nanotube arrays with that of Degussa P25. The efficiency of the nanoparticle suspension was less than that of the shortest nanotubes (0.5 µm). Despite the lower surface area of the tubes the tubular geometry

reduces the frequency of electron-hole recombination. The tubular structure also provides a shorter path for the dye molecule to travel from the solution to the active catalyst surface [97].

The work presented in this thesis will be based on the assessment of TiO_2 nanotubes as suitable photocatalysts for greywater treatment. Anodising is a cost-effective synthetic route which comes with several attractive properties not found in other methods. Anodising allows for the synthesis of well aligned tubes with high aspect ratios without the need of templating to produce the desired geometry. In anodising the tubes are grown directly from the substrate. The process parameters can also be easily modified to produce tubes with the dimensions required for a specific application [98]. Section 2.7 will provide a more in detail look into the mechanism behind the synthesis of the nanotubes and the effect of the anodising process parameters on the photocatalysts.

2.7 Anodising – A Facile Way of Producing Supported Photocatalysts

Anodisation of titanium allows for the synthesis of highly ordered nanometric self-assembling TiO_2 systems on a solid metallic surface. These nanometric arrays are obtained through a series of field assisted reactions, mainly the field assisted oxidation of titanium and the field assisted dissolution of the formed oxide. The electric field is generated when an external potential is applied on the metal exposed to an electrolyte. The electric field promotes the migration of species present in the electrolyte and in the oxide being formed. The Ti^{4+} cations generated when the voltage is applied can either be solvated by the electrolyte without ever redepositing on the surface as oxides. This is undesirable as it would lead to continuous dissolution of the metal i.e. corrosion. The interaction between the electrolyte and the cations being generated can be however beneficial as it can result in the formation of oxides. The oxidation reaction resulting in the formation of Ti^{4+} cations is given in equation 2.23.

Equation 2.23 $Ti\ (s) \rightarrow Ti^{4+}(aq) + 4e^-$

The process is mainly carried out in a two-electrode set-up with the electrode connected to the positive terminal of a DC power supply being termed the anode. The cathode is connected to the positive terminal. The anode is the electrode on which the oxide layer

is grown, whereas the cathodic reaction is typically the evolution of a gas at the electrode surface.

2.7.1 Mechanistic Details

The formation of the nanometric structures occurs through a series of steps listed below:

1. The surface of titanium metal is naturally covered with an oxide film which forms spontaneously when exposed to air. This is made thicker by the interaction of Ti^{4+} cations present in the oxide surface with O^{2-} and OH^- anions in the electrolyte. Under the influence of the applied electric field, the anions migrate through the oxide layer where they reach the oxide/metal boundary and react with the metal substrate.
2. Ti^{4+} cations migrate from the metal substrate through the metal/oxide boundary under the influence of the electric field. The cations will reach the oxide/electrolyte interface where they react with the anions present in the electrolyte to form the oxide.
3. The applied electric field causes polarisation of the Ti-O bond, weakening it, and causing its dissolution. The Ti^{4+} cations will migrate into the electrolyte whereas the O^{2-} anions migrate through the oxide/metal boundary, reacting with the metal substrate.
4. Modification of the oxide film affords the functionalisation of the oxide films by altering their geometry. The modifier most commonly used during anodising of titanium is the fluoride anion (F^-).

Field assisted oxidation and dissolution (Steps 1 to 3) result in the formation of a uniform thin oxide film over the whole anode. These reactions govern the initial stages of the anodisation process, and in the absence of fluoride, the thickening of the formed oxide would be the only morphological change. The reactions described in steps 1 to 3 can be summarised by using equations 2.24 to 2.26 [95]. The cathodic reaction, which is complementary to the anodic oxidation is given in equation 5. The overall reaction i.e. the combination of the cathodic and anodic reactions is given in equation 2.28 [95].

Equation 2.24 Ti^{4+} (aq) + $4OH^-$ (aq) → $Ti(OH)_4$ (s)

Equation 2.25 Ti^{4+} (aq) + 2 O^{2-} (aq) → TiO_2 (s)

Equation 2.26 $Ti(OH)_4$ (s) → TiO_2 (s) + 2 H_2O (l)

Equation 2.27 $4H^+$ (aq) + $4e^-$ → $2H_2$ (g)

Equation 2.28 Ti (s) + $2H_2O$ (l) → TiO_2 (s)+ H_2 (g)

The introduction of the modifier (Step 4) remodels the structure of the oxide whilst it is still forming. The interplay between growth and dissolution reactions, which occur at different rates and can be controlled, makes anodising a flexible synthetic pathway for nanostructure TiO_2 layers. Despite the fact that anodisation has been practised for nearly a century, research into the anodisation of titanium is more recent. Studies in the role of fluoride in the formation of nanometric structures is even more recent.

Kelly described the surface modification of the oxide film formed on titanium when this is oxidised in dilute sulfuric acid and sodium fluoride (source of F^-) [99]. Current density measurements revealed the role of F^- in the dissolution of the oxide layer formed. The morphology as studied by transmission electron microscopy (TEM) was described as porous with nanometric size pores. Twenty years later, the mechanistic relevance of F^-, was studied by Zwilling and his team [100]. The anodisation of titanium dioxide was carried out in chromic acid and in mixtures of chromic acid and hydrofluoric acid (HF). In the absence of F^- a compact, uniform oxide, was formed. The mixed electrolyte, resulted in the formation of a columnar nanoporous oxide. The thickness of the porous portion of the oxide increased with an increase in applied potential, and porous portion contributed to half the thickness of the oxide oxide. Potentiodynamic studies revealed that pitting preceded pore formation and that the various electrochemical reactions were never stifled but were competing with each other. The reactions at play are, as mentioned earlier, the formation of an oxide and its dissolution at the oxide/electrolyte interface. Zwilling argues that the Cr^{6+} cation poisons the continued growth of the oxide layer, in that once it reaches a specific thickness, further growth doesn't occur [100]. The F^- is seen as the antidote, where it dissolves the oxide layer formed, leading to a continued dissolution/reforming cycle.

The F^- anion is regarded as a pore former, as it initiates localised dissolution of the oxide layer. The F^- reacts with the TiO_2 layer or its hydrated form $Ti(OH)_4$ to produce highly

soluble complexes. This is referred to as chemical dissolution, in the sense that it occurs due to favourable Gibbs free energy of formation (ΔG), rather than due to the effects of the electric field. One such complex, is TiF_6^{2-} with a ΔG of -2118.4kJ/mol [101]. The TiF_6^{2-} complex can also form by combination of F^- and Ti^{4+}, the Ti^{4+} species being formed under field assisted dissolution conditions. The equation for the reaction is given in equation 2.29. Equations 2.30 and 2.31 describe the fluoride induced localised dissolution of the surface oxide layer which leads to pit initiation. A schematic summarising the anodising process for the formation of TiO_2 nanotubes is given in Figure 2.13.

Equation 2.29 $Ti^{4+}(aq) + 6F^-(aq) \rightarrow TiF_6^{2-}(aq)$

Equation 2.30 $TiO_2(s) + 6F^-(aq) + 4H^+ \rightarrow TiF_6^{2-}(aq) + 2H_2O$

Equation 2.31 $TiOH_4(s) + 6F^-(aq) \rightarrow TiF_6^{2-}(aq) + 4OH^-(aq)$

The F^- species can penetrate further into the surface layer under the influence of the electric field, concomitantly with the ejection of Ti^{4+}. The pit thins the oxide layer, resulting in an increase in the electric field density at the bottom of the pit. This increase further promotes migration to and from the surface which in turn results in the further deepening and widening of the pore bottom. Adjacent pores interfere with each other, hindering the growth of the individual pores. Eventually the current density at the surface is distributed evenly, resulting in the coalescence of the individual pores into larger pores. The growth of the nanotubes is dependent on the rate of dissolution at the top of the tube which is exposed to the electrolyte and the downward displacement of the oxide layer at the pore bottom. This oxide layer is referred to as the barrier layer, in that it separates the metal substrate from the electrolyte in the tube. Once a steady state between the two dissolution reactions is reached, the maximum tube length is achieved. Another phenomenon, closely related to the flow of ions under the influence of the field is that by which fluoride compounds present in the pore bottom migrate towards the top of the pore. This migration is due to plastic flow, in that the fluoride and oxide species flow to the surface due to electrostriction and volume expansion of the oxide layer. The fluoride species tend to accumulate in areas called cell boundaries i.e. the areas between pores. Species containing Ti-F and Ti-O-F bonds tend to be quite soluble, resulting in the formation of voids between the pores. These voids grow around the pores, resulting

in the transition from a porous morphology to a tubular one. Figure 2.14 outlines the steps involved in the evolution from surface oxide to nanotube.

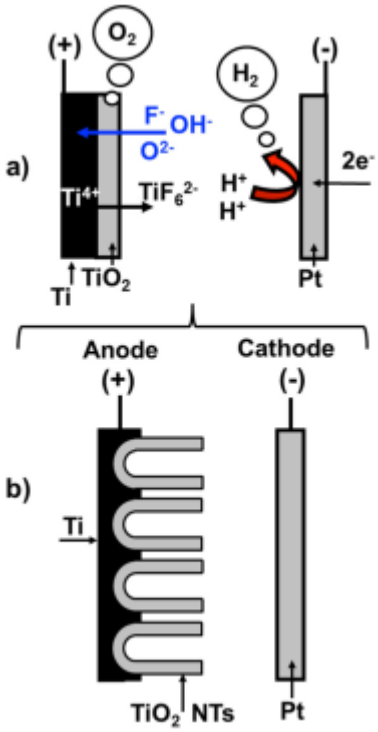

Figure 2. 13 Schematic diagram showing a) Polarity of electrodes in anodising process and reactions at the electrode surface b) Morphology of titanium oxide nano tubes. Adapted from [95]

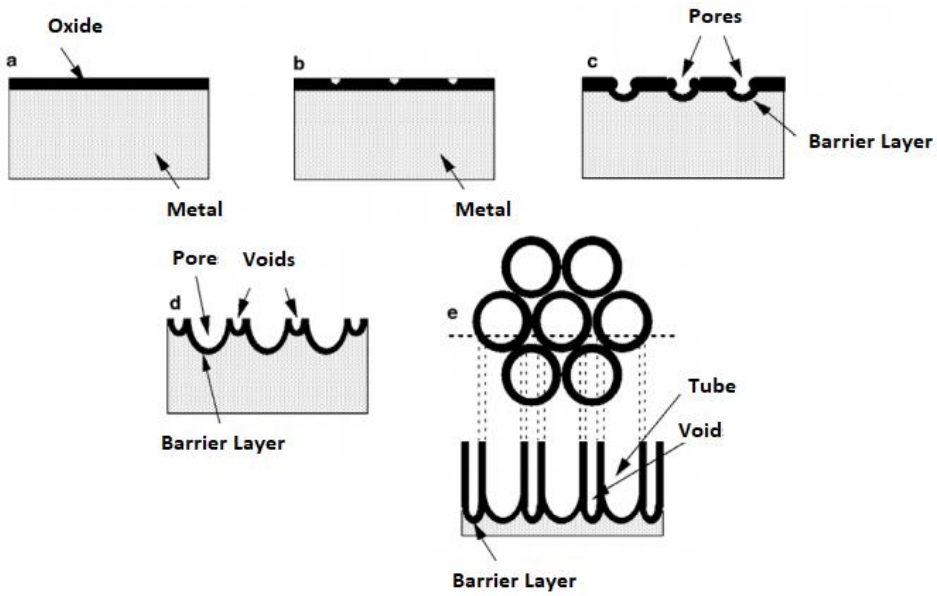

Figure 2. 14 Schematic diagram outlining the steps involved in the evolution of the compact oxide layer to the final nanotubular structure. Adapted from [102]

Figure 2.14 provides photographic evidence of the evolution of nanotubes from an initially compact oxide layer as discussed above and highlighted in figure 2.14.

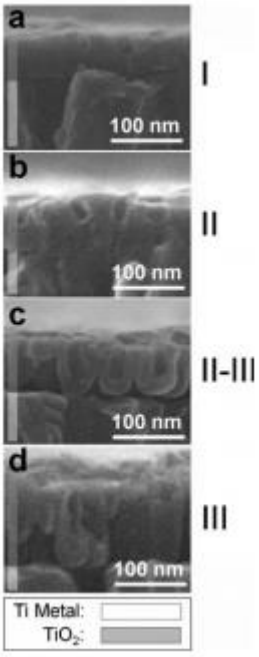

Figure 2. 15 Scannining Electron Micrograph showing the evolution of the oxide layer (a) During the first stage of anodisation a compact oxide layer is formed (b) pores formation by localised thinning of the oxide layer c) Nanotube "embryo" formation d) Stabilisation of growth process. Adapted from [103]

2.7.2 Anodisation Parameters

The mechanistic details given in section 2.7.1 provide a generalised overview on the processes involved in the growth of a stable array of TiO_2 nanotubes on a titanium substrate. Both complications and benefits arise when the process parameters are modified. It is thus imperative that the role of each parameter in the process is well understood together with the implications which arise from its change. The main process parameters are listed and described in detail below.

2.7.2.1 The Electrolyte

The nature of the electrolyte is the parameter with the most variables. A myriad of electrolyte compositions exists, and all modify the surface morphology obtained by the anodisation process. The electrolytes are mainly divided into aqueous and organic, with the main difference being the water content. Aqueous electrolytes are purely water based, whereas organic electrolytes contain lower amounts of water. Water is required

as an oxygen source and to support ionic migration and dissolution reactions. Despite being essential to the process, the water content must never exceed 5% [104]. Higher contents result in the presence of an oxide layer partially covering the pore, restricting the entry of the electrolyte into the growing pore.

The rate of chemical dissolution is dependent on the pH of the solution and the concentration of F^-. A low pH solution favours the dissolution of the formed oxide this is especially true when fluoride ions are added to acidic electrolytes. Such solutions etch the top of the pore, directly competing with the lengthening of the tube. Neutral or near neutral solutions tend to favour the formation of longer nanotubes since the etching effect is diminished. Gong *et al.* used dilute HF solutions (0.5 wt%) and managed to get 250nm long tubes which however had a poor surface arrangement in that the pore shape and diameter was extremely varied [105]. Typically, a F^- content between 0.3 and 0.5 wt% is used. This range allows the formation of nanotubes with excessive dissolution of both the oxide and the titanium substrate. Concentrations exceeding 1% result in electropolishing of the titanium.

The temperature of the electrolyte has an effect on the growth characteristics of the nanotubes. In aqueous electrolytes temperatures are kept close to room temperature (20 -25˚C).

2.7.2.2 Anodising Potential

Anodisation can be carried out either under potentiostatic or galvanostatic control. Galvanostatic conditions indicate a constant current being imparted on the anode. This is perhaps the least common method of anodising as although growth of nanometric features is fast, it lacks the control afforded by the galvanostatic method. Taveira *et al* reported fluctuations in the potential when the current density exceeded 2 mA cm^{-2}. This resulted in variation between runs despite using identical process parameters [106]. Overmeere attributed these fluctuations to stresses in the oxide layer which result in the breakdown in weakened spots on the oxide [107]. It is of interest to note that both Taveira and Overmeere used aqueous electrolytes. The galvanostatic method involves maintaining a constant potential difference between the anode and the cathode.

The type of electrolyte affects the applied potential range. Low potentials of up to 30V are used with aqueous electrolytes whereas potentials up to 60V can be used with

organic electrolytes. The applied potential affects the electric field strength which in turn affects ionic mobility. The ionic mobility governs the pore diameter, interpore distance and final tube length.

2.7.2.3 Anodisation Time

The selection of an appropriate time is dependent on the electrolyte, fluoride ion concentration and the potential. Anodisation periods not longer than 2 hours are used with aqueous acidic fluoride electrolytes despite the fact that nanoporous structures are obtained after as little as 10 minutes [97]. The additional anodisation time allows for the formation of self-arranged arrays of nanotubes. Regonini and Clemens reported the growth of nanotubes after 20 minutes of anodisation in an ethylene glycol-based electrolyte [108]. Anodising in the milder electrolyte appears to result in the synthesis of ordered nanotubular structures quicker than when aqueous electrolytes are used. One drawback of using an organic electrolyte, is the incomplete dissolution of the oxide layer at the pore mouth [109]. This reduces the ingress of F^- into the pore resulting in shorter nanotubes. Longer anodisation times of several hours are required to form longer nanotubes. Regonini *et al* however observed the collapse of the nanotubular array when extending the anodising time beyond 60 minutes. On anodising for 120 minutes, clusters of nanotubes, rather than a completely covered surface remained. This highlights the importance of the concentration of the oxygen sources, in this case water. Too high a water content results in the dissolution of areas of the synthesised nanotubes, resulting in their collapse[110, 111].

2.8 Photocatalytic Activity of TiO_2 Nanotube Arrays

Macak et al. reported the successful degradation of both acid orange 7 and methylene blue after UV exposure. Complete degradation was obtained for nanotubes with a length of 4.5µm. The authors also compared the photocatalytic efficiency of the nanotube arrays with that of Degussa P25. The efficiency of the nanoparticle suspension was less than that of the shortest nanotubes (0.5 µm). Despite the lower surface area of the tubes the tubular geometry reduces the frequency of electron-hole recombination. The tubular structure also provides a shorter path for the dye molecule to travel from the solution to the active catalyst surface[112].

Sreekantan reported the complete degradation of methyl orange after 5-hour exposure to UV light for nanotubes annealed at 500°C. Nanotubes annealed at 600 and 700°C showed a lower photocatalytic efficiency. This was explained by the conversion of anatase to rutile and breakdown at the nanotube base[113].

The introduction of transition metals has been reported to reduce the band-gap of the semiconductor, shifting the photocatalytic activity to the visible region. Gracien et al. described a three-step electrochemical method to introduce transition metal particles within the nanotubular arrangement. A primary anodization step produced a porous surface for electrodeposition of cobalt, chromium and manganese. The electrodeposited metal particles were incorporated into a nanoporous TiO_2 by a second anodization process. The authors reported the manganese doped TiO_2 as the more efficient photocatalyst [114]. A one step doping strategy was provided by Momeni and colleagues where potassium permanganate was added directly to the electrolyte used for anodising. The authors reported a decrease in the band gap from 3.22eV to 2.72eV. This was verified by the photodegradation of methylene blue in visible light, where after 120 minutes, a reduction in absorbance of 95% was reported. No visible light activity was reported for the undoped TiO_2[115]. Hua et al. reported a similar one step synthesis where iron was doped into the TiO_2 nanotubular structure. A band gap narrowing from 3.20 from 2.70 was reported. Visible light degradation efficiency of phenol was reported to be 75% after an exposure time of 240 minutes [116].

Non-metal doping has also been found to be suitable for band gap narrowing. Nitrogen doping has been found to be extremely attractive because of the formation of an energy level above the valance band of TiO_2. This causes the much-desired band gap narrowing. Mazierski et al. reported a one-step doping method where urea is added as the nitrogen source. The authors reported a band gap narrowing from 3.30eV to 2.75eV. They also reported the successful degradation of phenol under visible light exposure [117]. Lai et al. reported similar results despite using a different doping strategy. In their research, as anodised titanium sheets were immersed in 1M ammonia solution and left to impregnate for 10 hours after which the samples were annealed. The photocatalytic efficiency in visible light was assessed by the degradation of methyl orange. An 80% degradation rate was obtained after 60 minutes exposure with the same efficiency being recorded after 10 exposure cycles [118].

Nanotube arrays for use in photocatalytic reactors have only been reported in a small number of publications. A lab scale flat plate reactor using TiO_2 nanotube arrays has been used to study the photocatalytic degradation of parabens [119]. A continuous flow tubular reactor housing TiO_2 nanotubes has been used to acid orange 7, dichloroacetate and 4-chlorophenol [120]. The limited amount of research into the use of TiO_2 nanotubes in prototype reactors is regrettable as field applications are where photocatalysis can be fully exploited.

2.9 Photocatalysis – Limitations and the Way Forward

Despite the obvious capabilities of photocatalysis and AOPs in general for water treatment, their application in real world scenarios is limited. Photocatalysts tend to excel when they are tested in bench-scale reactors where their efficiency might be emphasised more than their limitations or drawbacks. Whilst the academic interest has never waned, with in depth mechanistic studies and advanced synthetic methods described, the industrial implication of photocatalysis is left lagging behind. This is expressed graphically and numerically in figure 2.16. The popularity of TiO_2 as a photocatalyst is immediately clear. The large amount of research involved in expanding the visible light activity is also evident. Both "TiO_2" and "Visible" are the keywords most associated to the total publication count. However on combining "TiO_2" "visible", "reactor" and "pilot" as keywords the number of publications drops down drastically [121].

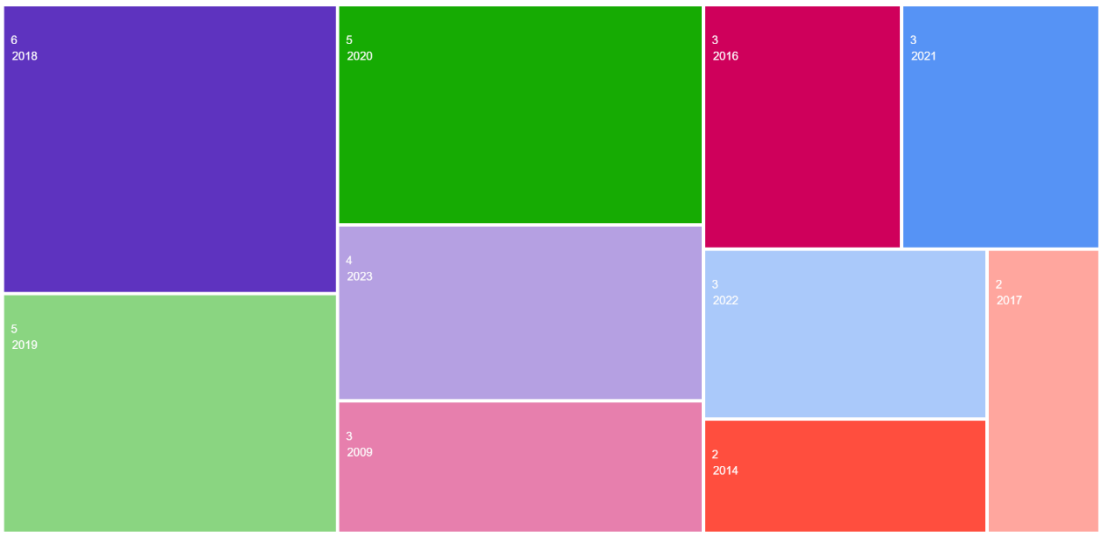

Figure 2. 16 Web of Science publication results for TiO_2 , Visible, Reactor and Pilot as keywords.

The low photo-conversion efficiency remains one of the main hurdles keeping photocatalysis from widespread adaptation. As is typical in a multi-step process, there are losses in efficiency at each step. The quantum yield (Φ), meaning the ratio of the molecules undergoing degradation over the number of photons absorbed by the photocatalysts is characteristically low [122]. One must also keep in mind that during photocatalytic degradation studies, the light applied typically has a single wavelength which is close to the band gap of the material. This ensures that the required energy is constantly and consistently provided. A quantum yield of around 50% was reported for decomposition of hydrogen peroxide using UVC at 254 nm. The quantum yield translated to a nearly 100% OH• production yield [123, 124]. This makes it more efficient than most photocatalytic processes. The paths which lead to a loss in efficiency and the actual efficiencies of a typical photocatalytic process are presented in figure 2.17.

The low quantum yields are further plagued by fact that not all the generated OH• react with the contaminants. The OH• are non-selective species with a high reactivity meaning that they will react with most species found in the water matrix. The presence of natural organic matter and the anions mentioned earlier can compete with the photocatalytic pathway by absorbing the incident light and scavenging the ROSs. Typical laboratory-based studies use simple water matrices to derive repeatable mechanistic data.

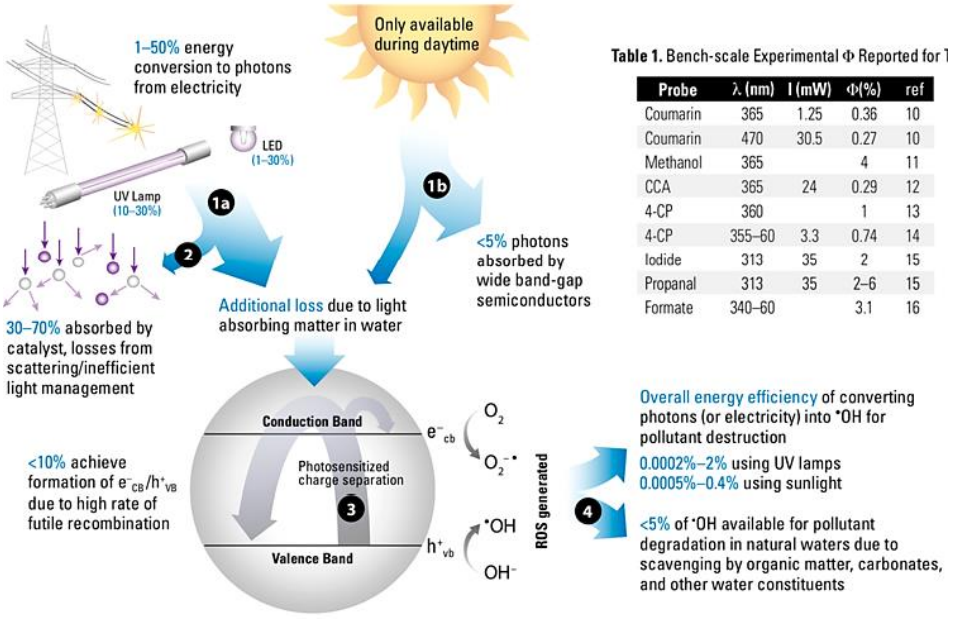

Table 1. Bench-scale Experimental Φ Reported for 1

Probe	λ (nm)	I (mW)	Φ(%)	ref
Coumarin	365	1.25	0.36	10
Coumarin	470	30.5	0.27	10
Methanol	365		4	11
CCA	365	24	0.29	12
4-CP	360		1	13
4-CP	355–60	3.3	0.74	14
Iodide	313	35	2	15
Propanal	313	35	2–6	15
Formate	340–60		3.1	16

Figure 2. 17 Schematic showing pathways by which photocatalytic reaction efficiency is lost .Adapted from [121]

Titanium dioxide is perhaps the most studied photocatalyst. Once its main limitations of high charger carrier recombination rate and wide band gap had been determined, strategies to overcome these difficulties were quickly sought. This constitutes the bulk of the work on photocatalysis. Researchers than ventured into the study and development of other materials without the same limitations as TiO_2. This has turned photocatalysis into more of a materials science area of focus rather than perhaps a more applicable discipline such as chemical engineering. A multitude of materials have been developed which are either expensive, difficult to upscale, chemically and mechanically unstable to overcome the limitations of TiO_2. Long term field assessments of activity, chemical and mechanical stability and cost-effective upscaling practices are scant.

One of the areas which will determine whether photocatalysis can be commercially viable is reactor design. Proper reactor design and optimisation can make up for some of the inherent limitations of photocatalysis. The reactor designs should overcome loss of incident light and slow reaction kinetics. The photocatalysts chosen should also be ideally supported on a substrate to avoid cumbersome separation procedures to recover the catalyst from the treated effluent. The geometry of reactors housing supported catalysts should maximise the incident irradiation by avoiding shadowing by geometrical features of the reactor itself.

Going forward research should shift from determining and enhancing the efficiency of the photocatalysts and into areas to make the technology marketable. Costs of both photocatalysts and other components of the reactors should be considered. The possibility of up-scaled production of both supported photocatalysts and the reactors is equally important. Long term field testing to determine the tendency of the material to foul, deactivate or worse degrade chemically and mechanically in the target water matrix should be carried out. The effect of different process parameters in the operation of the reactors to enhance the productivity of the reactors should be determined.

2.10 References

[1] S. K. Jain and V. P. Singh, "Chapter 1 - Introduction to Water Resources Systems," in *Developments in Water Science*. vol. 51, S. K. Jain and V. P. Singh, Eds., ed: Elsevier, 2003, pp. 3-46.

[2] W. J. Brownlie, H. J. Woods, K. E. Waters, A. L. Moore, A. M. Bruce, J. P. Olszewska*, et al.*, "Freshwater science for the benefit of society: a perspective from early career researchers," *Inland Waters,* vol. 7, pp. 227-235, 2017/04/03 2017.

[3] M. Kummu, J. H. A. Guillaume, H. de Moel, S. Eisner, M. Flörke, M. Porkka*, et al.*, "The world's road to water scarcity: shortage and stress in the 20th century and pathways towards sustainability," *Scientific Reports,* vol. 6, p. 38495, 2016/12/09 2016.

[4] (2018, 20 Oct). *Water Scarcity*. Available: http://www.investinginwater.org/Water+Scarcity/

[5] A. Van de Walle, M. Kim, M. K. Alam, X. Wang, D. Wu, S. R. Dash*, et al.*, "Greywater reuse as a key enabler for improving urban wastewater management," *Environmental Science and Ecotechnology,* vol. 16, p. 100277, 2023/10/01/ 2023.

[6] M. Sanchez, M. J. Rivero, and I. Ortiz, "Photocatalytic oxidation of grey water over titanium dioxide suspensions," *Desalination,* vol. 262, pp. 141-146, 2010/11/15/ 2010.

[7] D. M. Ghaitidak and K. D. Yadav, "Characteristics and treatment of greywater—a review," *Environmental Science and Pollution Research,* vol. 20, pp. 2795-2809, 2013/05/01 2013.

[8] C. Leong and L. Lebel, "Can conformity overcome the yuck factor? Explaining the choice for recycled drinking water," *Journal of Cleaner Production,* vol. 242, p. 118196, 2020/01/01/ 2020.

[9] Meehan, K. Ormerod, and S. Moore, "Remaking Waste as Water: The Governance of Recycled Effluent for Potable Water Supply," *Water Alternatives,* vol. 6, 03/01 2013.

[10] Y. Artioli, "Adsorption," in *Encyclopedia of Ecology*, S. E. Jørgensen and B. D. Fath, Eds., ed Oxford: Academic Press, 2008, pp. 60-65.

[11] A. Hess and E. Morgenroth, "Biological activated carbon filter for greywater post-treatment: Long-term TOC removal with adsorption and biodegradation," *Water Research X,* vol. 13, p. 100113, 2021/12/01/ 2021.

[12] D. E. Speed, "10 - Environmental aspects of planarization processes," in *Advances in Chemical Mechanical Planarization (CMP)*, S. Babu, Ed., ed: Woodhead Publishing, 2016, pp. 229-269.

[13] F. Hourlier, A. Massé, P. Jaouen, A. Lakel, C. Gérente, C. Faur*, et al.*, "Membrane process treatment for greywater recycling: investigations on direct tubular nanofiltration," *Water Science and Technology,* vol. 62, pp. 1544-1550, 2010.

[14] J. Guilbaud, A. Massé, Y. Andrès, F. Combe, and P. Jaouen, "Influence of operating conditions on direct nanofiltration of greywaters: Application to laundry water recycling aboard ships," *Resources, Conservation and Recycling,* vol. 62, pp. 64-70, 2012/05/01/ 2012.

[15] M. Rezakazemi, A. Khajeh, and M. Mesbah, "Membrane filtration of wastewater from gas and oil production," *Environmental Chemistry Letters,* vol. 16, pp. 367-388, 2018/06/01 2018.

[16] C. Preininger, I. Klimant, and O. S. Wolfbeis, "Optical Fiber Sensor for Biological Oxygen Demand," *Analytical Chemistry,* vol. 66, pp. 1841-1846, 1994/06/01 1994.

[17] S. Cortez, P. Teixeira, R. Oliveira, and M. Mota, "Rotating biological contactors: a review on main factors affecting performance," *Reviews in Environmental Science and Bio/Technology,* vol. 7, pp. 155-172, 2008/06/01 2008.

[18] E. Nolde, "Greywater reuse systems for toilet flushing in multi-storey buildings – over ten years experience in Berlin," *Urban Water,* vol. 1, pp. 275-284, 2000/12/01/ 2000.
[19] M. C. Chrispim and M. A. Nolasco, "Greywater treatment using a moving bed biofilm reactor at a university campus in Brazil," *Journal of Cleaner Production,* vol. 142, pp. 290-296, 2017/01/20/ 2017.
[20] E. Friedler, R. Kovalio, and A. Ben-Zvi, "Comparative Study of the Microbial Quality of Greywater treated by Three On-Site Treatment Systems," *Environmental Technology,* vol. 27, pp. 653-663, 2006/06/01 2006.
[21] K. Bani-Melhem, Z. Al-Qodah, M. Al-Shannag, A. Qasaimeh, M. Rasool Qtaishat, and M. Alkasrawi, "On the performance of real grey water treatment using a submerged membrane bioreactor system," *Journal of Membrane Science,* vol. 476, pp. 40-49, 2015/02/15/ 2015.
[22] D. Ghernaout and B. Ghernaout, "Sweep flocculation as a second form of charge neutralisation—a review," *Desalination and Water Treatment,* vol. 44, pp. 15-28, 2012/06/01 2012.
[23] C. Y. Teh, P. M. Budiman, K. P. Y. Shak, and T. Y. Wu, "Recent Advancement of Coagulation–Flocculation and Its Application in Wastewater Treatment," *Industrial & Engineering Chemistry Research,* vol. 55, pp. 4363-4389, 2016/04/27 2016.
[24] D. M. Ghaitidak and K. D. Yadav, "Reuse of greywater: effect of coagulant," *Desalination and Water Treatment,* vol. 54, pp. 2410-2421, 2015/05/29 2015.
[25] A. W. Kalsido, B. Tekola, B. Mogessie, and E. Alemayehu, "Chapter 19 - Excess fluoride issues and mitigation using low-cost techniques from groundwater: A review," in *Cost Effective Technologies for Solid Waste and Wastewater Treatment*, S. Kathi, S. Devipriya, and K. Thamaraiselvi, Eds., ed: Elsevier, 2022, pp. 241-263.
[26] S. Barışçı and O. Turkay, "Domestic greywater treatment by electrocoagulation using hybrid electrode combinations," *Journal of Water Process Engineering,* vol. 10, pp. 56-66, 2016/04/01/ 2016.
[27] P. Patel, S. Gupta, and P. Mondal, "Electrocoagulation process for greywater treatment: Statistical modeling, optimization, cost analysis and sludge management," *Separation and Purification Technology,* vol. 296, p. 121327, 2022/09/01/ 2022.
[28] J. M. Poyatos, M. M. Muñio, M. C. Almecija, J. C. Torres, E. Hontoria, and F. Osorio, "Advanced Oxidation Processes for Wastewater Treatment: State of the Art," *Water, Air, and Soil Pollution,* vol. 205, pp. 187-204, 2010/01/01 2010.
[29] D. Ma, H. Yi, C. Lai, X. Liu, X. Huo, Z. An*, et al.*, "Critical review of advanced oxidation processes in organic wastewater treatment," *Chemosphere,* vol. 275, p. 130104, 2021/07/01/ 2021.
[30] W. Chu and C.-W. Ma, "Quantitative prediction of direct and indirect dye ozonation kinetics," *Water Research,* vol. 34, pp. 3153-3160, 2000/08/15/ 2000.
[31] T. E. Agustina, H. M. Ang, and V. K. Vareek, "A review of synergistic effect of photocatalysis and ozonation on wastewater treatment," *Journal of Photochemistry and Photobiology C: Photochemistry Reviews,* vol. 6, pp. 264-273, 2005/12/01/ 2005.
[32] D. M. A. Alrousan and P. S. M. Dunlop, "Evaluation of ozone-based oxidation and solar advanced oxidation treatment of greywater," *Journal of Environmental Chemical Engineering,* vol. 8, p. 104309, 2020/10/01/ 2020.
[33] R. Vasquez-Medrano, D. Prato-Garcia, and M. Vedrenne, "Chapter 4 - Ferrioxalate-Mediated Processes," in *Advanced Oxidation Processes for Waste Water Treatment*, S. C. Ameta and R. Ameta, Eds., ed: Academic Press, 2018, pp. 89-113.
[34] W. H. Chin, "Greywater treatment by Fenton, Photo-Fenton and UVC/H2O2 processes," 2009.
[35] S. E. Braslavsky, "Glossary of terms used in photochemistry, 3rd edition (IUPAC Recommendations 2006)," *Pure and Applied Chemistry,* vol. 79, pp. 293-465, 2007.

[36] M. B. Tahir, T. Iqbal, M. Rafique, M. S. Rafique, T. Nawaz, and M. Sagir, "Chapter 5 - Nanomaterials for photocatalysis," in *Nanotechnology and Photocatalysis for Environmental Applications*, M. B. Tahir, M. Rafique, and M. S. Rafique, Eds., ed: Elsevier, 2020, pp. 65-76.

[37] A. Fujishima and K. Honda, "Electrochemical Photolysis of Water at a Semiconductor Electrode," *Nature,* vol. 238, pp. 37-38, 1972/07/01 1972.

[38] I. Dincer and C. Zamfirescu, "Chapter 5 - Hydrogen Production by Photonic Energy," in *Sustainable Hydrogen Production*, I. Dincer and C. Zamfirescu, Eds., ed: Elsevier, 2016, pp. 309-391.

[39] M. R. Hoffmann, S. T. Martin, W. Choi, and D. W. Bahnemann, "Environmental Applications of Semiconductor Photocatalysis," *Chemical Reviews,* vol. 95, pp. 69-96, 1995/01/01 1995.

[40] S. H. S. Chan, T. Yeong Wu, J. C. Juan, and C. Y. Teh, "Recent developments of metal oxide semiconductors as photocatalysts in advanced oxidation processes (AOPs) for treatment of dye waste-water," *Journal of Chemical Technology & Biotechnology,* vol. 86, pp. 1130-1158, 2011.

[41] K. M. Lee, C. W. Lai, K. S. Ngai, and J. C. Juan, "Recent developments of zinc oxide based photocatalyst in water treatment technology: A review," *Water Research,* vol. 88, pp. 428-448, 2016/01/01/ 2016.

[42] M. Y. Manuputty, C. S. Lindberg, J. A. H. Dreyer, J. Akroyd, J. Edwards, and M. Kraft, "Understanding the anatase-rutile stability in flame-made TiO2," *Combustion and Flame,* vol. 226, pp. 347-361, 2021/04/01/ 2021.

[43] N. Wetchakun, B. Incessungvorn, K. Wetchakun, and S. Phanichphant, "Influence of calcination temperature on anatase to rutile phase transformation in TiO2 nanoparticles synthesized by the modified sol–gel method," *Materials Letters,* vol. 82, pp. 195-198, 2012/09/01/ 2012.

[44] T. Luttrell, S. Halpegamage, J. Tao, A. Kramer, E. Sutter, and M. Batzill, "Why is anatase a better photocatalyst than rutile? - Model studies on epitaxial TiO2 films," *Scientific Reports,* vol. 4, p. 4043, 2014/02/10 2014.

[45] R. J. Barnes, R. Molina, J. Xu, P. J. Dobson, and I. P. Thompson, "Comparison of TiO2 and ZnO nanoparticles for photocatalytic degradation of methylene blue and the correlated inactivation of gram-positive and gram-negative bacteria," *Journal of Nanoparticle Research,* vol. 15, p. 1432, 2013/01/22 2013.

[46] B. Neppolian, S. Sakthivel, B. Arabindoo, M. Palanichamy, and V. Murugesan, "Degradation of textile dye by solar light using TiO2 and ZnO photocatalysts," *Journal of Environmental Science and Health, Part A,* vol. 34, pp. 1829-1838, 1999/10/01 1999.

[47] C. M. Taylor, A. Ramirez-Canon, J. Wenk, and D. Mattia, "Enhancing the photo-corrosion resistance of ZnO nanowire photocatalysts," *Journal of Hazardous Materials,* vol. 378, p. 120799, 2019/10/15/ 2019.

[48] D. Li and H. Haneda, "Morphologies of zinc oxide particles and their effects on photocatalysis," *Chemosphere,* vol. 51, pp. 129-137, 2003/04/01/ 2003.

[49] P. Salvador, "Mechanisms of water photooxidation at n-TiO2 rutile single crystal oriented electrodes under UV illumination in competition with photocorrosion," *Progress in Surface Science,* vol. 86, pp. 41-58, 2011/01/01/ 2011.

[50] A. Nakajima, S.-i. Koizumi, T. Watanabe, and K. Hashimoto, "Effect of repeated photo-illumination on the wettability conversion of titanium dioxide," *Journal of Photochemistry and Photobiology A: Chemistry,* vol. 146, pp. 129-132, 2001/12/13/ 2001.

[51] N. Roy, Y. Sohn, and D. Pradhan, "Synergy of Low-Energy {101} and High-Energy {001} TiO2 Crystal Facets for Enhanced Photocatalysis," *ACS Nano,* vol. 7, pp. 2532-2540, 2013/03/26 2013.

[52] T. Matsunaga, R. Tomoda, T. Nakajima, and H. Wake, "Photoelectrochemical sterilization of microbial cells by semiconductor powders," *FEMS Microbiology Letters,* vol. 29, pp. 211-214, 1985/08/01/ 1985.

[53] M. S. Vohra, S. M. Selimuzzaman, and M. S. Al-Suwaiyan, "NH4 +-NH3 removal from simulated wastewater using UV-TiO2 photocatalysis: effect of co-pollutants and pH," *Environmental Technology,* vol. 31, pp. 641-654, 2010/05/01 2010.

[54] Y. Li, W. Zhang, J. Niu, and Y. Chen, "Mechanism of Photogenerated Reactive Oxygen Species and Correlation with the Antibacterial Properties of Engineered Metal-Oxide Nanoparticles," *ACS Nano,* vol. 6, pp. 5164-5173, 2012/06/26 2012.

[55] Y. Boyjoo, M. Ang, and V. Pareek, "Photocatalytic Treatment of Shower Water Using a Pilot Scale Reactor," *International Journal of Photoenergy,* vol. 2012, p. 578916, 2012/08/09 2012.

[56] S. Tsoumachidou, T. Velegraki, A. Antoniadis, and I. Poulios, "Greywater as a sustainable water source: A photocatalytic treatment technology under artificial and solar illumination," *Journal of Environmental Management,* vol. 195, pp. 232-241, 2017/06/15/ 2017.

[57] S. Saran, P. Arunkumar, G. Manjari, and S. P. Devipriya, "Reclamation of grey water for non-potable purposes using pilot-scale solar photocatalytic tubular reactors," *Environmental Technology,* vol. 40, pp. 3190-3199, 2019/10/28 2019.

[58] O. Monfort and G. Plesch, "Bismuth vanadate-based semiconductor photocatalysts: a short critical review on the efficiency and the mechanism of photodegradation of organic pollutants," *Environmental Science and Pollution Research,* vol. 25, pp. 19362-19379, 2018/07/01 2018.

[59] S. Bae, P. Borse, S. Hong, J. Jang, J. Lee, E. Jeong*, et al.*, "Photophysical Properties of Nanosized Metal-Doped TiO2 Photocatalyst Working under Visible Light," *Journal of the Korean Physical Society,* vol. 51, pp. S22-S26, 07/31 2007.

[60] M. Khairy and W. Zakaria, "Effect of metal-doping of TiO2 nanoparticles on their photocatalytic activities toward removal of organic dyes," *Egyptian Journal of Petroleum,* vol. 23, pp. 419-426, 2014/12/01/ 2014.

[61] Y. Feng, W.-X. Ji, B.-J. Huang, X.-l. Chen, F. Li, P. Li*, et al.*, "The magnetic and optical properties of 3d transition metal doped SnO2 nanosheets," *RSC Advances,* vol. 5, pp. 24306-24312, 2015.

[62] D. Zhang, J. Gong, J. Ma, G. Han, and Z. Tong, "A facile method for synthesis of N-doped ZnO mesoporous nanospheres and enhanced photocatalytic activity," *Dalton Transactions,* vol. 42, pp. 16556-16561, 2013.

[63] C.-Y. Kuo, C.-H. Wu, J.-T. Wu, and Y.-R. Chen, "Synthesis and characterization of a phosphorus-doped TiO2 immobilized bed for the photodegradation of bisphenol A under UV and sunlight irradiation," *Reaction Kinetics, Mechanisms and Catalysis,* vol. 114, pp. 753-766, 2015.

[64] R. Li, T. Li, and Q. Zhou, "Impact of Titanium Dioxide (TiO2) Modification on Its Application to Pollution Treatment—A Review," *Catalysts,* vol. 10, p. 804, 07/20 2020.

[65] A. Takai and P. V. Kamat, "Capture, Store, and Discharge. Shuttling Photogenerated Electrons across TiO2–Silver Interface," *ACS Nano,* vol. 5, pp. 7369-7376, 2011/09/27 2011.

[66] X. Wang, S. Li, H. Yu, J. Yu, and S. Liu, "Ag2O as a New Visible-Light Photocatalyst: Self-Stability and High Photocatalytic Activity," *Chemistry – A European Journal,* vol. 17, pp. 7777-7780, 2011.

[67] W. Jiang, X. Wang, Z. Wu, X. Yue, S. Yuan, H. Lu*, et al.*, "Silver Oxide as Superb and Stable Photocatalyst under Visible and Near-Infrared Light Irradiation and Its Photocatalytic Mechanism," *Industrial & Engineering Chemistry Research,* vol. 54, pp. 832-841, 2015/01/28 2015.

[68] S. Kohtani, K. Yoshida, T. Maekawa, A. Iwase, A. Kudo, H. Miyabe*, et al.*, "Loading effects of silver oxides upon generation of reactive oxygen species in semiconductor photocatalysis," *Physical Chemistry Chemical Physics,* vol. 10, pp. 2986-2992, 2008.

[69] K. Hashimoto, H. Irie, and A. Fujishima, "TiO2 Photocatalysis: A Historical Overview and Future Prospects," *Japanese Journal of Applied Physics,* vol. 44, p. 8269, 2005/12/08 2005.

[70] Y.-W. Chen and Y.-H. Hsu, "Effects of Reaction Temperature on the Photocatalytic Activity of TiO2 with Pd and Cu Cocatalysts," *Catalysts,* vol. 11, p. 966, 2021.

[71] L. L. P. Lim, R. J. Lynch, and S. I. In, "Comparison of simple and economical photocatalyst immobilisation procedures," *Applied Catalysis A: General,* vol. 365, pp. 214-221, 2009/08/31/ 2009.

[72] S. Malato-Rodríguez, "Solar Detoxification and Disinfection," in *Encyclopedia of Energy*, C. J. Cleveland, Ed., ed New York: Elsevier, 2004, pp. 587-596.

[73] Y. Li, S. Sun, M. Ma, Y. Ouyang, and W. Yan, "Kinetic study and model of the photocatalytic degradation of rhodamine B (RhB) by a TiO2-coated activated carbon catalyst: Effects of initial RhB content, light intensity and TiO2 content in the catalyst," *Chemical Engineering Journal,* vol. 142, pp. 147-155, 2008/08/15/ 2008.

[74] N. Venkatachalam, M. Palanichamy, and V. Murugesan, "Sol–gel preparation and characterization of alkaline earth metal doped nano TiO2: Efficient photocatalytic degradation of 4-chlorophenol," *Journal of Molecular Catalysis A: Chemical,* vol. 273, pp. 177-185, 2007/08/01/ 2007.

[75] W. Bahnemann, M. Muneer, and M. M. Haque, "Titanium dioxide-mediated photocatalysed degradation of few selected organic pollutants in aqueous suspensions," *Catalysis Today,* vol. 124, pp. 133-148, 2007/06/30/ 2007.

[76] M. A. Rauf and S. S. Ashraf, "Fundamental principles and application of heterogeneous photocatalytic degradation of dyes in solution," *Chemical Engineering Journal,* vol. 151, pp. 10-18, 2009/08/15/ 2009.

[77] L. Gomathi Devi, B. Narasimha Murthy, and S. Girish Kumar, "Heterogeneous photo catalytic degradation of anionic and cationic dyes over TiO2 and TiO2 doped with Mo6+ ions under solar light: Correlation of dye structure and its adsorptive tendency on the degradation rate," *Chemosphere,* vol. 76, pp. 1163-1166, 2009/08/01/ 2009.

[78] A.-G. Rincón and C. Pulgarin, "Effect of pH, inorganic ions, organic matter and H2O2 on E. coli K12 photocatalytic inactivation by TiO2: Implications in solar water disinfection," *Applied Catalysis B: Environmental,* vol. 51, pp. 283-302, 2004/08/25/ 2004.

[79] D. Awfa, M. Ateia, M. Fujii, and C. Yoshimura, "Photocatalytic degradation of organic micropollutants: Inhibition mechanisms by different fractions of natural organic matter," *Water Research,* vol. 174, p. 115643, 2020/05/01/ 2020.

[80] J. Yu, X. Zhao, and Q. Zhao, "Effect of surface structure on photocatalytic activity of TiO2 thin films prepared by sol-gel method," *Thin Solid Films,* vol. 379, pp. 7-14, 2000/12/08/ 2000.

[81] E. Blanco, J. M. González-Leal, and M. Ramírez-del Solar, "Photocatalytic TiO2 sol–gel thin films: Optical and morphological characterization," *Solar Energy,* vol. 122, pp. 11-23, 2015/12/01/ 2015.

[82] H. J. Nam, T. Amemiya, M. Murabayashi, and K. Itoh, "Photocatalytic Activity of Sol−Gel TiO2 Thin Films on Various Kinds of Glass Substrates: The Effects of Na+ and

Primary Particle Size," *The Journal of Physical Chemistry B,* vol. 108, pp. 8254-8259, 2004/06/01 2004.

[83] S. Gelover, P. Mondragón, and A. Jiménez, "Titanium dioxide sol–gel deposited over glass and its application as a photocatalyst for water decontamination," *Journal of Photochemistry and Photobiology A: Chemistry,* vol. 165, pp. 241-246, 2004/07/15/ 2004.

[84] H. Li, Y. Hao, H. Lu, L. Liang, Y. Wang, J. Qiu*, et al.*, "A systematic study on visible-light N-doped TiO2 photocatalyst obtained from ethylenediamine by sol–gel method," *Applied Surface Science,* vol. 344, pp. 112-118, 2015/07/30/ 2015.

[85] V. Gombac, L. De Rogatis, A. Gasparotto, G. Vicario, T. Montini, D. Barreca*, et al.*, "TiO2 nanopowders doped with boron and nitrogen for photocatalytic applications," *Chemical Physics,* vol. 339, pp. 111-123, 2007/10/15/ 2007.

[86] M. K. Seery, R. George, P. Floris, and S. C. Pillai, "Silver doped titanium dioxide nanomaterials for enhanced visible light photocatalysis," *Journal of Photochemistry and Photobiology A: Chemistry,* vol. 189, pp. 258-263, 2007/06/25/ 2007.

[87] B. Heinrichs, S. D. Lambert, G. Léonard, C. Alié, S. Douven, J. Caucheteux*, et al.*, "Upscaling TiO2 sol-gel technology to make it a competitive way for coating manufacture and processing at an industrial scale," *Journal of Sol-Gel Science and Technology,* vol. 107, pp. 244-258, 2023/08/01 2023.

[88] J. G. Mahy, S. D. Lambert, G. L. M. Léonard, A. Zubiaur, P.-Y. Olu, A. Mahmoud*, et al.*, "Towards a large scale aqueous sol-gel synthesis of doped TiO2: Study of various metallic dopings for the photocatalytic degradation of p-nitrophenol," *Journal of Photochemistry and Photobiology A: Chemistry,* vol. 329, pp. 189-202, 2016/10/01/ 2016.

[89] R. W. Johnson, A. Hultqvist, and S. F. Bent, "A brief review of atomic layer deposition: from fundamentals to applications," *Materials Today,* vol. 17, pp. 236-246, 2014/06/01/ 2014.

[90] Z. Michalcik, M. Horakova, P. Spatenka, S. Klementova, M. Zlamal, and N. Martin, "Photocatalytic Activity of Nanostructured Titanium Dioxide Thin Films," *International Journal of Photoenergy,* vol. 2012, p. 8, 2012.

[91] M. Horakova, N. Martin, E. Aubry, and P. Spatenka, "Photocatalysis of Ag Doped TiOxFilms Prepared at Room Temperature," *Catalysis Letters,* vol. 132, pp. 244-247, September 01 2009.

[92] M. Quesada-González, N. D. Boscher, C. J. Carmalt, and I. P. Parkin, "Interstitial Boron-Doped TiO2 Thin Films: The Significant Effect of Boron on TiO2 Coatings Grown by Atmospheric Pressure Chemical Vapor Deposition," *ACS Applied Materials & Interfaces,* vol. 8, pp. 25024-25029, 2016/09/28 2016.

[93] L. Zhu, J. Xie, X. Cui, J. Shen, X. Yang, and Z. Zhang, "Photoelectrochemical and optical properties of N-doped TiO2 thin films prepared by oxidation of sputtered TiNx films," *Vacuum,* vol. 84, pp. 797-802, 2010/02/04/ 2010.

[94] V. Bessergenev and H. L. Gomes, "Electrical properties of thin-films wide-band gap semiconductor TiO2 prepared by CVD," *physica status solidi c,* vol. 7, pp. 949-952, 2010.

[95] D. Regonini, C. R. Bowen, A. Jaroenworaluck, and R. Stevens, "A review of growth mechanism, structure and crystallinity of anodized TiO2 nanotubes," *Materials Science and Engineering: R: Reports,* vol. 74, pp. 377-406, 2013/12/01/ 2013.

[96] J.-Y. Huang, K.-Q. Zhang, and Y.-K. Lai, "Fabrication, Modification, and Emerging Applications of TiO₂ Nanotube Arrays by Electrochemical Synthesis: A Review," *International Journal of Photoenergy,* vol. 2013, p. 761971, 2013/10/29 2013.

[97] J. M. Macak, M. Zlamal, J. Krysa, and P. Schmuki, "Self-Organized TiO2 Nanotube Layers as Highly Efficient Photocatalysts," *Small,* vol. 3, pp. 300-304, 2007/02/05 2007.

[98] R. R. Ikreedeegh, M. A. Hossen, M. Tahir, and A. A. Aziz, "A comprehensive review on anodic TiO2 nanotube arrays (TNTAs) and their composite photocatalysts for environmental and energy applications: Fundamentals, recent advances and applications," *Coordination Chemistry Reviews,* vol. 499, p. 215495, 2024/01/15/ 2024.

[99] J. J. Kelly, "The influence of fluoride ions on the passive dissolution of titanium," *Electrochimica Acta,* vol. 24, pp. 1273-1282, 1979/12/01/ 1979.

[100] V. Zwilling, E. Darque-Ceretti, A. Boutry-Forveille, D. David, M. Y. Perrin, and M. Aucouturier, "Structure and physicochemistry of anodic oxide films on titanium and TA6V alloy," *Surface and Interface Analysis,* vol. 27, pp. 629-637, 1999/07/01 1999.

[101] A. Bard, *Standard potentials in aqueous solution*: Routledge, 2017.

[102] G. K. Mor, O. K. Varghese, M. Paulose, N. Mukherjee, and C. A. Grimes, "Fabrication of tapered, conical-shaped titania nanotubes," *Journal of Materials Research,* vol. 18, pp. 2588-2593, 2003/11/01 2003.

[103] S. Berger, J. Kunze, P. Schmuki, D. LeClere, A. T. Valota, P. Skeldon*, et al.*, "A lithographic approach to determine volume expansion factors during anodization: Using the example of initiation and growth of TiO2-nanotubes," *Electrochimica Acta,* vol. 54, pp. 5942-5948, 2009/10/01/ 2009.

[104] M. Paulose, O. K. Varghese, G. K. Mor, C. A. Grimes, and K. G. Ong, "Unprecedented ultra-high hydrogen gas sensitivity in undoped titania nanotubes," *Nanotechnology,* vol. 17, p. 398, 2005/12/14 2006.

[105] D. Gong, C. A. Grimes, O. K. Varghese, W. Hu, R. S. Singh, Z. Chen*, et al.*, "Titanium oxide nanotube arrays prepared by anodic oxidation," *Journal of Materials Research,* vol. 16, pp. 3331-3334, 2001/12/01 2001.

[106] L. Taveira, J. Macak, K. Sirotná, L. Dick, and P. Schmuki, "Voltage Oscillations and Morphology During the Galvanostatic Formation of Self-Organized TiO2 Nanotubes," *Journal of The Electrochemical Society,* vol. 153, 04/01 2006.

[107] Q. Van Overmeere, F. Blaffart, and J. Proost, "What controls the pore spacing in porous anodic oxides?," *Electrochemistry Communications,* vol. 12, pp. 1174-1176, 2010/09/01/ 2010.

[108] D. Regonini and F. J. Clemens, "Anodized TiO2 Nanotubes: Effect of anodizing time on film length, morphology and photoelectrochemical properties," *Materials Letters,* vol. 142, pp. 97-101, 2015/03/01/ 2015.

[109] M. Paulose, L. Peng, K. C. Popat, O. K. Varghese, T. J. LaTempa, N. Bao*, et al.*, "Fabrication of mechanically robust, large area, polycrystalline nanotubular/porous TiO2 membranes," *Journal of Membrane Science,* vol. 319, pp. 199-205, 2008/07/01/ 2008.

[110] D. Regonini, A. Groff, G. D. Sorarù, and F. J. Clemens, "Photoelectrochemical study of anodized TiO2 Nanotubes prepared using low and high H2O contents," *Electrochimica Acta,* vol. 186, pp. 101-111, 2015/12/20/ 2015.

[111] D. Regonini, A. Satka, A. Jaroenworaluck, D. W. E. Allsopp, C. R. Bowen, and R. Stevens, "Factors influencing surface morphology of anodized TiO2 nanotubes," *Electrochimica Acta,* vol. 74, pp. 244-253, 2012/07/15/ 2012.

[112] J. M. Macak, M. Zlamal, J. Krysa, and P. Schmuki, "Self-organized TiO2 nanotube layers as highly efficient photocatalysts," *Small,* vol. 3, pp. 300-4, Feb 2007.

[113] S. Sreekantan, k. a. Saharudin, and C. w. Lai, *Formation of TiO2 nanotubes via anodization and potential applications for photocatalysts, biomedical materials, and photoelectrochemical cell* vol. 21, 2011.

[114] E. B. Gracien, J. Shen, X. Sun, D. Liu, M. Li, S. Yao*, et al.*, "Photocatalytic activity of manganese, chromium and cobalt-doped anatase titanium dioxide nanoporous electrodes produced by re-anodization method," *Thin Solid Films,* vol. 515, pp. 5287-5297, 2007/05/07/ 2007.

[115] M. M. Momeni, M. Hakimian, and A. Kazempour, "In-situ manganese doping of TiO2 nanostructures via single-step electrochemical anodizing of titanium in an electrolyte containing potassium permanganate: A good visible-light photocatalyst," *Ceramics International,* vol. 41, pp. 13692-13701, 2015/12/01/ 2015.

[116] Z. Hua, Z. Dai, X. Bai, Z. Ye, H. Gu, and X. Huang, "A facile one-step electrochemical strategy of doping iron, nitrogen, and fluorine into titania nanotube arrays with enhanced visible light photoactivity," *Journal of Hazardous Materials,* vol. 293, pp. 112-121, 2015/08/15/ 2015.

[117] P. Mazierski, M. Nischk, M. Gołkowska, W. Lisowski, M. Gazda, M. J. Winiarski*, et al.*, "Photocatalytic activity of nitrogen doped TiO2 nanotubes prepared by anodic oxidation: The effect of applied voltage, anodization time and amount of nitrogen dopant," *Applied Catalysis B: Environmental,* vol. 196, pp. 77-88, 2016/11/05/ 2016.

[118] Y.-K. Lai, J.-Y. Huang, H.-F. Zhang, V.-P. Subramaniam, Y.-X. Tang, D.-G. Gong*, et al.*, "Nitrogen-doped TiO2 nanotube array films with enhanced photocatalytic activity under various light sources," *Journal of Hazardous Materials,* vol. 184, pp. 855-863, 2010/12/15/ 2010.

[119] J. Gomes, J. Lincho, E. Domingues, M. Gmurek, P. Mazierski, A. Zaleska-Medynska*, et al.*, "TiO2 nanotube arrays-based reactor for photocatalytic oxidation of parabens mixtures in ultrapure water: Effects of photocatalyst properties, operational parameters and light source," *Science of The Total Environment,* vol. 689, pp. 79-89, 2019/11/01/ 2019.

[120] H.-i. Kim, D. Kim, W. Kim, Y.-C. Ha, S.-J. Sim, S. Kim*, et al.*, "Anodic TiO2 nanotube layer directly formed on the inner surface of Ti pipe for a tubular photocatalytic reactor," *Applied Catalysis A: General,* vol. 521, pp. 174-181, 2016/07/05/ 2016.

[121] S. K. Loeb, P. J. J. Alvarez, J. A. Brame, E. L. Cates, W. Choi, J. Crittenden*, et al.*, "The Technology Horizon for Photocatalytic Water Treatment: Sunrise or Sunset?," *Environmental Science & Technology,* vol. 53, pp. 2937-2947, 2019/03/19 2019.

[122] R. Li and C. Li, "Chapter One - Photocatalytic Water Splitting on Semiconductor-Based Photocatalysts," in *Advances in Catalysis*. vol. 60, C. Song, Ed., ed: Academic Press, 2017, pp. 1-57.

[123] J. C. Mierzwa, R. Rodrigues, and A. C. S. C. Teixeira, "Chapter 2 - UV-Hydrogen Peroxide Processes," in *Advanced Oxidation Processes for Waste Water Treatment*, S. C. Ameta and R. Ameta, Eds., ed: Academic Press, 2018, pp. 13-48.

[124] C.-H. Liao and M. D. Gurol, "Chemical Oxidation by Photolytic Decomposition of Hydrogen Peroxide," *Environmental Science & Technology,* vol. 29, pp. 3007-3014, 1995/12/01 1995.

Chapter 3: Suitability of Anodic TiO_2 Nanotube Arrays (ANTA) for Greywater Reclamation

This chapter will look into the whether ANTA can be viable materials for greywater treatment for further reuse. Despite its widespread applications and wildly claimed capabilities, photocatalysis for water treatment has not progressed to field use [1]. Prototype reactors tend to use photocatalyst powders or slurries which provide a high surface area for reaction [2, 3]. The used catalysts need to be recovered to avoid their release when the treated water is discharged. The need for recovery has been addressed by using supported photocatalysts such as ANTA.

3.1 Methodology

3.1.1 Synthesis of ANTA

Grade 2 commercially pure titanium was used as the substrate (anode) on which the ANTA were grown (99.6, Grandis). A 110 x 25 mm strip was slotted at 25mm intervals to form 4 separate, 25 x 25 mm coupons. Around 1mm of material was retained to hold the 4 coupons together so that they can be anodised together. To the remaining material, a 1 mm titanium wire with the same composition of the material was spot welded. The wire served as a terminal to which the power supply was connected. The geometry of the coupon is presented in figure 3.1. The cathode was made from a strip of the same material having the same width but 120mm in length. The longer cathode ensures that a more uniform electric field is present on the anode [4].

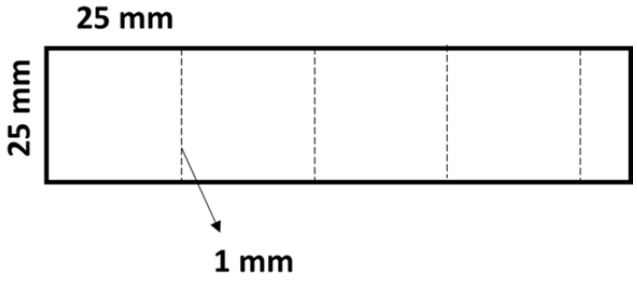

Figure 3. 1 Anode Geometry

The anodisation process was carried out in a typical two-electrode process with the inter-electrode distance fixed at 30mm. Prior to anodising, the electrodes were sonicated sequentially for 10 min in acetone, isopropyl alcohol (IPA) and finally in deionised (DI) water. A Delta Elektronika SM300-20 power supply was used. The process was carried out at room temperature with a magnetic stirrer to agitate the solution. The anodising bath was placed in a water bath to absorb the heat generated during the anodising process. Two litres of electrolyte were used. A schematic of the set-up is presented in figure 3.2. The synthesis of the materials is summarised in table 3.1 and a detailed methodology follows. The main aim of this exercise was to reproduce nanometric structures previously reported in literature and to determine their stability and resistance to fouling over a long period in use (chapter 4) and the possibility of upscaling for use in pilot reactors (chapter 5). In this way a cost-effective solution for possible use in commercial domestic greywater treatment reactors could possibly be found.

The composition of the organic electrolyte was 3 wt% DI water, 0.5 wt% ammonium fluoride (NH4F, Sigma Aldrich) and ethylene glycol (EG, Scharlau) as the balance. A potential of 70 V was applied for 1 h and the resulting TiO_2 nanotube array termed TiO_2NT-EG [5]. Samples of TiO_2 NT-EG were modified by the addition of silver to the surface. A colloidal silver solution was prepared by boiling 200 mL of 5 mM trisodium citrate (Sigma Aldrich) under reflux. To the boiling solution 1 mL of 0.25 mM silver nitrate solution was added and the solution was refluxed for a further 20 minutes. The solution was allowed to reach room temperature after which an equivalent volume of Milli-Q water was added [6]. The nanotube samples were immersed in the solution for 24 hours, after which, the samples rinsed gently with deionized water. These samples were termed TiO_2 NT-Ag

Two materials were synthesised in an aqueous medium. For these materials a lower potential was applied as higher potentials, dissolution of the nanostructure occurs. A potential of 20 V was applied in both instances. The first bath consisted of a solution of 0.5 wt% sodium fluoride (NaF, Sigma Aldich) in 1M phosphoric acid (H_3PO_4, Scharlau) [7]. The process duration was 3 hours and the material was termed TiO_2NT-PA. For second aqueous bath, a 0.5 wt% sodium fluoride solution in 1 M sodium sulfate (Na_2SO_4, Sigma Aldrich) was used [8]. The arrays produced are termed TiO_2 NT-SS and required 6 hours of processing. The as produced materials were rinsed gently with acetone and air-dried. The materials were then annealed for 2 hours at 450°C using a

ramp time of 5°C per minute from room temperature. At the end of the 2-hour process, the materials were allowed to reach room temperature in the furnace. The annealed samples were sonicated for 5 minutes in IPA and air dried.

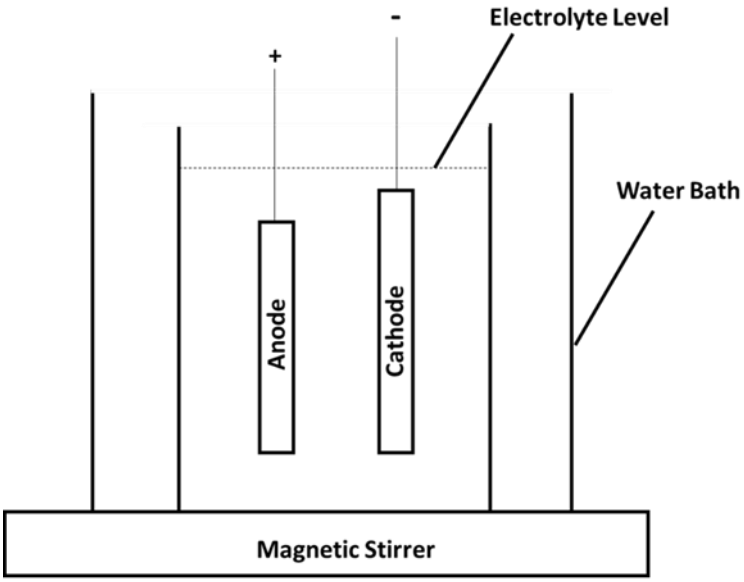

Figure 3. 2 Anodising Setup

Table 3. 1 Summary of Anodising Conditions

Material	Voltage (V)	Duration (Hours)	Electrolyte
TiO_2NT-EG/Ag	70	1	0.5 wt% NH_4F 3 wt% H_2O EG Balance
TiO_2NT-SS	20	6	0.5 wt% NaF 1M Na_2SO_4
TiO_2 NT-PA	20	3	0.5 wt% NaF 1M H_3PO_4

3.1.2 Morphology and Structural Analysis

The morphology of the materials was studied using a Zeiss Merlin field emission scanning electron microscope (SEM, Zeiss). The chemical composition of the surfaces was measured with an Apollo EDAX EDX detector. ImageJ was used for image analysis. Fractographs of the samples were obtained by mechanically cracking the samples and mounting them on a 45° pre-tilted sample holder. The measurements were conducted by calibrating ImageJ against a 200 nm scale bar from one of the SEM images. After calibration, the measure function was used whereby lines were drawn over the morphological feature of interest and the resulting dimensions extracted automatically. When tube diameter and tube wall thicknesses were measured, 50 measurements on each of three randomly chosen samples were carried out. To determine the layer thickness (tube length), ten measurements on each of three randomly chosen samples were carried out. The standard deviation of the measurements was calculated and is presented as the error in table 3.2.

The crystal structure of the catalysts was analysed using a Rigaku Ultima IV Cu-Source X-ray diffractometer. A step size of 0.02 s with a dwell time of 1 s was used spanning a range from 20° to 90°.

3.1.3 Surface Wettability

The surface wettability was determined by measuring the optical contact angle. A 15 µl drop volume was delivered by Dataphysics OCA 25 system. Prior to testing, the surfaces were cleaned by irradiating the samples for 1 h at a wavelength of 365 nm at 10 mW/cm^2 using a UWAVE led This ensured the removal of adsorped hydrocarbons on the surfaces [9]. The surfaces were tested before and after UV exposure. The photoinduced changes to the contact angle were measured after irradiation using a wavelength of 365 nm at 10 mW/cm^2 for 1 hour. Ten independent measurements were carried out on each of three randomly chosen samples. The standard deviation was determined and used to generate the error bars in figures 3.18-3.20.

3.1.4 Optical Properties

Diffuse reflectance spectra (DRS) were recorded on a Shimadzu SolidSpec-3700 UV-VIS spectrophotometer housing an integrating sphere. The scan range was between 200 and 1200nm, sampling at 1nm intervals at medium speed. The data from the DRS was then computed using the Kubelka-Munk function from which the Tauc plot was obtained.

3.1.5 Measurement of Photocatalytic Activity

3.1.5.1 Photocatalytic Degradation of Methylene Blue

The photocatalytic activity of the surfaces towards the degradation of methylene blue (MB) was tested using three different types of radiation. Given that TiO_2 is a wide-band gap semiconductor it was tested using UVA light at 365 nm. To assess the possibility of visible light activity, artificial solar radiation was used, omitting the wavelengths below 400nm. Since MB might contribute towards dye-sensitisation of the photocatalyst, test using visible light was repeated, this time omitting the wavelengths between 500 and 700 nm.

The photocatalytic degradation of methylene blue (MB) under UV light is an oft used method to assess the viability of a material and has been compiled in ISO 10678:2010 [10]. In this work a variation of this method was employed, whereby a lower solution volume of 10 mL was used to ensure ease of comparison between the activities of the different materials. The effect of different solution volumes on the photocatalytic activity is summarised in figure A.1 found in Annex A.

The samples were irradiated at a wavelength of 365nm with an intensity 10 mW/cm^2 using the UWAVE system. This ensured that the only species degraded is the MB molecule by removing any adsorped adventitious hydrocarbons. A single sample was immersed in 10 mL of a 1.5×10^{-5} M MB solution contained in a low-form borosilicate weighing bottle. The height of the solution was around 6 mm. The bottle was closed with its lid and left for one hour in the dark to attain the absorption—desorption equilibrium. The lid was replaced with a quartz sheet to avoid evaporation of the MB solution. The absorbance of the irradiated solution was measured at thirty-minute intervals over four hours. A scan range between 500 and 800 nm was used and the

absorbance at 664 nm was measured on a Perkin Elmer Lambda 35 UV-VIS spectrophotometer. This work was conducted at the Consiglio Nazionale delle Ricerche in Catania,as part of a research placement during the Micro WatTs project. A schematic of the set-up is presented in figure 3.3.

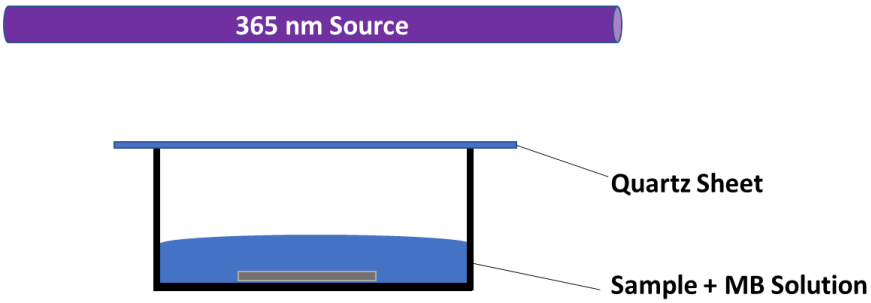

Figure 3. 3 Set-up for chemical pollutant degradation tests

To determine the extent of mineralisation of the MB molecule, the change in total organic carbon (TOC) was determined. The TOC of the solution after four hours of exposure was measured using a Shimadzu TOC-L analyser.

The MB test was repeated using an Oriel VeraSol-2 solar simulator. The instrument covers a range between 300 and 1200nm. The wavelengths below 400 nm i.e. UV were omitted. The TOC value after irradiation was measured. To determine the contribution, if any, of dye sensitisation towards visible light activity, the test was repeated by removing the 500–700 nm range. This range is within which the absorbance of the MB molecule falls.

The activity of 10 randomly chosen coupons was measured. The change in absorbance C/C^0 with time was plotted. The absorbance at an exposure time *t* is termed C and C^0 the starting concentration. The ratio C/C^0 is plotted as the ordinate and the different exposure time intervals as the abscissa. The maximum and minimum error were computed and used to generate the error bars in figures 3.21-3.26.

3.1.5.2 Photocatalytic Degradation of Paracetamol

The tests were conducted using UVA light and repeated using the solar simulator, omitting the wavelengths below 400 nm.

The materials' ability to degrade paracetamol, a ubiquitous analgesic and antipyretic drug was assessed. Paracetamol was found in quantifiable amounts in greywater, despite it not being a common constituent of this wastewater stream [11]. The procedure employed was nearly identical to that for MB. A 1.5×10^{-5} M solution of paracetamol in deionized water was used. The degradation of molecule was followed by measuring the absorbance peak at 243 nm.

The TOC value after four hours of testing was measured to determine the efficiency of the materials for the mineralisation of the pollutant. A 100 ppm as TOC stock solution was prepared from potassium hydrogen phthalate was prepared. From this stock a 10ppm working solution was prepared. Calibration curves ranging from 0-2ppm and 0-10ppm were prepared using the instruments calibration wizard.

Paracetamol was used to study the visible light degradation of a molecule that does not absorb in the visible range of the solar spectrum. The degradation experiment was this time conducted using a reduced solar spectrum omitting the wavelengths below 400nm.

The activity of 10 randomly chosen coupons was measured. The change in absorbance C/C^0 with time was plotted. The absorbance at an exposure time *t* is termed C and C^0 the starting concentration. The ratio C/C^0 is plotted as the ordinate and the different exposure time intervals as the abscissa. The maximum and minimum error were computed and used to generate the error bars in figures 3.27-3.30.

3.1.5.3 Ultraviolet Degradation of Sodium Dodecyl Sulfate

The ability of the ANTA to degrade the anionic surfactant sodium dodecyl sulfate (SDS) was also measured. The surfactant is found in most personal care products and will thus be one of the components of greywater. The test methodology was identical to that used for the two previous contaminants. A 1.5×10^{-5} M solution was similarly used. The absorbance of the solutions before and after irradiation was measured on a HACH DR3900 spectrophotometer. Cuvette kits LCK 332 and LCK 432 for ranges between 0.05- 2.0 and 0.1-4.0 mg/l respectively were used depending on the degree of degradation.

The activity of 3 randomly chosen coupons was measured. The change in absorbance C/C^0 with time was plotted. The absorbance at an exposure time *t* is termed C and C^0 the starting concentration. The ratio C/C^0 is plotted as the ordinate and the different

exposure time intervals as the abscissa. The maximum and minimum error were computed and used to generate the error bars in figures 3.31 and 3.33.

3.1.5.4 Antibacterial Activity Under UV Light

The antibacterial activity of the ANTA was measured as a function of bacterial survival after exposure to UV light. A colony of Escherichia coli strain ATCC® 25922 was transferred aseptically to 100 mL of sterile Luria Bertani (LB) broth (Sigma-Aldrich). The inoculum was incubated overnight at 37°C at 180 RPM constant agitation under aerobic conditions. The optical density at 600 nm was measured the next morning. Suitable 1/10 serial dilutions were prepared from the starting culture. A total of 50 µL from the last three serial dilutions were plated on LB agar plates (Sigma-Aldrich) and incubated overnight at 37°C.

A 'climatic chamber' was produced for each sample. This was composed of a 35 mm petri dish filled with water over which a glass microscope slide was placed. The ANTA samples and a titanium blank were placed over the glass. A 200 µL aliquot from the second serial dilution was transferred to the photocatalyst and spread homogenously over the surface to ensure complete coverage. A quartz glass was placed over the coupons whilst ensuring that the two did not touch. The quartz together with the climatic chamber eliminated the risk of the bacterial culture evaporating. The photocatalysts were irradiated for one hour with a Philips TL8 blacklight at a wavelength of 365nm with an intensity of 3.5 mW/cm^2. The photocatalyst was transferred to a 35 mm petri dish containing 10 mL of phosphate buffered saline (PBS). The petri dish was covered, and the contents shaken manually for one minute. A 50 µL aliquot from the petri dish was plated on LB agar without any further dilution. A series of 1:10 dilutions of the extracted bacteria, were prepared and plated. The plates were then incubated upside down at 37°C overnight. The colonies were counted in the morning. The set-up used for assessing the antibacterial activity is shown in figure 3.4.

The activity of 3 randomly chosen coupons was measured. The maximum and minimum error were computed and used to generate the error bars in figure 3.34.

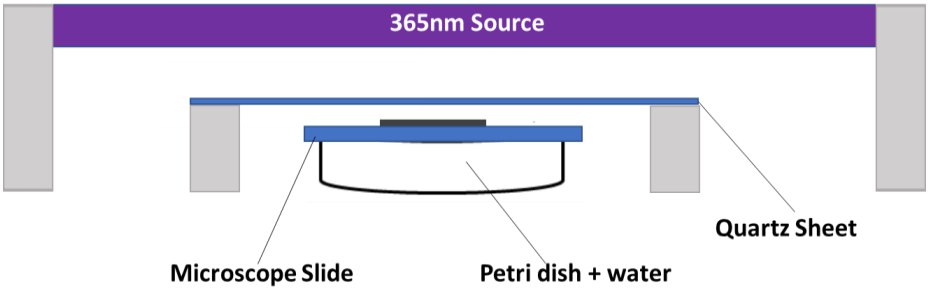

Figure 3.4 Schematic of Antibacterial Activity Assessment

3.1.6: Re-use of Anodising Solution

The stability of the solution and its ability to produce ANTA with a high photocatalytic activity after each cycle was determined.

For the aqueous solutions, the used solutions were left to settle for one hour, after which the supernatant was decanted off. The suspension at the bottom was filtered through a filter paper under gravity. The solution was then stored in an airtight polypropylene (PP) container. Another anodising cycle was conducted the day after. The glycol electrolyte was stored in an identical container and used the day after. The produced samples were processed in an identical fashion to those produced in the fresh solution.

The samples were analysed using electron microscopy and EDX measurements as a simple quality control procedure to study the morphology of the samples. The MB UV degradation test was conducted on the samples produced in the progressively aging electrolyte.

For each anodising cycle 4 coupons were produced. The photocatalytic activity of each was determined and the maximum and minimum error was computed. The errors are presented in figure 3.35.

3.2: Results and Discussion

3.2.1 Preparation and Properties of the Photocatalysts

3.2.1.1 Morphology of the Materials

Nanotubular structures were obtained for the three different anodising processes. The main morphological parameters which contribute towards the photocatalytic activity are listed in table 3.2. Free standing nanotube arrays were produced regardless of the synthetic strategy, but on the other hand the different morphologies are immediately evident. The thicker nanotube arrays belong to TiO_2NT-EG which also possesses the wider tubes. The aqueous electrolytes produced thinner arrays with the thinnest array belonging to TiO_2NT-PA. This is attributed to the low potentials used in conjunction with the aqueous media. The mechanistic details describing the different morphological features follow.

A top view of the nanotubes forming the TiO_2 NT-EG arrays is presented in 3.5(a) The tubes in do not appear as discrete units and are devoid of any spacing between them. Figure 3.5b reveals the presence of a surface layer over the tube walls which appears to be keeping the individual tubes connected together. This layer is part of the compact titanium oxide and hydroxide layer formed within the first stage of the anodising process [12-14]. The remnants of this layer are the result of its incomplete etching. The tubes could have been separated using a longer anodisation process and extensive sonication of the samples. When a longer process was employed, most of the coupons produced suffered from delamination within minutes of being removed from the organic electrolyte. A similar occurrence was recorded when they were rinsed with IPA using a wash bottle. Cao *et al.* reported that large residual stresses are generated at the nanotube-substrate interface which are more likely to lead to poor adhesion in thick layers [15]. The stresses are relieved when the layer delaminates which typically occurs when the surfaces are drying. The presence of a fluoride rich layer at the tube bottom-substrate interface has also been linked to the poor adhesion between the two [16]. Delamination also occurs when the as produced samples are rinsed in water due to the dissolution of the fluoride rich layer [17]. To prevent delamination, the samples were hung from the titanium wire which served as the electrical contact and the excess electrolyte was

allowed to run off the surface. The samples were then rinsed gently with acetone which as a non-polar solvent would dissolve little if any of the soluble oxi-fluoride species fund in the fluoride rich layer.

The layer thickness, shown in figure 3.6, at nearly 10µm stands out immediately and is the result of the applied potential. The use of organic electrolytes allows for potential higher than 20V to be employed without the nanotubular structure collapsing. Application of potentials in excess of 20V in aqueous electrolytes tends to result in anodic dissolution rather than the growth-dissolution mechanism required for nanotube formation. The advantage of using higher potentials is that a stronger electric field is produced which accelerates the migration of fluoride ions towards the anode [18]. The fluoride ions etch the initial compact oxide layer to initiate the nanotube formation mechanism. Higher potentials allow for faster etching rates leading to thicker layers. The tubes are wide, with a range of diameters between 80 and 125 nm. The tube wall thickness is around 10nm.

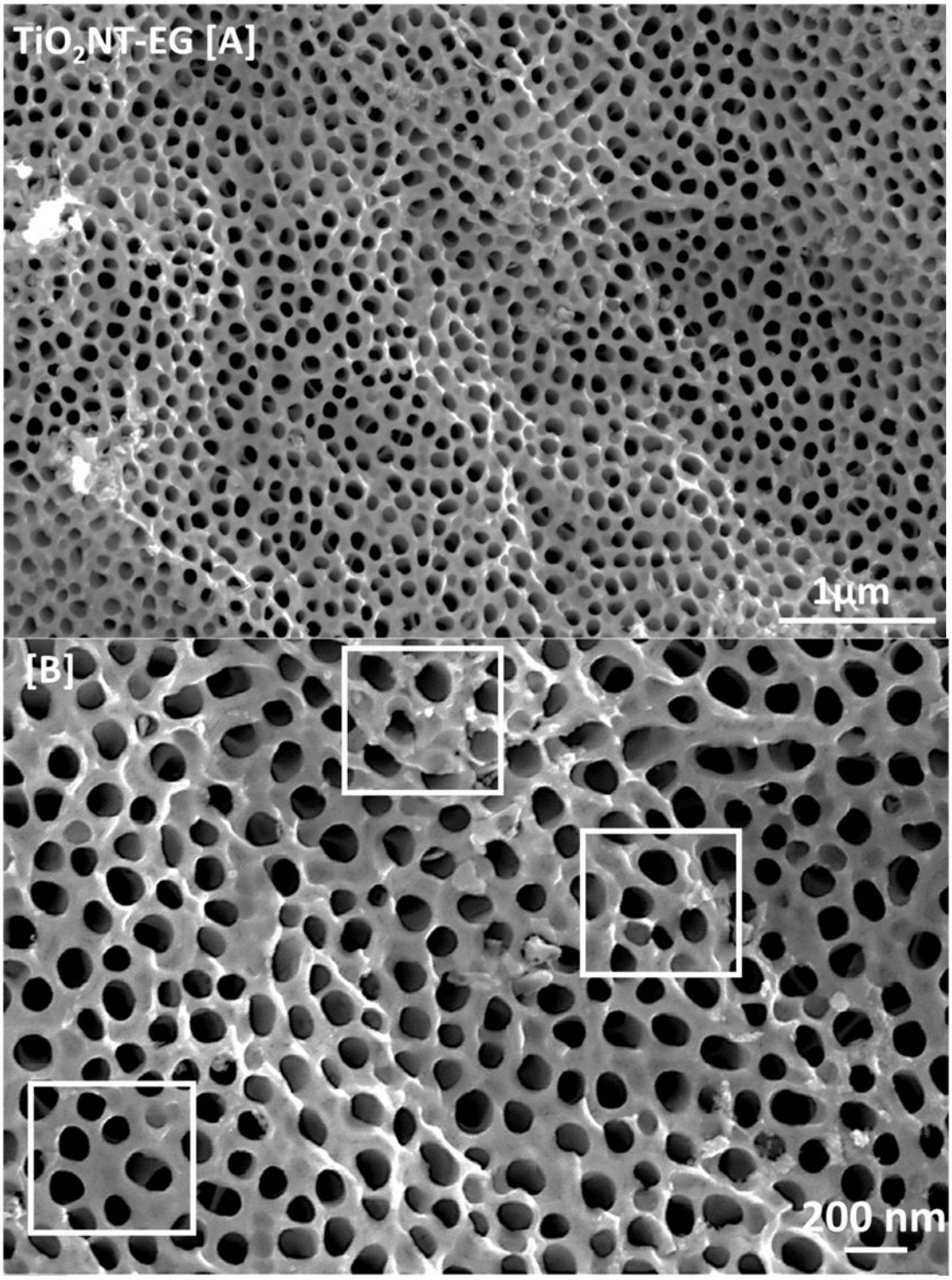

Figure 3.5 (a) Top view of TiO_2 NT-EG arrays **(b)** Detail of remnants of compact oxide-hydroxide layer

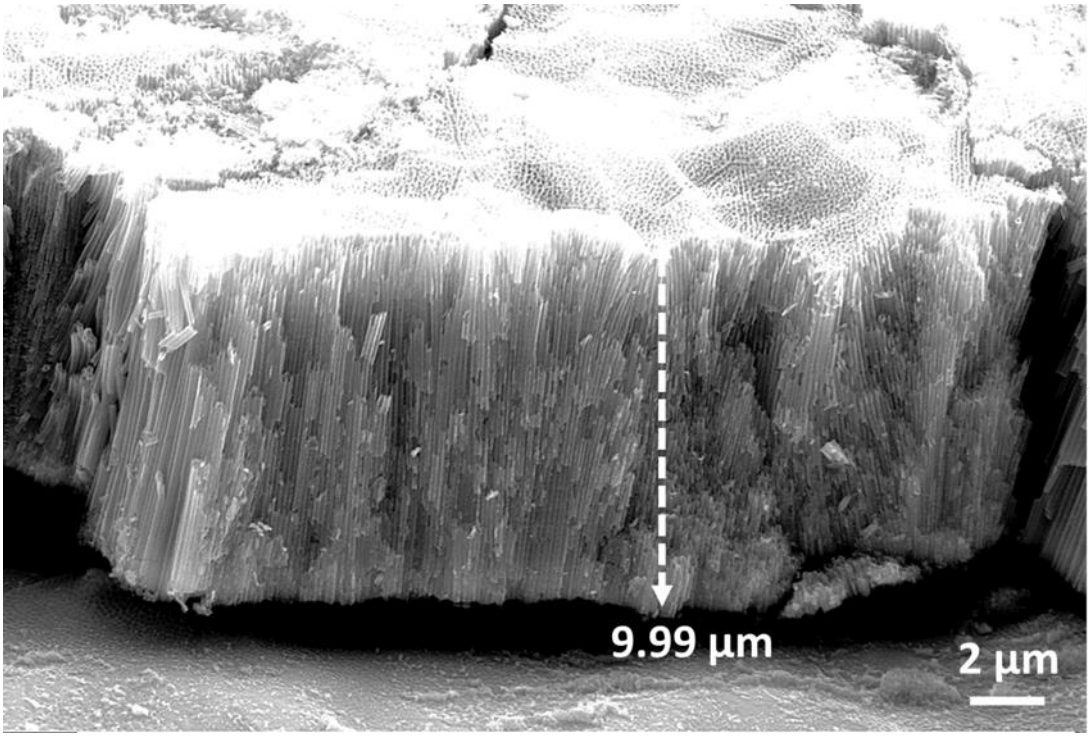

Figure 3. 6 Cross-section view of TiO_2 NT-EG layer

The main morphological parameters for the TiO_2NT-Ag are well within the experimental error and are basically identical. The morphology of the TiO_2NT-Ag nanotubes is given in figure 3.7 a and this however shows some differences when compared to that of TiO_2NT-EG. The individual nanotubes are better defined than those for TiO_2NT-EG and the surface oxide layer appears to be absent. Despite using the same procedure for producing both arrays this difference in morphology highlights the effect of slight variations in current density. A slight increase in current density can result in higher etching rates and thus the better-defined tube tops. Steps such as the larger cathode surface area and mixing the solution were taken to avoid excessive variations in current density. Given that the tube length, diameter and wall thickness are basically identical this slight variation in morphology should not impart any appreciable difference in activity. The other difference is that the surface is decorated with discrete spherical silver nanoparticles ranging between 30 to 110 nm in diameter. The nanoparticles are highlighted in figure 3.7b and their approximate chemical composition is given in the inset. The distribution of the particles over the surface is not uniform and they are wholly absent in some areas. The chemical composition of an area devoid of the nanoparticles is given in figure 3.8. The nanotube pores appear to be blocked by a deposit which has an appreciable silver content. It is likely that silver was deposited as

an oxide or hydroxide within the tubes and also as an agglomerate of several nanoparticles [19]. Ideally all the silver would be deposited in its metallic form in a homogenous manner to form a Schottky Junction at the silver-TiO_2 interface. This junction can prevent the recombination of the electron/hole pairs and extend the activity of the material into the visible spectrum. Despite the lack of homogeneity in the silver content distribution, the silver loaded nanotubes can release silver ions to provide an antibacterial effect. This effect is beneficial as the photocatalysts will have a passive antibacterial effect even in the absence of light [20]. Silver oxide in nanoparticle form has also been reported to possess antibacterial properties [21].

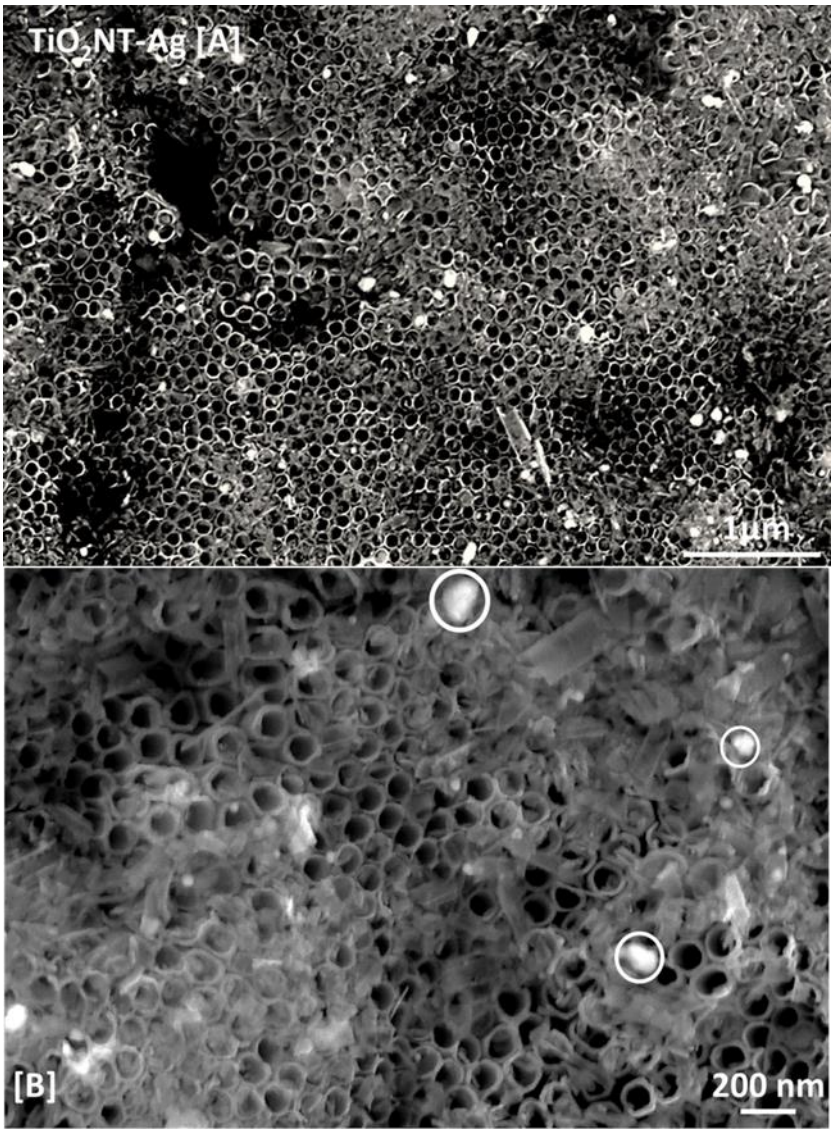

Figure 3. 7 a) Surface morphology of TiO_2 NT-Ag showing Ag nanoparticles b) detailed view of Ag nanoparticles.

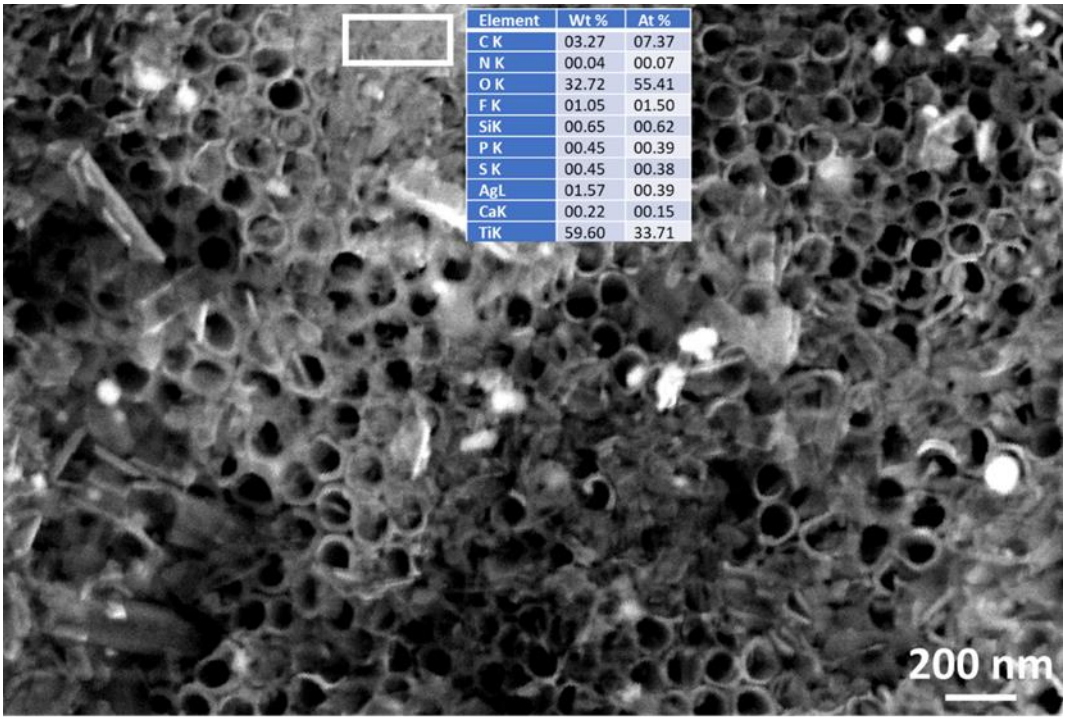

Figure 3. 8 Detail and approximate chemical composition of TiO_2 NT-EG

The TiO_2NT-SS array is presented in figure 3.9a. In contrast to TiO_2 NT-EG it composed of discrete tubes with well-defined inter-tube spaces (figure 3.9b). The stark difference in morphology is attributed to the conductivity of the electrolyte. Aqueous electrolytes have a higher conductivity and can thus promote higher etching rates which as discussed previously can have a deleterious effect at high potentials. The high etch rates also contribute to the more complete dissolution of the initial compact layer. The removal of this layer allows for the formation of nanotubes which are spaced out from their neighbouring tubes [22].

The layer has the second largest thickness at 1.45µm, which is far less than that of materials synthesised in the organic electrolyte (figure 3.10). Despite the longer process duration and the high etch rates afforded by the aqueous electrolyte, the process is most reliant on the applied potential.

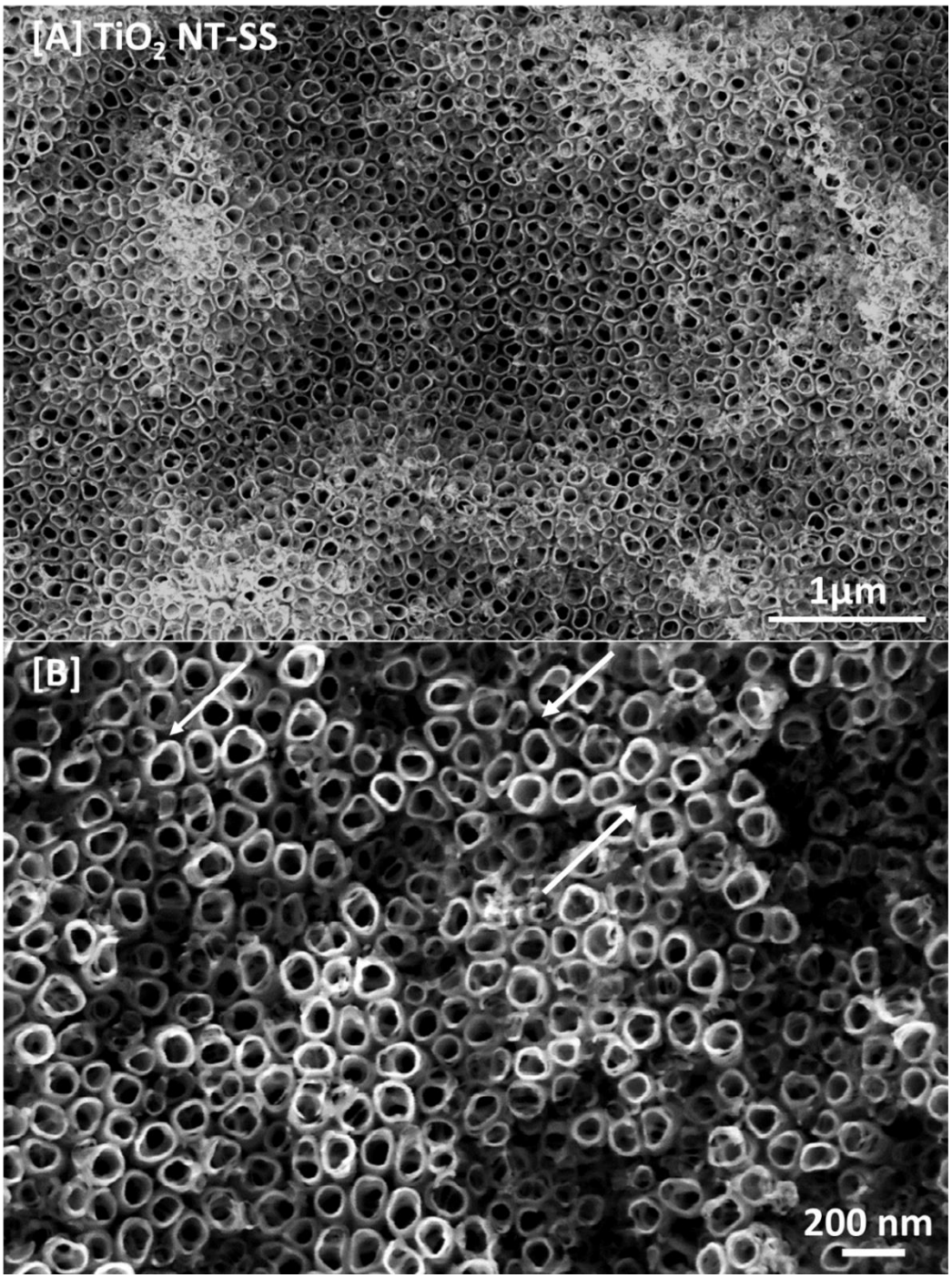

Figure 3. 9 a) Surface morphology of TiO_2 NT-SS array **b)** detail of inter-tube spacing

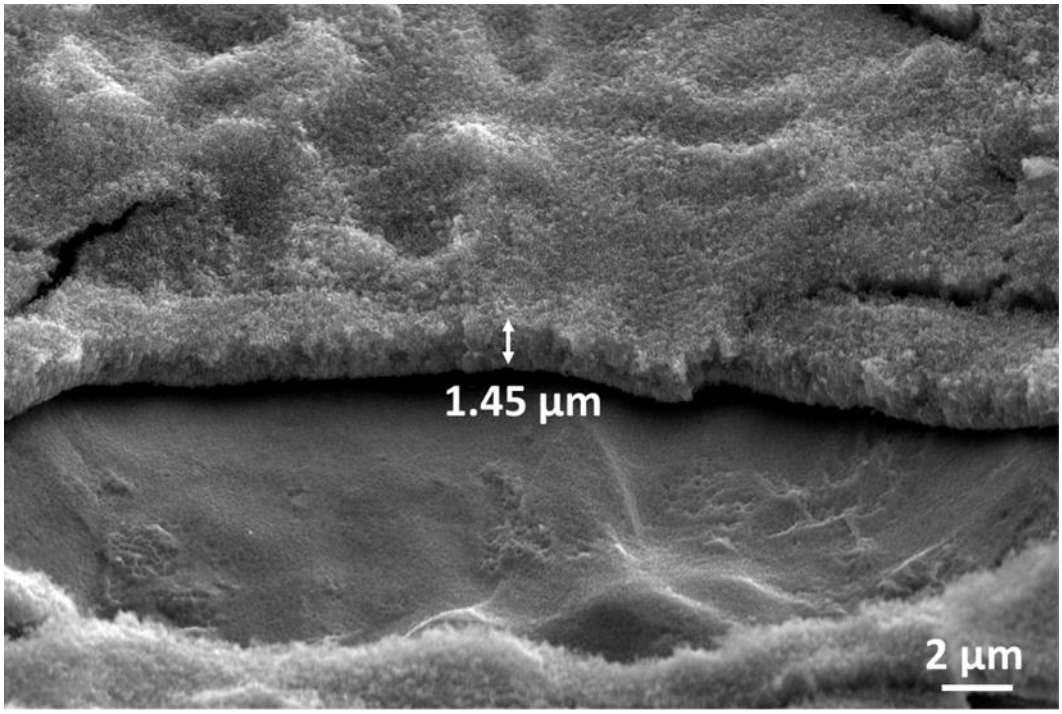

Figure 3. 10 Cross-section view of TiO_2 NT-SS array

The TiO_2 NT-PA array shows a similar surface morphology to that of TiO_2 NT-SS (figure 3.11a). Discrete nanotubes are produced and both materials have the same range of nanotube diameters (figure 3.11b). The cross-section view in figure 3.12 reveals that the main difference between the two materials is the layer thickness. TiO_2 NT-PA at 0.67µm is half as thick as TiO_2 NT-SS. The lower thickness in this case is the result of the shorter process duration when the acidic electrolyte is used

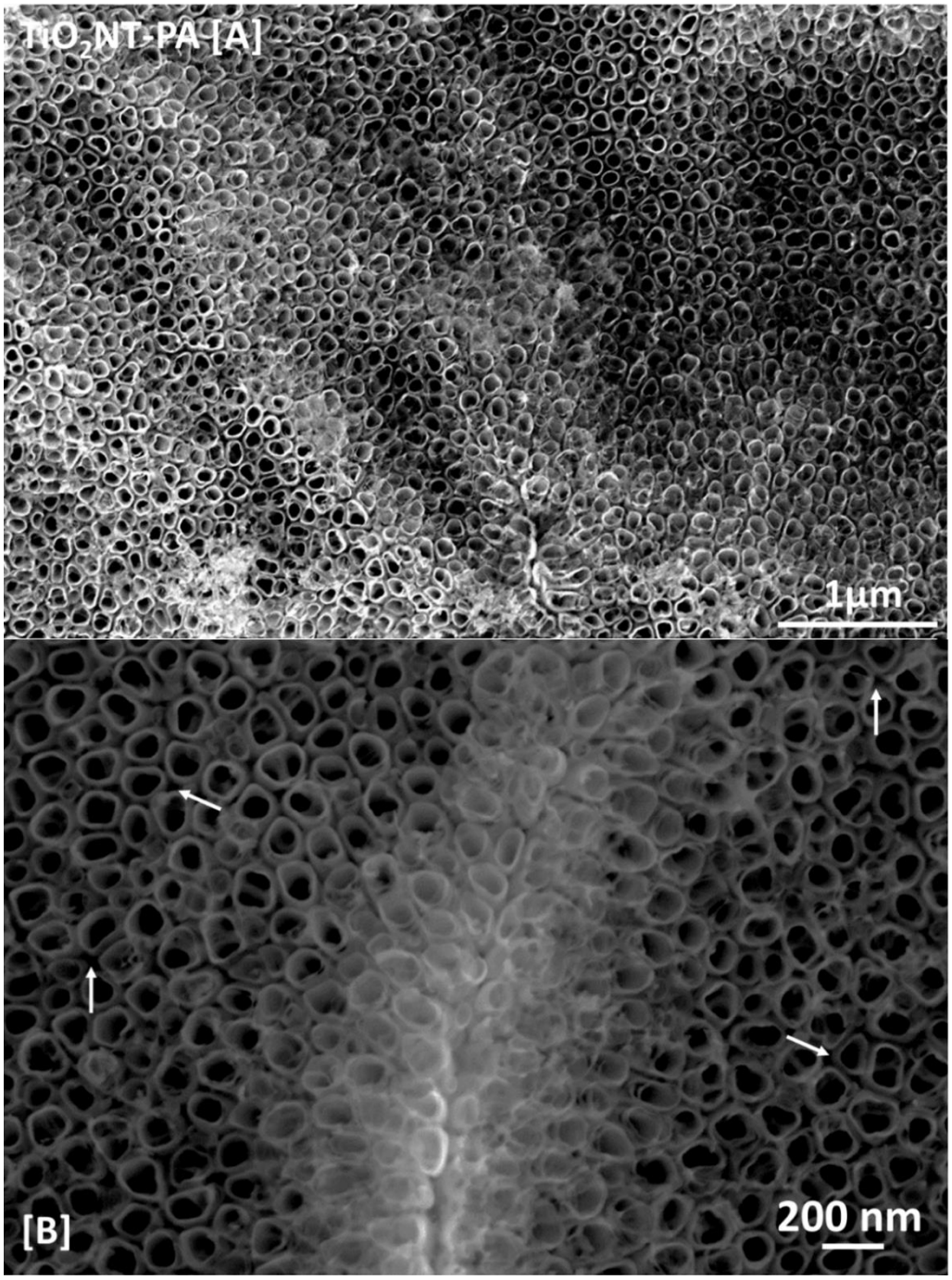

Figure 3. 11 a) Surface morphology of TiO_2 NT-PA array **b)** Detail showing inter-tube spacing

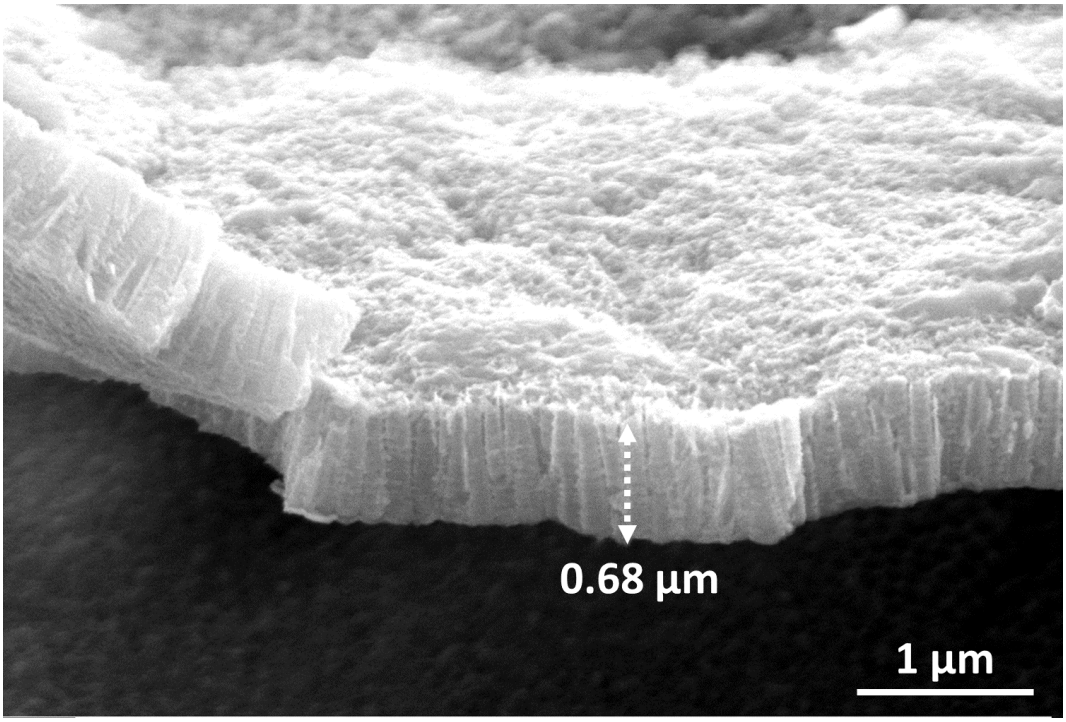

Figure 3. 12 Cross-section view of TiO_2 NT-PA array

The structural features of the nanotubes are one of the factors which contribute to the photocatalytic activity. Adan *et al.* discussed that wider and longer nanotubes tend to enhance the array's activity [23]. Wider nanotubes tend to allow the pollutant molecules to more easily diffuse down the tube length and allow the surfaces to absorb more light both of which enhance the activity of the materials. The same authors also pointed out some drawbacks of having large lengths and diameters. With wider and longer tubes light absorbed deeper into the tube structure will generate charge carriers further away from the surface with the pollutant molecules having to travel further in order to react. By the time the molecule travels down the tube length the charge carriers could potentially already have recombined as their lifespan is typically a few picoseconds [24]. Wider nanotubes also have less photocatalytic material. One advantage of having longer nanotubes might however be their longer longevity. If the tubes are eventually sheared off during use, the overall activity is not hampered as residual material is available for reaction.

Table 3.2 Morphological Parameters of Anodic Nanotube Arrays. Error bars show the standard deviation.

Material	Parameters	Layer Thickness (μm)	Tube Diameter (nm)	Wall Thickness (nm)	Aspect Ratio
TiO_2 NT-EG	70V 1hr	9.99 ± 0.48	85-125 ± 9.3	10.00 ± 2.1	79.92 - 117.52
TiO_2 NT-Ag	70V 1hr	10.11 ± 0.39	85-125 ± 9.3	9.88 ± 1.7	79.92 - 117.52
TiO_2 NT-SS	20V 6hrs	1.45 ± 0.07	60-100 ± 5.8	13.99 ± 2.3	14.50 - 24.17
TiO_2 NT-PA	20V 3hrs	0.68 ± 0.02	60-105 ± 7.1	11.71 ± 2.8	6.48 - 11.33

3.2.2 Crystalline Structure

The possible use of amorphous TiO_2 nanoparticles is extremely attractive, given its ubiquity and low cost. Amorphous TiO_2 nanostructures, however tend to have a high density of defects which reduce the life-time of the generated charge carriers. The fast recombination times severely limit the scope of the material for photocatalytic degradation. To enhance their activity the materials must be either doped or incorporated in a hybrid material.

The annealing temperature and holding time were chosen to promote the formation of anatase over rutile. Rutile forms between 500°C and 600°C and depending on the temperature used a mixed anatase-rutile crystalline structure can be obtained [25]. The ordered nanotubular arrays tend to collapse at temperatures exceeding 600°C [26]. The process time was chosen as it is enough for complete crystallisation of nanomaterial. Longer process times would increase the production costs and the environmental burden of the process. It has been widely reported that anatase is the better photocatalyst of the two allotropes despite it having the larger band-gap. The larger band-gap limits the

activity of the photocatalyst to the UV range. The larger band-gap however has the possibility of increasing the valence band maximum to higher energy levels than the redox potentials of the adsorped molecules. This improves the electron transfer process from the photocatalyst to the molecule, effectively increasing the oxidising capability of the material [27]. Anatase also possesses an indirect band-gap which is at a lower energy value than its direct band-gap which increases the life time of the charge carriers [28].

The XRD patterns of the four materials are presented in figure 3.13. The diffractograms show that the main constituents of all the materials are anatase and titanium. The presence of anatase confirms that the annealing conditions were suitable. The presence of the titanium peaks indicates the pick-up of the substrate during analysis. At 37° a low intensity rutile shoulder was recorded for TiO_2NT-EG and TiO_2NT-Ag. The shoulder is connected to the anatase (103) and (104) phases which are coupled as a bifurcated peak at around 38°. The composition of the electrolyte has also an effect on the preferred crystal orientation of anatase. The materials grown in the organic solution tend to favour the [201] direction whereas those in the aqueous media the [220] direction.

Despite the positive confirmation by both SEM imaging and EDX of the presence silver or silver rich particles on the surface, the relevant peaks were not recorded. Several authors report the detection of the Ag (111) and (002) planes [29-31]. This absence can be attributed to highly dispersed result of the deposition process with the metallic particles being extremely spaced out from each other. This would give rise to a dilution of the signal by that of the more abundant TiO_2 substrate. The immersion process could have also caused the silver bearing solution to enter the tubes whereby any deposition would occur within the length of the tubes. This would undoubtedly make the detection of the metallic particles more difficult. Some authors claim that there is a minimum % wt silver which allows the phases to be detected. Mogal *et al.* recorded distinct peaks belonging to Ag (111), (200) and (220) when a silver content in excess of 2.5 wt% was incorporated within the material [32]. This significant loading was possible as the authors used a sol gel method, which enhances the incorporation of silver within the TiO_2 matrix. Liu *et al.* obtained low intensity peaks at around 1%wt silver by loading silver on TiO_2 nanotube powders under agitation which provides more extensive coverage [33]. For Liang *et al.* to obtain a strong XRD response, the anodic nanotube layer produced had to be nearly fully covered with silver particles [34].

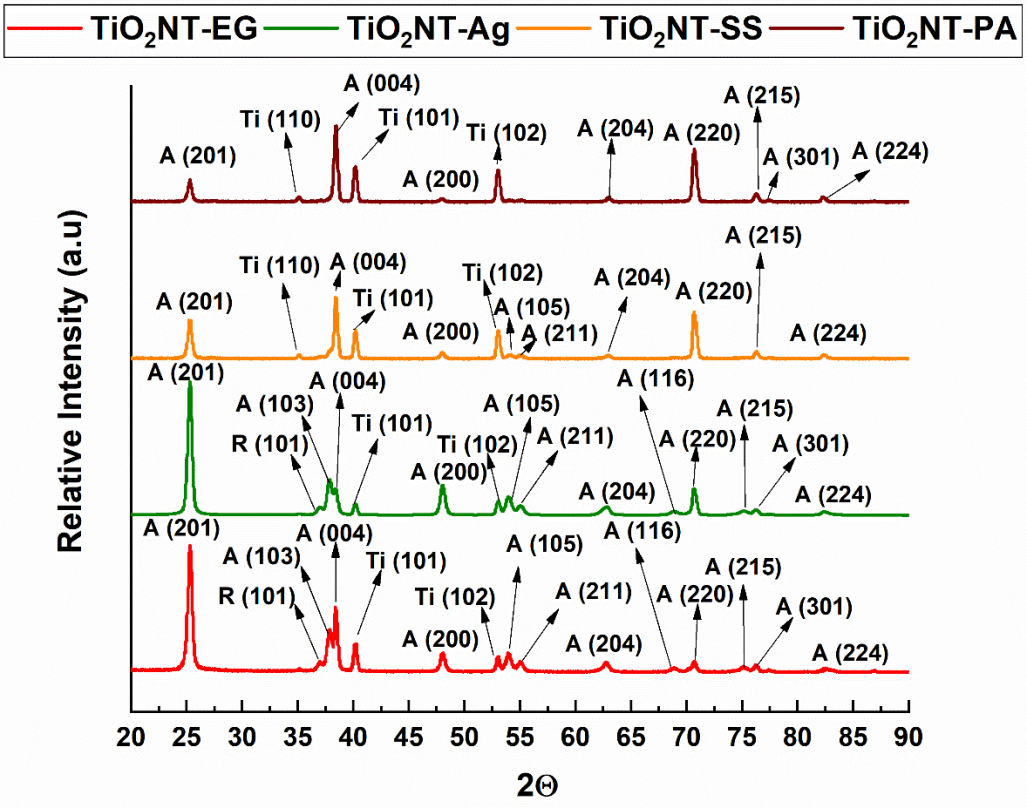

Figure 3. 13 X-Ray Diffratograms of the annealed materials

3.2.3: Optical Properties and Band gap Estimation

The band gap of a photocatalyst determines the wavelength of light required to promote valence electrons to the conduction band [35]. Photocatalysts with band gaps below 3 eV can be activated by visible light. Anatase possesses both an indirect (≈3.2 eV) and direct band gap (≈ 3.5 eV) [36]. Charge carrier lifetimes are longer for semiconductors having an indirect band-gap. The lower energy band-gap is taken as the reference value for bulk anatase. Narrowing the band gap of anatase is desirable as this pairs favourably with its low cost, non-toxicity, chemical stability and inherent high photocatalytic activity.

The band gap of anodic TiO_2 nanotube layers can be obtained from diffuse reflectance spectra (DRS). The DRS values can be can be converted to an absorption coefficient by applying the Kubelka-Munk function. The function assumes that the layer is infinitely thick and thus the contribution of the substrate is negligible.

Equation 3.1 Kubelka-Munk Function

$$F(R_\infty) = \frac{K}{S} = \frac{(1-R)^2}{2R}$$

The terms K and S refer to the absorption and scattering coefficients respectively and R the reflectance. The band-gap is determined by plotting $[F(R\infty)hv]^2$ against hv where h is Planck's constant and v the frequency of the photon. The resulting plot is called a Tauc plot and from it an approximate value of the band-gap can be extrapolated.

The DRS and Tauc plot for TiO_2NT-EG are presented side by side in figure 3.14. The DRS does not feature a region of low reflectance in the UV range. Given that the material should predominantly absorb UV light this seems rather unusual. Whilst an analysis of DRS spectra usually gives a good understanding of the optical properties, in this case it is not as informative. The Tauc plot for TiO_2 NT-EG has a distinct linear region which on extrapolation gives a band-gap of close to 3.44 eV. This result implies that the material needs wavelengths of around 360nm to be activated. This value is higher than that given for bulk anatase and also to those reported for anodic nanotube arrays. Several authors have in fact reported band-gaps close to and in several cases lower than that of bulk pristine anatase [37-39]. Narrowing of the band-gap due to a non-stoichiometric structure was achieved by Valeeva et.al without the addition of dopants or modifiers [40]. The absence of a continuous reflectance minimum in the UV region has contributed to the position of the linear portion of the Tauc plot. Whilst the substrate was picked up by the X-ray diffractometer this result is unlikely to be due to its interference. The penetration depth of UV light in anatase is around 17nm, significantly less than the thickness of the layer [41]. Roy *et al.* have attributed this phenomenon to the mirroring effect caused by wide tube tops [42]. In the case of TiO_2NT-EG the absence of spaces between the tubes provided the 'mirror' surfaces for the light to reflect off of.

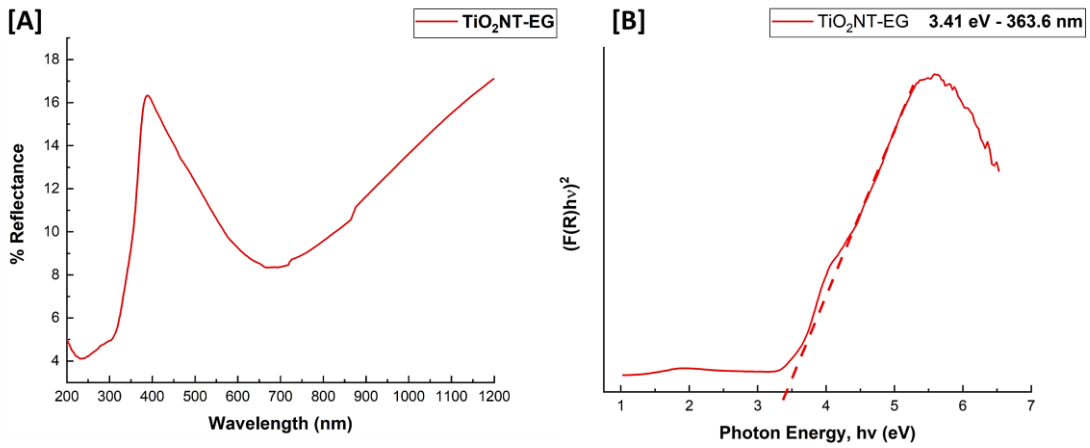

Figure 3. 14 a) DRS b) Tauc Plot for TiO_2NT-EG

The DRS plot for TiO_2 NT-Ag (figure 3.15 a) is remarkably different to that of TiO_2 NT-EG. There is still no reflectance minimum in the UV wavelengths but also the reflectance does not increase significantly until after 450nm. The reflectance of the surface at the higher wavelengths is also higher than that of the undecorated material. The plot does not provide any concrete insights on the light absorbing properties of the material. The x-intercept of the Tauc plot in figure 3.15(b) is nearly 3.8 eV meaning that the material requires a wavelength of about 326.3 nm to be activated. This makes decorating the surface a counterproductive exercise as the bare material has a lower band-gap. It is however also likely that the texture of the surface affected the interaction of light with the surface [43]. The oxides on the surface together with the silver particles could have reflected some of the light which would otherwise penetrate the tubular structure.

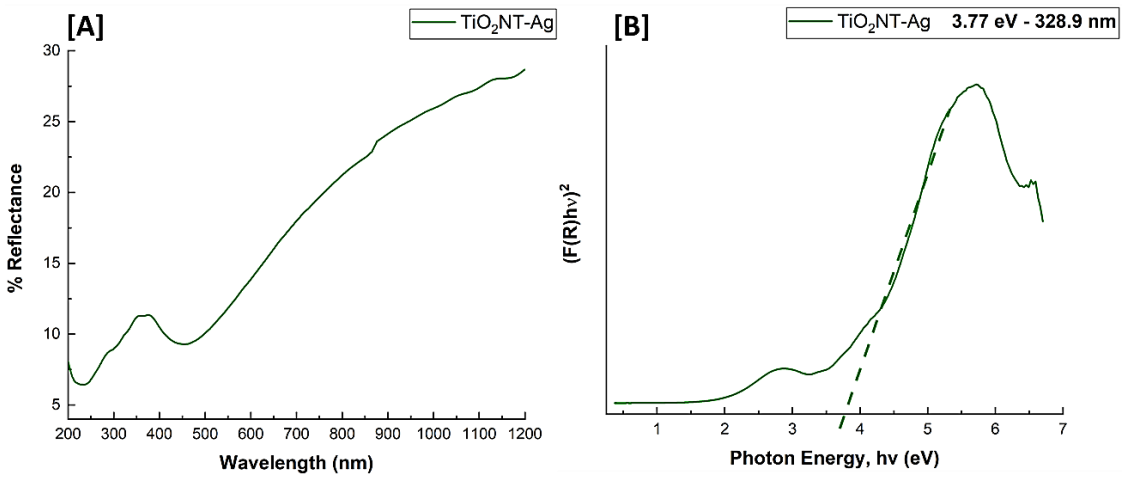

Figure 3. 15 (a) DRS (b) Tauc Plot for TiO_2NT-Ag

The DRS of TiO_2 NT-SS is shown in figure 3.16 (a). The spectrum differs to those of the layers grown in ethylene glycol. This spectrum is typical of anodic TiO_2 nanotube layers composed of anatase. There is no ambiguity as to the higher absorbance of UV over visible light. The band-gap of the material is also much easier to determine, with the extrapolated value being around 3.13 nm (figure 3.16 b).

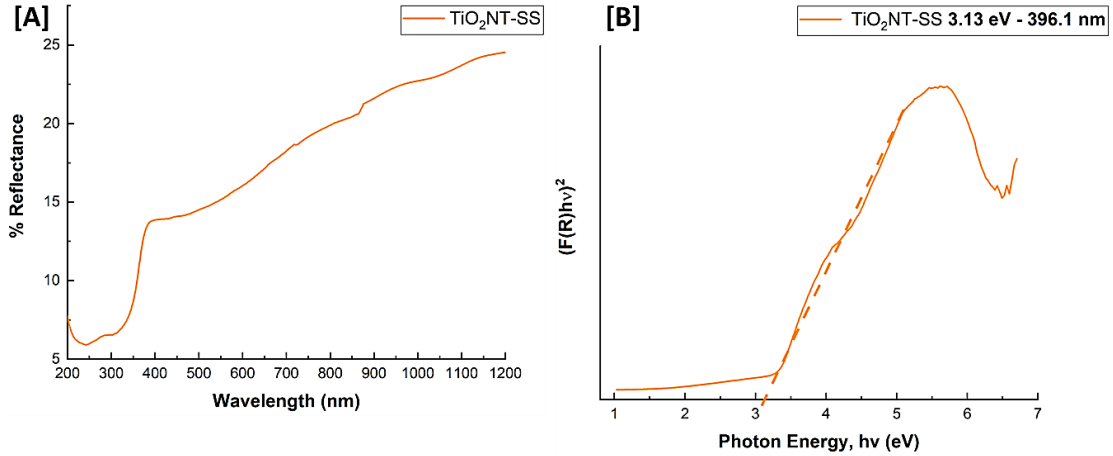

Figure 3. 16 (a) DRS (b)Tauc Plot for TiO_2NT-SS

There is no immediately discernible difference in the spectra of TiO_2 NT-SS and TiO_2 NT-PA within the UV-VIS part of the spectrum (figure 3.17a). The band-gap obtained by extrapolation is 3.11 eV (figure 3.17b). The materials synthesised in the aqueous media appear to have near identical optical properties.

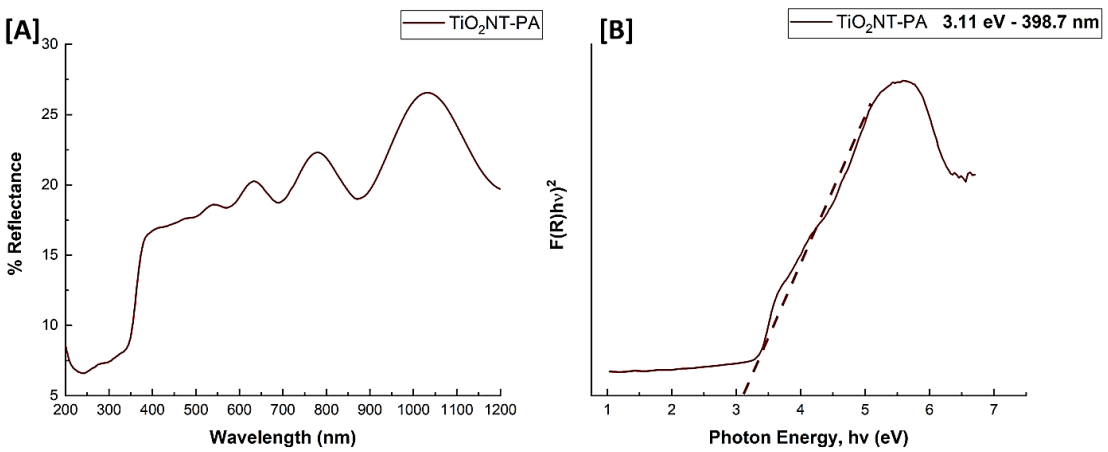

Figure 3. 17 (a) DRS (b)Tauc Plot for TiO_2NT-PA

3.2.4: Surface Wettability

Proper wettability ensures the optimal contact of the liquid containing the pollutants with the surface over which the ROS are produced. The extent of wettability is determined by the surface's morphology, free energy and chemistry together with the properties of the liquid itself. The most common way of assessing wettability is by measuring the water contact angle. Contact angles greater than 90° are termed hydrophobic and those exceeding 150° superhydrophobic. Surfaces with contact angles lower than 90° are referred to as hydrophilic. Superhydrophilic surfaces are those with contact angles less than 10° [44].

Anodic TiO_2 layers tend to have low contact angles mainly due to the formation of hydroxide compounds and the ability of the nanotubes to contain water. The main morphological features which influence the wetting behaviour are the nanotube diameter and length. Wider nanotubes allow for easier ingress of the liquid and longer tubes can hold more water. Exposure to the atmosphere can alter the wetting behaviour even in the absence of photocatalytic activation. Newly annealed TiO_2 nanotubular surfaces tend to possess the highest wettability as the high annealing temperatures favour the removal of organic contaminants [27]. Conversely, the wettability of the surfaces decreases if these are kept exposed to air as atmospheric organic contaminants can adsorb to the surfaces.

Whilst annealed nanotube layers have excellent wetting properties, these can be further improved by exposure to light, a phenomenon called photoinduced hydrophilicity [45]. The wavelength of the light depends on the material, with UV light being required for

the activation of TiO_2. Several mechanisms have been postulated to explain this phenomenon and it is likely that a combination of mechanisms is at work. The first mechanism proposed involves the formation of light-induced oxygen vacancies. These vacancies result in the formation of hydrophilic domains due to their enhanced attraction for hydroxyl groups [9]. Another mechanism involves the remodelling of the Ti-O bonds due to the migration of electron holes to the surface. The hole can get trapped a lattice oxygen which weakens the bond to the extent that they can be broken apart by water molecules and hydroxyl bonds formed in their stead [46]. The last mechanism relies on the photooxidation of surface adsorped organic molecules resulting in a decrease in their surface coverage. Atmospheric contaminants tend to be hydrophobic and thus their removal results in the spreading of the liquid over the surface [47].

The effect of the formation of the anodic oxide was studied by comparing the contact angles of the titanium substrate with those of the layers. The effect of UV illumination was studied on both the blank and the separate materials. The wettability of the titanium substrate before and after illumination is shown graphically in figure 3.18. Despite having a contact angle below 90° and thus can be classified as hydrophilic, the titanium surface is not extensively wetted. Metals must be chemically or mechanically treated in order to modify its wetting behaviour. There also appears to be no significant difference to the wettability after exposure to UVA light indicating that none of mechanisms discussed above are activated.

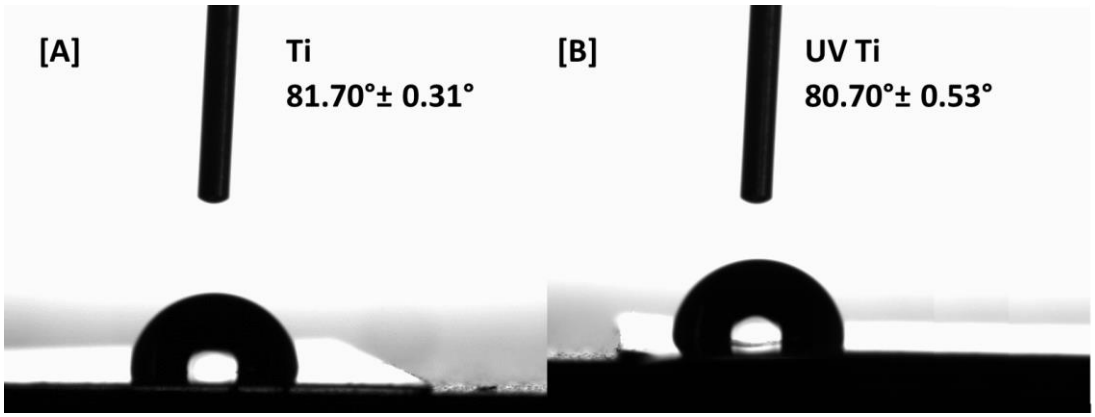

Figure 3. 18 Water contact angle of titanium a) prior to UV exposure b) after 60 minutes UV exposure. Error obtained from the standard deviation obtained from 30 independent measurements.

The wettability of the arrays synthesised in the organic medium is presented in figure 3.19. Both arrays show extensive wettability aided by the wide nanotubes and significant tube length. The TiO_2NT-Ag layer has a slightly lower contact angle of 35.02° against that of TiO_2NT-EG at 36.92°. This can be attributed to slight differences in the morphology of the two materials. Despite both arrays being produced using the same methodology, some variability between batches is to be expected. This is especially true when a naturally passivated metal such as titanium is anodised as inconsistencies in this oxide layer can alter the current generated during the process. The use of a potentiostatic process also does not supply a constant current output which can give rise to further structural differences. The inclusion of the silver and silver rich species within the tubes did not hamper the wettability of the surface, with the possibility of their uneven texture helping the droplet spread.

The illumination by the UVA source served to equalise the wettability of the surfaces, with complete wettability being achieved. This is the result of photoinduced wetting and is indicative of a photocatalytically active surface. Evans *et al.* compared the contact angle measurements post irradiation with the results from the reduction of the dye Resazurin [48]. The authors reported that materials with high activities towards the reduction of Resazurin, indicated by a colour change from blue to pink, also had low contact angles.

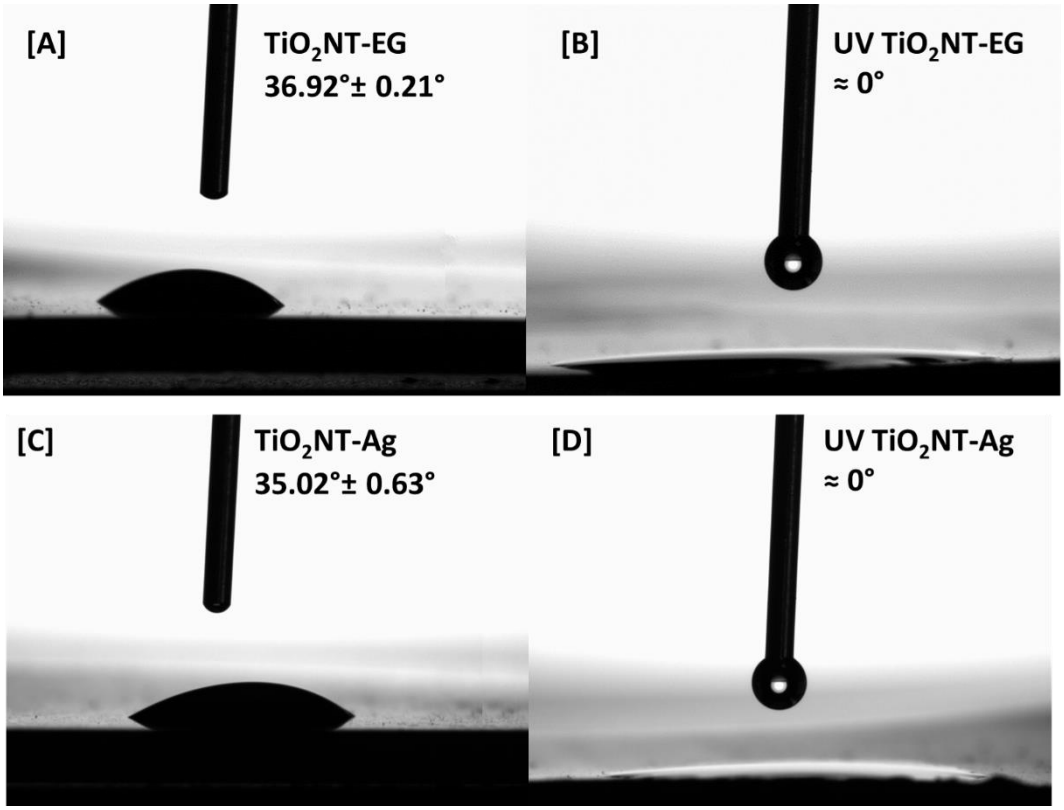

Figure 3. 19 Water contact angle of materials synthesised in ethylene glycol a) TiO_2NT-EG prior to UV exposure b) after 60 minutes UV exposure c) TiO_2NT-Ag prior to UV exposure d) after 60 minutes UV exposure. Error obtained from the standard deviation obtained from 30 independent measurements.

The wettability of the materials synthesised in the aqueous medium is shown in figure 3.20. There appears to be no great disparity in the wettability of TiO_2 NT-SS when compared to that of TiO_2 NT-EG and TiO_2 NT-Ag. The similarity of the contact angle without exposure to UV light indicates that past a certain length the rate of filling of the tubes is significantly diminished. Kim *et al.* postulate that the capillary forces within the tubes can be insufficient to allow the liquid to completely fill the tubes [49]. The authors also describe the increased concentration of hydroxyl groups near the tube top as increasing the velocity of the liquid down the tube length. This leads to quicker spreading of the liquid over the surface. The contact angle of TiO_2 NT-PA is the highest of the four materials. Despite a significant decrease in the contact angle after irradiation with UV, complete wetting was not achieved. It appears that the length of the tubes could be a limiting factor for TiO_2 NT-PA. The TiO_2 NT-PA morphology features prominent inter-tube spacing, which should allow for the liquid to seep into the gaps. The TiO_2 NT-SS array has a similar morphology, with the exception of the length, which is around twice that of TiO_2NT-PA. The shorter length might result in weaker adhesive

forces. The incomplete wetting after irradiation indicates that the efficiency of the mechanisms which enhance the hydrophilicity is lower for this material.

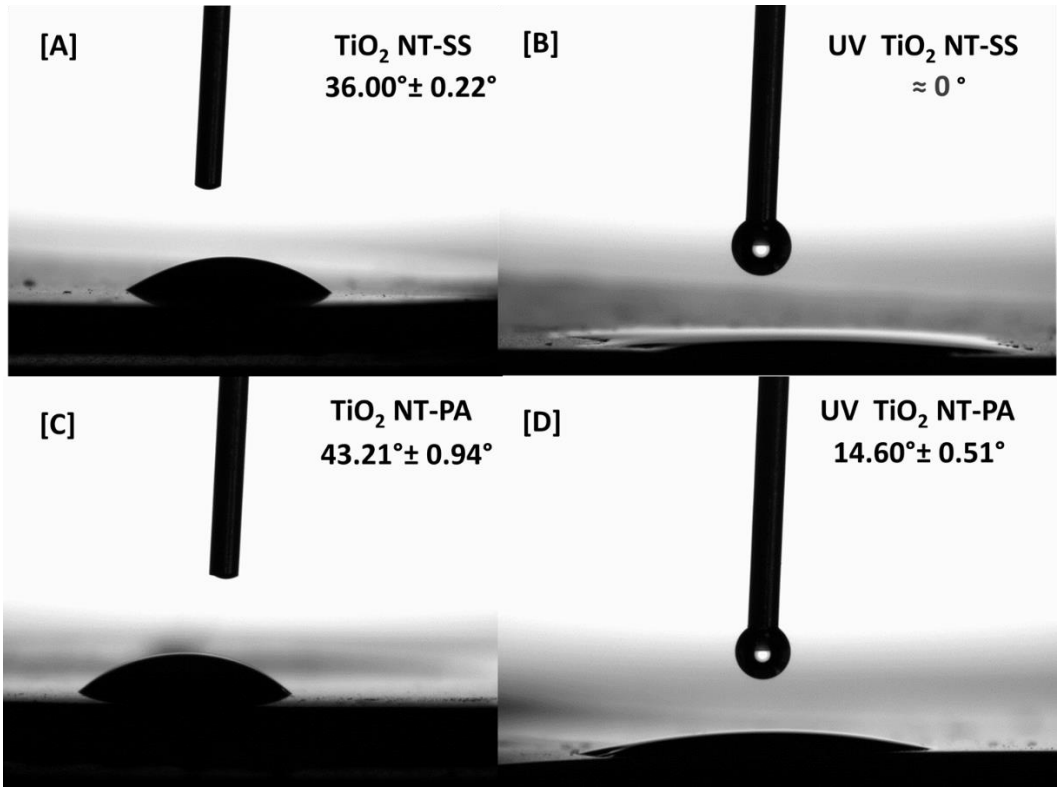

Figure 3. 20 Water contact angle of materials synthesised in aqueous media a) TiO_2NT-SS prior to UV exposure b) after 60 minutes UV exposure c) TiO_2NT-PA prior to UV exposure d) after 60 minutes UV exposure. Error obtained from the standard deviation obtained from 30 independent measurements.

3.2.5: Measurement of Photocatalytic Activity

3.2.5.1: Degradation of Methylene Blue

The variation in the absorbance of the dye after exposure to UV light is provided in figure 3.21. A reduction in the absorbance indicates that the conjugation of the molecule has been broken. The lower the absorbance, the greater the number of molecules which have been degraded. The effect of UV light on the dye is negligible indicating that that the structure of the molecule is basically unchanged. Similar results are obtained when the Ti substrate is added. The MB molecule has an absorbance minimum in the low energy UV region (350-400nm) and thus the light source used in this work cannot significantly photodegrade the molecule [50].

The absorbance value of the solution reached zero after UV activation of all four of the materials. This confirms the ability of the materials to generate ROS which in turn react

with the dye molecule. This is in agreement with Lin *et al.*'s findings who reported the complete degradation of the molecule over similar periods of irradiation [51]. The effect of the array's morphology was studied by Pasikhani *et al.* The authors concluded that tubes with the highest aspect ratios promoted the highest photocatalytic activity [52]. Despite the band gaps of TiO_2 NT-EG and TiO_2 NT-Ag indicating that the UV source at 365nm might not activate the materials, the MB degradation results reveal otherwise. This confirms that the surfaces provided some form of interference to reflection behaviour of the material which translated into inaccurate band gap measurements.

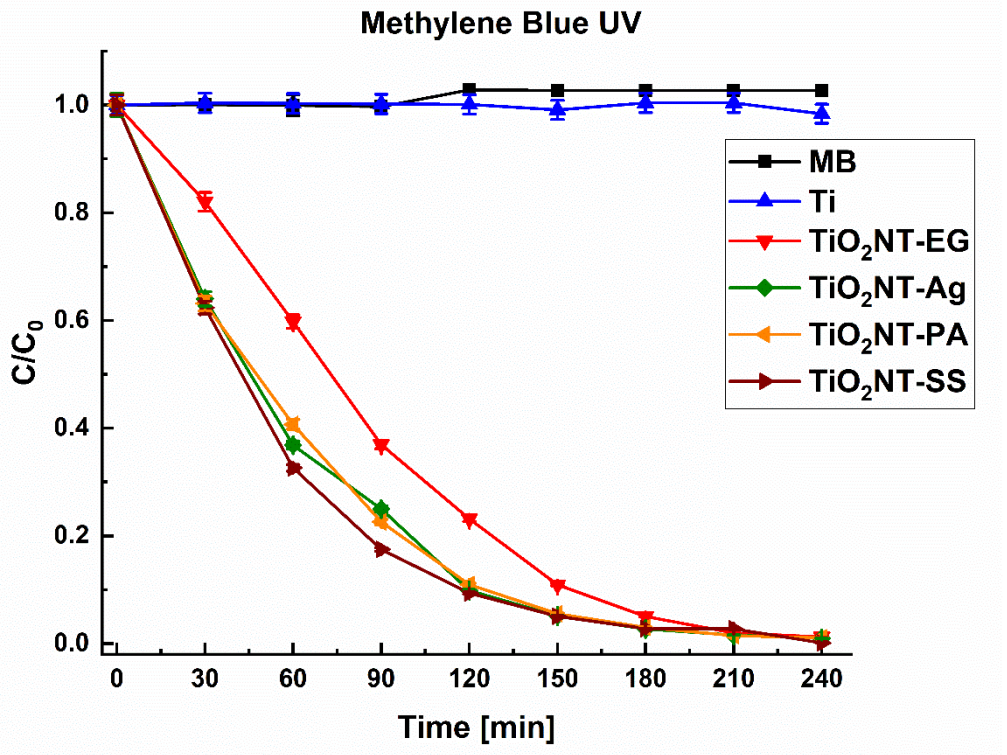

Figure 3. 21 Degradation Efficiency of Methylene Blue Under UVA. Error bars represent the maximum and minimum error of 10 independent measurements.

Despite the encouraging results obtained for the reduction in absorbance, for water purification to be effective the contaminants must be mineralised. The reduction in the absorbance value does not indicate the extent to which the molecule has been converted to small inorganic molecules. Matthews confirmed that it is possible to completely mineralise the MB molecule and has summarised the reaction in equation 3.2 [53].

Equation 3.2: $C_{16}H_{18}N_3SCl + 25\frac{1}{2}O_2 \rightarrow 16\ CO_2 + 6\ H_2O + 3\ HNO_3 + H_2SO_4 + HCl$

One possible photocatalytic degradation mechanism has been elucidated by Houas *et al* [54]. The authors describe how the destruction of the molecule starts with the cleavage of the bonds forming the C–S+=C portion of the molecule. Another route has been described by Chithambararaj *et al.* where the degradation starts at the dimethylamino ends of the molecule [55]. The difference in mechanisms is to be expected given that ROS are not selective oxidants. The initial sites of attack are marked in figure 3.22.

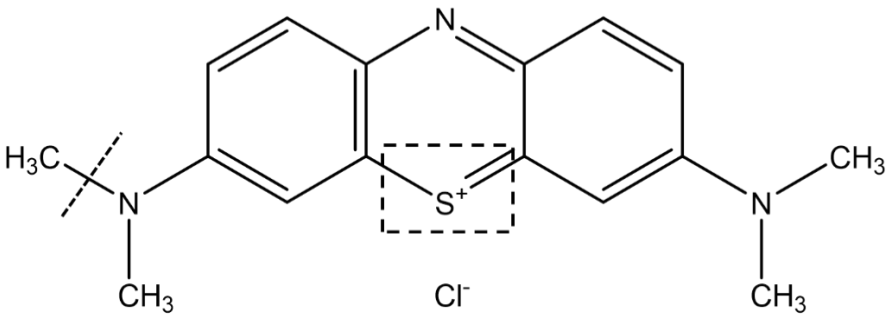

Figure 3. 22 Mechanistic Sites of Attack on Methylene Blue Molecule

The absorbance and TOC values are compared in figure 3.23. Despite the change in absorbance indicating the complete degradation of the molecule, the TOC values contrast this finding. The materials synthesised in the organic medium provided a considerable degree of mineralisation, with TiO_2 NT-Ag having the edge. The extent of mineralisation for TiO_2 NT-SS and TiO_2 NT-PA is considerably less but still significant. The glycol-based materials with their longer nanotubes have a large area over which light can be absorbed. Similarly, the longer tubes translate in a higher amount of anatase. The indirect band-gap of anatase extends the lifetime of the photogenerated charge carriers. The charge carriers generated by anatase are also capable to travel further from the bulk of the layer towards the pollutant/photocatalyst interface. Having a higher amount of anatase by way of longer nanotubes enhances the activity of the materials and their ability to degrade the material more fully. The slightly higher mineralisation efficiency can indicate that enough nanometric silver particles were deposited on the surface to introduce the Schottky Junction.

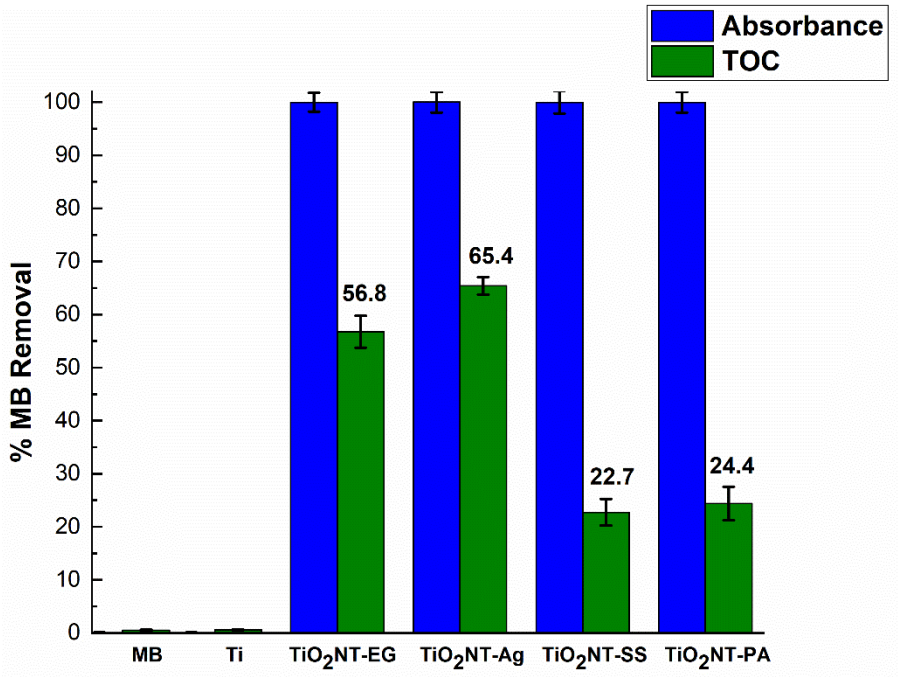

Figure 3. 23 Mineralisation Efficiency of Methylene Blue Compared to Change in Absorbance. Error bars represent the maximum and minimum error of 10 independent measurements.

The protocol used was identical to that used for the UV degradation tests except for the wavelength of light used. The tests were carried out using simulated solar irradiation omitting the wavelengths below 400nm. The results of the experiment are shown in figure 3.24.

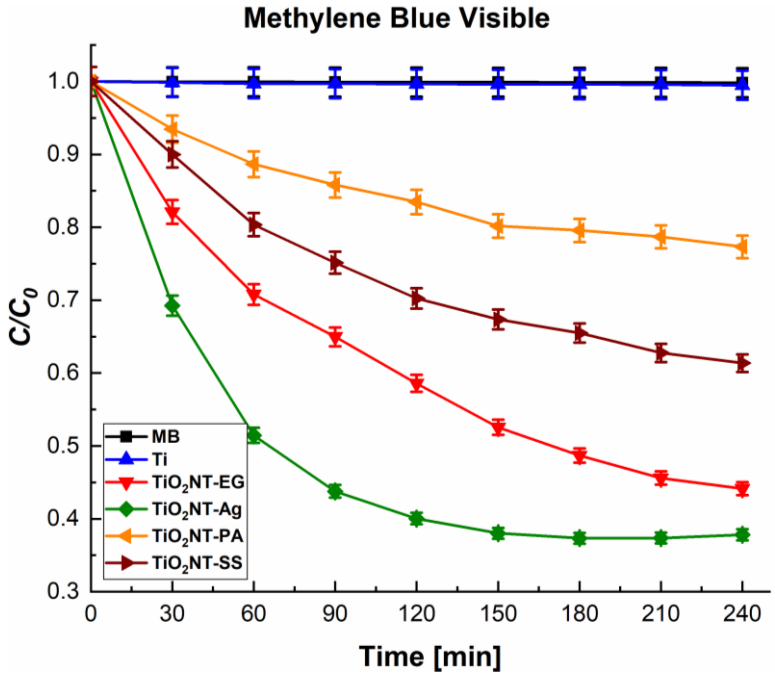

Figure 3. 24 Degradation Efficiency of Methylene Blue Under Simulated Solar Irradiation. Error bars represent the maximum and minimum error of 10 independent measurements.

The same trend in activity recorded in the earlier degradation tests was retained. All materials appear to be active under this restricted spectrum. The activity is lower to that of UV exposure but still appreciable. Narrow band gap materials whilst having high visible light activity have lower activities under UV light. Composites of narrow and wide bandgap semiconductors are used to produce materials with high visible and UV activity [56]. The mechanisms by which visible light activity is sustained are varied and are dependent of the material [57].

In order to investigate the optical properties of TiO_2NT-EG and TiO_2 NT-Ag further, a series of degradation experiments were devised. The reflectance spectra especially that of TiO_2 NT-Ag indicate that the material should be able to absorb visible light. When the same spectrum is computed using the Kubelka-Munk function and plotted as a Tauc plot, the plot shows the opposite. Despite perhaps only a small contribution from visible light this should help exploit more of the solar spectrum and add to the overall activity.

The visible light activity was such that some degree of mineralisation was recorded for all materials, but TiO_2NT-PA. The degree of removal with respect to the absorbance and TOC is shown in figure 3.25. This indicates that the longevity of the charge carriers and the amount of ROS produced was sufficient to completely oxidise portions of the molecule.

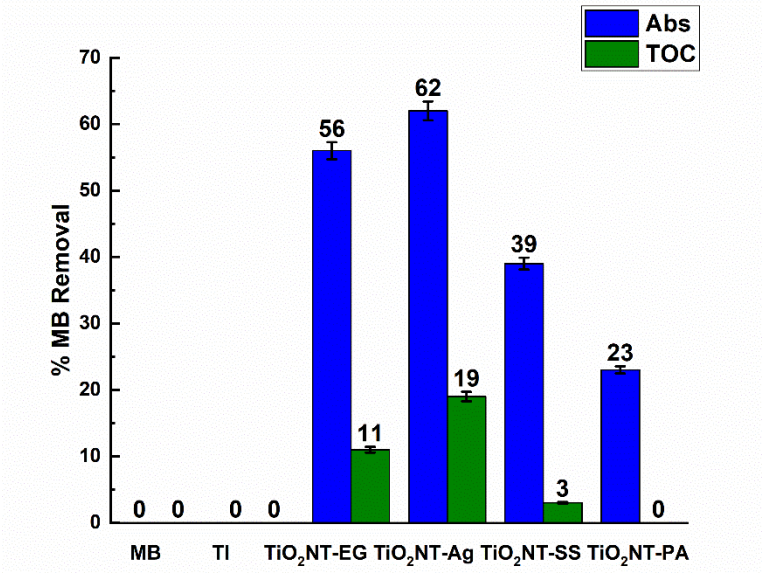

Figure 3. 25 Mineralisation Efficiency of Methylene Blue Under Simulated Solar Irradiation Compared to Change in Absorbance. Error bars represent the maximum and minimum error of 10 independent measurements.

To determine whether another factor apart from the material contributed to the visible light activity a further modification to the dye degradation test was included. A UV-VIS scan between 200 and 800 revealed that MB absorbs over a range of 500 to 700 nm with an absorption maximum at around 664 nm. This implies that a significant portion of the simulated solar spectrum was absorbed not by the material but by the solution itself. The visible light absorption of dye molecules has been used to impart visible light activity to materials which would otherwise have none. This process is called dye-sensitisation. The dye molecule reaches its excited state after irradiation with visible light and the excited electrons are injected in the conduction band of the semiconductor. These electrons can be used for several reduction reactions, including the formation of ◦OH radicals.

To discern between dye-sensitisation and visible light activity the range between 500 and 700nm was omitted and the MB degradation test was repeated. The order of reactivity was identical to that of figure 3.26. The activity of the materials is however much lower and unlikely to be a major contributor to the overall activity. Despite MB having the right chemistry to be a photosynthesiser, it is seldomly used to sensitise photocatalysts. In fact, authors such as Yang *et al.* to study the visible light degradation of MB opted to functionalise with another more efficient photosensitiser [58].

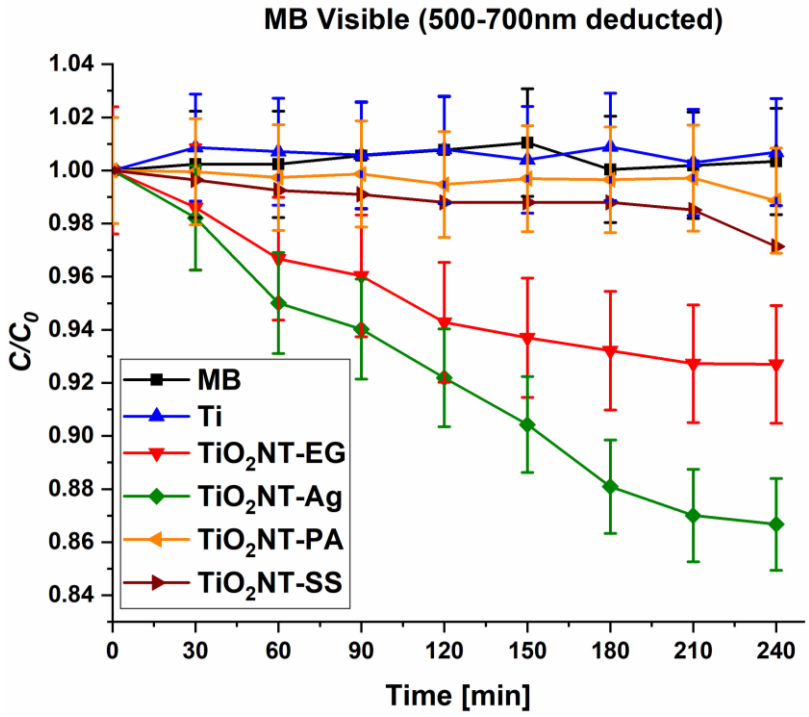

Figure 3. 26 Degradation Efficiency of Methylene Blue Under Reduced Solar Spectrum. Error bars represent the maximum and minimum error of 10 independent measurements.

3.2.5.2: Degradation of Paracetamol

The absorbance maximum for the paracetamol molecule is found at 243nm and is due to the n- $\pi*$ transition of the carbonyl group. The change in the absorbance value at 243nm was used to determine the rate of degradation of the molecule.

The reduction in absorbance value of the paracetamol solution reveals some distinct differences to those of the dye (figure 3.27). Whereas all materials had degraded the dye molecule sufficiently to lower the absorbance value to zero, for paracetamol only TiO_2 NT-EG and TiO_2 NT-Ag were successful. The final absorbance was 15% and 46% of that of the starting solution for TiO_2NT-SS and TiO_2NT-PA respectively. A degradation mechanism was elucidated by Yang *et al.* [59]. The benzene ring is attacked first, and depending on the reaction site, the amide group can be lost in a subsequent step. The absorbance value at 243nm declines in a proportional manner with the loss of the amide group. Another mechanism was described by Moctezuma *et al.* where the carbonyl group is lost as ethanoic acid, leaving the aromaticity whole [60]. Figure 3.28 marks the parts of the molecule where the degradation mechanism is initiated. This pathway will inevitably produce lower absorbance values after exposure. Based on the absorbance values, one can assume that several molecules were not cleaved at the carbonyl end when TiO_2 NT-SS and TiO_2 NT-PA were used.

The absorbance and TOC values after 4 hours of exposure are shown in figure 3.29. The TOC values mirror the absorbance values. The activity of TiO_2NT-EG and TiO_2NT-Ag was sufficiently high to oxidise the molecule towards higher levels of mineralisation. Once again TiO_2 NT-Ag is slightly more active than its undecorated counterpart. The absorbance values of TiO_2 NT-SS and TiO_2NT-PA are accompanied by lower but still appreciable mineralisation levels.

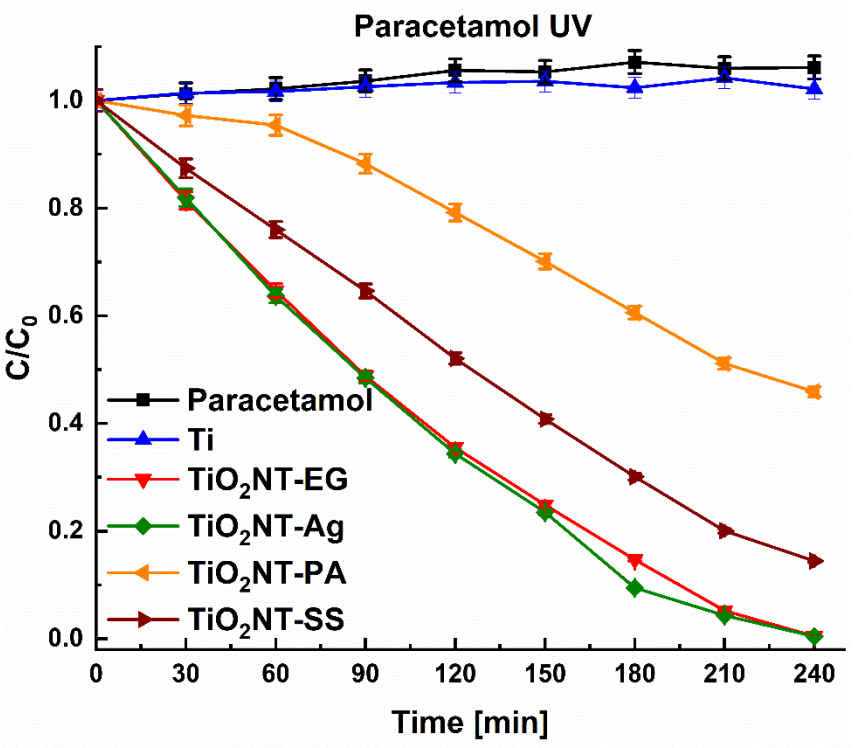

Figure 3. 27 Degradation Efficiency of Paracetamol Under UVA Light. Error bars represent the maximum and minimum error of 10 independent measurements.

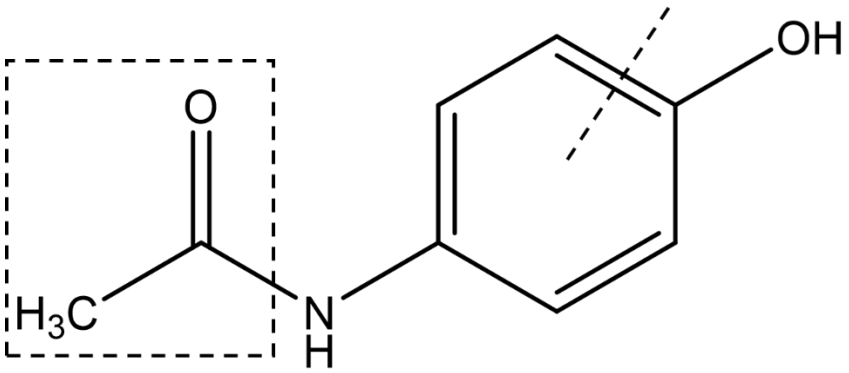

Figure 3. 28 Mechanistic sites of attack paracetamol molecule

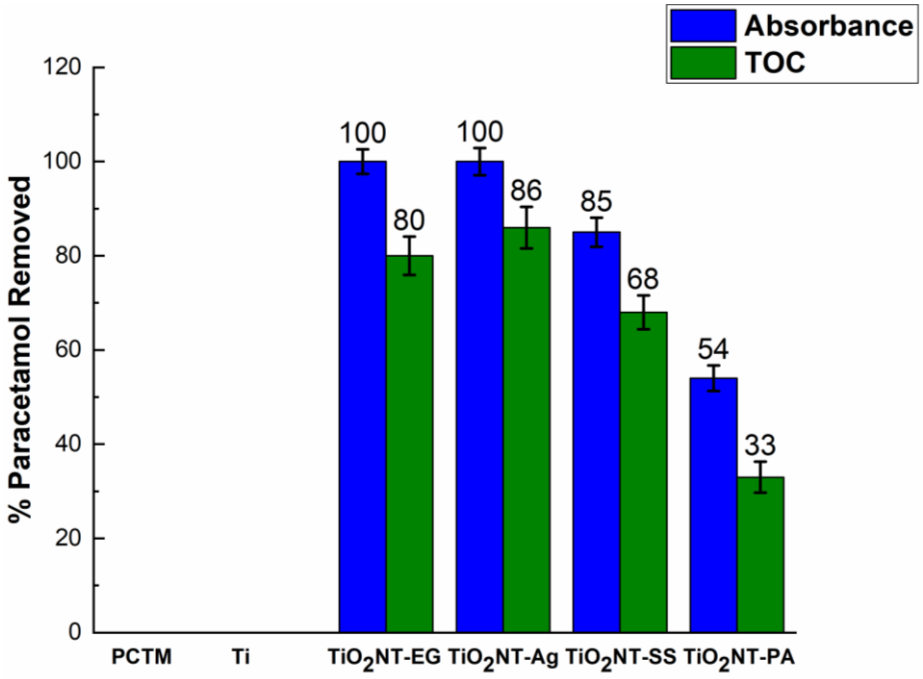

Figure 3. 29 Mineralisation Efficiency of Paracetamol Compared to Change in Absorbance. Error bars represent the maximum and minimum error of 10 independent measurements.

The visible light activity of the materials was further test using paracetamol. Paracetamol does not absorb in the VIS region and thus can be used to unambiguously determine whether any significant activity exists. The traces in figure 3.30 do not reveal any modification to the molecule and thus the absorbance values were unchanged over the 4-hour testing period.

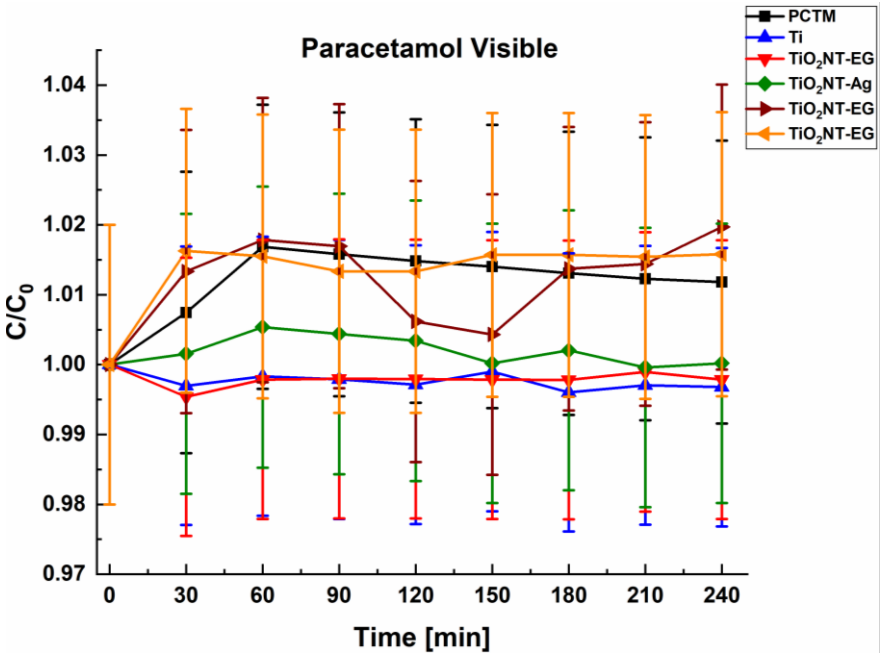

Figure 3. 30 Degradation Efficiency of Paracetamol Under Simulated Solar Irradiation. Error bars represent the maximum and minimum error of 10 independent measurements.

3.2.5.3: Degradation of Sodium Dodecyl Sulfate

The analytical method involved in measuring the remaining concentration of SDS differs from that of the other probe molecules. Rather than just measuring the absorbance of the solution after different time points directly, the test solution needs to be reacted further. An aqueous solution containing SDS is acidified and to it a solution containing methylene blue is added. The cationic methylene blue and the anionic SDS molecules form an ion-pair which is then extracted from the aqueous phase using chloroform. The intensity of the blue colouration of the organic layer is proportional to the SDS content of the solution.

The reactivity of the photocatalytic materials towards the surfactant is lower than that of the other probe molecules. The degradation efficiencies are shown in figure 3.31. A portion of the molecules in the solution was always unmodified whatever material was used. As with the degradation of paracetamol, the lowest activity was that of TiO_2 NT-PA with 64% of the original concentration remaining. The reactivity of TiO_2 NT-SS was higher with 29% of the starting concentration left. The glycol synthesised materials were more effective with a 7% and 10% residual for TiO_2NT-Ag and TiO_2NT-EG respectively. The difference between these materials is in this case minimal.

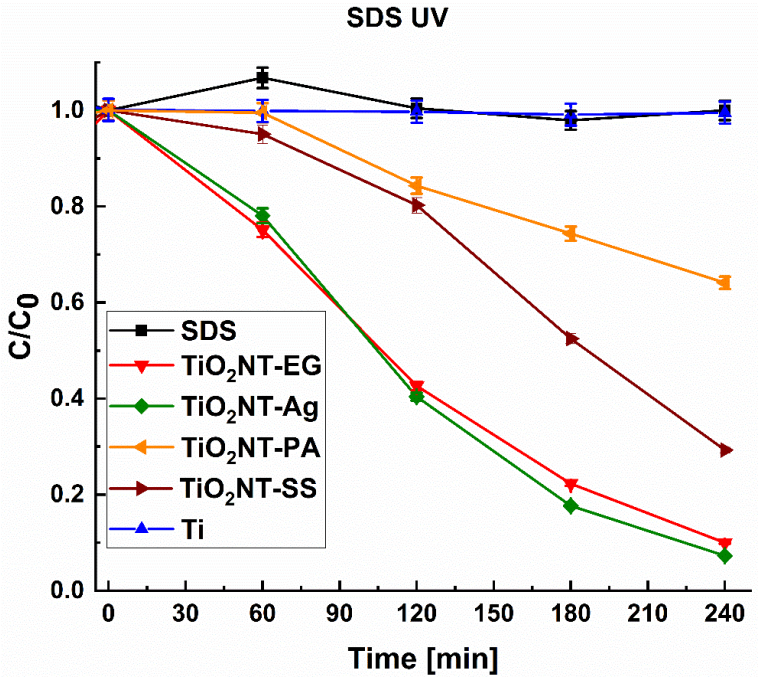

Figure 3. 31 Degradation Efficiency of Sodium Dodecyl Sulfate Under UVA Light. Error bars represent the maximum and minimum error of 3 independent measurements.

A mechanism by which the sulfate group is attacked first was outlined by Lea *et al* [61]. The authors describe how the generated electron holes act as sites to which the molecule chemisorbs at the sulfate end. This increases the probability of the sulfate group being attacked first by the ROS produced at the surface. The absence of the sulfate end will hamper the formation of the ion-pair and its migration to the organic phase. The absorbance values will thus be low.

The degradation mechanism of SDS in the presence of OH◦ radicals has been discussed in detail by Eriksson *et al* [62]. The authors describe that the tail of the molecule tends to be more susceptible to attack by the OH◦ radicals. The use of the hydroxyl radical in solution mimics the reactivity away from the surface. The hydrophobicity of the ion-pair might change significantly with the modification to the tail end. This negative interference gives lower absorbance values as the ion pair tends to remain in the aqueous phase. If the tail is not significantly modified, the hydrophobicity only changes slightly and thus the ion-pair will be extracted in the organic layer. The sulfate group and tail end of the molecule are marked in figure 3.32.

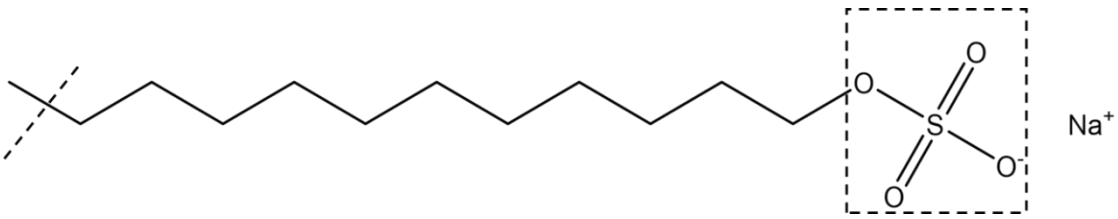

Figure 3. 32 Mechanistic Sites of Attack on Sodium Dodecyl Sulfate Molecule

Whilst the absorbance values do not indicate the location of reaction sites, they still give an indication of the extent to which the molecule was modified. The low C/C_0 values for TiO_2NT-EG and TiO_2NT-Ag indicate that the molecule was extensively reacted (figure 3.31). If the sulfate end was attacked, the results indicate that around 90% of the sulfate groups were removed. The same rationale can be extended to the other two materials, whereby the number of molecules modified was significantly lower. The degree of mineralisation is reported in figure 3.33. For TiO_2NT-EG (60%) and TiO_2NT-Ag (61%) this was nearly identical. In this instance the benefits of a possible Schottky Junction were not recorded. The reduction for the other materials was significantly

lower at 39 and 20% respectively. These values indicate that portions of tail end of the molecule were oxidised completely to CO_2 in all instances.

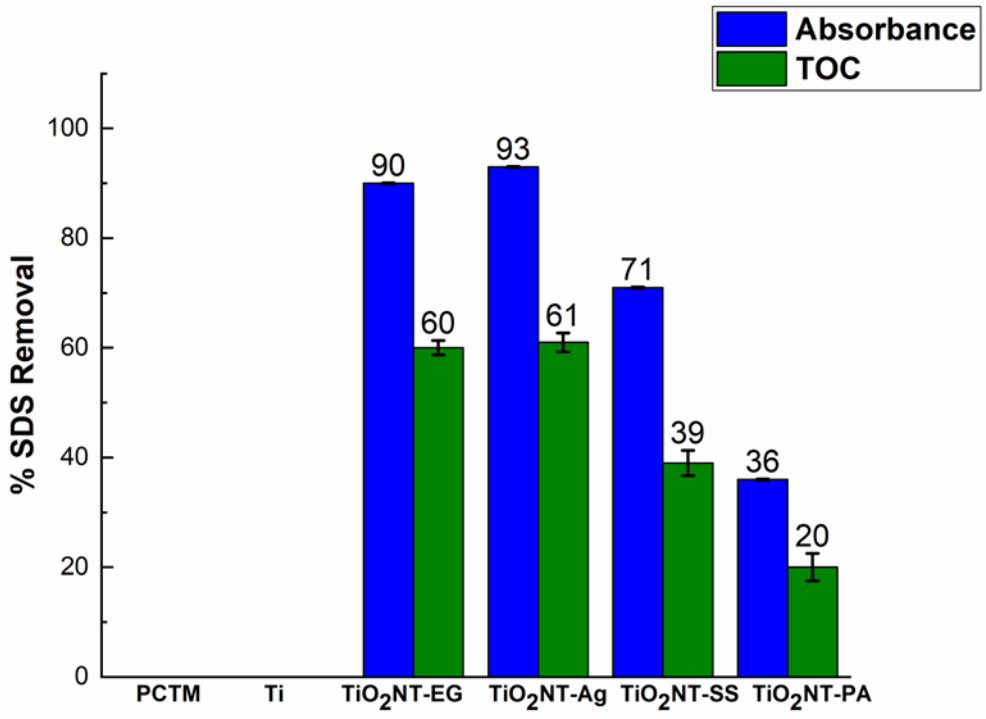

Figure 3. 33 Mineralisation Efficiency of Sodium Dodecyl Sulfate Compared to Change in Absorbance. Error bars represent the maximum and minimum error of 3 independent measurements.

3.2.5.4: Antibacterial Activity

The photocatalytic disinfection mechanism differs to that involved in the degradation of organic molecules. Contact between the bacteria and the surface whilst beneficial is not required. The ROS generated can migrate through the solution and react with the bacterial cell wall. The antibacterial effect is achieved through different routes. The ◦OH radical and the other ROS generated, are thought to induce the peroxidation of the cell wall and on entering the cell cause damage to the organelles and DNA. The electrons forming part of the generated pair of charge carriers, can enter the cell and cause reductive damage to its contents.

The order of the antibacterial activity reported in figure 3.34 mirrored that for the organic species.Complete inactivation of the *E.coli* culture was achieved when TiO_2NT-EG and TiO_2 NT-Ag were used. The effect of the silver particles could thus not be ascertained. This was not the case with the other materials, with TiO_2NT-SS and

TiO¬2NT-PA having 21 and 16% survival rates respectively. The inactivation mechanism, assuming an appreciable migration of ROS through the film of bacterial culture, indicates that less ROS were produced by the water-based materials.

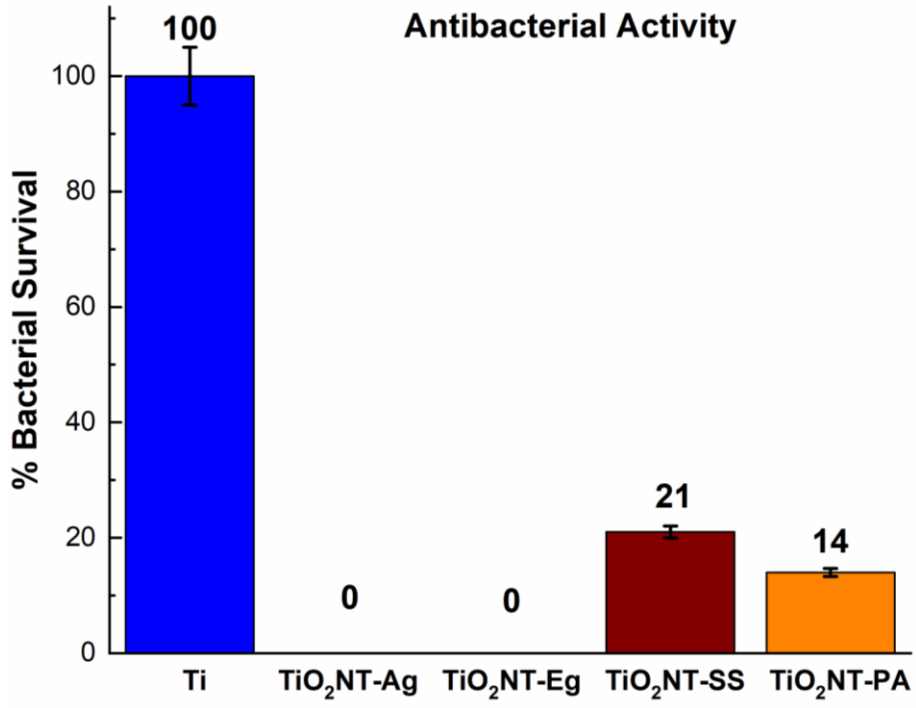

Figure 3. 34 Antibacterial Activity of Anodic Nanotube Arrays. Error bars represent the maximum and minimum error of 3 independent measurements.

3.2.6: Stability of Anodising Solution and Photocatalytic Activity after Reuse.

For photocatalysis to find widespread use in real-world applications the economic and environmental impact of the technology need to be studied. In the formation of anodic nanotubes, the electrolyte has both an economic and environmental cost. This is especially true of the glycol-based media. It is thus required that the longevity of the solution is sufficiently high. In order to determine their lifespan, the solutions were re-used and the quality of the arrays produced assessed.

The stability of the glycol bath is dependent on the water content. Ethylene glycol can absorb moisture from the atmosphere through hydrogen bonding [63]. A small percentage of water is required to dissolve the ammonium fluoride, an excess can on the other hand results in the dissolution of the tubular structure [64]. The performance of

the glycol electrolyte after repeated use was studied by Sopha *et al.* [65]. The study looked into the effect of electrolyte age on morphological and mechanical changes and did not address the photocatalytic activity. The authors reported that a solution with an age up to 44 hours retained enough potency to produce well-ordered and highly adherent nanotube arrays. Suhadolnik *et al.* reported the effect of electrolyte age on the degradation of caffeine under UVC light. The authors report that after 20, 6-hour cycles at 60V a reduction in activity from 60 to 44% [66].

The trend in activity up to 10 anodising cycles when the glycol medium was used is presented in figure 3.35. The activity declines steadily until it plateaus around the 8th cycle. These results are different to those obtained by Suhadolnik however the authors reported a similar plateauing in activity. Whilst a direct comparison between the current results and those of other authors cannot be drawn, the possibility of reusing the solution is highly encouraging. This makes the glycol-based chemistry suitable despite the local yearlong high humidity.

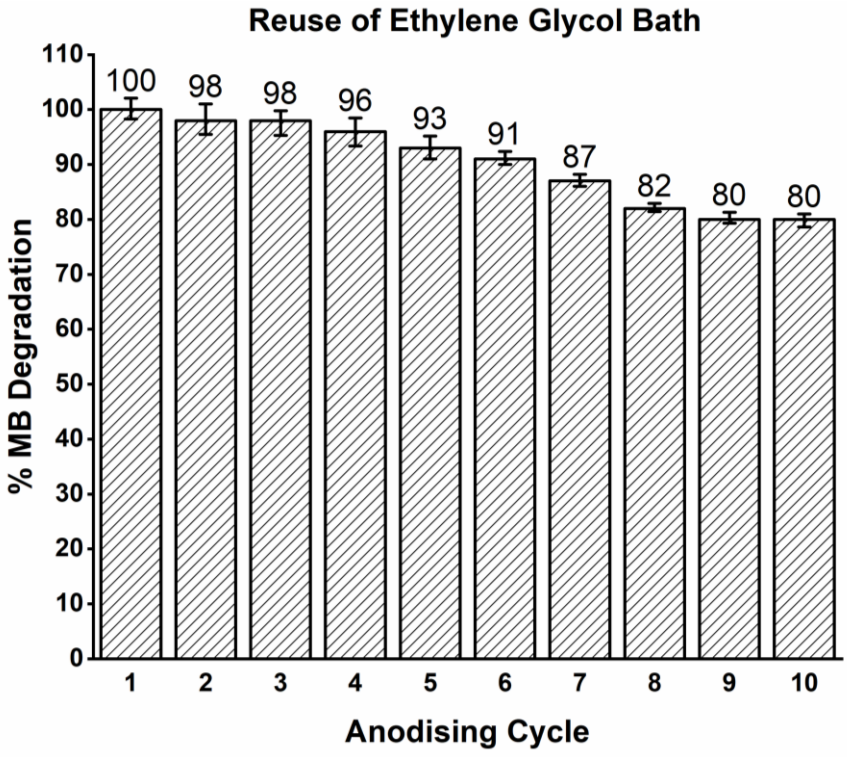

Figure 3. 35 Effect of Ethylene Glycol Solution Age on the Degradation Efficiency of Methylene. Error bars represent the maximum and minimum error of 4 independent measurements.

.

At the time of writing a study of the reuse of the sodium sulfate electrolyte has not been published and thus no complete or partial comparison is possible. The trend in activity with solution age is shown in figure 3.36. The decline in activity occurs at a faster rate, with half the activity being lost by the fourth cycle.

The longevity of the phosphoric acid solution was even shorter (figure 3.37). A 68% decline in activity was obtained after the second anodising cycle. This result coupled with that of the sodium sulfate bath perhaps limit the large-scale suitability of these electrolytes.

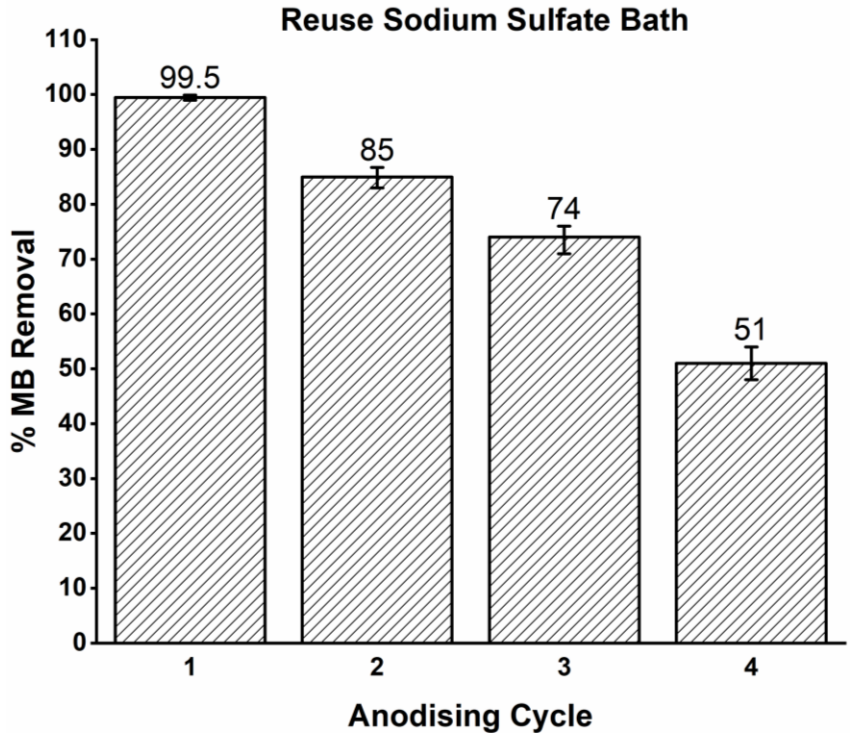

Figure 3. 36 Effect of Sodium Sulfate Solution Age on the Degradation Efficiency of Methylene. Error bars represent the maximum and minimum error of 4 independent measurements.

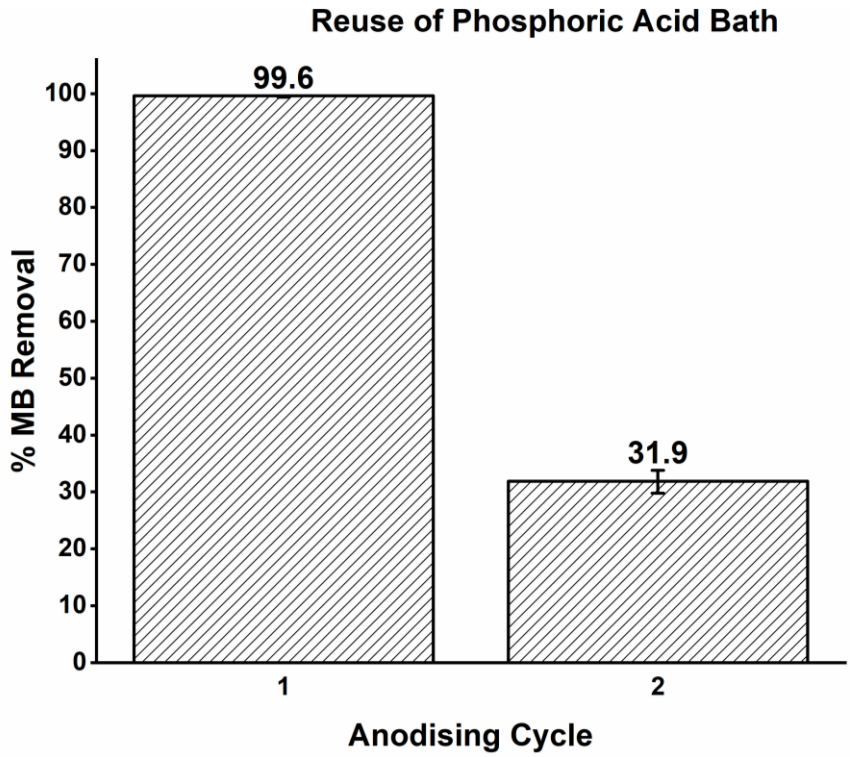

Figure 3. 37 Effect of Phosphoric Acid Solution Age on the Degradation Efficiency of Methylene. Error bars represent the maximum and minimum error of 4 independent measurements.

This decline in activity was studied by analysing the surfaces. The surfaces for TiO_2NT-EG and Ag, TiO_2NT-SS and TiO_2NT-PA after their last anodising sample are compared in figure 3.38. The surface of the glycol-based materials appears to be devoid of a continuous bulk TiO_2 layer and the surface is covered with nanometric perforations. The surface is also devoid of loose debris. One notable difference is the incomplete etching of the surface leading to a lower nanotube density overall. The lower nanotube density lowers the overall surface area available for reaction.

The nanotube density produced by the aged sodium sulfate solution remains overall unchanged. The surface is however covered by a fine debris which occludes both nanotubes and the spaces around them. This debris is probably composed of fine TiO_2 containing nanocrystals which accumulate with each anodising cycle. These nanometric particles appear to be adhere strongly to the surface and resistant to the sonication cycles.

The use of the aged phosphoric acid electrolyte produced a surface which was devoid of any nanotubes or nanopores. The surface is uneven and covered with irregularly shaped ‘growths. The approximate chemical composition of one of these features is given in figure 3.39. The chemical composition indicates that the surface is composed

of an oxide of titanium possibly TiO_2. The bath by the second use could only grow a bulk layer devoid of any localised etching. The lower surface area of bulk layers is likely to be the cause of this reduced activity. Bauer *et al.* reported similar results when fluoride concentrations below 0.025 wt% were used [67]. The authors report that the electrochemical behaviour of the titanium during anodising was that of a quickly passivated material. The changes in current density associated with pitting of the oxide layer were absent. Krasicka-Cydzik reported on the competition between the fluoride and phosphate ion [68]. In solutions where the phosphate ions were in a large excess, the formation of a continuous layer was favoured. It is possible that the lower availability of fluoride ions after the solution was used was offset by the adsorption of the more abundant phosphate ion. In this instance the rate of growth exceeds that of the dissolution of the layer.

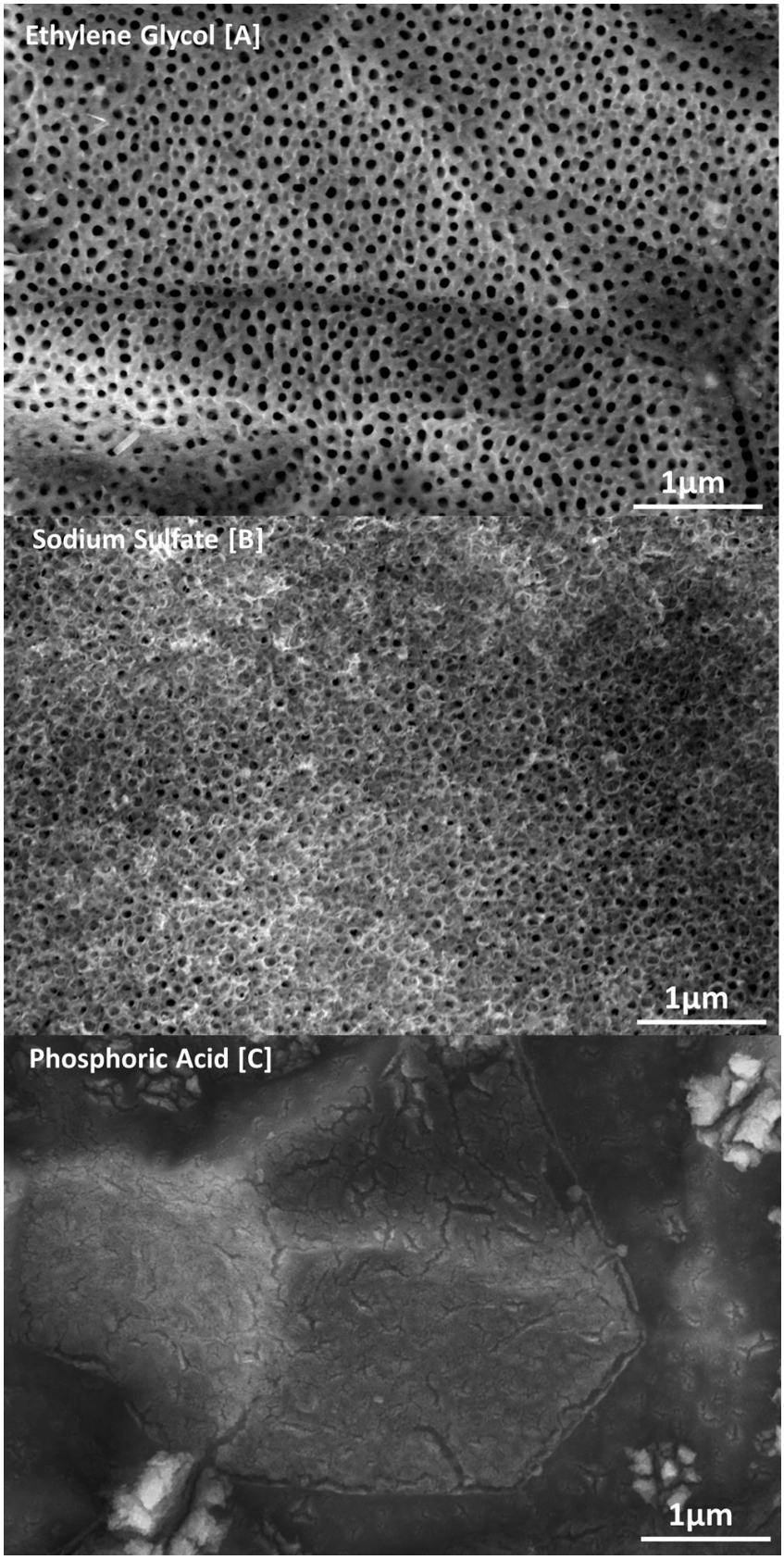

Figure 3. 38 Surface morphologies of the nanotube arrays obtained at the oldest solution age.

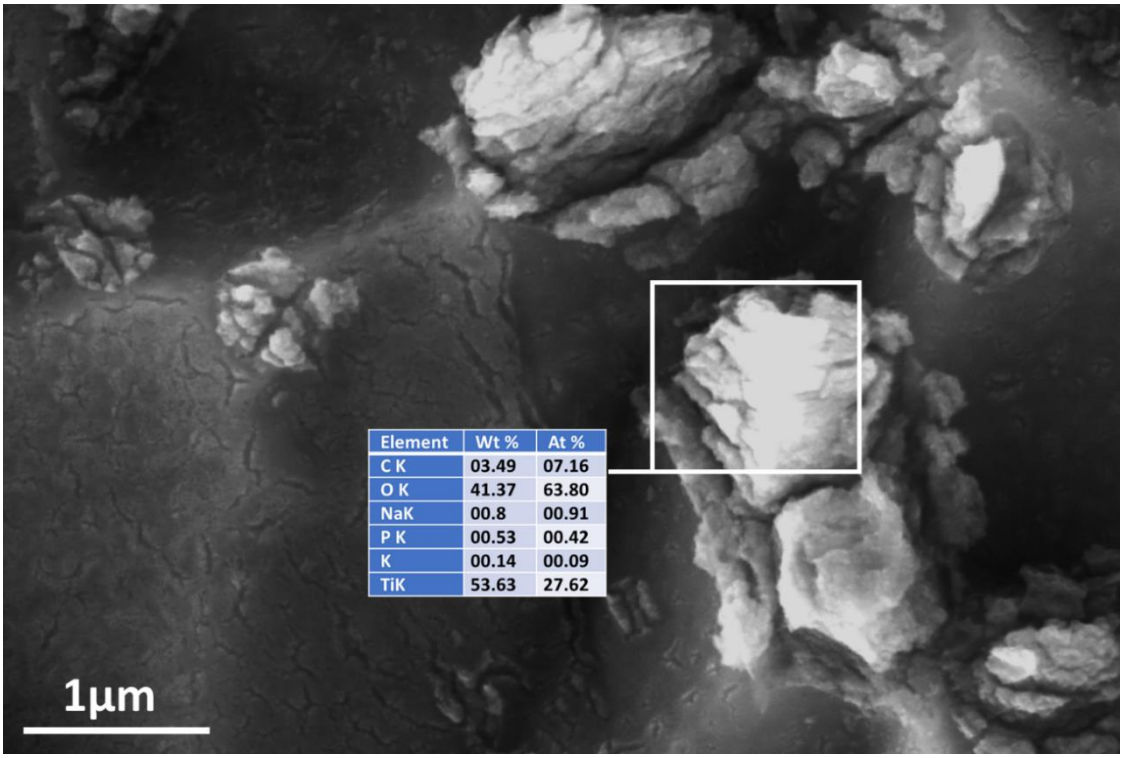

Figure 3. 39 Detail of Surface of TiO_2NT-PA produced in Aged Solution. Inset – Approximate Chemical Composition

3.3 Chapter Conclusions

- Three different anodic nanotube morphologies were ranked based on their ability to degrade contaminants.
- All the synthesised materials were able to reduce the concentration of a variety of contaminants, both microbial and in the form of organic molecules.
- Out of the materials investigated, the arrays synthesised in ethylene glycol, namely TiO_2NT-EG and TiO_2NT-Ag had the superior photocatalytic activity The combination of increased layer thickness, tube diameters and high anatase content provided the basis this efficiency. The high reactivity of the TiO_2NT-EG template overshadowed any possible beneficial effect of the silver nanoparticles. The duration of the anodising process of these two materials is the shortest, making its large-scale production more attractive. The effect of the addition of silver does not bolster the efficiency of TiO_2NT-EG to any great degree. As it stands TiO_2NT-EG is a highly active material with a facile synthesis.
- The overall order of reactivity is: TiO_2NT-Ag > TiO_2NT-EG > TiO_2NT-SS > TiO_2NT-PA.

- All materials could be sensitised by MB and gain some level of activity in the visible region of the solar spectrum. True, albeit limited, visible light activity was recorded for TiO_2NT-EG and TiO_2NT-Ag. Despite the band gap values of TiO_2NT-Ag working out to be 3.77 eV, it possessed the highest visible light activity. This indicates that whilst DRS is useful for determining the optical properties of a material, certain intrinsic properties such as the surface texture and roughness might provide inaccurate values. As such quantitative measurements for photocatalytic activities should be obtained. Conversely, TiO_2NT-SS and TiO_2NT-PA with a band gap translating to near visible absorbance, they showed no visible light activity.

3.4 References

[1] S. K. Loeb, P. J. J. Alvarez, J. A. Brame, E. L. Cates, W. Choi, J. Crittenden, *et al.*, "The Technology Horizon for Photocatalytic Water Treatment: Sunrise or Sunset?," Environmental Science & Technology, vol. 53, pp. 2937-2947, 2019/03/19 2019.

[2] T. Sauer, G. C. Neto, H. Jose, and R. Moreira, "Kinetics of photocatalytic degradation of reactive dyes in a TiO_2 slurry reactor," Journal of Photochemistry and Photobiology A: Chemistry, vol. 149, pp. 147-154, 2002.

[3] E. M. Virgilio, M. E. Sad, and C. L. Padró, "Kinetic analysis of the conversion of aqueous erythritol solution on Ir/ReOx/TiO_2 in a batch slurry reactor," Applied Catalysis A: General, vol. 643, p. 118691, 2022/08/05/ 2022.

[4] K. Indira, U. K. Mudali, T. Nishimura, and N. Rajendran, "A Review on TiO_2 Nanotubes: Influence of Anodization Parameters, Formation Mechanism, Properties, Corrosion Behavior, and Biomedical Applications," Journal of Bio- and Tribo-Corrosion, vol. 1, p. 28, 2015/10/07 2015.

[5] S. Wantawee, R. Vongwatthaporn, and U. Tipparach, "Fabrication and Characterization of Titania (TiO_2) Nanotube Dye-Sensitized Solar Cells by Anodization Method," Integrated Ferroelectrics, vol. 165, pp. 153-158, 2015/09/02 2015.

[6] A. Di Mauro, F. Mirabella, A. D'Urso, R. Randazzo, R. Purrello, and M. E. Fragalà, "Spontaneous deposition of polylysine on surfaces: role of the secondary structure to optimize noncovalent coating strategies," J Colloid Interface Sci, vol. 437, pp. 270-276, Jan 1 2015.

[7] E. Krasicka-Cydzik, K. Kowalski, A. Kaczmarek, I. Glazowska, and K. Heltowski, "Competition between phosphates and fluorides at anodic formation of titania nanotubes on titanium," Surface and Interface Analysis, vol. 42, pp. 471-474, 06/01 2010.

[8] D. Regonini, C. R. Bowen, R. Stevens, D. Allsopp, and A. Jaroenworaluck, "Anodised TiO_2

nano-tubes: voltage ramp influence on the nano-structured oxide and investigation of phase changes promoted by thermal treatments," physica status solidi (a), vol. 204, pp. 1814-1819, 2007.

[9] R. Wang, K. Hashimoto, A. Fujishima, M. Chikuni, E. Kojima, A. Kitamura, *et al.*, "Light-induced amphiphilic surfaces," Nature, vol. 388, pp. 431-432, 1997/07/01 1997.

[10] I. O. f. Standardisation, "Fine ceramics (advanced ceramics, advanced technical ceramics) — Determination of photocatalytic activity of surfaces in an aqueous medium by degradation of methylene blue," ed, 2010.

[11] R. D. R. Turner, M. S. J. Warne, L. A. Dawes, K. Thompson, and G. D. Will, "Greywater irrigation as a source of organic micro-pollutants to shallow groundwater and nearby surface water," Sci Total Environ, vol. 669, pp. 570-578, Jun 15 2019.

[12] J. W. Schultze, M. M. Lohrengel, and D. Ross, "Nucleation and growth of anodic oxide films," Electrochimica Acta, vol. 28, pp. 973-984, 1983/07/01/ 1983.

[13] L. Taveira, J. M. Macák, H. Tsuchiya, L. F. P. Dick, and P. Schmuki, "Initiation and Growth of Self-Organized TiO_2

Nanotubes Anodically Formed in NH4FB (NH4) 2SO4 Electrolytes," Journal of The Electrochemical Society, vol. 152, 2005.

[14] B. Chen, J. Hou, and K. Lu, "Formation Mechanism of TiO_2

Nanotubes and Their Applications in Photoelectrochemical Water Splitting and Supercapacitors," Langmuir, vol. 29, pp. 5911-5919, 2013/05/14 2013.

[15] S. Cao, W. Huang, L. Wu, M. Tian, and Y. Song, "On the Interfacial Adhesion between TiO_2

Nanotube Array Layer and Ti Substrate," Langmuir, vol. 34, pp. 13888-13896, 2018/11/20 2018.

[16] H. Habazaki, K. Fushimi, K. Shimizu, P. Skeldon, and G. E. Thompson, "Fast migration of fluoride ions in growing anodic titanium oxide," Electrochemistry Communications, vol. 9, pp. 1222-1227, 2007/05/01/ 2007.

[17] D. Yu, X. Zhu, Z. Xu, X. Zhong, Q. Gui, Y. Song, *et al.*, "Facile Method to Enhance the Adhesion of TiO_2

Nanotube Arrays to Ti Substrate," ACS Applied Materials & Interfaces, vol. 6, pp. 8001-8005, 2014/06/11 2014.

[18] K.-C. Sun, Y.-C. Chen, M.-Y. Kuo, H.-W. Wang, Y.-F. Lu, J.-C. Chung, *et al.*, "Synthesis and characterization of highly ordered TiO_2 nanotube arrays for hydrogen generation via water splitting," Materials Chemistry and Physics, vol. 129, pp. 35-39, 2011/09/15/ 2011.

[19] M. F. Brugnera, M. Miyata, C. Q. Fujimura Leite, and M. V. B. Zanoni, "Silver ion release from electrodes of nanotubes of TiO_2 impregnated with Ag nanoparticles applied in photoelectrocatalytic disinfection," Journal of Photochemistry and Photobiology A: Chemistry, vol. 278, pp. 1-8, 2014/03/15/ 2014.

[20] J. Gamage McEvoy and Z. Zhang, "Antimicrobial and photocatalytic disinfection mechanisms in silver-modified photocatalysts under dark and light conditions," Journal of Photochemistry and Photobiology C: Photochemistry Reviews, vol. 19, pp. 62-75, 2014/06/01/ 2014.

[21] D. Li, S. Chen, K. Zhang, N. Gao, M. Zhang, G. Albasher, *et al.*, "The interaction of Ag2O nanoparticles with Escherichia coli: inhibition–sterilization process," Scientific Reports, vol. 11, p. 1703, 2021/01/18 2021.

[22] J. M. Macak, H. Tsuchiya, L. Taveira, S. Aldabergerova, and P. Schmuki, "Smooth Anodic TiO_2 Nanotubes," Angewandte Chemie International Edition, vol. 44, pp. 7463-7465, 2005.

[23] C. Adán, J. Marugán, E. Sánchez, C. Pablos, and R. van Grieken, "Understanding the effect of morphology on the photocatalytic activity of TiO_2 nanotube array electrodes," Electrochimica Acta, vol. 191, pp. 521-529, 2016/02/10/ 2016.

[24] M. Sachs, E. Pastor, A. Kafizas, and J. R. Durrant, "Evaluation of Surface State Mediated Charge Recombination in Anatase and Rutile TiO_2 ," The Journal of Physical Chemistry Letters, vol. 7, pp. 3742-3746, 2016/10/06 2016.

[25] S. M. Liu, L. M. Gan, L. H. Liu, W. D. Zhang, and H. C. Zeng, "Synthesis of Single-Crystalline TiO_2

Nanotubes," Chemistry of Materials, vol. 14, pp. 1391-1397, 2002/03/01 2002.

[26] O. K. Varghese, D. Gong, M. Paulose, C. A. Grimes, and E. C. Dickey, "Crystallization and high-temperature structural stability of titanium oxide nanotube arrays," Journal of Materials Research, vol. 18, pp. 156-165, 2011.

[27] M. Batzill, "Fundamental aspects of surface engineering of transition metal oxide photocatalysts," Energy & Environmental Science, vol. 4, pp. 3275-3286, 2011.

[28] M. Xu, Y. Gao, E. M. Moreno, M. Kunst, M. Muhler, Y. Wang, *et al.*, "Photocatalytic Activity of Bulk TiO_2

Anatase and Rutile Single Crystals Using Infrared Absorption Spectroscopy," Physical Review Letters, vol. 106, p. 138302, 03/29/ 2011.

[29] W.-Y. Wu, C.-F. Hsu, M.-J. Wu, C.-N. Chen, and J.-J. Huang, "Ag–TiO_2

composite photoelectrode for dye-sensitized solar cell," Applied Physics A, vol. 123, 04/18 2017.

[30] M. Guli, M. Deng, T. Bimenyimana, Z. Hu, and S. Dai, "Plasmon TiO_2

nanotube arrays doped with silver nanoparticles act as photo-anode film in solar cells," Applied Physics A, vol. 124, 02/12 2018.

[31] H. Yaqi, H. Chen, D. Deng, Z. Yang, S. Xue, R. Zhu, *et al.*, "An Efficient Photocatalyst for Fast Reduction of Cr(VI) by Ultra-Trace Silver Enhanced Titania in Aqueous Solution," Catalysts, vol. 8, p. 251, 06/19 2018.

[32] S. I. Mogal, V. G. Gandhi, M. Mishra, S. Tripathi, T. Shripathi, P. A. Joshi, *et al.*, "Single-Step Synthesis of Silver-Doped Titanium Dioxide: Influence of Silver on Structural, Textural, and Photocatalytic Properties," Industrial & Engineering Chemistry Research, vol. 53, pp. 5749-5758, 2014/04/09 2014.

[33] C. Liu, T. Li, Y. Zhang, T. Kong, T. Zhuang, Y. Cui, *et al.*, "Silver nanoparticle modified TiO_2

nanotubes with enhanced the efficiency of dye-sensitized solar cells," Microporous and Mesoporous Materials, vol. 287, pp. 228-233, 2019/10/01/ 2019.

[34] Y. Q. Liang, Z. D. Cui, S. L. Zhu, Y. Liu, and X. J. Yang, "Silver nanoparticles supported on TiO_2

nanotubes as active catalysts for ethanol oxidation," Journal of Catalysis, vol. 278, pp. 276-287, 2011/03/07/ 2011.

[35] H. Yan, X. Wang, M. Yao, and X. Yao, "Band structure design of semiconductors for enhanced photocatalytic activity: The case of TiO_2

," Progress in Natural Science: Materials International, vol. 23, pp. 402-407, 2013/08/01/ 2013.

[36] N. G, D. R. A, A. I. A, and J. R.L, "Tuning the optical band Gap of pure TiO_2

via photon induced method," Optik, vol. 179, pp. 889-894, 2019/02/01/ 2019.

[37] N. Pishkar, Z. Jedi-soltanabadi, and M. Ghoranneviss, "Reduction in the band gap of anodic TiO_2

nanotube arrays by H2 plasma treatment," Results in Physics, vol. 10, pp. 466-468, 2018/09/01/ 2018.

[38] S. Bharathi Bernadsha, V. Anto Feradrick Samson, J. Madhavan, M. Victor Antony Raj, and S. Prathap, "Embellishing the bandgap of neodymium (Nd3+) doped TiO_2

for the fabrication of high efficiency DSSCs," Materials Today: Proceedings, vol. 50, pp. 2703-2706, 2022/01/01/ 2022.

[39] N. S. Peighambardoust, S. Khameneh Asl, R. Mohammadpour, and S. K. Asl, "Band-gap narrowing and electrochemical properties in N-doped and reduced anodic TiO_2

nanotube arrays," Electrochimica Acta, vol. 270, pp. 245-255, 2018/04/20/ 2018.

[40] A. A. Valeeva, E. A. Kozlova, A. S. Vokhmintsev, R. V. Kamalov, I. B. Dorosheva, A. A. Saraev, *et al.*, "Nonstoichiometric titanium dioxide nanotubes with enhanced catalytical activity under visible light," Scientific Reports, vol. 8, p. 9607, 2018/06/25 2018.

[41] A. Stevanovic, M. Büttner, Z. Zhang, and J. T. Yates, Jr., "Photoluminescence of TiO_2

: Effect of UV Light and Adsorbed Molecules on Surface Band Structure," Journal of the American Chemical Society, vol. 134, pp. 324-332, 2012/01/11 2012.

[42] P. Roy, S. P. Albu, and P. Schmuki, "TiO_2

nanotubes in dye-sensitized solar cells: Higher efficiencies by well-defined tube tops," Electrochemistry Communications, vol. 12, pp. 949-951, 2010/07/01/ 2010.

[43] A. Témun, L. Mattsson, and I. Heikkilä, "Localizing micro-defects on rough metal surfaces," in 4M 2006 - Second International Conference on Multi-Material Micro Manufacture, W. Menz, S. Dimov, and B. Fillon, Eds., ed Oxford: Elsevier, 2006, pp. 169-172.

[44] K.-Y. Law, "Definitions for Hydrophilicity, Hydrophobicity, and Superhydrophobicity: Getting the Basics Right," The Journal of Physical Chemistry Letters, vol. 5, pp. 686-688, 2014/02/20 2014.

[45] J. Xue, Z. Wang, W. Hu, Q. Shen, X. Liu, and H. Jia, "The surface wettability of TiO_2

nanotube arrays: which is more important—morphology or chemical composition?," Journal of Porous Materials, vol. 26, pp. 91-98, 2019/02/01 2019.

[46] N. Sakai, A. Fujishima, T. Watanabe, and K. Hashimoto, "Quantitative Evaluation of the Photoinduced Hydrophilic Conversion Properties of TiO_2

Thin Film Surfaces by the Reciprocal of Contact Angle," The Journal of Physical Chemistry B, vol. 107, pp. 1028-1035, 2003/01/01 2003.

[47] T. Zubkov, D. Stahl, T. L. Thompson, D. Panayotov, O. Diwald, and J. T. Yates, "Ultraviolet Light-Induced Hydrophilicity Effect on TiO_2

(110)(1×1). Dominant Role of the Photooxidation of Adsorbed Hydrocarbons Causing Wetting by Water Droplets," The Journal of Physical Chemistry B, vol. 109, pp. 15454-15462, 2005/08/01 2005.

[48] P. Evans, S. Mantke, A. Mills, A. Robinson, and D. W. Sheel, "A comparative study of three techniques for determining photocatalytic activity," Journal of Photochemistry and Photobiology A: Chemistry, vol. 188, pp. 387-391, 2007/05/20/ 2007.

[49] D. Kim, J. M. Macak, F. Schimidt-Stein, and P. Schmuki, "Capillary effects, wetting behavior and photo-induced tube filling of TiO₂nanotube layers," Nanotechnology, vol. 19, p. 305710, 2008/06/16 2008.

[50] A. Mills and C. O'Rourke, "Adsorption and Destruction of Methylene Blue by Semiconductor Photocatalysis," vol. 1, pp. 105-113, 2011.

[51] C.-J. Lin, W.-Y. Yu, Y.-T. Lu, and S.-H. Chien, "Fabrication of open-ended high aspect-ratio anodic TiO_2 nanotube films for photocatalytic and photoelectrocatalytic applications," Chemical Communications, pp. 6031-6033, 2008.

[52] J. V. Pasikhani, N. Gilani, and A. E. Pirbazari, "The effect of the anodization voltage on the geometrical characteristics and photocatalytic activity of TiO_2 nanotube arrays," Nano-Structures & Nano-Objects, vol. 8, pp. 7-14, 2016/10/01/ 2016.

[53] R. W. Matthews, "Photocatalytic oxidation and adsorption of methylene blue on thin films of near-ultraviolet-illuminated TiO_2," Journal of the Chemical Society, Faraday Transactions 1: Physical Chemistry in Condensed Phases, vol. 85, pp. 1291-1302, 1989.

[54] A. Houas, H. Lachheb, M. Ksibi, E. Elaloui, C. Guillard, and J.-M. Herrmann, "Photocatalytic degradation pathway of methylene blue in water," Applied Catalysis B: Environmental, vol. 31, pp. 145-157, 2001/05/04/ 2001.

[55] A. Chithambararaj, N. S. Sanjini, A. C. Bose, and S. Velmathi, "Flower-like hierarchical h-MoO3: new findings of efficient visible light driven nano photocatalyst for methylene blue degradation," Catalysis Science & Technology, vol. 3, pp. 1405-1414, 2013.

[56] C. T. Mehmood, Z. Zhong, H. Zhou, C. Zhang, and Y. Xiao, "Immobilizing a visible light-responsive photocatalyst on a recyclable polymeric composite for floating and suspended applications in water treatment," RSC Advances, vol. 10, pp. 36349-36362, 2020.

[57] S. Banerjee, S. C. Pillai, P. Falaras, K. E. O'Shea, J. A. Byrne, and D. D. Dionysiou, "New Insights into the Mechanism of Visible Light Photocatalysis," The Journal of Physical Chemistry Letters, vol. 5, pp. 2543-2554, 2014/08/07 2014.

[58] C. Yang, W. Dong, G. Cui, Y. Zhao, X. Shi, X. Xia, *et al.*, "Highly-efficient photocatalytic degradation of methylene blue by PoPD-modified TiO_2 nanocomposites due to photosensitization-synergetic effect of TiO_2

with PoPD," Scientific Reports, vol. 7, p. 3973, 2017/06/21 2017.

[59] L. Yang, L. E. Yu, and M. B. Ray, "Photocatalytic Oxidation of Paracetamol: Dominant Reactants, Intermediates, and Reaction Mechanisms," Environmental Science & Technology, vol. 43, pp. 460-465, 2009/01/15 2009.

[60] E. Moctezuma, E. Leyva, C. A. Aguilar, R. A. Luna, and C. Montalvo, "Photocatalytic degradation of paracetamol: Intermediates and total reaction mechanism," Journal of Hazardous Materials, vol. 243, pp. 130-138, 2012/12/01/ 2012.

[61] J. Lea and A. A. Adesina, "The photo-oxidative degradation of sodium dodecyl sulphate in aerated aqueous TiO_2 suspension," Journal of Photochemistry and Photobiology A: Chemistry, vol. 118, pp. 111-122, 1998/10/30/ 1998.

[62] M. Eriksson, R. Andersson, and L. Kloo, "Reaction of SDS with Ozone and OH Radicals in Aqueous Solution," Ozone: Science & Engineering, vol. 29, pp. 131-138, 2007/04/05 2007.

[63] J. Zhang, P. Zhang, K. Ma, F. Han, G. Chen, and X. Wei, "Hydrogen bonding interactions between ethylene glycol and water: density, excess molar volume, and spectral study," Science in China Series B: Chemistry, vol. 51, pp. 420-426, 2008/05/01 2008.

[64] Y. Sun, Q. Zhao, G. Wang, and K. Yan, "Influence of water content on the formation of TiO_2 nanotubes and photoelectrochemical hydrogen generation," Journal of Alloys and Compounds, vol. 711, pp. 514-520, 2017/07/15/ 2017.

[65] H. Sopha, L. Hromadko, K. Nechvilova, and J. M. Macak, "Effect of electrolyte age and potential changes on the morphology of TiO_2 nanotubes," Journal of Electroanalytical Chemistry, vol. 759, pp. 122-128, 2015/12/15/ 2015.

[66] L. Suhadolnik, Ž. Marinko, M. Ponikvar-Svet, G. Tavčar, J. Kovač, and M. Čeh, "Influence of Anodization-Electrolyte Aging on the Photocatalytic Activity of TiO_2 Nanotube Arrays," The Journal of Physical Chemistry C, vol. 124, pp. 4073-4080, 2020/02/20 2020.

[67] S. Bauer, S. Kleber, and P. Schmuki, "TiO_2 nanotubes: Tailoring the geometry in H3PO4/HF electrolytes," Electrochemistry Communications, vol. 8, pp. 1321-1325, 2006/08/01/ 2006.

[68] E. Krasicka-Cydzik, K. Kowalski, A. Kaczmarek, I. Glazowska, and K. B. Heltowski, "Competition between phosphates and fluorides at anodic formation of titania nanotubes on titanium," Surface and Interface Analysis, vol. 42, pp. 471-474, 2010.

Chapter 4: Aging of TiO2 ANTA - Assessment of the Chemical and Mechanical Stability and the Retention of Photocatalytic Activity.

This chapter will assess the longevity of the materials following different aging cycles which will replicate the conditions encountered during field use will be assessed. A short-term, laboratory based aging regime, preceded a year-long aging cycle under solar irradiation. The surface morphology, crystalline structure and the photocatalytic activity towards the degradation of MB and inactivation of *E.Coli* after aging were evaluated. A series of cleaning regimens for the recovery of any lost photocatalytic activity were examined and the most effective solution used to reactivate the solar aged samples.

4.1 Methodology

4.1.1 Short Term Aging Lab Based Reactors – Set-up and Aging Regimen

The test reactors were composed of glass tanks which could hold a 40L volume of synthetic greywater. The reactors were constructed by Econetique, with the author of this work providing technical advice in all steps of the design process. A separate tank was used for each material being aged i.e., TiO_2NT-EG, TiO_2NT-AG, TiO_2NT-SS and TiO_2NT-PA. A glass flume with an elevation of 6° was installed in the tanks. The applied elevation was such that the water cascaded towards a single direction. The flume housed 18, 25mm by 25mm photocatalytic coupons, arranged in six groups of three. The samples were attached to the flume using a pressure sensitive adhesive putty. The photocatalysts were synthesised as described in section **3.1.1**.

A synthetic greywater mixture was circulated over the photocatalysts supported on the flume at 144 L/h whilst being maintained at 30°C by a submersible heater. The flow and the elevation of the flume ensured that the coupons were continuously covered by a 3 mm thick film of greywater. The synthetic greywater was based on the composition reported by Thompson *et al* [1]. The chemical composition provided by Thompson is shown in table 4.1. The bacterial seeding of the chemical component of the synthetic greywater was done by mixing 1L of real greywater to 19L of the chemical mixture. The

greywater was obtained from the capture tank of the MCAST greywater treatment facility. The greywater was collected from the wash hand basins installed in one of its buildings. Three samples from different batches of synthetic greywater were sent for analysis to Water Services Corporation. The chemical and bacteriological composition of the final greywater mixture is summarised in table 4.2. The tanks were cleaned on a weekly basis and the synthetic greywater replaced with a new batch of synthetic greywater. The water change was implemented to accelerated the degradation of the materials, whereby fresh chemical components which might deactivate or damage the material are introduced. The weekly water changes thus ensured that none of the single components of the synthetic mixture were depleted completely.

The overhead light source intended to mimic sunlight was composed of two 26 W Exoterra UVB-100 bulbs together with two 25 W Exoterra Natural Light bulbs. The bulbs were mounted 9 cm above the sample surface. The UV component of the global irradiance over the 18 coupons was calculated and found to lie between 1 and 1.2 mW/cm^2. A representation of the aging reactors is shown in figure 4.1.

The aging cycle was composed of a 12-hour period with illumination and flow, followed by a 12-hour dark period with flow being maintained. The total duration of the aging regimen was 12 weeks divided in sampling intervals at 1,4,6,8 and 12 weeks. At each sampling interval 3 samples from each tank were removed.

After removal, the samples were swabbed gently with a piece of cottonwool to remove the loose macroscopic debris. The samples were then soaked three times in isopropanol for 10 minutes the soaked three times for 1 hour in DI water and allowed to air dry.to air dry. After removal, the samples were swabbed gently with a piece of cottonwool to remove the loose macroscopic debris. The samples were then soaked three times in isopropanol for 10 minutes the soaked three times for 1 hour in DI water and allowed to air dry.

Table 4. 1 Chemical constituents of synthetic greywater mixture

Chemical	Concentration (mg/L)	Brand
Ammonium chloride	12.2	Fluka
Calcium carbonate	2.1	Scharlau
Calcium chloride	63.5	Sigma Aldrich
Cocamidopropyl betaine	4.0	Sigma Aldrich
Polyquaternium-10	4.0	Sigma Aldrich
Anhydrous magnesium sulfate	110	Scharlau
Potassium Chloride	7.3	Sigma Aldrich
Sodium hydrogen carbonate	29.5	Fischer
Sodium Chloride	120	Scharlau
Sodium dodecyl sulfate	15	Scharlau
Sodium nitrate	4.0	Scharlau
Sodium sulfate	100	Scharlau
Yeast extract	49.0	Oxoid

Table 4. 2 Identity and Concentration of Synthetic Greywater Components

Chemical or Biological Parameter	**Concentration (Actual)**
Chloride (Cl^-)	640.00 mg/L
Calcium Hardness	225.00 mg/L
Total Hardness	380.00 mg/L
Nitrate (NO_3^-)	17.40 mg/L
Nitrite (NO_2^-)	2.60 mg/L
Ammonia (NH_3)	4.67 mg/L
Total Phosphorus	0.43 mg/L
Total Surfactants	1.14 mg/L
Total Coliforms	10285.5 ± 3322.5 CFU/mL
E.Coli	855.5 ± 610.7 CFU/mL

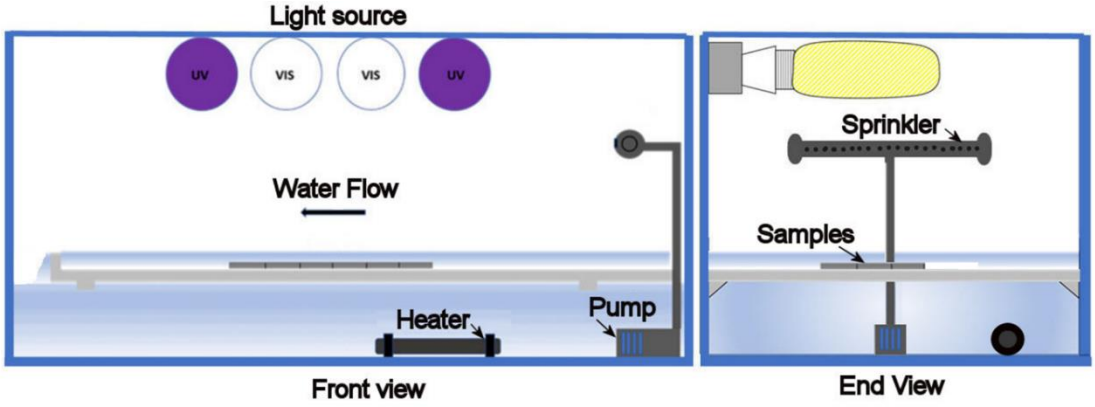

Figure 4. 1 Front and end view of laboratory based aging reactor.

4.1.2 Post-Short Term Aging Testing

4.1.2.1 Characterisation

The morphology of the aged samples and the chemical composition of the surfaces were examined as described in section 3.1.2. ImageJ was used for image analysis of the surfaces in order to obtain the approximate percentage of the surface area which was not covered with debris. Fractography of the samples was obtained by mechanical cracking of the samples and mounting them on a 45° pre-tilted sample holder. The crystal structure of the catalysts was analysed according to the procedure described in section 3.1.2.

4.1.2.2 Spectral Absorptance of Aged Samples

Diffuse reflectance spectra were obtained using a Shimadzu SolidSpec-3700 UV-VIS spectrometer housing an integrating sphere. The spectra were obtained at 1nm intervals, using a medium scan speed, over the range between 280 and 700nm. The absorptance values were corrected to account for the solar global tilt described in standard ASTM G173-03 [2]. The total spectral absorptance was calculated using equation 4.1. This procedure was employed to help determine whether any changes to the ability of the surfaces to absorb certain wavelengths had occurred.

Equation 4.1: $$\alpha = \frac{\int_{\lambda_1}^{\lambda_2} \alpha_\lambda G_\lambda d_\lambda}{\int_{\lambda_1}^{\lambda_2} G_\lambda d_\lambda}$$

Where λ is the wavelength, α_λ is the absorptance at a specific wavelength and G_λ is the spectral irradiance at a specific wavelength.

4.1.2.3 Assessment of Photocatalytic Activity

4.1.2.3.1 MB Degradation after Aging

The method based on in ISO 10678:2010 described in section 3.1.5.1 was used once more to quantify the degradation rate of MB [3]. A different light source was used for irradiation of the samples. The aged samples were irradiated for one hour at a

wavelength of 365 nm and an intensity of 1.2 mW/cm^2 using an Opsytec BS-02 chamber with a UV MAT controller. This was employed to potentially remove the adsorped organic species on the surfaces [4]. Following this initial procedure, the samples were immersed in 10 mL of a 1.5 x 10^{-5} M MB solution and left in the dark to reach the adsorption-desorption equilibrium. The absorbance of the solution after irradiation was measured over a period of four hours at 30-minute intervals. A scan ranging between 500 and 800 nm was used to read the absorbance value at 664nm using a Shimadzu SolidSpec 3700i.

4.1.2.3.2 Antibacterial activity after Aging

The microbiological experiments were carried out by one of the researchers of Micro WatTs project partners, MCAST, as a contribution to the aforementioned project. An *E.coli* ATCC® 8739™ culture was incubated at 37°C with shaking at 120 RPM under aerobic conditions for eight hours. After incubation the optical density of the culture was set to 0.5 abs units at 600 nm using tryptic soy broth. The bacterial content at 0.5 abs units was equivalent to $1.5x10^8$ CFU. The aged samples and a titanium metal blank were placed on a glass microscope slide place over an open petri dish with a 5 cm diameter. A 200 µL volume of the bacterial culture was spread evenly over the aged coupons and over a Ti coupon which acted as a blank. To prevent the bacterial solution pipetted over the surface from drying out, the petri dish was filled with 10 mL of water in order to act as a climatic chamber. A quartz glass cover was placed over the samples taking care not to make contact with the bacterial culture spread over the surface. After 1 hour of irradiation at 365nm with an irradiance of 1 mW/cm^2 the coupon was transferred to a sterile 5 cm diameter petri dish to which 1mL of sterile phosphate buffered saline (PBS) was added. The petri dish was gently shaken to transfer the bacterial solution from the surface into the PBS. The PBS extract was transferred to a sterile Eppendorf tube from which aliquots were sampled to prepare a range of serial dilutions with a range of 10^2 to 10^6. A 50 µL aliquot from each dilution was plated onto total count agar and incubated upside down for 10 hours at 37°C. The number of colonies grown after incubation were counted and the number of colonies resulting from the irradiated Ti coupon were used to represent act as a control. The number of colonies for the aged samples were then compared to the number grown on the control.

4.1.3 Solar Long Term Aging Reactors – Set-up and Aging Regimen

4.1.3.1 Reactor layout and properties.

The change in climatic conditions and their resulting effect on the irradiation falling on the photocatalytic surfaces during field use required a longer, more comprehensive aging regimen.

The design of the long-term aging set-up followed from the information obtained from the lab-based experiment. The layout of the lab-based unit involved the use of a flume which created an open channel through which water could flow freely without any particular directionality dictated by fixed boundaries. This simplistic configuration, whilst useful, was not a real representation of water treatment units or installations. A closed system ensures that there are no evaporative losses and risks of contamination to the environment outside of the unit. The use of a closed channel dictates the thickness of the water film over the photocatalytic surface and also the direction the water will take. This ensures that contact between the water and the photocatalytic surfaces is good, thus increasing the efficiency of the photocatalytic reaction. By circulating a thin film of water between a UV transparent cover and the photocatalytic surface mass transfer limitations are overcome.

A photograph of the aging set-up is shown in figure 4.2. The reactor was designed such that each coupon experienced the same hydrodynamic conditions of the others whilst having a separate inlet and outlet for each coupon. The reactor is composed of six windows, with each window containing the complement of coupons for a specific aging interval. The exploded view of one of the reactor windows, showing the seating of the coupons and the pipework for the flow is presented in figure 4.3. The distance between the backing plate and the glass was 4 mm. The sample itself was 1 mm thick, thus allowing for a 3 mm thick film of greywater.

The greywater was supplied to from an inlet located at the bottom, thus ensuring that the system was purged from air bubbles and each sample is continuously covered with greywater.

Four, twenty-five litre reservoirs, one for each material being tested, were used to feed the pipework leading to each of the different material types. The tanks were each fitted with a circulation pump to circulate the greywater over the samples being aged.

A 5 µm and a 2 µm cartridge filters were installed in series to filter any debris which might be flowing in the system. Debris could not only scatter the incident falling over the unit, preventing it from reaching the photocatalysts but also cause blockages in the system. These could result in pressure build ups leading to the glass covers fracturing.

The flow rate at 146 L/h was near identical of that used in the short-term aging experiment and would also be employed in the prototype reactors discussed in the next chapter.

The materials selected for long-term aging were TiO_2NT-EG, TiO_2NT-Ag and TiO_2NT-SS. The omission of TiO_2NT-PA was based on the inherently low activity of the material and its tendency to foul early within the short-term aging regimen.

Figure 4. 2 (L) Aging reactor (R) Sample Windows. Adapted from [5].

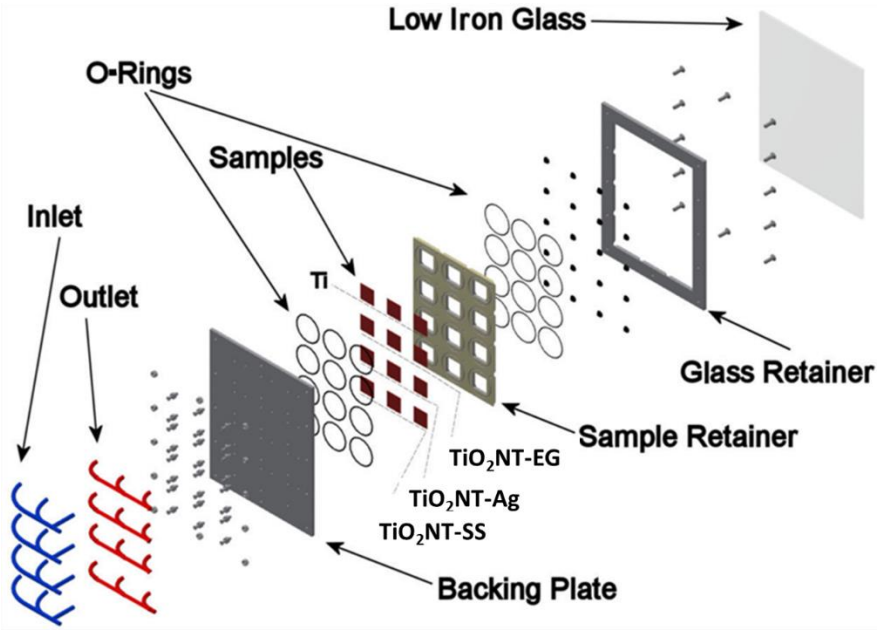

Figure 4. 3 Exploded view of sample window assembly. Adapted from [5].

4.1.3.2 Synthetic Greywater Composition

A variation of the Thompson chemical composition was employed once more [1]. One notable variation is the removal of the insoluble kaolin and cellulose. The removal of the substances was to avoid blockages in the inlet and outlet pipes of the sample window which had a small internal diameter. These would have been inevitably been filtered out by the filter array nonetheless.

Laboratory bacterial strains were used instead of spiking the chemical mixture with real greywater. Bacterial strains which are likely to be present in greywater and could be handled safely as they are rated biosafety level 1 were used. The strains used were Escherichia coli ATCC® 8739™, Staphylococcus epidermidis ATCC® 12228™, Klebsiella aerogenes ATCC® 13048™ and Brevundimonas diminuta ATCC® BAA-2474. The concentration of each bacterial strain was 5 X 10^4 CFU/mL.

The unit was drained once a week and rinsed with a 100ppm hydrogen peroxide solution to limit the proliferation of biofilm layers which would block the water circulation circuit. The unit was then filled once more with the synthetic greywater mixture.

4.1.3.3 Sample Extraction

Samples were extracted after 1,4,8,16,32 and 52 weeks. The setup was such that samples for each single time point were loaded in the same sample window. The extracted samples were replaced with titanium blanks, such that there were no alterations to the hydrodynamic properties of the unit.

The extracted samples were first swabbed gently with cottonwool. This was followed by soaking three times in isopropanol for 10 minutes and finally three times for 1 hour in DI water. The samples were then allowed to air dry.

4.1.4 Post Long Term Aging Testing

4.1.4.1: Assessment of Morphology and Crytalline Structure

The morphology of the materials was examined using a Zeiss Merlin FESEM. The approximate chemical composition of debris on the surface was measured with an Apollo EDAX EDX detector. ImageJ was used for image analysis. Fractographs were obtained by mechanically cracking the samples and mounting them on a 45° pre-tilted sample stub.

The crystalline structure of the ANTA was analysed using a Rigaku Ultima IV Cu-Source X-ray diffractometer. A step size of 0.02s with a dwell time of 1s was used spanning a range from 20° to 90°.

4.1.4.2: Assessment of Photocatalytic Activity

In order to remove surface adsorped organic species the aged samples were irradiated 1 hour at a wavelength of 365 nm and an intensity of 1.2 mW/cm^2 using an Opsytec BS-02 chamber with a UV MAT controller [4]. The samples were then immersed in 10 mL of a 1.5 x 10^{-5} M MB solution and left for 1 hour in the dark to reach the adsorption-desorption equilibrium. The absorbance of the solution was measured over a period of four hours of irradiation at 30-minute intervals. A scan ranging between 500 and 800 nm was used to read the absorbance value at 664nm using a Shimadzu SolidSpec 3700i. The methods described in sections 4.1.2.3.1 and 4.1.2.3.2 were employed.

The experiments quantifying the antibacterial activity were carried out by MCAST as part of their contribution to the Micro WatTs project. The procedure described in 4.1.2.3.2 was carried out.

4.1.5 Reactivation of Aged Photocatalyst

4.1.5.1 Accelerated Aging

This step was necessary to develop a regenerative protocol which will be applied on the naturally aged samples.

In order to study the possibility of restoring the activity of the aged ANTA an accelerated aging experiment was carried out. This experiment was carried out to study the efficiency of cleaning/reactivation processes before applying the best option on the aged samples. TiO_2 NT-EG coupons were prepared and installed in the same set-up described in section 4.1.1. The chemical component of the synthetic greywater without the kaolin and cellulose was circulated over the surfaces. The samples were irradiated with UVA 365 nm at 1.2 mW/cm^2 using UVA LED strips. The samples were aged for 8 weeks with 24 hours of irradiation and flow. The 24-hour irradiation was adopted to continuously activate the surfaces, which should hasten their deactivation. The synthetic greywater was changed weekly. After 8 weeks the samples were extracted and cleaned as per section 4.1.1.

4.1.5.2 Post Accelerated Aging Testing

4.1.5.2.1 Assessment of Morphology

The morphology of the aged samples and the chemical composition of the surfaces were examined as described in section 3.1.2. In brief, the surfaces were imaged using the same Zeiss Merlin FESEM used previously. The probe current, working distance and electron high tension settings used were chosen ad hoc depending on the degree of fouling of each imaged surface. Where required, the approximate chemical composition of features on the surface, was determined on the Apollo EDAX EDX detector.

4.1.5.2.2 Assessment of Photocatalytic Acivity (MB Degradation)

The procedure described in section 4.1.2.3.1 was followed. Surface adsorbed organic species on the sample surfaces were removed by irradiating the surfaces for 1 hour at a wavelength of 365 nm and an intensity of 1.2 mW/cm^2 using an Opsytec BS-02 chamber with a UV MAT controller [4]. This was followed by immersing the samples in 10 mL of a 1.5 x 10^{-5} M MB solution, allowing the surface to reach the absorption-desorption equilibrium for 1 hour in the dark. The absorbance of the solution was measured over a period of four hours of irradiation at 30-minute intervals. The absorbance value at 664nm was obtained by scanning the range between 500 and 700 nm using a Shimadzu SolidSpec 3700i.

4.1.5.3 Reactivation Strategies

Four cleaning regimens were devised to attempt to recover some if not all, the activity lost during aging. The solutions were selected with the domestic end-user in mind; simple to apply and low-cost. The set-up described in 4.1.1 was used once more to hold the aged coupons. The difference in this experiment was that a cleaning solution, rather than one meant to foul the surfaces was circulated. The solutions were run for 8-hours, and samples were extracted after 1,3 and 8 hours. The cleaning solutions selected and the rationale behind the choice are listed below:

- 0.1M NaOH (Removes acidic residues, organic species and replenishes OH groups)
- 0.1M HCl (Removes insoluble precipitates)
- 0.1M H2O2 + 1.2 mw/cm2 UVA (Oxidises organic remnants)
- 1.2 mw/cm2 UVA + DI Water (Photocatalytic cleaning of surfaces and regeneration)

4.1.5.3 Post Reactivation Testing

4.1.5.3.1 Assessment of Morphology

The morphology of the aged samples and the chemical composition of the surfaces wasere examined as described in section 3.1.2. The surfaces were imaged using the same Zeiss Merlin FESEM used previously.

4.1.5.3.2 Assessment of Recovery of Photocatalytic Acivity (MB Degradation)

The procedure described in section 4.1.2.3.1 was followed once more. The samples after cleaning were irradiated to remove any surface adsorbed organic species. The samples were added to 10mL of 1.5 x 10^{-5} M MB solution. After equilibration in the dark, the surfaces were irradiated for 4 hours at 365 nm at 1.2 mW/cm^2 using the Opsytec BS02 UV chamber. The absorbance of the solution at 664 nm was measured at 30-minute intervals using a Shimadzu SolidSpec 3700i UV-VIS spectrophotometer.

4.2 Results and Discussion

4.2.1 Changes to the Surface Morphology after Lab Based Aging

The surfaces' mechanical and chemical stability together with their propensity towards fouling was assessed by SEM imaging. The changes in morphology of the TiO_2NT-EG with time are presented in figure 4.4 a-j. The left-hand side of the panel provides a view of the surface at 20k magnification which allows for a gross view of the structures. A more detailed view is presented on the right-hand side at 50k magnification.

The surfaces do not reveal any mechanical damage and indications of detachment of the tubes from the substrate are absent. The crack-like features observed revealed the location of the grain boundaries, where the higher energy grain boundaries experienced a greater etching rate. The nanotubes became better defined with aging and the single nanotubes are more easily visible. The synthetic production approach taken used a high voltage with a short duration to produce long tubular structures whilst retaining some of the bulk oxide layer between the individual nanotubes. This bulk oxide layer is the one that forms during the initial stages of the anodising process and is eventually etched by the field assisted migration of fluoride ions. This layer makes the separate tubes less discernible. The oxide layer was desired to hold the adjacent tubes together and to act as a barrier against the aggregation of debris between the tubes. The increase in the definition of the tube tops could possibly be due to the fluoride induced etching of the surface. Fluoride rich layers are found at the nanotube-substrate interface [6, 7] and also between the tube walls [8]. The fluoride would then have dissolved in the flowing synthetic greywater and continued to dissolve the oxide. Similarly, loosely bound oxide particles could have been washed off by the flowing water. A similar cleaning action has been described by Olabarrieta *et al* [9].

The surfaces are also relatively clean after the conclusion of the aging regimen. By the 6th week the accumulation of material over the surface can be seen. Larger debris particles were deposited over the surface by the end of the 12th week. The 20k magnification images show that the debris is made up of voluminous particles. The higher magnifications reveal translucent particles through which the nanotube surfaces are visible. The nanotube openings themselves are also mostly free from occluding particles and deposits within the tube structure mostly occurred at the 12th week. A

close-up look and the approximate chemical composition of the thin translucent and more voluminous particles is presented in figure 4.5. The translucent particles appear to be kaolin crystals. A hexagonal or prismatic morphology is known for Kaolin [10]. Further confirmation is obtained from the EDX analysis. The silicon and aluminium contents identified these particles as being Kaolin [11]. Low values for the two elements were measured when the particles are thin as some of the substrate is picked up by the EDX detector. When the particles are larger, the silicon and aluminium contents are much higher. All elements were derived from the additives in the synthetic greywater. The ability of the surface to resist occlusion despite the weekly loading with the insoluble components of the synthetic greywater is remarkable.

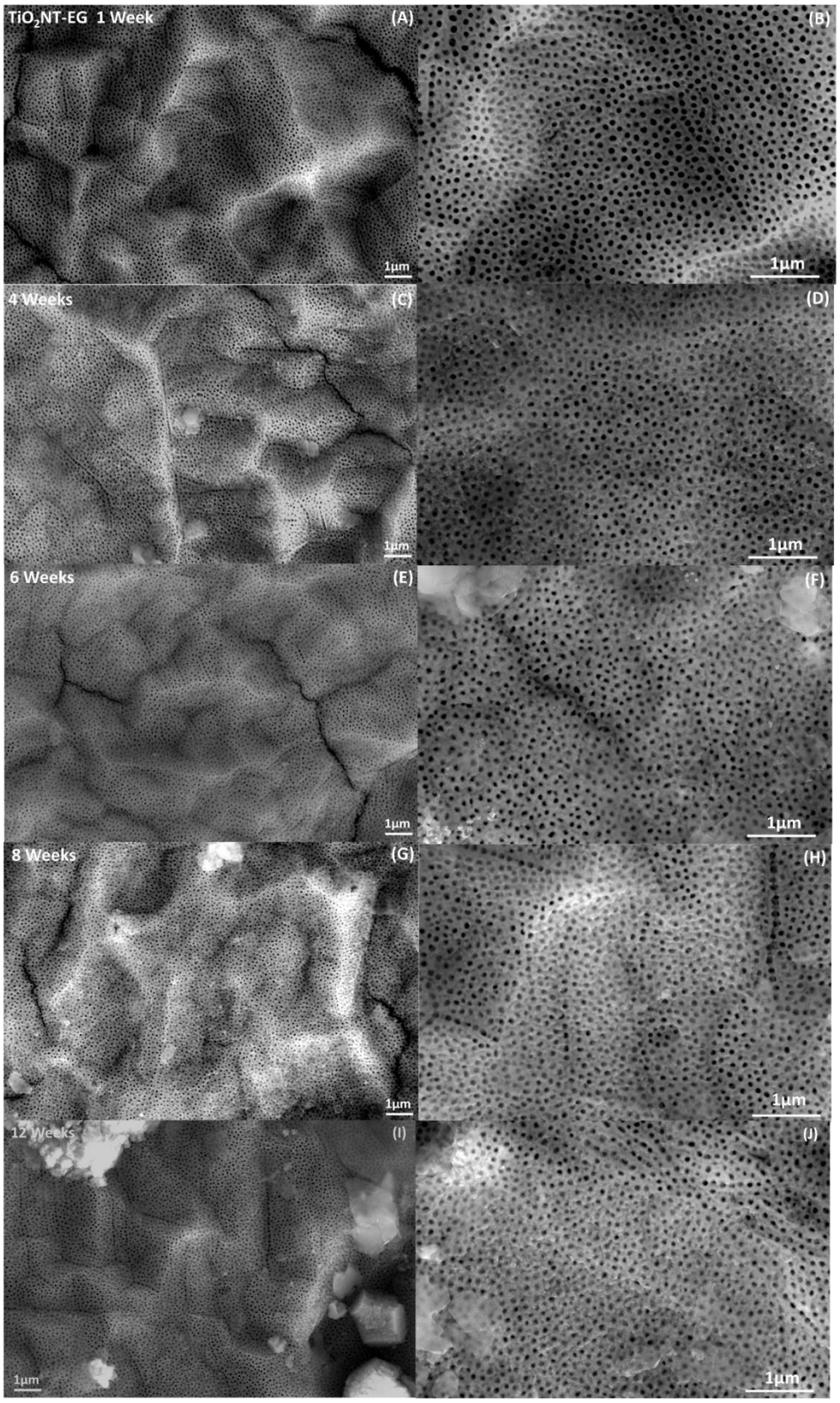

Figure 4. 4 Surface morphology of laboratory aged TiO_2NT-EG at the different aging intervals.

Magnification: 20K – A, C, E, G, I 50K – B, D,F,H,J

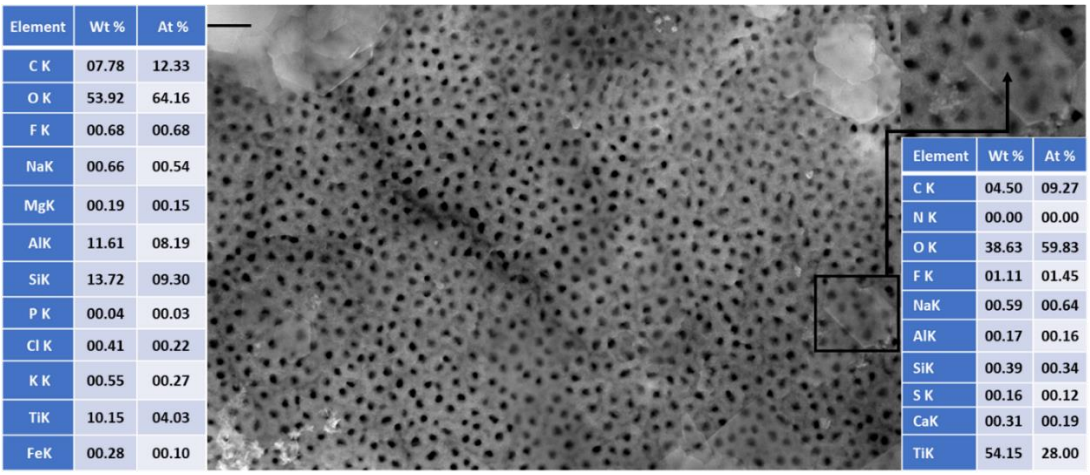

Figure 4. 5 Detail of debris deposited on TiO_2NT-EG aged for 12 weeks. Inset – Approximate chemical composition obtained by EDX. Magnification – 50K

The surface morphology of the TiO_2NT-Ag samples after aging is presented in figure 4.6 a-j. For the TiO_2NT-Ag surface assessment a 5k magnification instead of the 20K used previously to study the loss of the silver particles from the surface throughout the aging experiment. A higher magnification of 50K was used to obtain a more in detail look. The results with regards to the fouling and occlusion of the nano structure are basically identical to those of the TiO_2NT-EG. This is not surprising given that the materials have the same synthetic method. The surface remained relatively clean and the nanotube array didn't present any mechanical or photo-induced damage. The most noticable change to the surface is the distribution of the silver particles. After 1 week of aging the particles are still more or less evenly spread. The identity of these particles was confirmed by EDX analyis of the particles appearing as bright spots as shown in figure 4.7. However by the 4^{th} week, the particles started to accumulate along the spaces generated at the grain boundaries. The quantity accumulated diminishes with each subsequent time point, finally leaving the surface bare by the end of the aging exercise. This does not however mean that the silver content of the surface is nil. Surface EDX measurements reveal that some of silver colloidal solution has impregnated the nanotube arrays. Figure 4.8 shows that residual silver was retained within the material after 12 weeks of aging, despite the absence of silver particles. Similarly to TiO_2NT-EG there are no indications of mechanical damage to the nanotubular array.

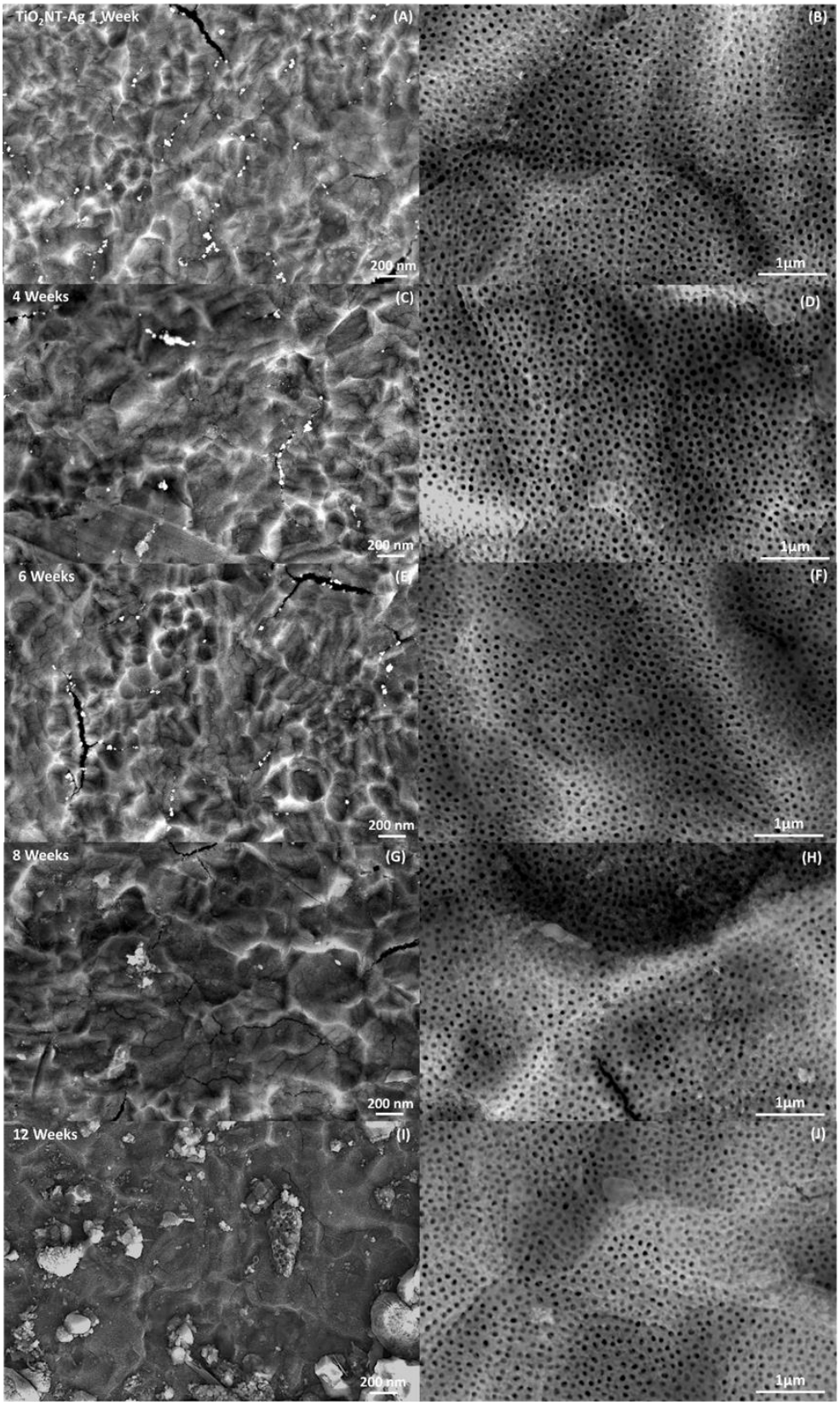

Figure 4. 6 Surface morphology of laboratory aged TiO_2NT-Ag at the different aging intervals.

Magnification: 5K – A, C, E, G, I 50K – B, D, F, H, J

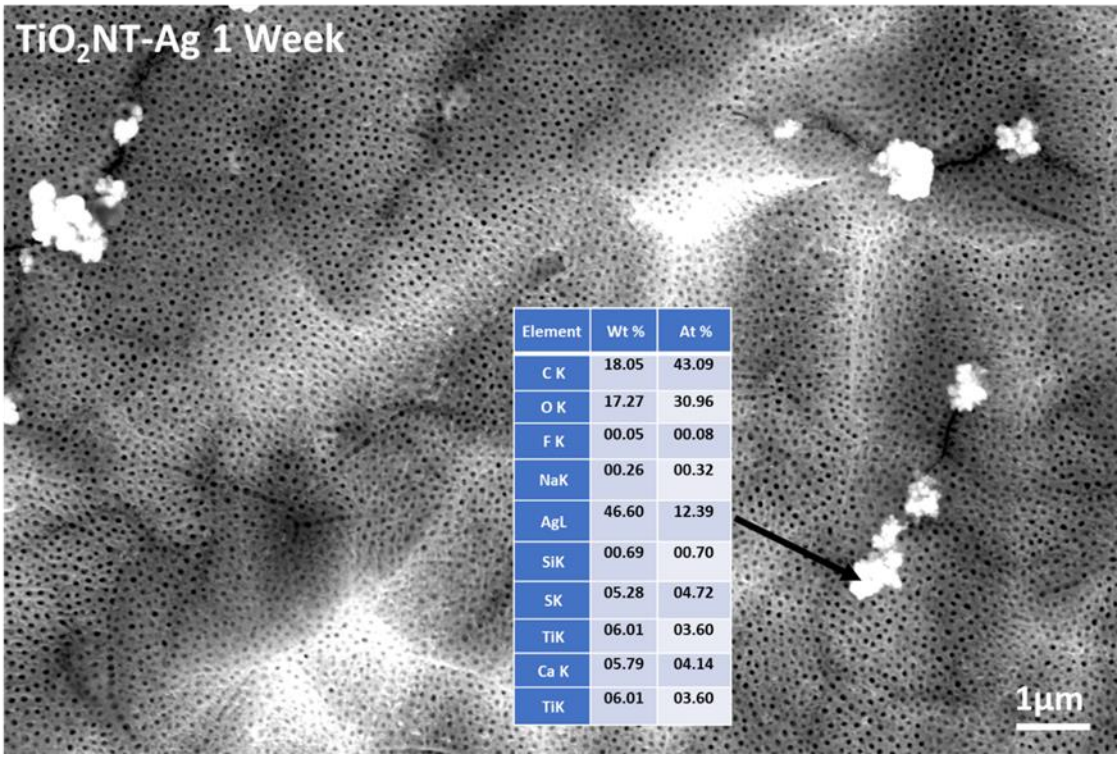

Figure 4. 7 Low magnification image of TiO_2NT-Ag after 1 week of aging. Inset – Verification of the identity of particle by EDX. Magnification – 5K

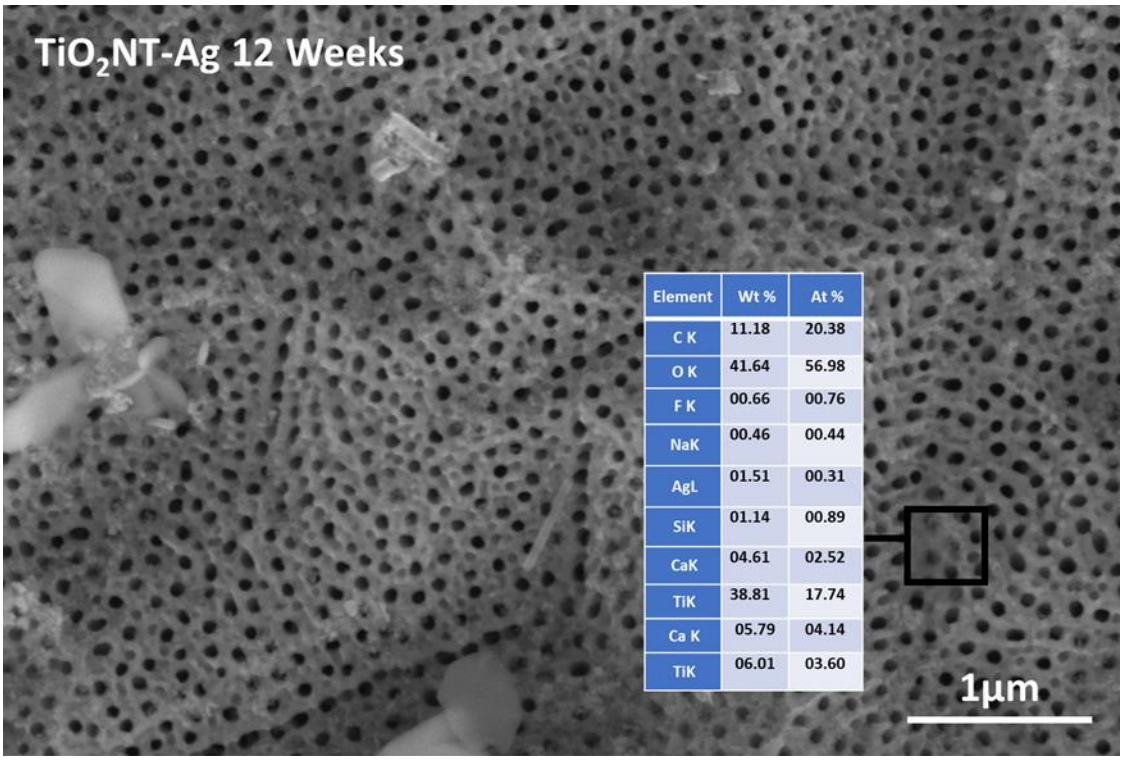

Figure 4. 8 Verification of retention of silver within nanostructure after 12 weeks of aging. Inset – Approximate chemical composition of random location on aged surface. Magnification - 50K

The surface condition of TiO2NT-SS along the aging intervals presented in figure 4.9, portrays a significant difference when compared to the two previous materials. After the 1st week of aging the surface is still relatively clean, despite being more soiled than that of TiO2NT-EG and TiO2NT-Ag. A compact debris layer starts forming by the 4th week and this is revealed when the surface was imaged at 20k (figure c). The 50k magnification (figure d) shows that the number of occluded tubes is still low. The lower range of the tube diameters (≈ 60nm) could act as a barrier against entry of solids. The existence of inter-tube space however seems to negate some of this barrier effect. The morphology of the material is uneven with a recession forming on the surface where there is a region with shorter tubes. The tubes within the recessions appear to be less occluded, with the debris being caught by the longer tubes, leading to a lower surface coverage. A significant portion of the surface was still uncovered by the 6th week. The amount of accumulated material increased throughout the last two aging time-points, but rather remarkably, the nanostructured surface was still not wholly occluded. The dark areas featured in figures g) and i) could be due to the build-up of material affecting the focus of the SEM. Another explanation has been provided by Fischer *et al.* whereby the dark areas are the result of fouling by organic matter [12]. The mechanical integrity of the tubes in the uncovered areas was retained.

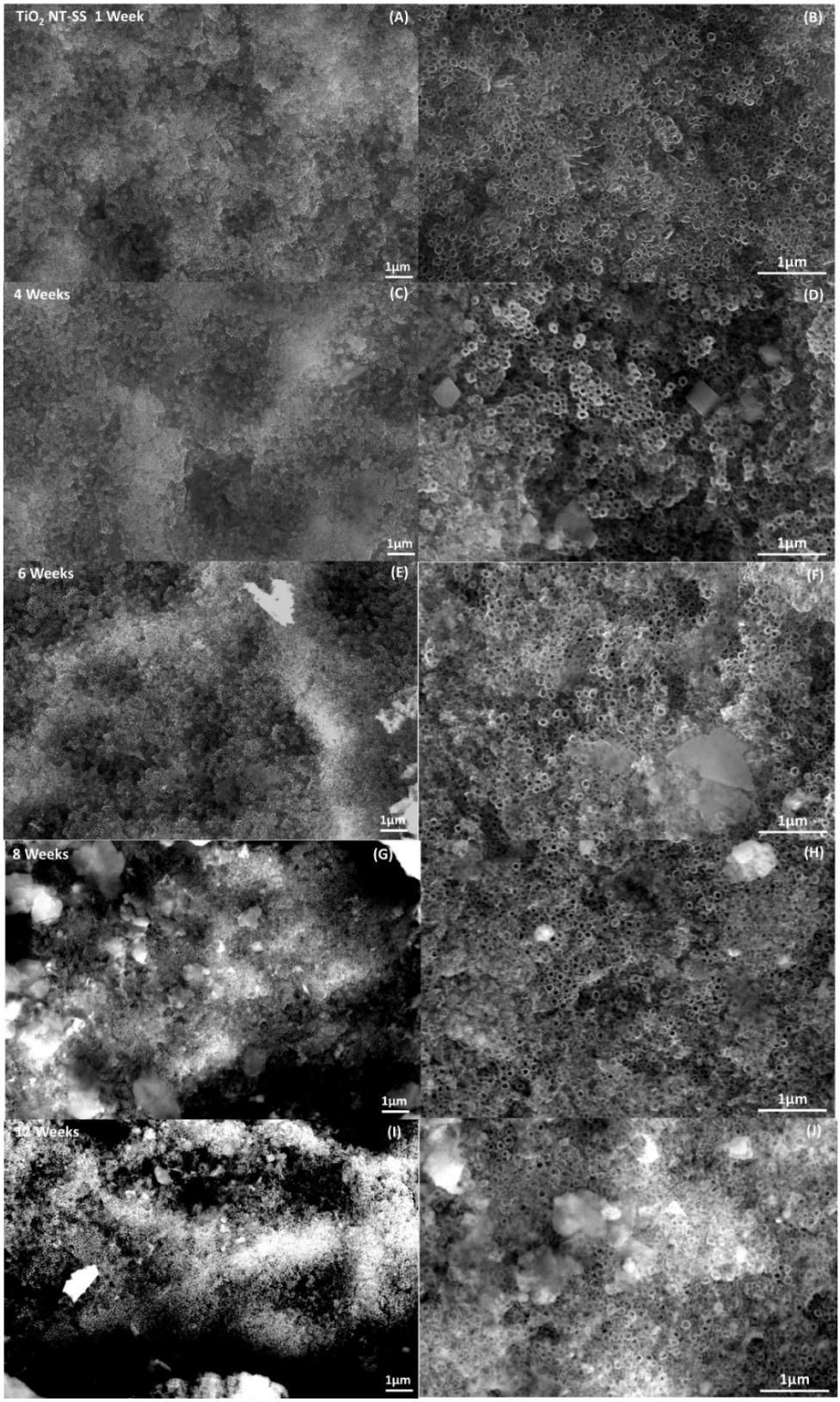

Figure 4. 9 Surface morphology of laboratory aged TiO_2NT-SS at the different aging intervals.

Magnification: 20K – A, C, E, G, I 50K – B, D, F, H, J

The change in surface condition of TiO_2NT-PA with aging is shown in figure 4.10. After just one week of aging (figure b), debris started accumulating in the inter-tube spaces of TiO_2NT-PA. The extent of tube occlusion was also more significant than that of TiO_2NT-SS at the same timepoint. This is somewhat unexpected given that the diameters of the tubes are similar to those of TiO_2NT-SS. The formation of a compact layer similar to that for TiO_2NT-SS was recorded by the 4^{th} week (figure d). The surface coverage continued to increase and by the 12^{th} week, and the debris started to gather in mounds. Dark areas like those on the TiO_2NT-SS surface were also formed. A detailed view of the surface is presented in figure 4.11. The arrays remained mechanically sound at the end of the aging regime.

The results in this section highlight the effect of morphology on the fouling resistance of the surface. The TiO_2NT-EG and Ag surfaces remained significantly clean despite having the widest tube diameters (85-125 nm). Conversely the narrower tubes of TiO_2NT-SS and PA should have been more resistant to occlusion. The main feature which differentiates the materials produced in the organic and aqueous electrolytes is the presence of spaces between the individual tubes. The spaces act as catchment areas where debris accumulates. The uneven tube lengths of TiO_2NT-SS limited the number of occluded tubes. The more regular tube lengths of TiO_2NT-PA led to a more even coverage of the tube tops.

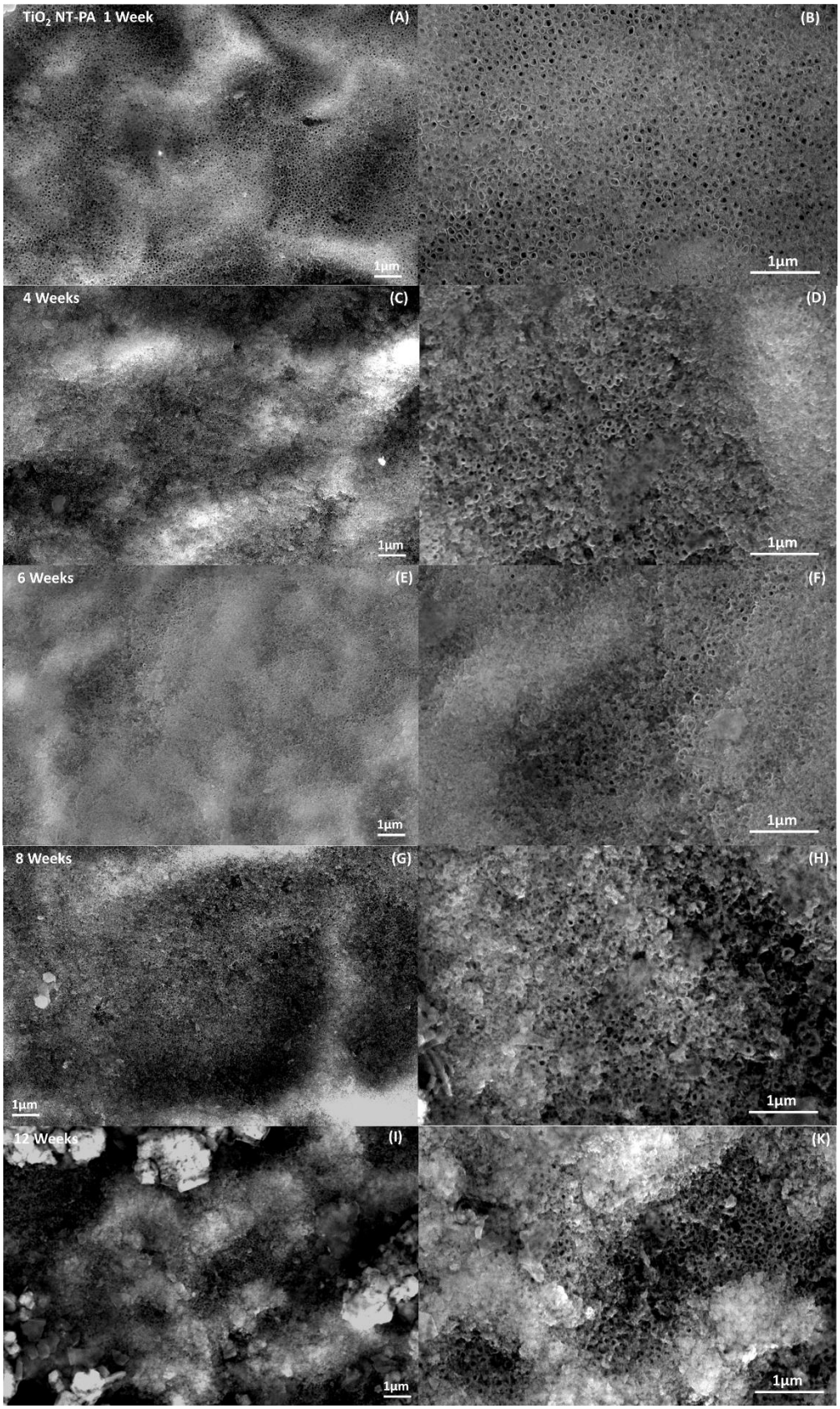

Figure 4. 10 Surface morphology of laboratory aged TiO_2NT-PA at the different aging intervals.

Magnification: 20K – A, C, E, G, I 50K – B, D, F, H, J

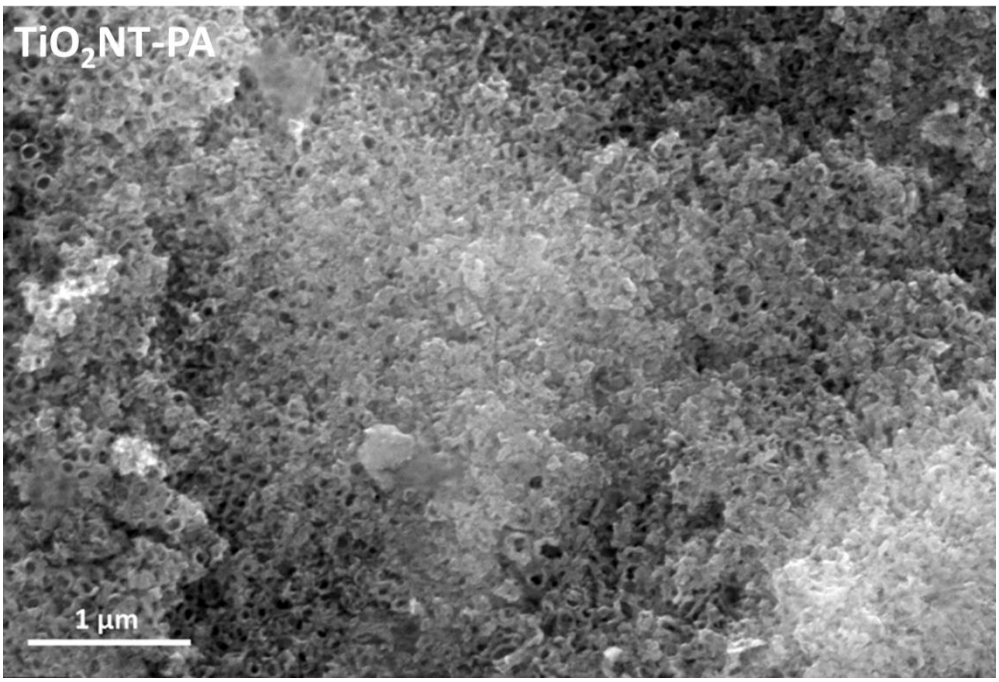

Figure 4. 11 Accumulation of compact debris on TiO_2NT-PA after 12 Weeks of Aging.

Magnification – 50K

To provide a quantitative way of expressing the extent of fouling of the surface, the percentage exposed area of the array has been estimated by image analysis using ImageJ. The analysis was done using the 20k magnification as this made quantification easier. The change in the uncovered surface with each aging interval is plotted in figure 4.12. The percentage exposed area for TiO_2NT-EG decreased gradually with time point, ending with 86% of the surface exposed. For TiO_2NT-Ag the same trend is followed, with a final value of 89%. On the TiO_2NT-SS surface the exposed surface area drops to 61% after just 4 weeks. A further slight decrease was recorded by the 6^{th} week. By the 8^{th} week less than half of the surface remained exposed. The final value at 17% was extremely low when compared to those of TiO_2NT-EG and Ag. For TiO_2NT-PA, the coverage up to the 4^{th} week was still low, with around 89% of the surface exposed. This dropped significantly and by the 6^{th} week, only 4% of surface was exposed, which decreased further to 2% by the 12^{th} week.

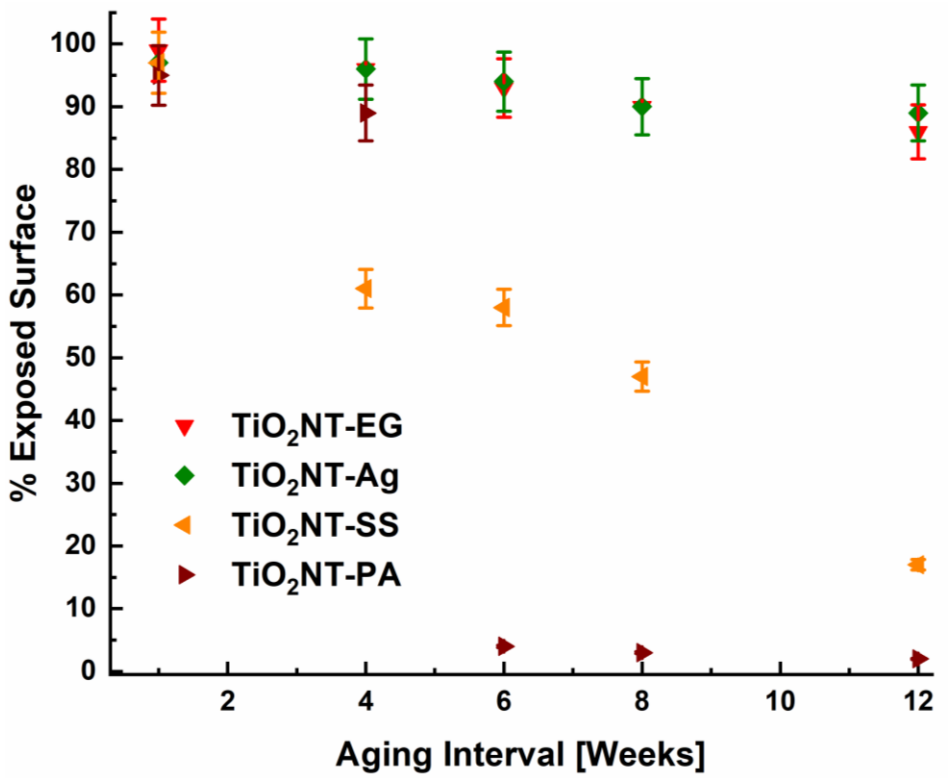

Figure 4. 12 Change in exposed surface area along the aging period. Error bars represent the maximum and minimum error obtained from the determination of the exposed surface of three aged samples.

4.2.2 Changes in Crystalline Structure with Aging

The XRD profiles of the unaged materials and at each aging interval are presented in figure 4.13 a-d. The stability of the annealed ANTA crystalline structure after long term UV exposure and immersion in water has as of the time of writing not been reported. The typically defect rich anodic ANTA crystalline structure together with the bond changes when exposed to UV light might cause changes to the original structure. There is no evident anatase-rutile transition for any material, despite anatase being the metastable polymorph. The anatase-rutile transition typically requires high temperatures, for which prolonged photocatalytic activation is not a substitute. One remarkable change is the detection of two additional peaks at 2θ ≈27.46° and ≈31.60°. There was a general increase in the intensity of the peaks with each aging timeline. The higher intensity peaks were those belonging to TiO_2NT-SS and TiO_2NT-PA. On indexing, the peaks were identified as belonging to halite with the peak belonging at 27.46 belonging to the (111) plane and that at 31.60 to the (200) plane. Despite rinsing the samples to remove the loose macroscopic debris, the highly soluble halite was not

completely removed. The surface debris might have retained the salt within its structure. Similarly solubilised halite from within the nanostructure might have soaked into the surface debris. A further confirmation as to the presence of halite on the surface was the formation of cubic crystals over the surface. The morphology of these crystals and their approximate chemical composition are presented in figure 4.14. The higher intensity of the peaks for TiO_2NT-SS and TiO_2 NT-PA can be attributed to the higher surface coverage of the aged samples. The debris acted as wicks which retained the salts contained in the synthetic greywater.

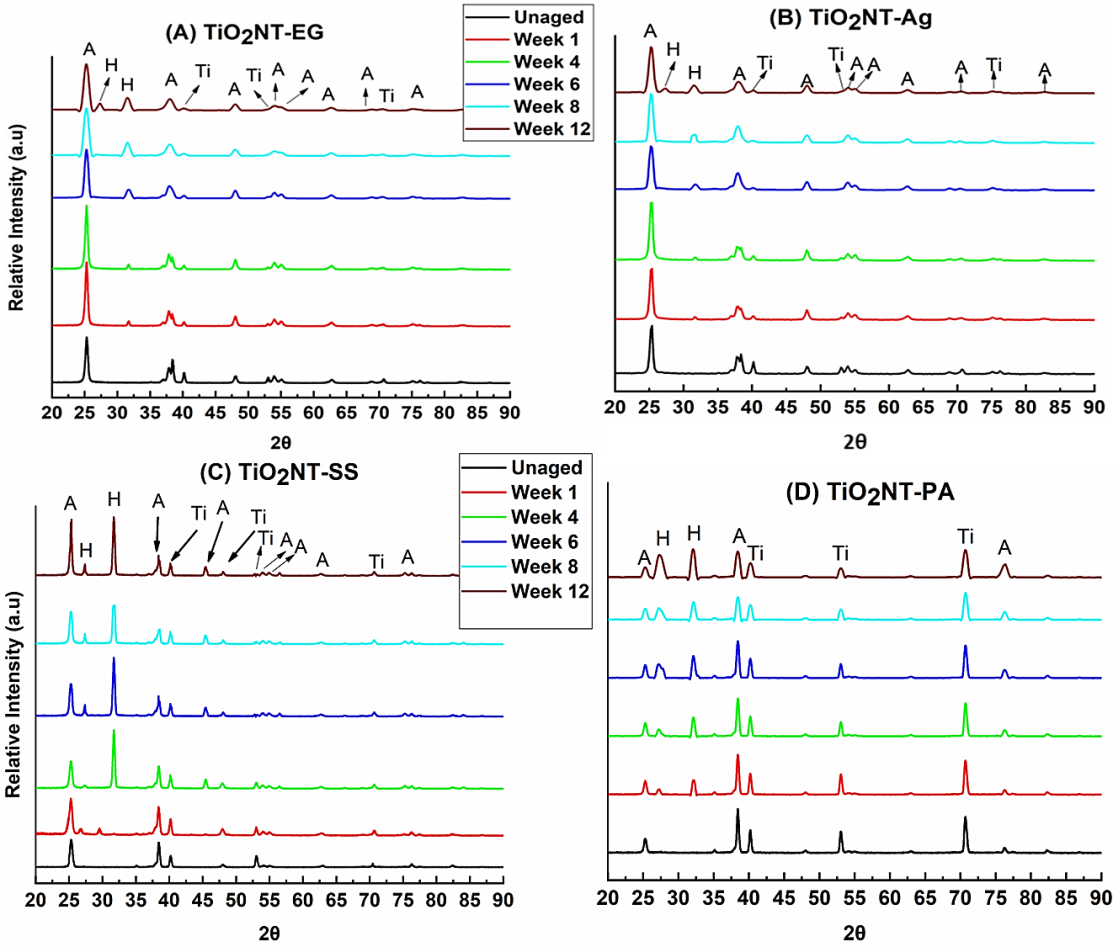

Figure 4. 13 Changes in crystallographic structure with aging a) TiO_2NT-EG b) TiO_2NT-Ag c) TiO_2NT-SS d) TiO_2NT-PA**. A=Anatase, H= Halite, Ti = Titanium**

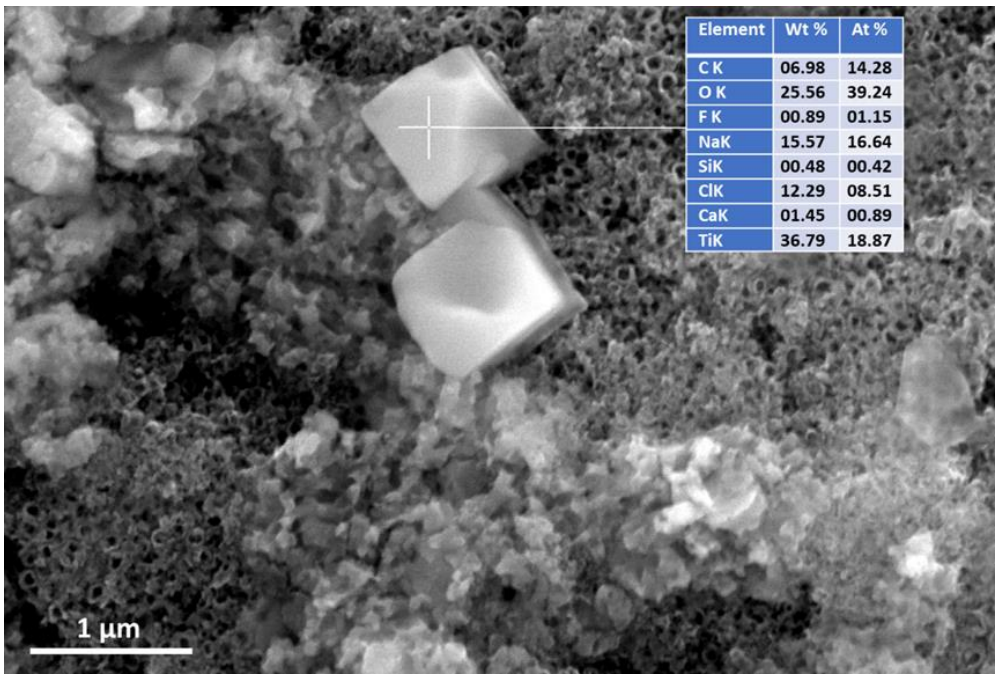

Figure 4. 14 Detail of surface showing cubic particles on TiO_2NT-PA surface aged for 12 weeks. Inset – Approximate chemical composition of cubic particles. Magnification – 50K

4.2.3 Changes in Optical Properties with Aging

The ability of the surface to absorb the UV and visible portion of the solar spectrum as it ages was studied. The absorptance plots for the different materials at different aging intervals are presented in figure 4.15. The absorptance of the unaged materials is complementary to the DRS presented in figures 3.14 to 3.17. The ability of TiO_2NT-EG and TiO_2 NT-Ag to absorb visible light is better shown in the absorptance plots. For TiO_2NT-EG following the high UVB absorptance, a gradual decline over the UVA region is recorded. What follows is a near plateau in values up to 550nm, where by a second decrease occurs at the longer wavelengths. The traces of the aged materials do not lend towards easy graphical analysis. One would expect a clear trend in the values of the abscissa, with the position of the trace being representative of the aging interval. There is an apparent loss in absorptance as the materials age but no particular relationship with the individual intervals. The translucent debris could have acted as mirrors, with a similar effect to that of the tube tops reported by Roy *et al* [13]. The TiO_2NT-Ag traces reveal that the absorptance did not vary significantly with aging. A

high absorptance between 280 and 500nm was retained throughout the duration of the aging exercise. The high efficiency of silver nanoparticles to absorb UV and visible light has been reported by Evanoff *et al* [14]. This could have contributed to the initial high absorptance values. The removal of silver with aging resulted in some changes to the absorptance curves, changes which still make discerning changes with aging difficult. For the unaged TiO_2NT-SS and TiO_2NT-PA the plots indicate that the materials absorb less between 370 and 450nm. In the case of TiO_2NT-PA the absorbance after 370 nm oscillates around 84 and 86% absorptance. The dissimilarity is attributed to the lower layer thickness. Thin transparent layers irradiated by low energy light produce these oscillations [15]. These oscillations are absent by the fourth week of aging, with the accumulation of debris increasing the opacity of the surface. As the TiO_2NT-SS surface ages, the plots seem to indicate that the surfaces absorb more strongly in the UV range. This however does not imply that this extra radiation is being absorbed by the photocatalyst. To provide a quantitative view of the optical properties with aging the total spectral absorptance of the different arrays was calculated and tabulated. The absorptance of both UV and visible light for TiO_2NT-EG increased with aging. The UV values for TiO_2NT-Ag were more or less unchanged, with a slight reduction in visible absorptance. The UV and visible values for both TiO_2NT-SS and TiO_2NT-PA increased over the aging period. The changes in absorptance appear to be related to the degree of surface fouling. The effect of these changes on photocatalytic activity cannot be inferred directly from the plots and values. The summation of the spectral absorptance at different wavelength ranges is presented in table 4.3.

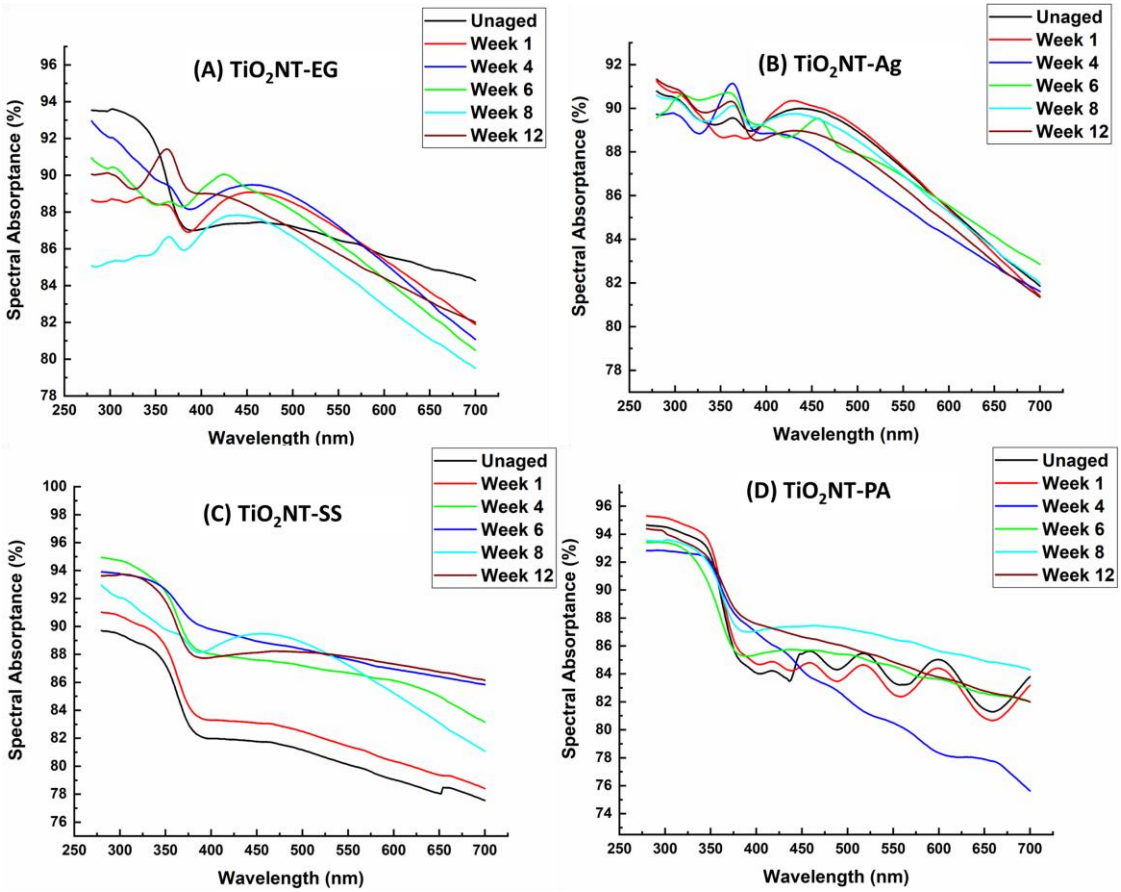

Figure 4. 15 Change in spectral absorptance of aged surfaces a) TiO_2NT-EG b) TiO_2NT-Ag c) TiO_2NT-SS d) TiO_2NT-PA

Table 4. 3 Total spectral absorptance (280 nm – 700 nm) and UVA (365 nm, 280 nm-400 nm) and visible components (400 nm – 700 nm)

Material	Spectrum	Unaged	Week 1	Week 4	Week 6	Week 8	Week 12
TiO_2NT-EG	UV	86.1 ± 1.3%	87.9 ± 1.2%	89.3 ± 1.1%	88.7 ± 1.2%	90.2 ± 1.3%	90.0 ± 1.4%
	UV-365	86.7 ± 0.03%	88.5 ± 0.12%	89.5 ± 0.08%	88.6 ± 0.05%	89.2 ± 0.12%	91.4 ± 0.07%
	VIS	84.4 ± 1.2%	86.3 ± 1.5 %	86.5 ± 1.2%	85.9 ± 1.1 %	87.4 ± 1.3%	85.7 ± 1.1%
	Total	84.6 ± 1.1%	86.7 ± 1.4%	86.8 ± 1.2%	86.1 ± 1.3%	87.7 ± 1.4%	86.1 ± 1.6%
TiO_2NT-Ag	UV	89.3 ± 1.1%	89.0± 1.2%	89.7 ± 1.5%	90.0 ± 1.2%	89.6 ± 1.3%	89.5 ± 1.3%
	UV-365	89.5 ±0.16	88.8 ± 0.04%	91.1 ± 0.07%	90.6 ± 0.06%	90.1 ± 0.13%	90.3 ± 0.06%
	VIS	85.5 ± 1.4%	85.5 ± 1.1%	84.4 ± 1.0%	85.3 ± 1.4%	85.4 ± 1.5%	84.9 ± 1.1%
	Total	87.1 ± 0.6%	87.1 ± 1.1%	85.9 ± 1.1%	86 ± 1.1%	85.7 ± 1.0%	85.2 ± 1.2%
TiO_2NT-PA	UV	88.7 ± 1.0%	89.3 ± 1.2%	89.8 ± 1.1%	88.0 ± 1.1%	89.6 ± 1.4%	90.2 ± 1.2%
	UV-365	84.6 ± 0.08%	89.0 ± 0.07%	89.6 ± 0.05%	87.2 ± 0.09%	89.2 ± 0.06%	90.1 ± 0.10%
	VIS	83.9 ± 1.1%	83.4 ± 1.2%	80.7 ± 1.3%	84.3 ± 1.0%	86.3 ± 1.2%	84.8 ± 1.1%
	Total	84.6 ± 1.2%	84.0 ± 1.3%	81.6 ± 1.4%	84.6 ± 1.2%	86.6 ± 1.1%	85.3 ± 1.3%
TiO_2NT-SS	UV	84.9 ± 1.0%	86.3 ± 1.1%	90.6 ± 1.3%	91.5 ± 1.2%	89.3 ± 1.1%	89.9 ± 1.4%
	UV-365	88.6 ± 0.17%	86.0 ± 0.08%	90.4 ± 0.06%	91.5 ± 0.05%	89.1 ± 0.09%	89.6 ± 0.08%
	VIS	80.0 ± 1.5%	81.3 ± 1.4%	86.4 ± 1.0%	87.7 ± 1.3%	85.3 ± 1.0%	87.6 ± 1.2%
	Total	80.5 ± 1.4%	81.8 ± 1.0%	86.8 ± 1.1%	88.1 ± 1.4%	85.4 ± 1.2%	87.8 ± 1.5 %

4.2.4 Changes in Photocatalytic Activity Following Laboratory Aging

4.2.4.1 Changes in The Rate of Degradation of MB

The effect of aging on the photocatalytic activity of the materials was studied by comparing the rates of reaction of the unaged materials with those at each interval. The natural log (ln) of C/C_0 was was plotted against time. All plots had correlation coefficients (R^2) exceeding 0.95 and thus the reaction follows pseudo first order kinetics [16, 17]. The equation representing first order kinetics is given in equation 4.2, where k is the apparent rate constant and t is time. The rate constant is obtained from the slope of the plot.

Equation 4.2: $\ln(C/C_0) = -kt$

The change in activity of TiO_2NT-EG with aging is shown in figure 4.16. The unaged TiO_2NT-EG has a rate constant of 0.01425 min^{-1}. The rate dropped by 30% to 0.01011 min^{-1} after 1 week with a further decline of 53% to 0.00479 min^{-1} by the 4th week of aging. The rate after the 4th week was essentially unchanged with a final value of 0.00433 min^{-1}. Whilst the condition of the aged surfaces was very close to that of the unaged sample the reactivity of the surfaces was inhibited. One possibility is the accumulation of adsorped organic compounds on the surfaces. These tend to be the degradation products of the photocatalytic reaction and can be derived from chemical species or microorganisms [18, 19]. These remnants can react further with the generated ROS, reducing the amount of ROS able to react with the target pollutant. Inorganic ions such as phosphate, nitrate, sulfate and carbonate when present in solution have been found to lower the rate of reaction. A competitive inhibition mechanism through adsorption on the surface or direct reaction with the ROS has been reported [20-22]. Guillard *et al.* described the formation of a salt layer on the TiO_2 surface when inorganic anions present in solution are strongly adsorped at positive $TiOH_2^+$ sites [23]. The authors suggested that the anions can scavenge some of the OH° generated. The anions listed are ubiquitous and are present in the synthetic greywater employed in this study. The presence of halite on the surface lends to agreement with Guillard's findings, where the authors claimed that chloride ions are strong inhibitors. Rinsing the aged samples in DI water is not sufficient to leach out all the soluble species from the nanostructure.

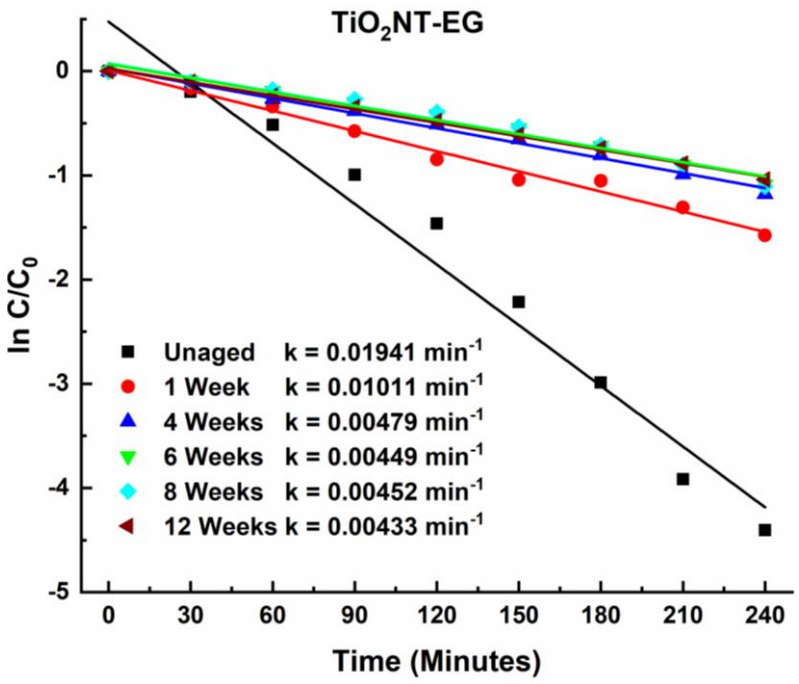

Figure 4. 16 Change in MB degradation activity with aging time for TiO_2NT-EG

The activity of TiO_2 NT-Ag with aging is shown in figure 4.17. The reaction rate of the unaged TiO_2 NT-Ag samples is 0.02021 min^{-1}, which is significantly faster than that of TiO_2NT-EG. The silver content of the surface could have hastened the degradation reaction by decreasing the recombination of charge carriers [24]. The initially fast reaction rate declines by more than half after one week of exposure. The rate of reaction on the 4th and 6th week were similar to those of TiO_2NT-EG. Whilst the reaction rate plateaued for TiO_2NT-EG after the 4th week, the rate of TiO_2NT-Ag continued to decline until the 12th week. The final value at 0.00247 min^{-1} was just 12% of the starting rate. Given that silver should enhance the activity of the material, a decline greater than that of the undecorated material is both unexpected and undesirable. The oxidation of silver nanoparticles to oxides of silver during photocatalytic degradation has been reported by Ziashahabi *et al* [25]. The dissolution of silver nanoparticles by OH◦ has also been reported [26]. The prolonged exposure to UV light and the greywater could have catalysed the oxidation of the nanoparticles. This could have lessened the activity of the materials. The nanoparticles synthesised in this study were capped by citrate ligands which are amenable to photocatalytic degradation. This unintentional oxidation pathway could have contributed to the deactivation of the materials possibly due to the accumulation of residues of the citrate ligands. Any deactivation mechanism is coupled

to others such as the formation of a salt layer leading to a lower activity than that of TiO_2NT-EG.

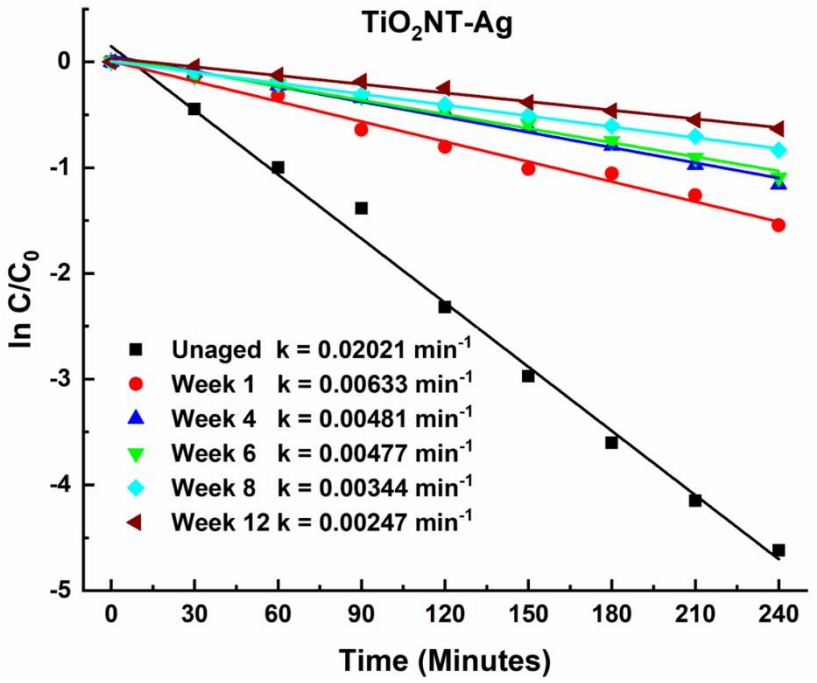

Figure 4. 17 Change in MB degradation activity with aging time for TiO_2NT-Ag

The results for TiO_2NT-SS are presented in figure 4.18. The rate of the unaged TiO_2NT-SS array at 0.00797 min^{-1} was significantly lower than that of the two previous materials. The reaction rate drops by 60% by the 4th week of aging, after which the reaction rate did not decline drastically. This trend in loss of activity monitors that TiO_2NT-EG and Ag. The TiO_2NT-PA arrays' change in activity with aging is presented in figure 4.19. The rate constant for the unaged arrays at 0.00715 min-1 is slightly lower than that of TiO_2NT-SS. As with all the other materials, the greatest drop-in activity occurred within the first 4 weeks of aging. A direct correlation between the surface coverage and loss in activity is not evident. Despite the lower surface coverage of TiO_2NT-EG and Ag, the reduction in the rate of reaction was still considerable. The most remarkable result is despite the heavy fouling of TiO¬2NT-SS and PA the final reaction rate is nearly identical to that of TiO¬2NT-Ag. Despite the high surface coverage of TiO_2NT-PA and SS their activity was not wholly stifled. This indicates that the solution still managed to reach the surface despite notwithstanding the material covering the surface. Similarly, light is still being absorbed by the surface, possibly due to the transparency of Kaolin

for low energy UV [27]. The loss in activity is probably the result of both physical coverage of the surface and also chemical inactivation.

To complement the reaction rate data, the percentage change in activity with aging is presented in figure 4.20. The highest activity was retained by TiO_2NT-EG at 65%. This contrasts greatly with the lower value of 47% for TiO_2NT-Ag. The final value of TiO_2NT-SS at 51% was marginally higher than that of TiO_2NT-PA which retained 47% of its activity.

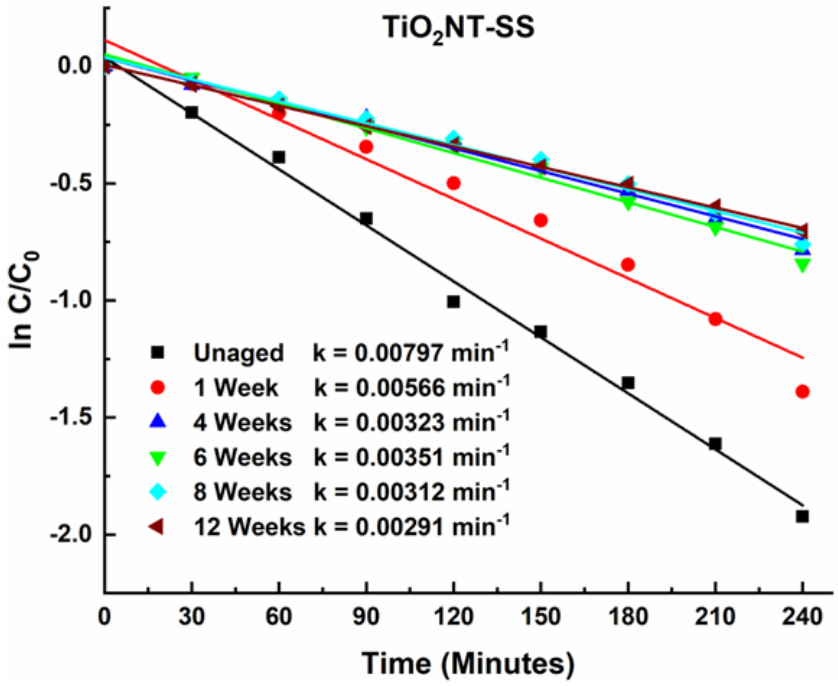

Figure 4. 18 Change in MB degradation activity with aging time for TiO_2NT-SS

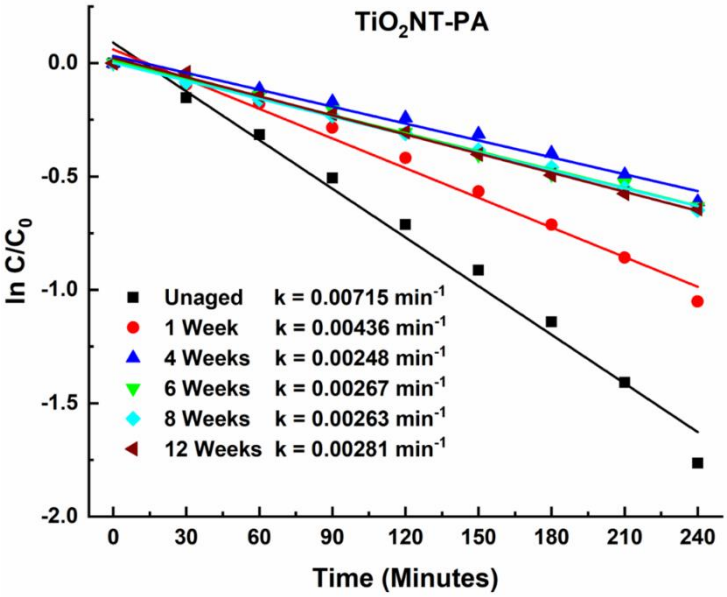

Figure 4. 19 Change in MB degradation activity with aging time for TiO_2NT-PA

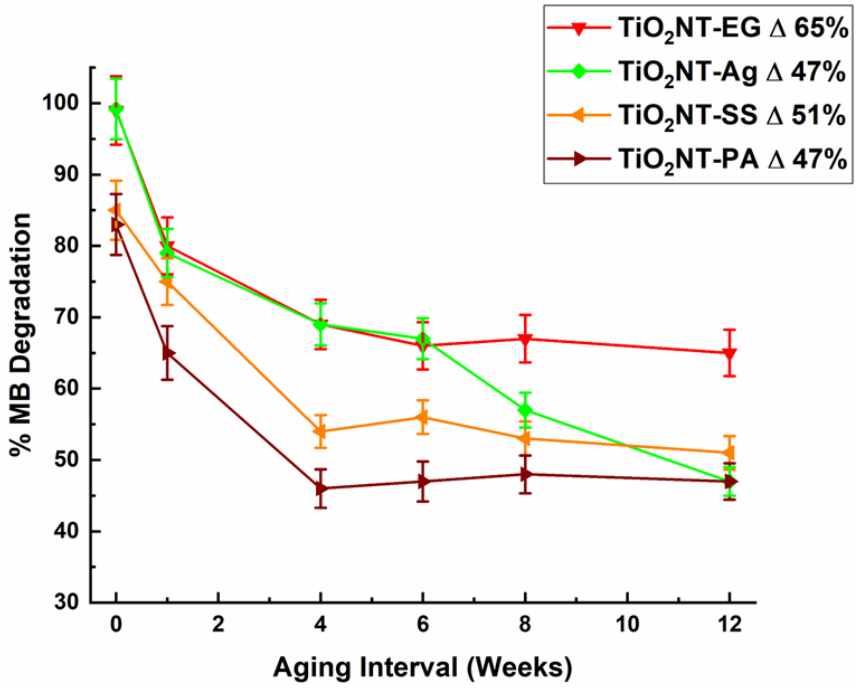

Figure 4. 20 Comparison of activity of the 4 photocatalysts with aging. Legend - % MB degradation at 12 weeks of aging. Error bars represent the maximum and minimum error of the photocatalytic activity of 3 samples.

4.2.4.2 Changes in Antibacterial Activity

The antibacterial mechanism requires the generation of ROS in much the same way as that required in the degradation of organic pollutants. The main difference is the necessity for the organic molecules to adsorb to the surface, whereas the antibacterial effect can reach out away from the surface. The results for the change in antibacterial activity with aging are provided in figure 4.21.

For TiO_2NT-EG the loss in activity over the 12-week aging period is just over 13%. This is lower than that recorded for the degradation of MB by the same material. The trend in anti-bacterial activity of the aged TiO_2NT-Ag mirrored that for the degradation of MB. There is a gradual reduction in activity of 4% at each timepoint up to 6 weeks. The level of activity dropped by around 10% on the 8th week, falling by a further 20%, reaching a final activity level of 57% at the end of the aging exercise. This indicates that the deactivation mechanism/s had the same effect on both the activity at the surface and also on the migration of ROS away from the surface. As discussed for degradation of MB, the oxidation of the silver and its capping agent could have exhausted the surface. The amount of silver itself was not enough for its inherent antibacterial activity to compensate for the decline in photocatalytic activity.

Up until the 6th week of aging there was only a slight decline for TiO_2NT-SS. After the 6th week the activity drops by about 30%, leading to a final value of 45%. This decline in related to the increased surface coverage with aging. Where surface coverage is concerned there seems to be a degree of coverage which once exceeded significantly hinders the activity of the material. The dense debris layer can impede the migration of the ROS whereby reaction with the microorganism does not occur. The activity of TiO_2NT-PA declined by only 6% throughout the first 6 weeks. A further reduction of 10% was recorded by the 8th week. The final value was near identical to that of TiO_2NT-SS at 46%. The trend in activity is identical to that of TiO_2NT-SS and is also related to the accumulation of debris on the surfaces.

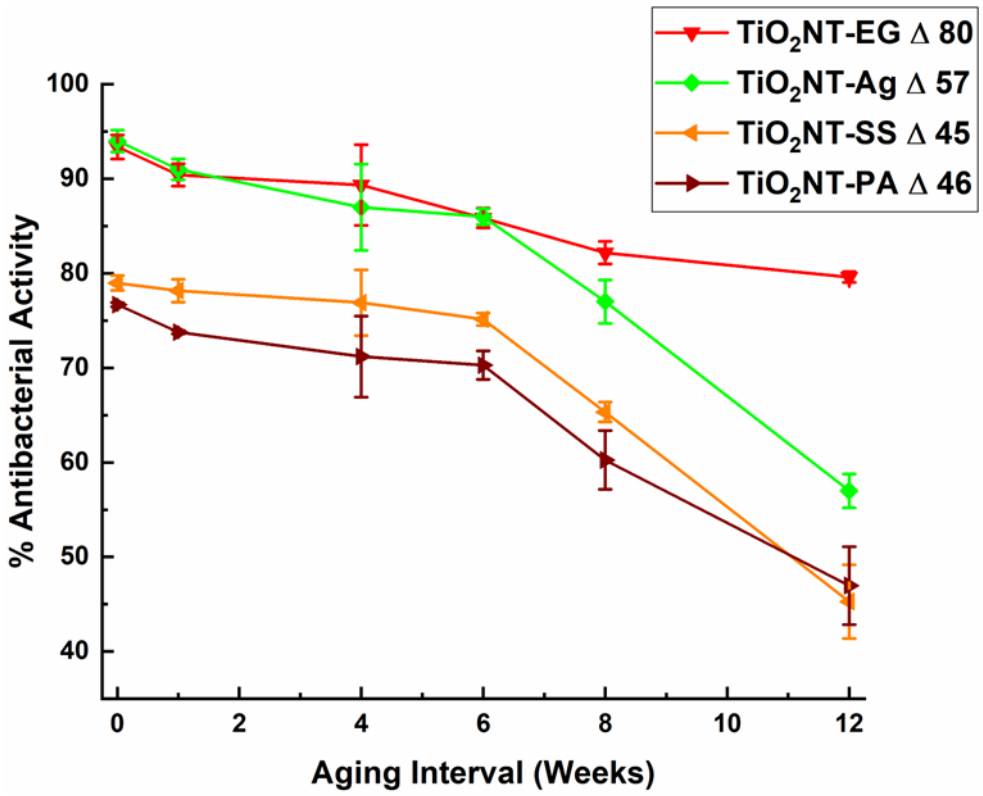

Figure 4. 21 Variation in antibacterial activity with aging. Legend - % antibacterial activity at 12 weeks of aging. Error bars represent the maximum and minimum error of the photocatalytic activity of 3 samples.

4.2.5 Changes to the Surface Morphology Following Solar Long-Term Aging

The morphology of the samples following long term aging was investigated for signs of mechanical degradation and emergence of features not found in the unaged materials. The images at each timepoint were taken at 20k and 50k magnifications which are presented on the left- and right-hand side of the panels respectively.

The morphology of the aged TiO_2 NT-EG arrays is presented in figure 4.22 a-l. The surfaces up to the 8th week of aging were mostly devoid of precipitates. The formation of filamentous precipitates over the surface was recorded on the samples aged for 16 weeks. These filaments resided over the surface and did not occlude the tube pores through penetration. The filamentous precipitates became more voluminous with throughout the rest of the aging exercise. The nanotubular structure was less discernible by the 32nd week of exposure. The loose filaments reported for the 16th week of aging were also mostly absent as the debris on the surface became more closely packed. This accumulation of debris proceeded until the end of the aging regimen at the 52nd week of exposure. The approximate chemical composition of the debris at the end of the aging regimen is given in figure 4.23. The concentration of the elements belonging to the inorganic component of the synthetic greywater is much lower than that reported for the short-term aging exercise. This change in composition can be attributed to the design of the aging set up. The long-term aging set-up housed the coupons in closed channels where the water flowed over the coupon surface and beneath a sheet of glass. The samples in the short-term aging experiment were placed over a flume which was exposed to the atmosphere. The open set-up favours evaporation leading to the deposition of the salts originally dissolved in the synthetic greywater. Of interest is the aluminium and silicon content recorded despite the absence of kaolin in the synthetic greywater mixture. This is likely caused by release from the silicone gaskets used to ensure water tightness. The debris present over the surfaces following long-term aging is most likely biological in nature. The synthetic greywater mixture used did not contain any organic or inorganic species which would form the fibrous structure. It was however seeded with bacterial cultures which represented the bacteria naturally present on human skin and would contaminate water used for bathing and cleaning. Anitha *et al.* reported

extensive biofilm formation on ANTA surfaces [28]. The authors reported that the propensity for biofilm formation was extremely high on ANTA which possessed pore diameters lower than 140nm. The biofilm formed also had a fibrous structure similar to that reported in this study. The presence of biofilms after long-term aging contrasts the findings following short-term aging. One possibility is that biofilm formation required longer periods longer than 12 weeks. The absence of kaolin in the long-term aging exercise also eliminated the mild abrasive action of the clay, which could interfere with biofilm formation.

The aged TiO_2 NT-Ag samples are presented in figure 4.24 a-l. The approximate chemical composition of debris found on the surface at the end of the aging regimen is given in figure 4.25. The surface condition of the TiO_2NT-Ag samples mirrored that of TiO_2NT-EG. The surface after the first week of aging had some deposits over the surface but also retained some of the silver particles. The surface was free from fibrous precipitates up to the 8th week. The appearance of fibrous debris was recorded on the 16th week of exposure with the surface coverage still relatively sparse. The surface coverage increased by the 32nd week and the surface was devoid of single fibres. Despite the increased coverage, several unoccluded nanotube tops were still visible. This could be the result of some silver still being retained within the nanostructure impeding the proliferation of bacteria. Despite no silver being detected by the EDX measurements this does not necessarily confirm its absence. The silver signal might have been attenuated by the debris on the surface or was below the detection limit of the instrument. The surface condition by the 52nd week was indistinguishable from that of TiO_2NT-EG. Any residual silver retained in the surface did not completely stifle biofilm formation.

The TiO_2NT-SS morphology shown in figure 4.26 a-l had early signs of fouling early on in the aging exercise. In the short-term aging exercise, the inter-tube spaces served as anchorage sites for the insoluble kaolin and cellulose. Despite the absence of these components, the nanotubular structure revealed signs of occlusion of both the tube pores and inter-tube spaces after just 1 week of aging. Signs of bacterial fouling were already present by the 1st aging interval, whereas for the other two materials this was recorded at longer aging periods. The inter-tube spacing provided sites where bacterial attachment could occur. A gradual increase in surface coverage was recorded with each subsequent

aging interval, finally achieving the same fibrous morphology of the other two materials. The chemical composition shown in figure 4.27 reveals that the elemental composition of the debris was similar to that of the other materials.

A quantitative look into the reduction in exposed surface area is given in figure 4.28. The surface coverage of TiO_2 NT-EG and Ag was similar up to the 8th week of aging whereas that of TiO_2NT-SS decline to 62%. The resistance to fouling of TiO_2NT-EG was especially high, retaining 34% of its surface area uncovered, with that of the other materials around half that. At the end of the year-long exposure all three materials were essentially covered in the fibrous debris.

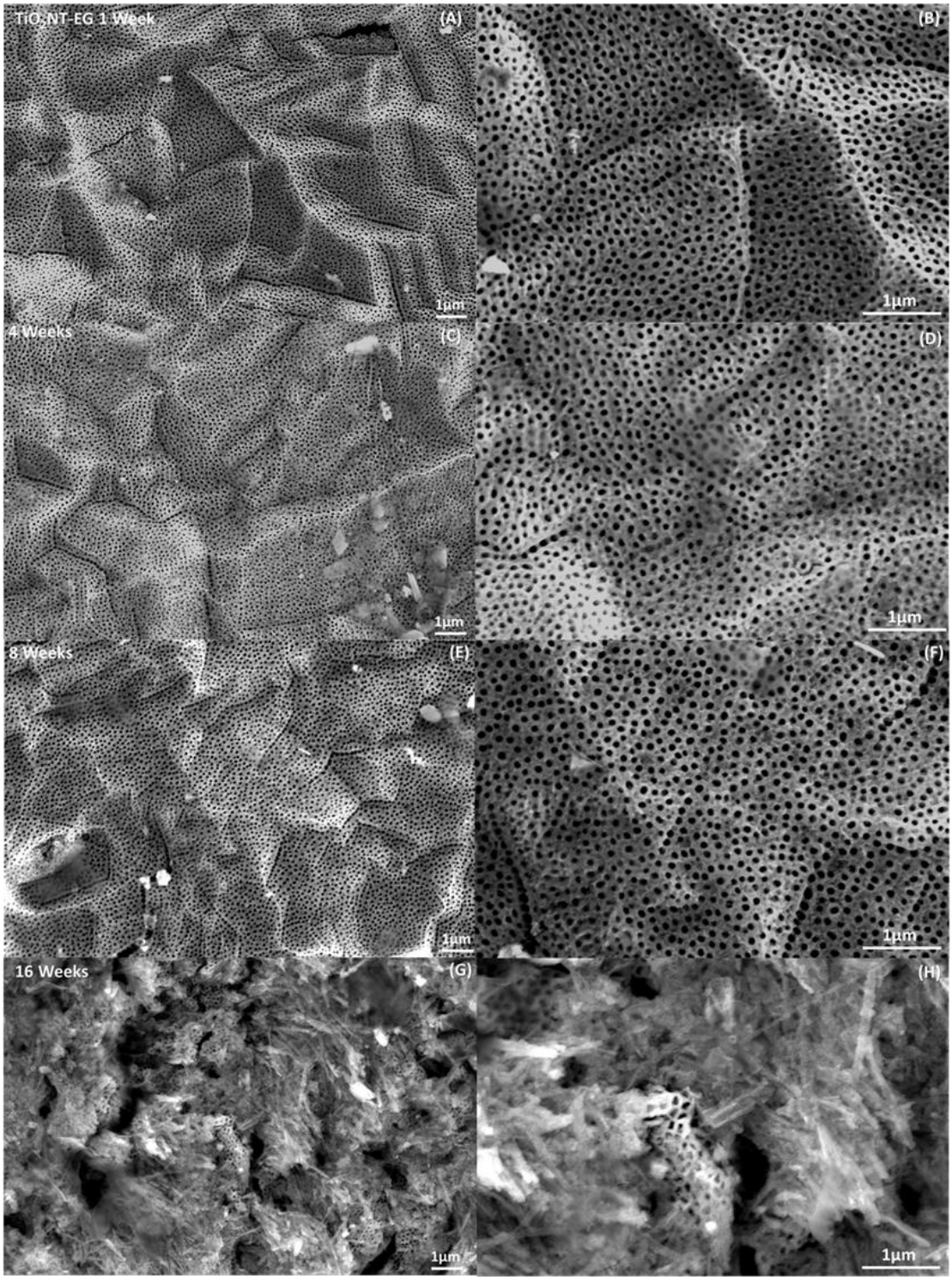
TiO2 NT-EG 1 Week
(A)
1µm
(B)
1µm
4 Weeks
(C)
1µm
(D)
1µm
8 Weeks
(E)
1µm
(F)
1µm
16 Weeks
(G)
1µm
(H)
1µm

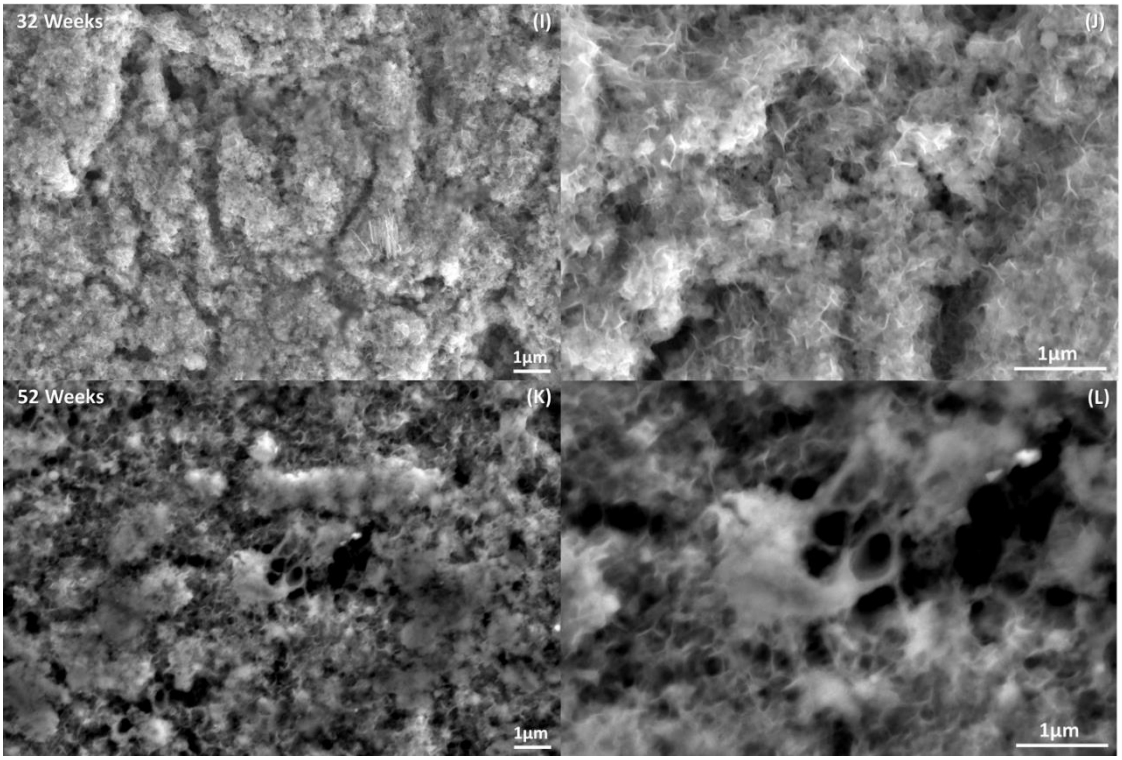

Figure 4. 22 Change in surface morphology after long-term aging of TiO_2NT-EG. Magnification – 20K -A, C, E G, I, K 50K – B, D, F, H, J, L

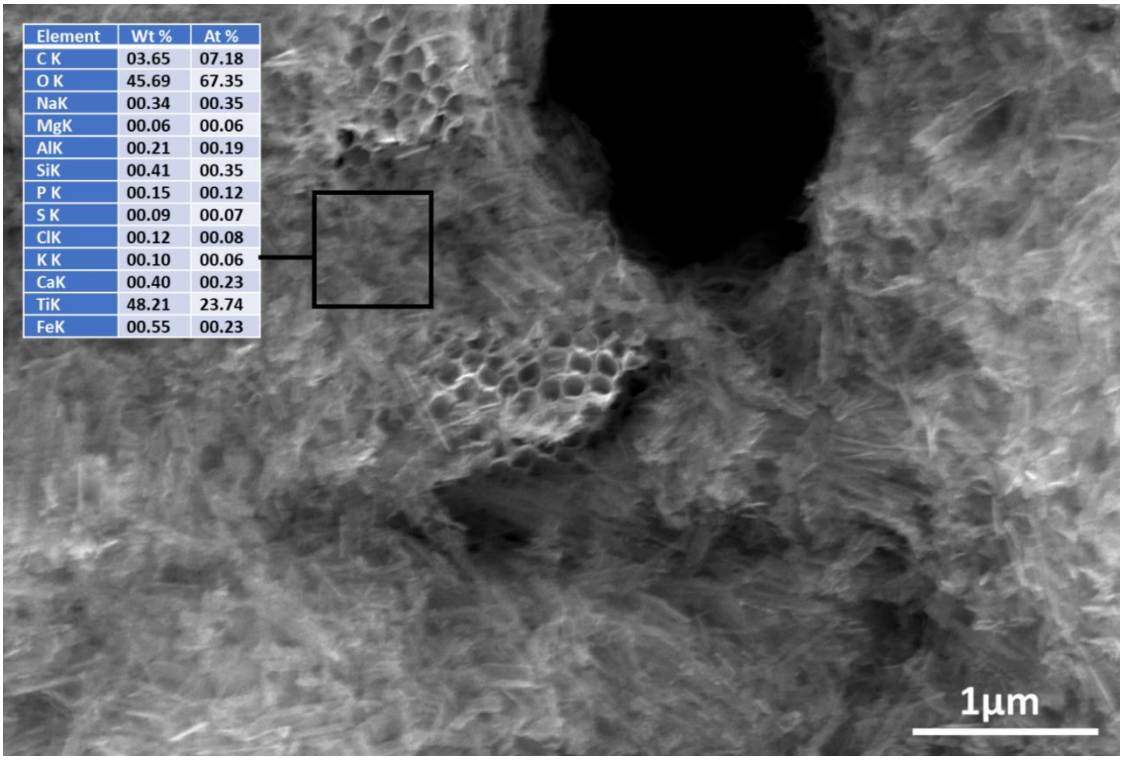

Figure 4. 23 Detail of TiO_2NT-EG surface aged for 52 weeks. Inset – Approximate chemical composition obtained by EDX. Magnification – 50K

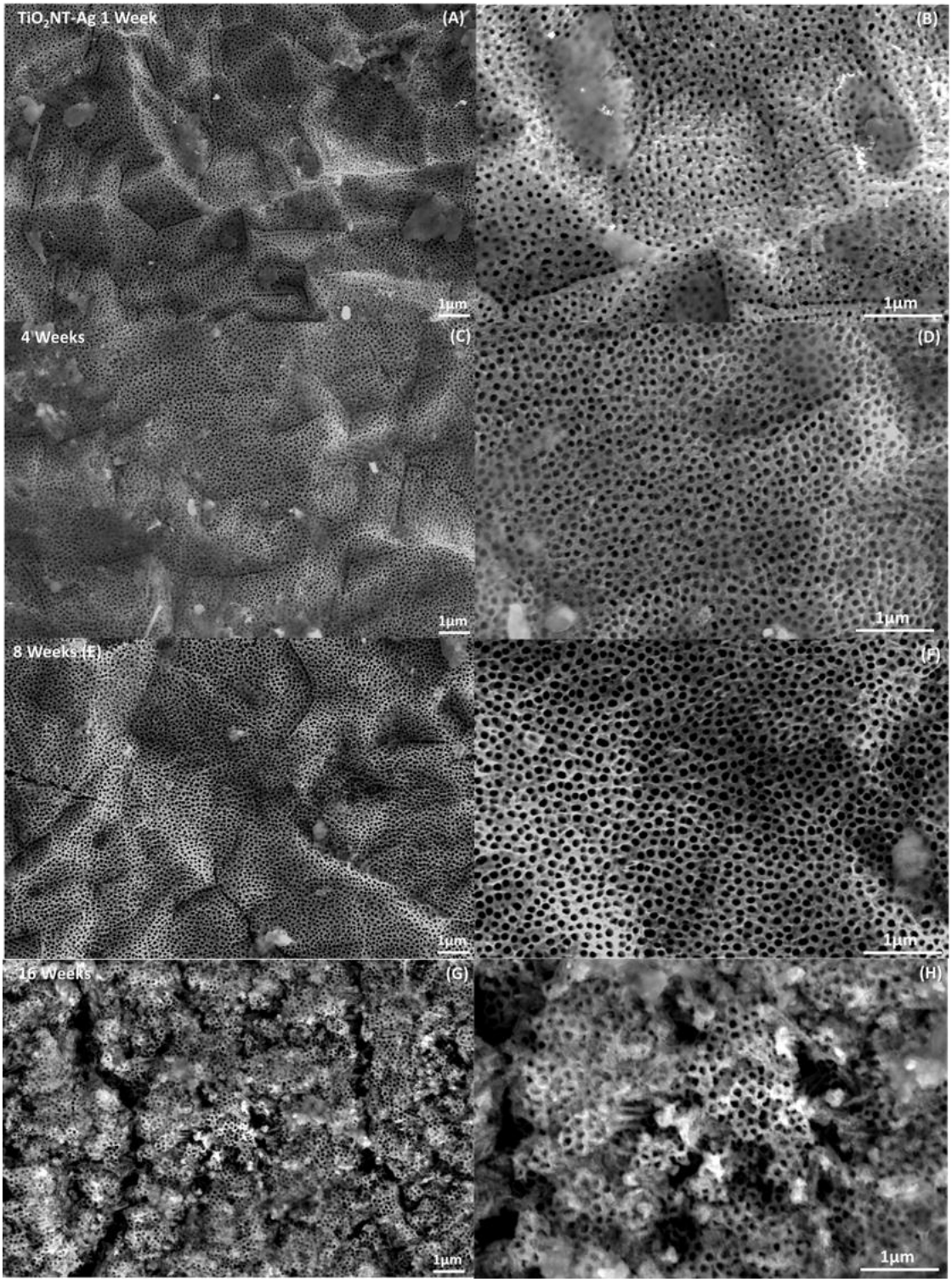
TiO2NT-Ag 1 Week
(A)
1µm
(B)
1µm
4 Weeks
(C)
1µm
(D)
1µm
8 Weeks (E)
1µm
(F)
1µm
16 Weeks
(G)
1µm
(H)
1µm

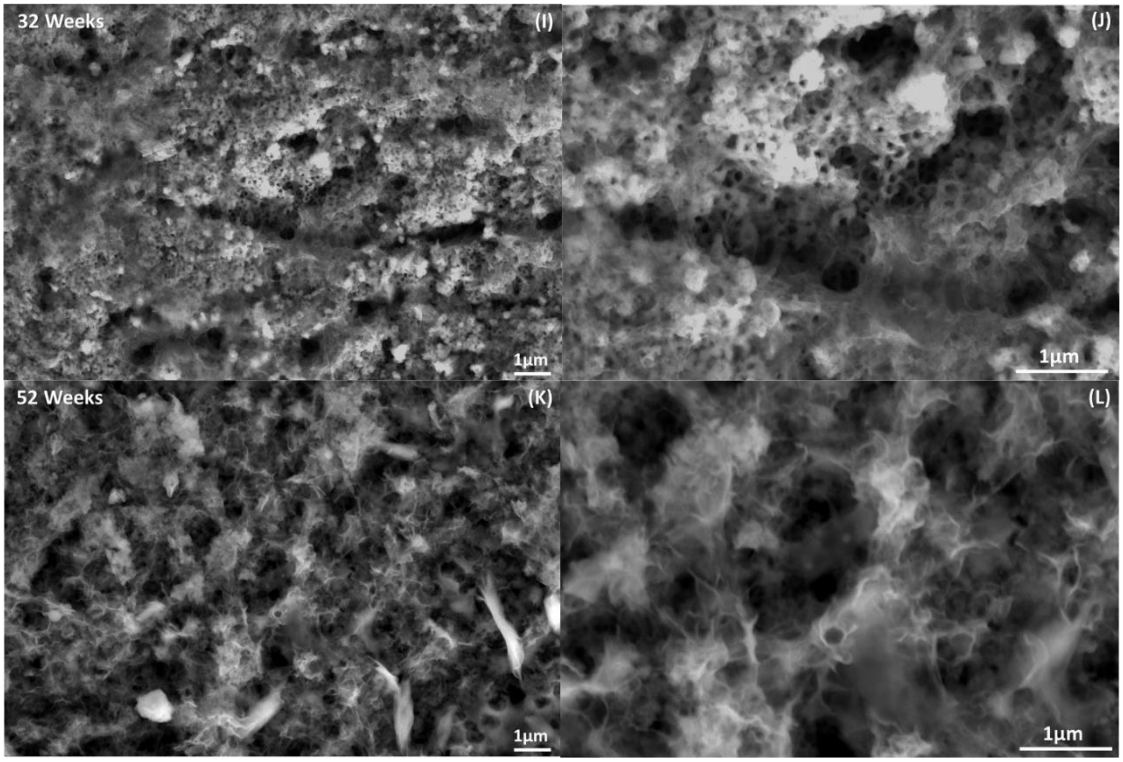

Figure 4. 24 Change in surface morphology after long-term aging of TiO_2NT-Ag.

Magnification – 20K -A, C, E G, I, K 50K – B, D, F, H, J, L

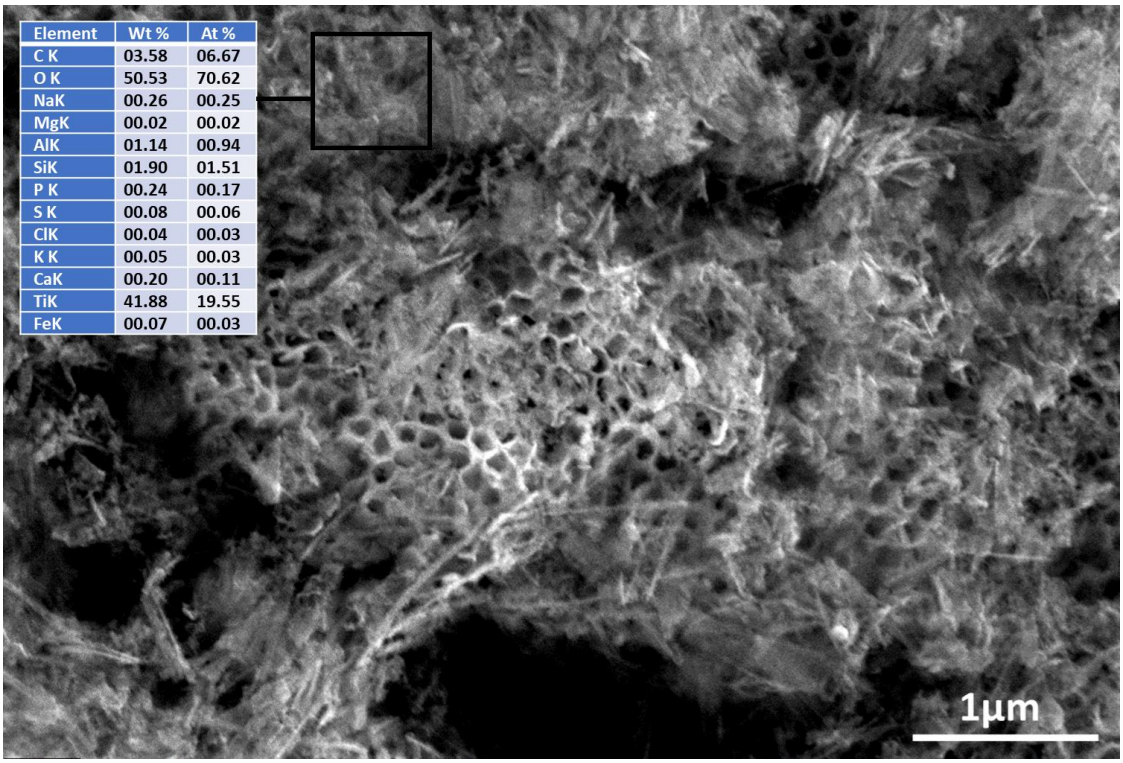

Figure 4. 25 Detail of TiO_2NT-Ag surface aged for 52 weeks. Inset – Approximate chemical composition obtained by EDX. Magnification – 50K

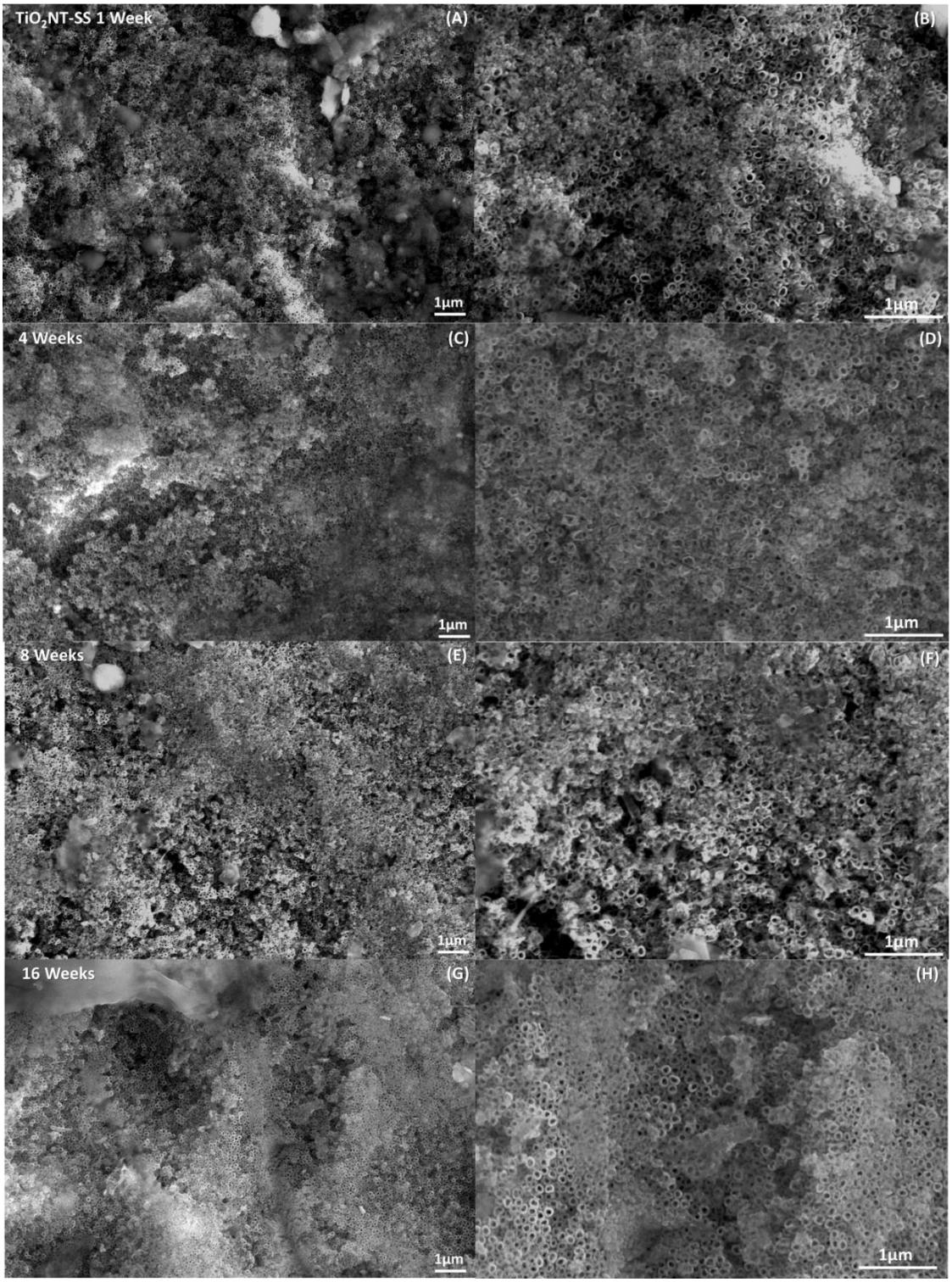
TiO2NT-SS 1 Week
(A)
1µm
(B)
1µm
4 Weeks
(C)
1µm
(D)
1µm
8 Weeks
(E)
1µm
(F)
1µm
16 Weeks
(G)
1µm
(H)
1µm

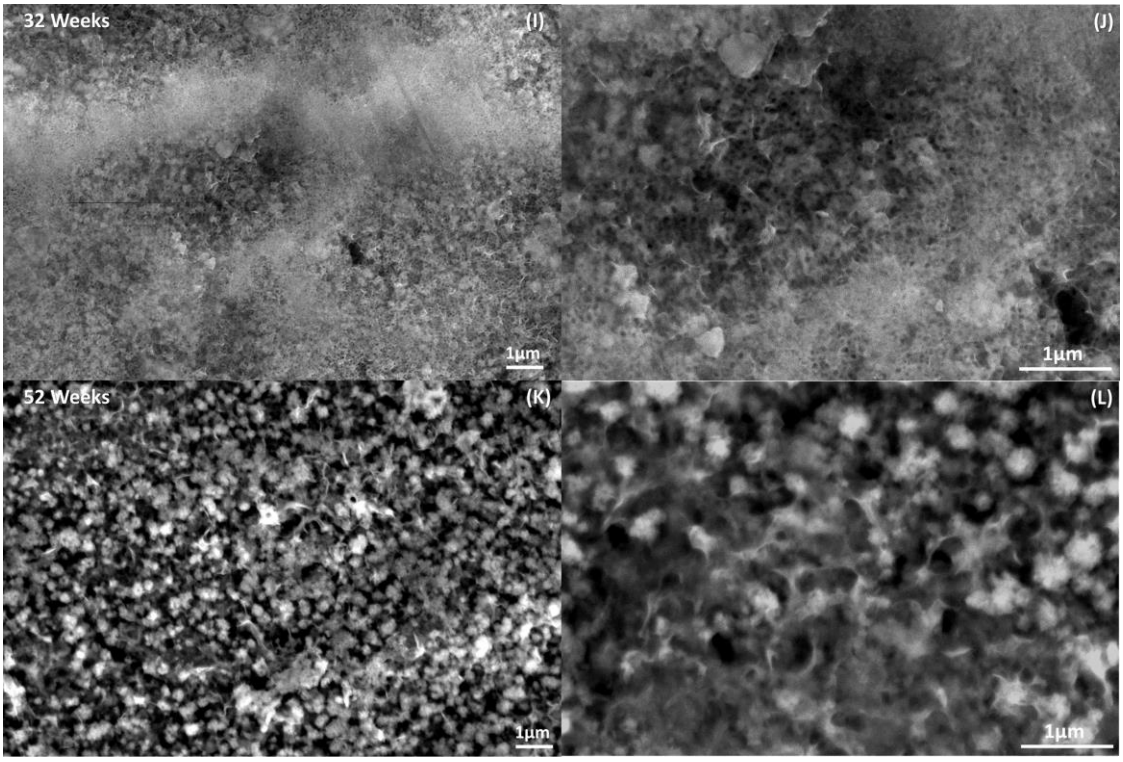

Figure 4. 26 Change in surface morphology after long-term aging of TiO_2NT-SS.

Magnification – 20K -A, C, E G, I, K 50K – B, D, F, H, J, L

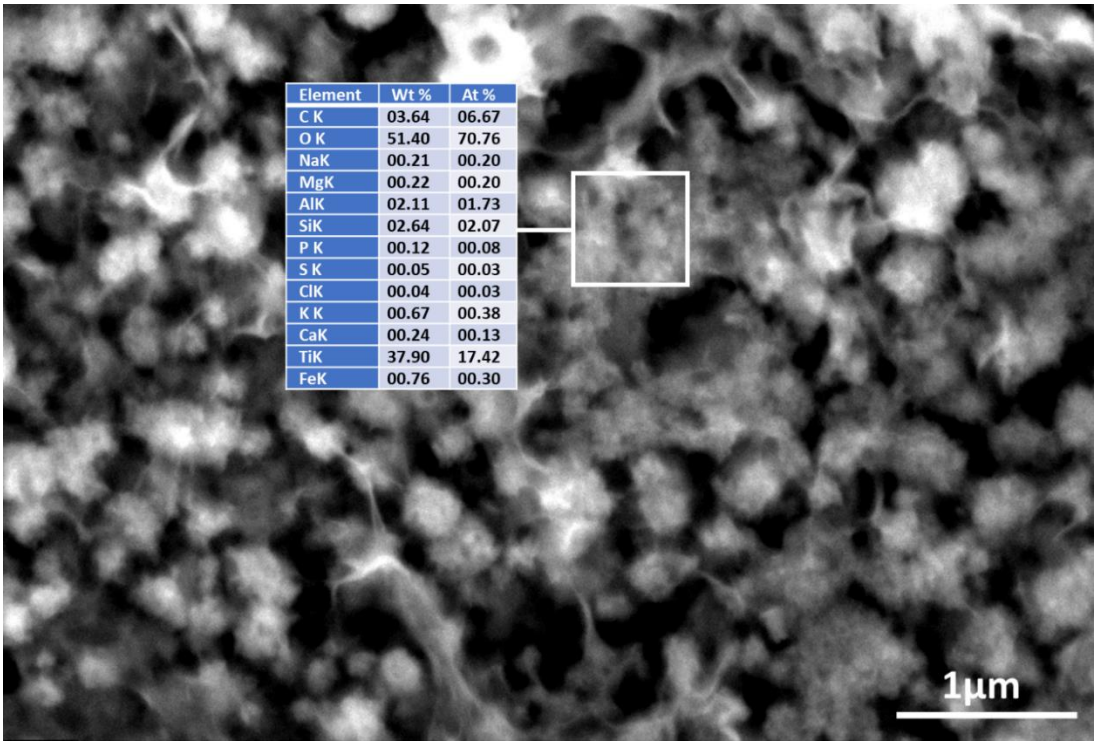

Figure 4. 27 Detail of TiO_2NT-SS surface aged for 52 weeks. Inset – Approximate chemical composition obtained by EDX. Magnification – 50K

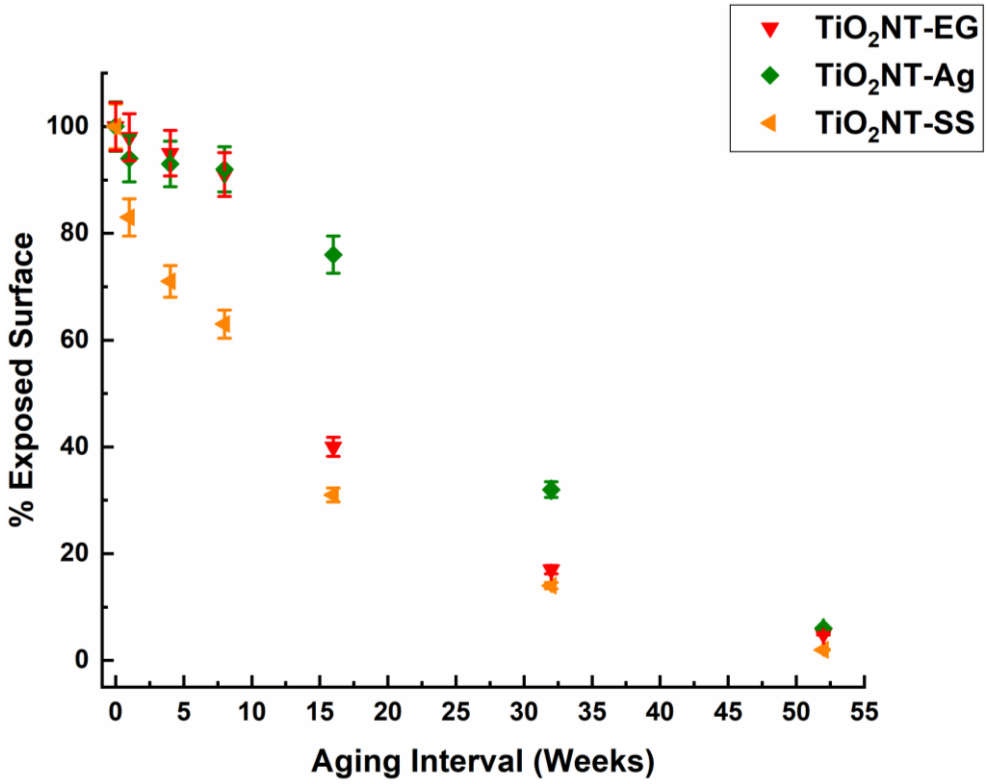

Figure 4. 28 Variation in surface coverage of ANTA with aging

4.2.6 Changes to the Crystalline Structure Following Solar Long-Term Aging

The XRD profiles of the unaged materials and at each aging interval are presented in figures 4.29 a-c. As with the short-term aging exercise, there is no indication of the anatase-rutile transition occurring. This confirms that anatase, the more active TiO_2 polymorph, is stable after long-term field use despite the repeated activations. The activations could have introduced defects which modified the crystal structure of the material. Despite the extensive fouling the halite peaks at $2\theta \approx 27.46°$ and $\approx 31.60°$ were absent in the TiO_2NT-EG and TiO_2NT-Ag diffractographs. This can be attributed to the lower salt loading of the nanostructure by evaporation. Evaporation of the synthetic greywater resulted in the concentration of the dissolved ionic species within the nanostructure and any surface debris. The sealed unit used for the solar aging experiment precluded evaporative losses. Similarly, after rinsing the aged samples, the looser biofilm layer, released more of its retained ionic species, including sodium chloride. Low intensity peaks were detected on TiO_2NT-SS after 16 weeks of aging. The presence

of the peaks for TiO_2NT-SS are due to the retention of debris within the inter-tube spaces. The accumulation of material was evident after the 1st week of exposure. This debris could have retained some of the sodium chloride structure. The absence of evaporative losses resulted in the lower intensity of the peaks.

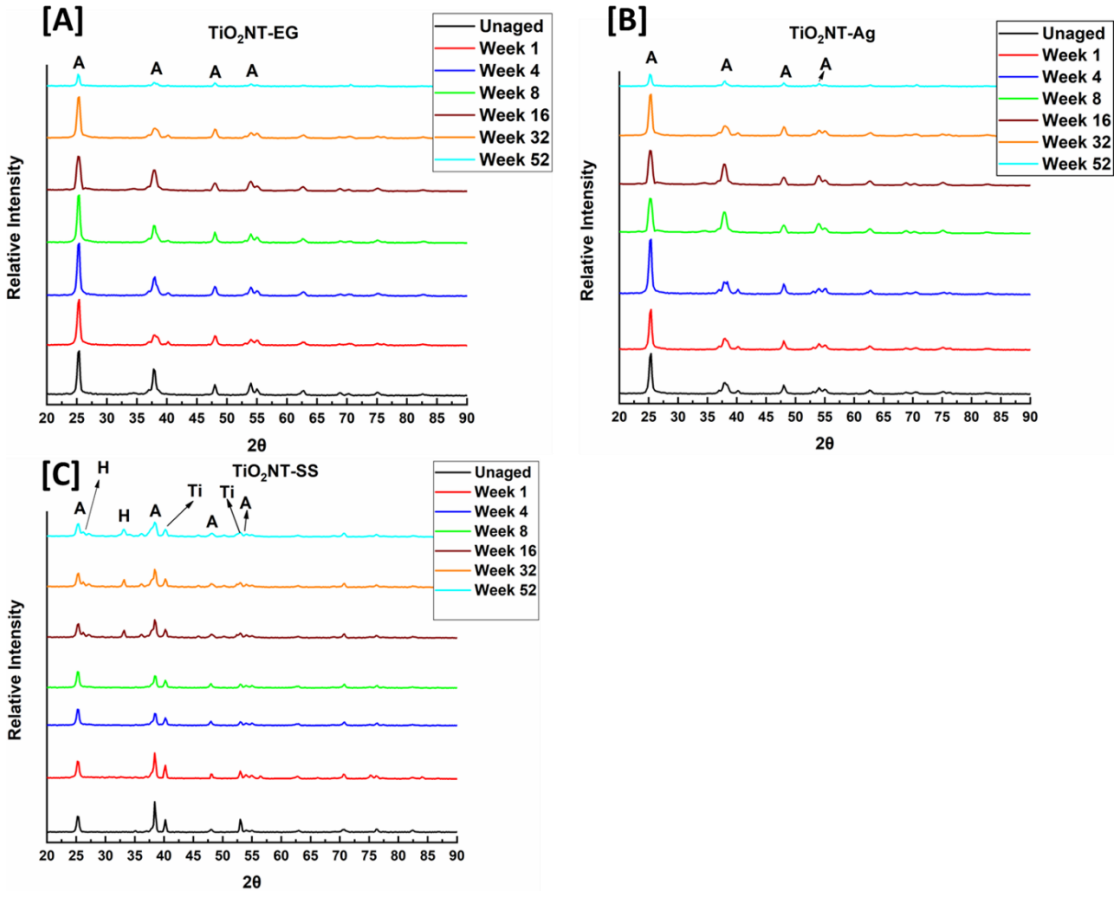

Figure 4. 29 Changes in crystalline structure during long-term aging. A) TiO_2NT-EG B) TiO_2NT-Ag C) TiO_2NT-SS. **A** = Anatase **H** = Halite **Ti** = Titanium

4.2.7 Changes in Photocatalytic Activity After Following Solar Long-Term Aging

4.2.7.1 Changes in the Degradation of MB During Solar Aging

The effect of aging on the photocatalytic degradation of MB was once more studied by following the rates of reaction of the aged materials. The reduction in reaction rate of TiO_2NT-EG is shown in figure 4.30. The overall reaction rate was higher than that of

the short-term aging at all but the 1st aging interval. Despite the higher surface coverage, the materials aged for 52 weeks retained a faster kinetics than those aged for 12 under the laboratory-based regimen. This can be attributed to the absence or lower coverage by the salt layer described by Guillard *et al*, lessening its inhibitive effect [23]. A proportional relationship between reaction rate and surface coverage does not appear to exist. This can be seen when the rate of reaction and surface coverage of the surfaces aged for between 1 and 16 weeks are compared. After 1 week of aging the, % exposed surface dropped to 98% whilst the reaction rate dropped by 57%. The reaction rate between the 8th and 16th week declined only by 4%, whilst the exposed surface area dropped by 51%.

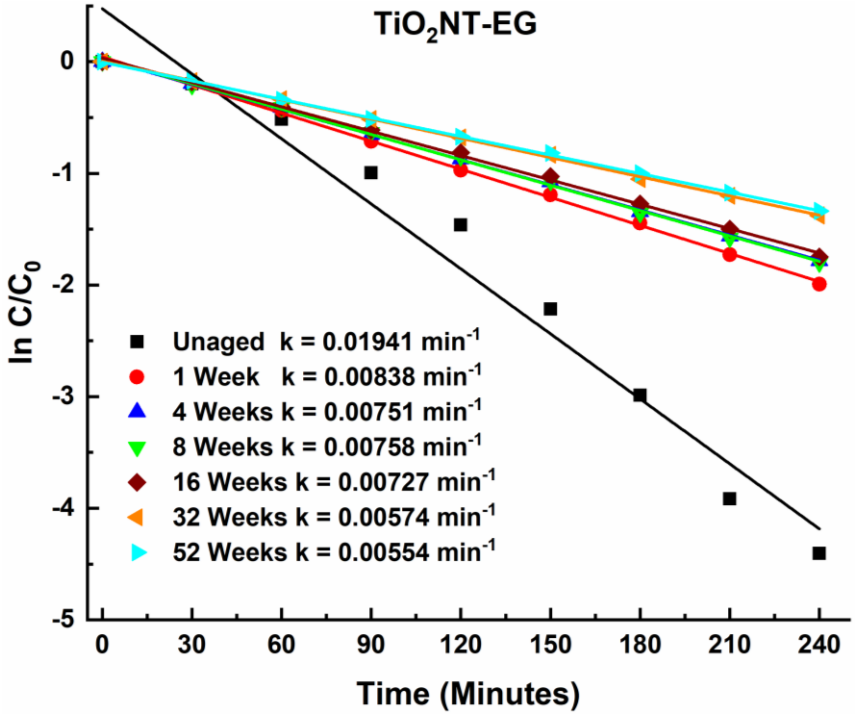

Figure 4. 30 Change in MB degradation after solar aging for TiO_2NT-EG

The change in reaction rate of TiO_2NT-Ag as it aged is plotted in figure 4.31. Of note is the rate constant for the 16th week of exposure. The rate constant of TiO_2NT-EG 0.00727 min^{-1} with an exposed area of 40% is higher than that of TiO_2NT-Ag (0.00683 min^{-1}) with an exposed area of 76%. The reaction rate at the end of the experiment was essentially identical to that of TiO_2NT-EG. Higher rate constants than those of the lab-aged material were also retained after the 52nd week had elapsed.

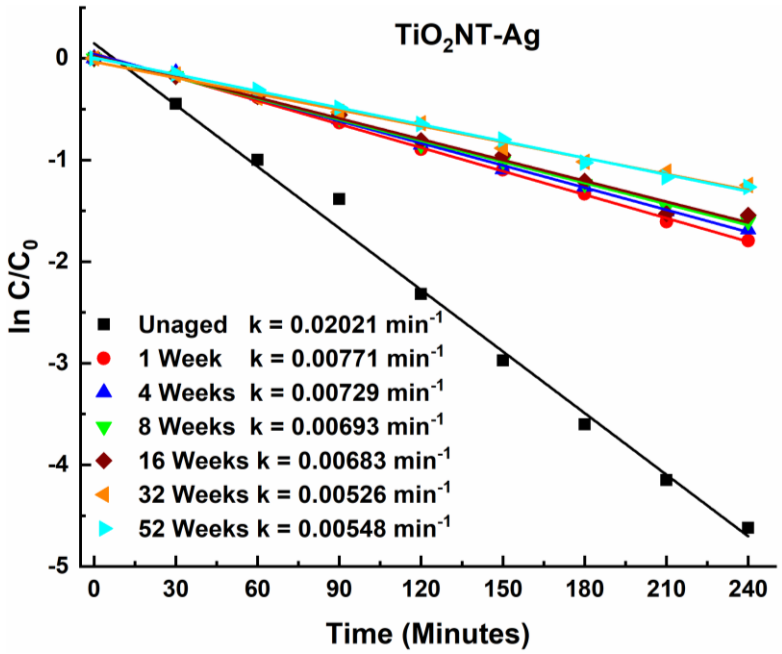

Figure 4. 31 Change in MB degradation after solar aging for TiO_2NT-Ag

The rate constant for TiO_2 NT-SS was essentially unchanged for the first four weeks of aging (figure 4.32). This is despite a reduction of 29% in exposed surface area. The slowing down of the reaction might in this case be due to accumulation of sodium chloride within the nanostructure which was not retained by other materials. As with the other two materials the final rate constant was higher than that for the 12th week of the lab-aged material.

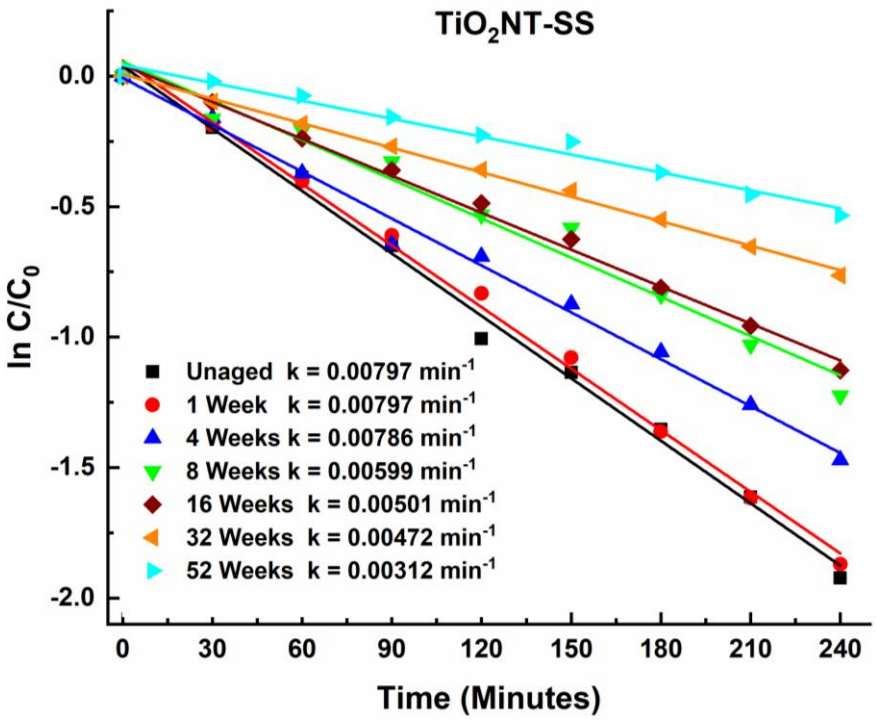

Figure 4. 32 Change in MB degradation after solar aging for TiO_2NT-SS

The percentage MB degradation with aging is plotted in figure 4.33. The percentage MB degradation and rate constants at the end of both aging exercises are compiled in table 4.4.

The solar-aged TiO_2NT-EG fared better than its lab-based equivalent. Both kinetics and degradation activity slightly exceeded that reported at the end of the lab-based experiment. The ability of TiO_2NT-EG to degrade MB after short term aging at 47% as well as the rate constant was significantly less than that for the material aged for longer. The rate constants for TiO_2NT-SS after both experiments were near identical, but the degradation of the dye after 1 year of aging, was 10% less than that for its short-term counterpart. For TiO_2NT-EG surface coverage does not appear to be the factor which limited the longevity of the material. The presence of ionic species within a salt layer contributed to the inactivation of the surface. The situation with TiO_2NT-Ag is however different. As already discussed, oxidation of silver could have contributed to the deactivation of the surface. The silver over the surface was retained longer in the lab-aged regimen than the solar-aging likely due to a combination of factors. The salt layer most likely retained some of the silver as the exposed flume contributed to its formation.

The spaced morphology of TiO_2NT-SS contributed to the largest decline in activity recorded. The retention of a still appreciable reaction rate however renders the decline less significant.

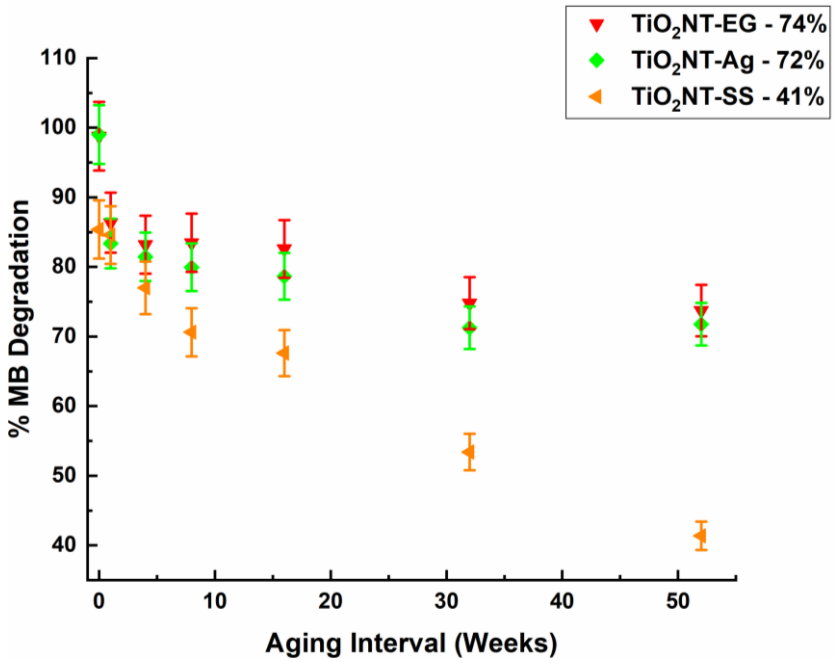

Figure 4. 33 Comparison of percentage variation in MB degradation with aging of the 3 nanomaterials. Error bars represent the maximum and minimum errors of the activity of 3 samples.

Table 4. 4 Comparison of rate of MB degradation at the end of short-term and long-term aging

	12 Weeks		52 Weeks	
Material	**Rate Constant**	**% Degradation**	**Rate Constant**	**% Degradation**
TiO_2NT-EG	0.00433	65%	0.00554	74%
TiO_2NT-Ag	0.00247	47%	0.00548	72%
TiO_2NT-SS	0.00291	51%	0.00312	41%

4.2.7.2 Changes in Antibacterial Activity During Solar Aging

The change in antibacterial activity for the different materials is summarised in figure 4.34. For TiO_2NT-EG the loss in activity over the 52-week aging period is around 81%. A quick drop from the starting 96% activity to 79% was recorded after the first week of testing. The activity declined slightly until it reached 75% after the 16th week. Another rapid decline followed, finally reaching 19% at the end of the regimen. A similar quick decline was reported for TiO_2NT-Ag. A drop from 97% to 70% was recorded after 1

week. A further reduction was reported before plateauing at around 55% between the 16th and 32nd week. The final value after 52 weeks was 27%, marginally higher than 19%. The activity of TiO_2NT-SS exhibited a sharp drop, falling from 80% to around 18% over the first 16 weeks. This was followed a near plateau in activity, with the final value reaching 16%.

There is a clearer relationship between surface coverage and antibacterial activity, with an increase in the former resulting in a decline in the latter. Similarly, the longer the exposure, the lower the final activity as is shown in table 4.5. The reason behind trends in activity within the aging regimen is difficult to attribute to a single mechanism, or one that is immediately obvious. Given the complexity of photocatalytic mechanisms and the inherent complexity of bacteria, finding the cause behind the loss in activity requires more controlled conditions. The aging exercises were structured to mimic field use rather than to provide in depth mechanistic studies.

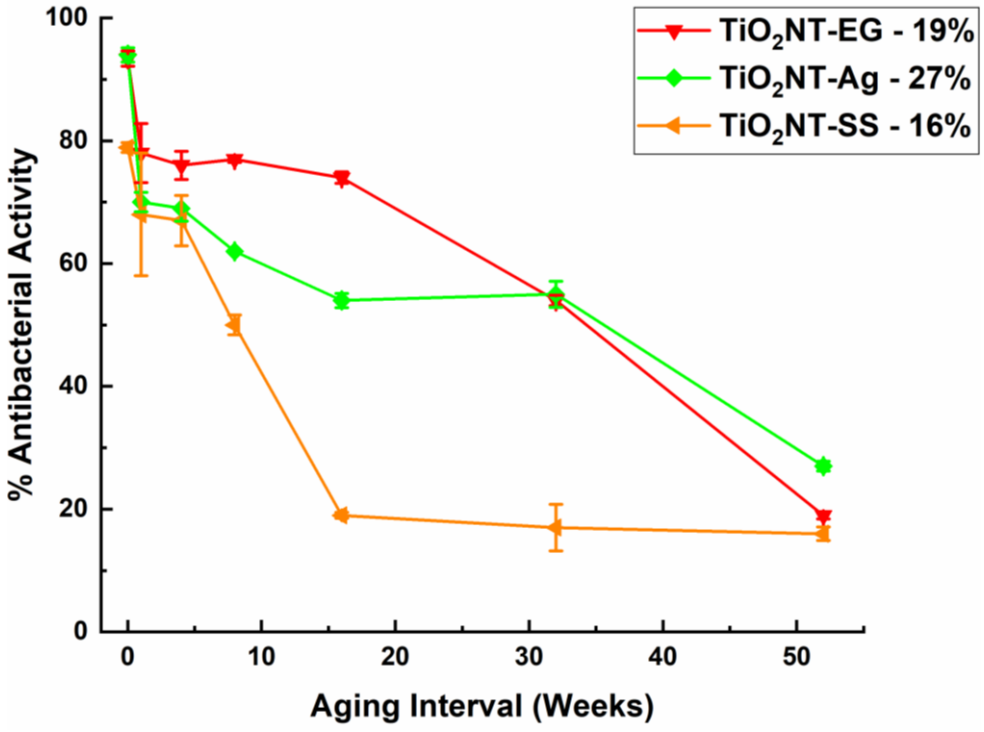

Figure 4. 34 Comparison of antibacterial activity with aging of the three nanomaterials. Error bars represent the maximum and minimum errors of the activity of 3 samples

Table 4. 5 Comparison of antibacterial activity at the end of short-term and long-term aging

	12 Weeks	**52 Weeks**
TiO_2NT-EG	80%	19%
TiO_2NT-Ag	57%	27%
TiO_2NT-SS	45%	16%

4.2.8 Reactivation of Photocatalysts Following Accelerated Aging

4.2.8.1 Selection of a Facile Regeneration Strategy

The most effective regeneration strategy for TiO_2 nanomaterials has been found to be calcination in air at temperatures around 400°C [29, 30]. Thermal treatment facilitates the desorption of the adsorped species which reduce the activity of the photocatalyst. This regeneration method is suitable for some industrial environments but unlikely to be implemented in a widespread fashion. As such, a simpler method, one which does not require complex equipment and a high technical competence is desirable. A cleaning method can be such an alternative.

Analysis of the aged surfaces by SEM imaging revealed the tendency of the surfaces towards fouling by solid deposits. The X-Ray diffractograms showed that an accumulation of ionic species can occur concomitantly with the deposition of insoluble material. Despite not being able to elucidate a specific deactivation mechanism for the aged samples, steps can be taken to enhance the longevity of the materials. In this case, a cleaning protocol can be used to remove the debris from the surface, exposing some if not all of the photocatalyst surface. In real-life applications the surfaces are likely to accumulate calcium and magnesium scales, both elements being detected on the aged surfaces. Similarly, biofilms can form in over the surfaces as greywater contains a bacterial load which might propagate and form biofilms.

The cleaning protocol should similarly address some of the established photocatalyst deactivation pathways which might also be at work during the aging experiment. Liu *et al.*, Gandhi *et al.*, Ren *et al.*, reported the following as possible causes for deactivation [31-33]:

1. Accumulation of debris over the surfaces

2. Depletion of the oxygen within the TiO_2 lattice (Ti-O) when this acted as an oxygen source in the photocatalytic pathway.

3. Inorganic ions resulting from mineralisation

4. Adsorption of reaction intermediates over photocatalyst surface some of which contain acidic groups.

4.2.8.1 Morphology of Surfaces After Accelerated Aging

The surface morphology of the accelerated aging samples is presented in figure 4.35. The morphology resembled that of the solar aged samples and had ample surface coverage to make assessment of the suitability or otherwise of a cleaning easy. The approximate chemical composition of the deposits found is presented in figure 4.36. The range of elements detected is lower than that of the samples used in the lab-based and solar aged samples. This is due to the absence of a continuous biofilm layer, which being a complex biological structure contains a variety of molecules with different chemical makeups.

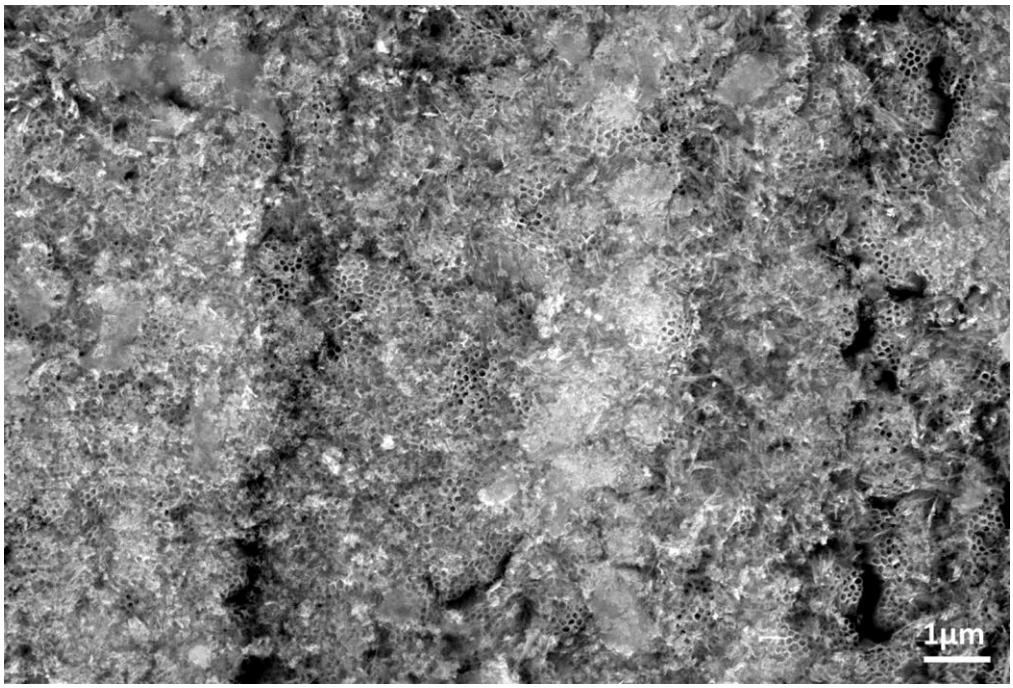

Figure 4. 35 Surface morphology after accelerated aging. Magnification 20K.

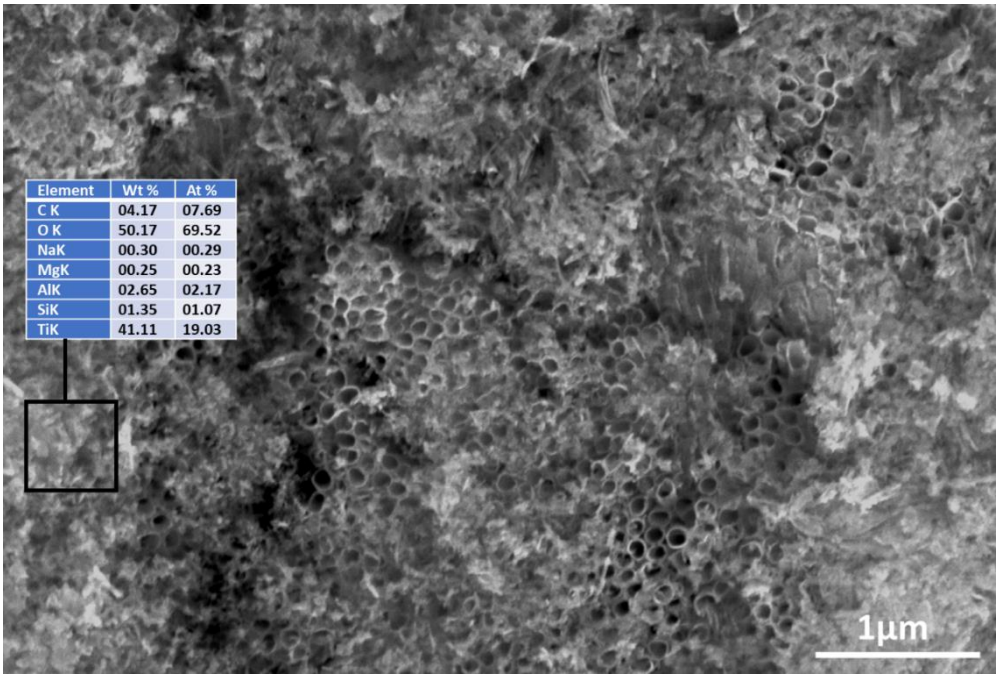

Figure 4. 36 Detail of surface after accelerated aging. Inset – Approximate chemical composition of debris. Magnification 50K

4.2.8.2 Recovery in the Activity for the Degradation of MB

The recovery in activity of the material using UVA and DI water is presented in figure 4.37. For the aged material, the final concentration was 27% of the initial concentration. This was a significant decline from the 1% remained for the unaged material. A 12% recovery in activity was recorded after cleaning the surfaces for 1 hour. A slight further increase of 3% was recorded at the conclusion of the cleaning cycle.

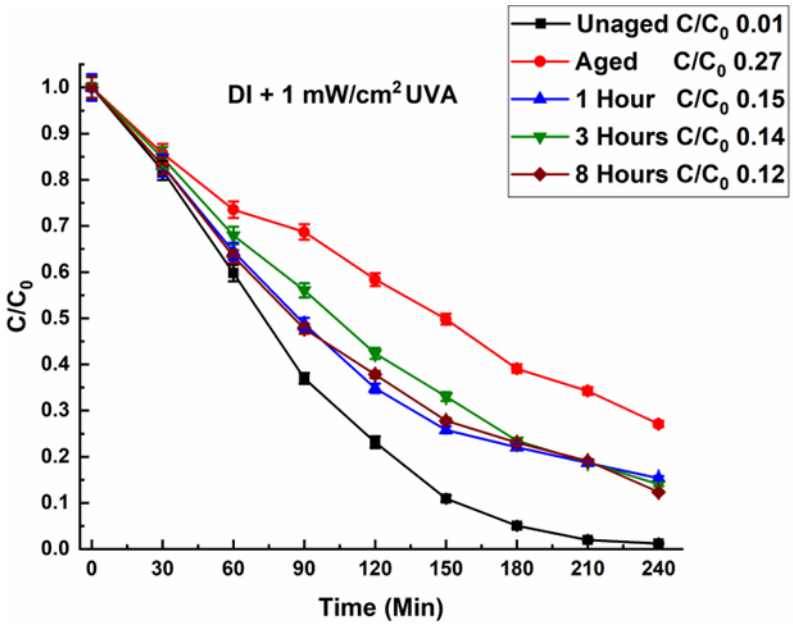

Figure 4. 37 Recovery of MB degradation activity at different timepoints during DI + 1 mW/cm^2 UVA rinse.

The SEM images of the aged surface and of the surface after the 8-hour cleaning cycle are shown in figure 4.38 a-b. The more densely packed debris found of the aged surface has been removed to a great extent, once more exposing the nanotube openings. The remaining debris is looser and devoid of any discernible crystal habit. The remaining debris is likely to be composed of biofilm remnants. Despite no bacterial seed being added, microfauna is found everywhere in the environment.

Regeneration of TiO_2 nanoparticles with water was reported by Liqiang *et al.*[34]. The authors reported that the activity of the nano powders used in their study was nearly fully restored by sonicating the nanoparticles in water. The authors attributed the removal of adsorped species as the cause for the recovery. The recovery in this study is lower than that reported by Liqiang *et al.* but a direct comparison cannot be drawn. The

authors degraded gaseous contaminants which did not leave any solid deposits on the spent photocatalysts and most importantly no biological accumulation was reported.

The facile cleaning method described in this study is perhaps not adequate for surfaces which undergo continual use over a long period of time. The aging procedure used in this part of the study was intended to accelerate the aging process and involved 24/7 activation barring the time taken for the weekly water change. If this procedure is employed more frequently its effect would undoubtedly by be more pronounced.

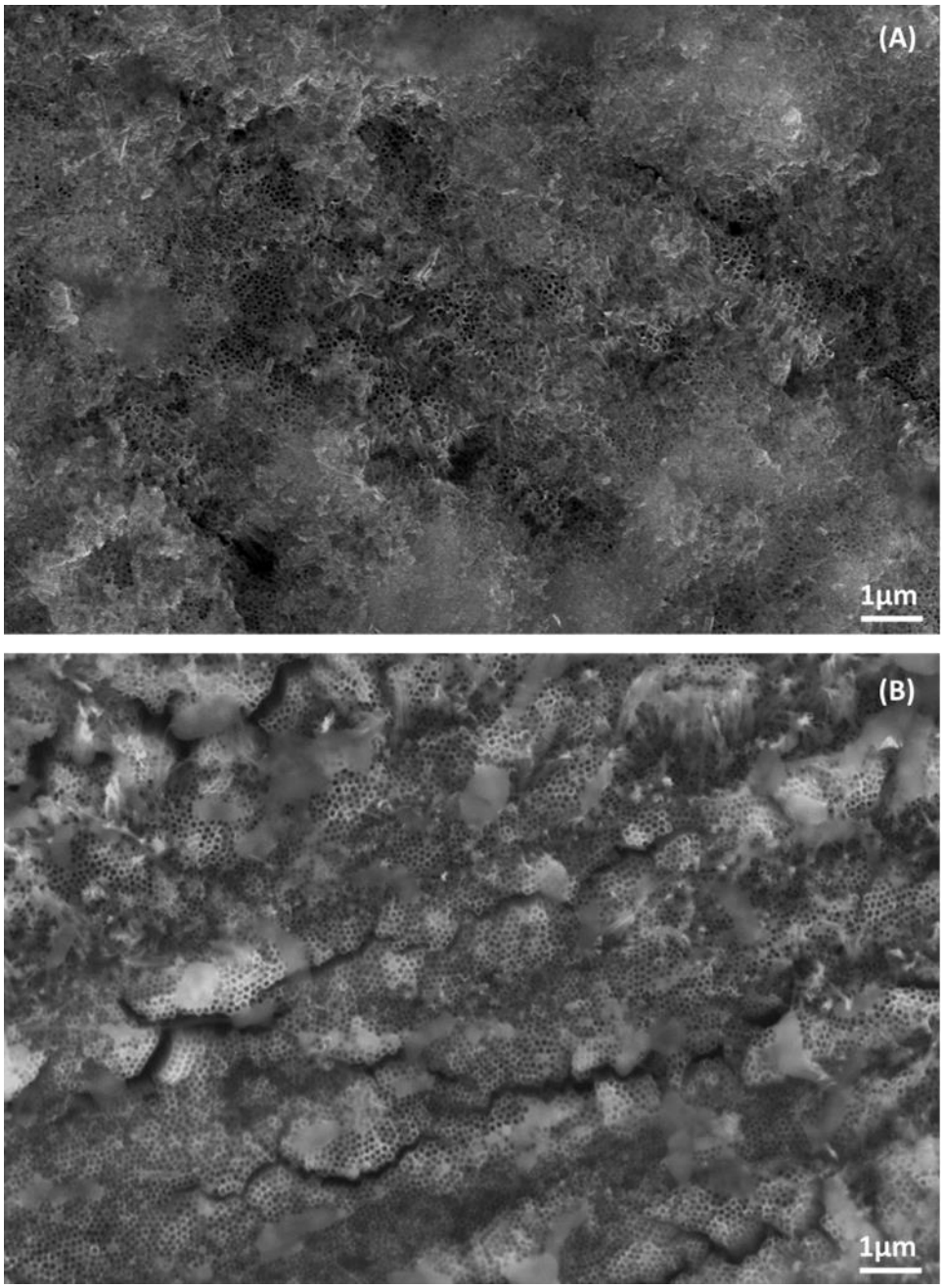

Figure 4. 38 ANTA surface A) prior B) after DI + 1 mW/cm^2 rinse. Magnification – 20K.

The recovery of the aged samples following an alkaline rinse with different durations is presented in figure 4.39. After the 1st hour, where a 10% recovery was recorded, there was no further improvement. The results are also not exceedingly different than those recorded for the DI + UVA rinsing cycle.

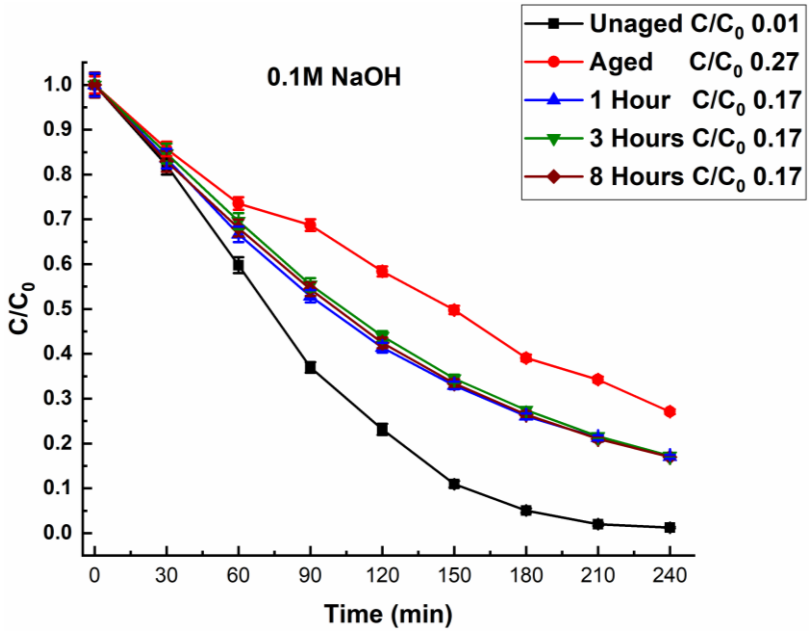

Figure 4. 39 Recovery of MB degradation activity at different timepoints during 0.1M NaOH rinse. Error bars represent the maximum and minimum error of the photocatalytic activity of 3 samples.

An inspection of the surface reveals that the cleaning of the surface was substantial but some debris is still discernible (figure 4.40 a-b). Most of the remaining particles are of the denser variety with a lower amount of the material associated with the degradation of microbial matter present. The higher surface coverage is likely to be due to the inefficiency of the solution to remove biological residues. The DI and UVA treatment, allowed the material to degrade the microbially derived material from the surface through photocatalysis, releasing other debris from the surface. Jonstrup *et al.* reported that regeneration using 3M NaOH resulted in a partial recovery of the material's activity with respect to the degradation of remazol red [35]. In this study a 0.1M solution was used to give a pH value higher than 12 without introducing the possibility of dissolving the TiO_2 nanostructure within the 8-hour rinsing regimen [36]. A pH of 12 was used to aid in the dissolution of certain oxides and hydroxides such as those of silicon whilst reacting with acidic organic degradation products.

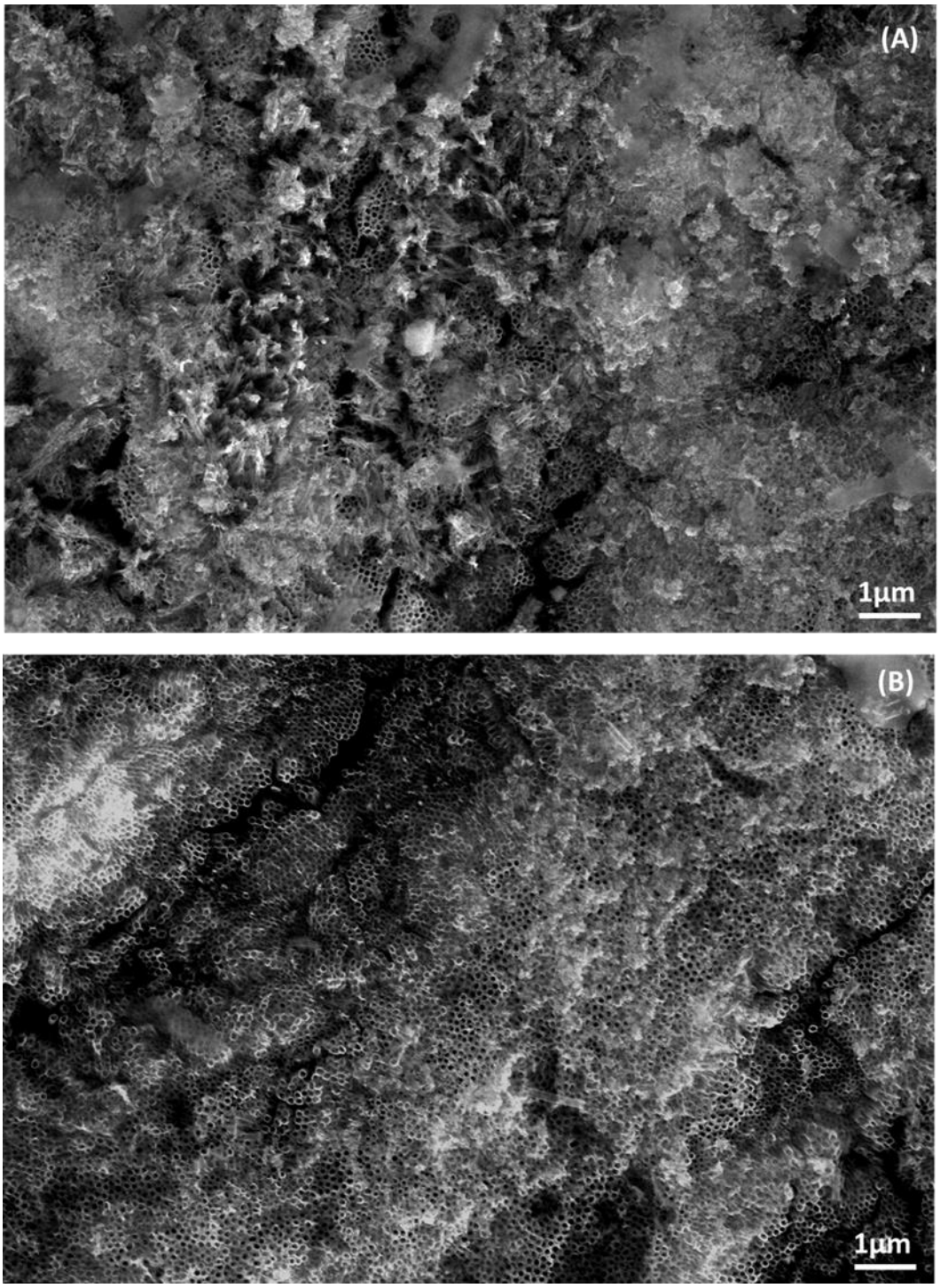

Figure 4. 40 ANTA surface A) prior B) after 0.1M NaOH rinse. Magnification – 20K.

The recovery in activity following the acidic rinse is presented in figure 4.41. The acidic solution was intended to remove oxides and metal ions adsorbed to the photocatalyst. The effect of the rinse was somewhat delayed as no improvement in activity was recorded after 1 hour. An 11% increase in activity was recorded after 3 hours of cleaning

and a further 4% increase was recorded after 8 hours. A total recovery of 15% was recorded by the end of the rinsing cycle.

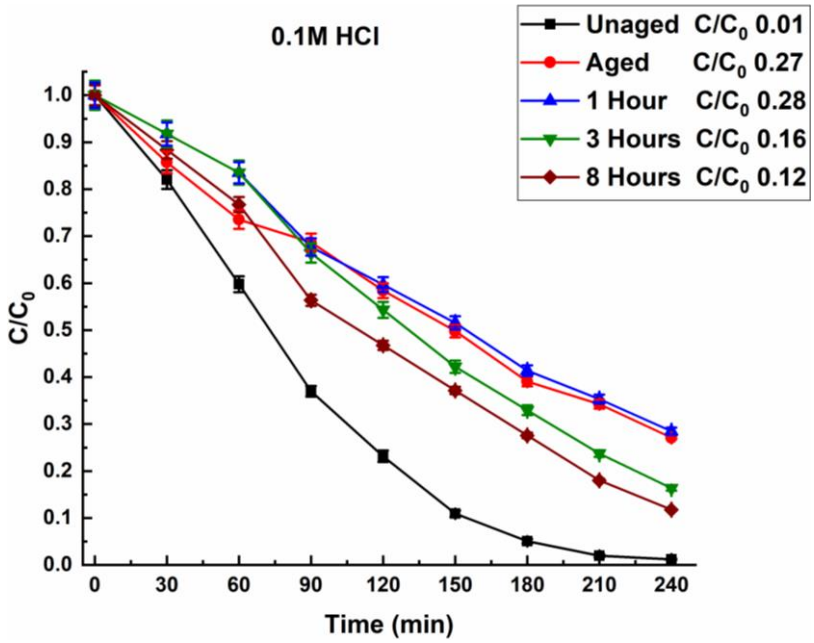

Figure 4. 41 Recovery of MB degradation activity at different timepoints during 0.1M HCl rinse. Error bars represent the maximum and minimum error of the photocatalytic activity of 3 samples.

The surface morphology following cleaning is presented in figure 4.42. Of note, is that most of the compact debris layer was removed. Some remnants of the biological debris are however still visible. The acid rinse was successful in removing acid soluble debris but the biological material was resistant to both the effect of the acid and the flow of the solution.

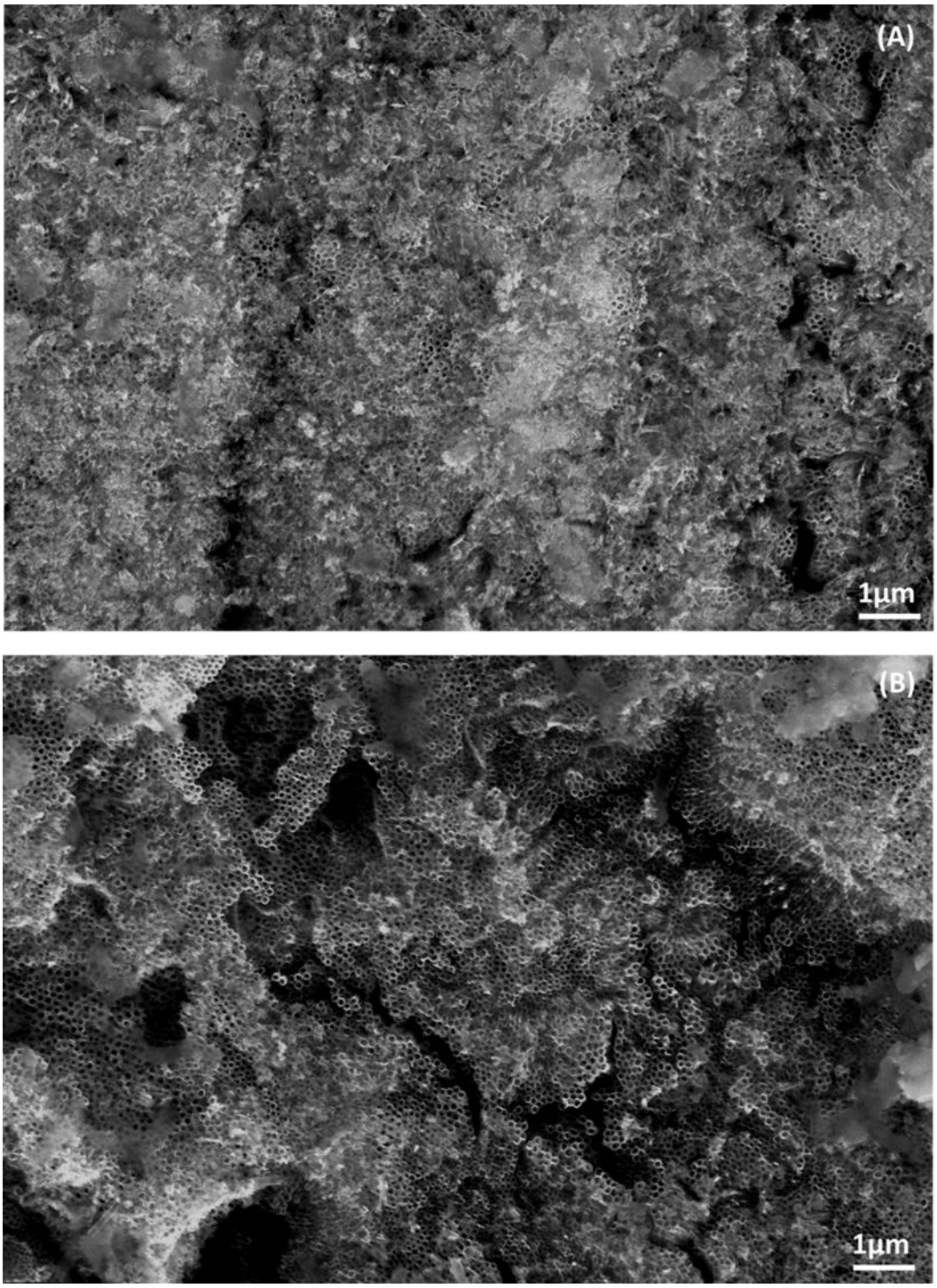

Figure 4. 42 ANTA surface A) prior B) after 0.1M HCl rinse. Magnification – 20K

The recovery of the ability of the material to degrade MB after cleaning with 0.1M H_2O_2 under UVA light is shown in figure 4.43. A recovery of 14% was recorded after 1 hour of aging. A slight recovery of 2% was recorded after 3 hours of cleaning and a further recovery of 2% by the end of the cleaning cycle. This cleaning solution provided the highest recovery of the four used. Once more, a complete recovery was never achieved. Gandhi *et al.* reported a near complete recovery of Degussa P25 used for the recovery after treating the spent photocatalyst with 30% H_2O_2 (9.8 M). Apart from the obvious higher concentration, the photocatalysts were not exposed to as rigorous an aging regime [33]. Miranda-Garcia *et al.* used 1M H_2O_2 and solar radiation as a way of reactivating spent TiO_2 coated spheres used for the degradation of emerging contaminants [37]. The authors report that this was an effective strategy for recovery of activity, but complete recovery was not achieved.

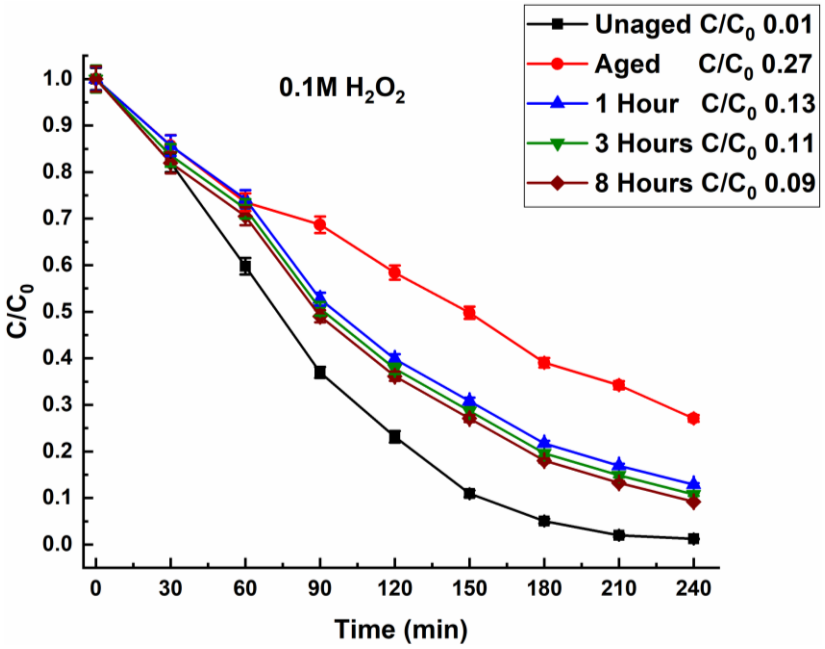

Figure 4. 43 Recovery of MB degradation activity at different timepoints during 0.1M H_2O_2 rinse. Error bars represent the maximum and minimum error of the photocatalytic activity of 3 samples.

The surface morphology after cleaning for 8 hours is presented in figure 4.44 a-b. The morphology of the surface is the cleanest obtained. The denser debris was nearly wholly removed as was the biological debris. One possible reason is that the oxygen bubbles produced by the decomposition of H_2O_2 helped lift the debris off the surface. Higher peroxide concentrations would have resulted in higher volumes of oxygen being generated. Higher concentrations, however, tend to result in the degradation of adhesives, sealants and other polymers used in actual reactors.

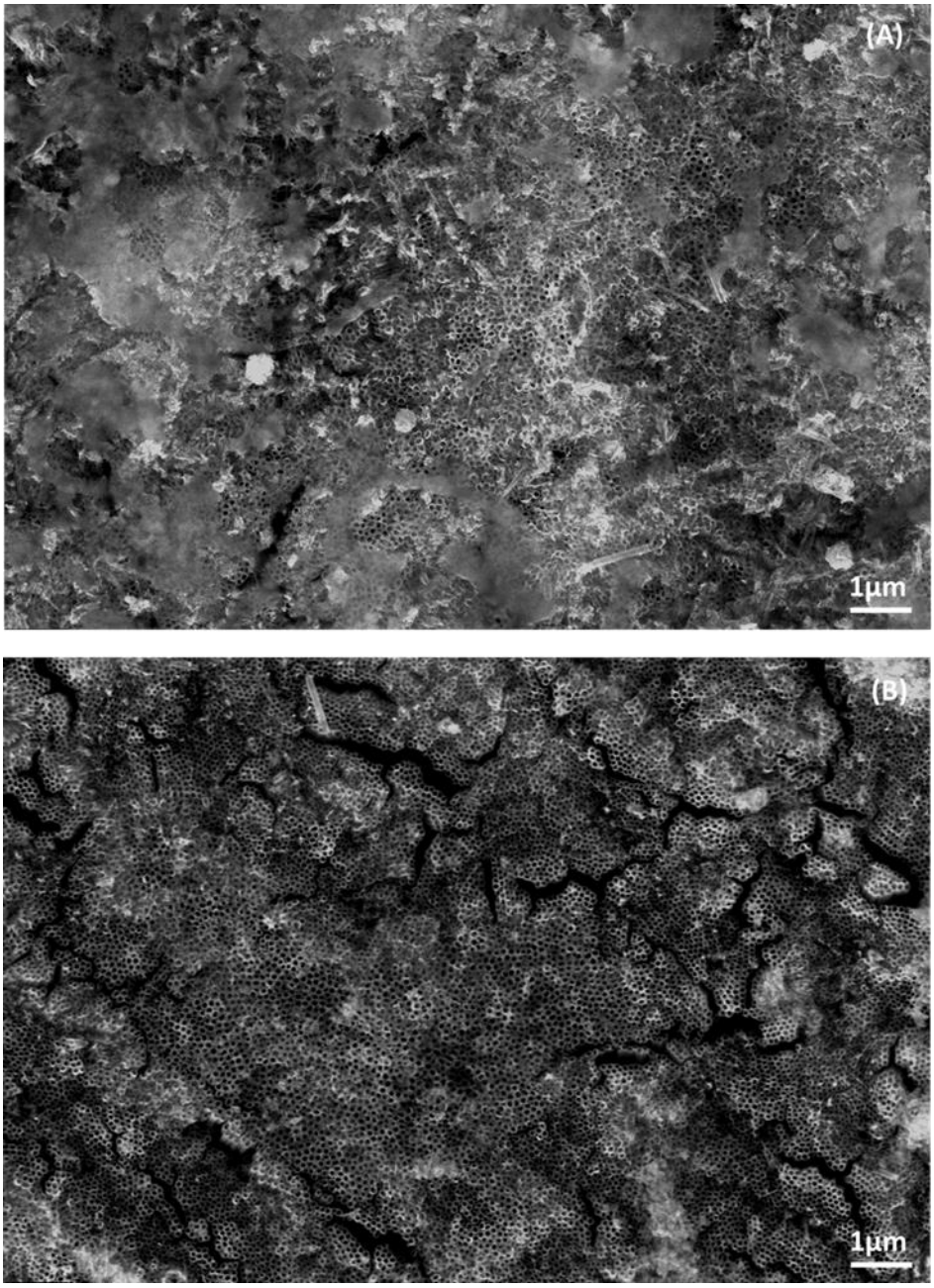

Figure 4. 44 ANTA surface A) prior B) after 0.1M H_2O_2 rinse. Magnification – 20K.

The difference in recovery between the rinse using DI water and H_2O_2 is marginal, making both methods suitable. The H_2O_2 rinse however has the added advantage of more thoroughly removing the debris from the surface. Another added advantage is that the peroxide can aid in the removal of microbial growths within the reactor in areas which might not be easily accessible.

4.29 Reactivation of Long-Term Aged Samples

The cleaning protocol using the 0.1M H_2O_2 and UVA rinse was implemented on the solar aged samples. In this way the possibility of recovering some, if not all, the activity of the more soiled samples was studied.

A side-by-side comparison of the morphology of the aged TiO_2 NT-EG coupons and the morphology after cleaning is presented in figure 4.45 a-l. The rinsing regimen was successful in removing most of the debris from the surfaces even after 52 weeks of aging. In part this might be due to the looser structure of the debris which is most likely biologically derived. The flowing water could have loosened the debris and the oxygen bubbles from the peroxide degradation contributed to the breakdown of the debris. Photocatalytic activation under UVA light could also have helped in the degradation of extracellular polymeric substances holding the debris together.

The recovery in activity with respect to the degradation of methylene blue is presented in figure 4.46 and table 4.6. A near complete regeneration was recorded for the samples aged up to 16 weeks. A significant recovery in activity was also recorded for the last two aging timepoints. The results continue to strengthen the hypothesis that additional deactivation mechanisms other than the fouling of the surface by insoluble material are in at play. Despite the near complete removal of debris in all instances the degree of regeneration for the 32nd and 52nd week is lower than that of the previous aging intervals.

The lack of a significant recovery in antibacterial activity is remarkable. The difference between the aged and the cleaned surfaces is shown in figure 4.47 and table 4.7. The discrepancy in the recovery of the activity towards the degradation of the two pollutants can be addressed in terms of the mechanisms involved. The inactivation of bacteria might be hindered because the ROS species produced were being consumed prior to

their reaction with the bacterial cell wall. Given that the bacterial inactivation is not primarily a surface process, any adsorped species will scavenge the ROS preferentially.

The MB molecules during the 1-hour equilibration step prior to illumination with UVA light can adsorb to the surface reacting with both charge carriers and ROSs. This helps in offsetting the scavenging of ROSs by other surface adsorbed species. The formation of layer saturated with MB molecules close to the surface allow for the replacement of degraded MB molecules with new MB molecules [38].

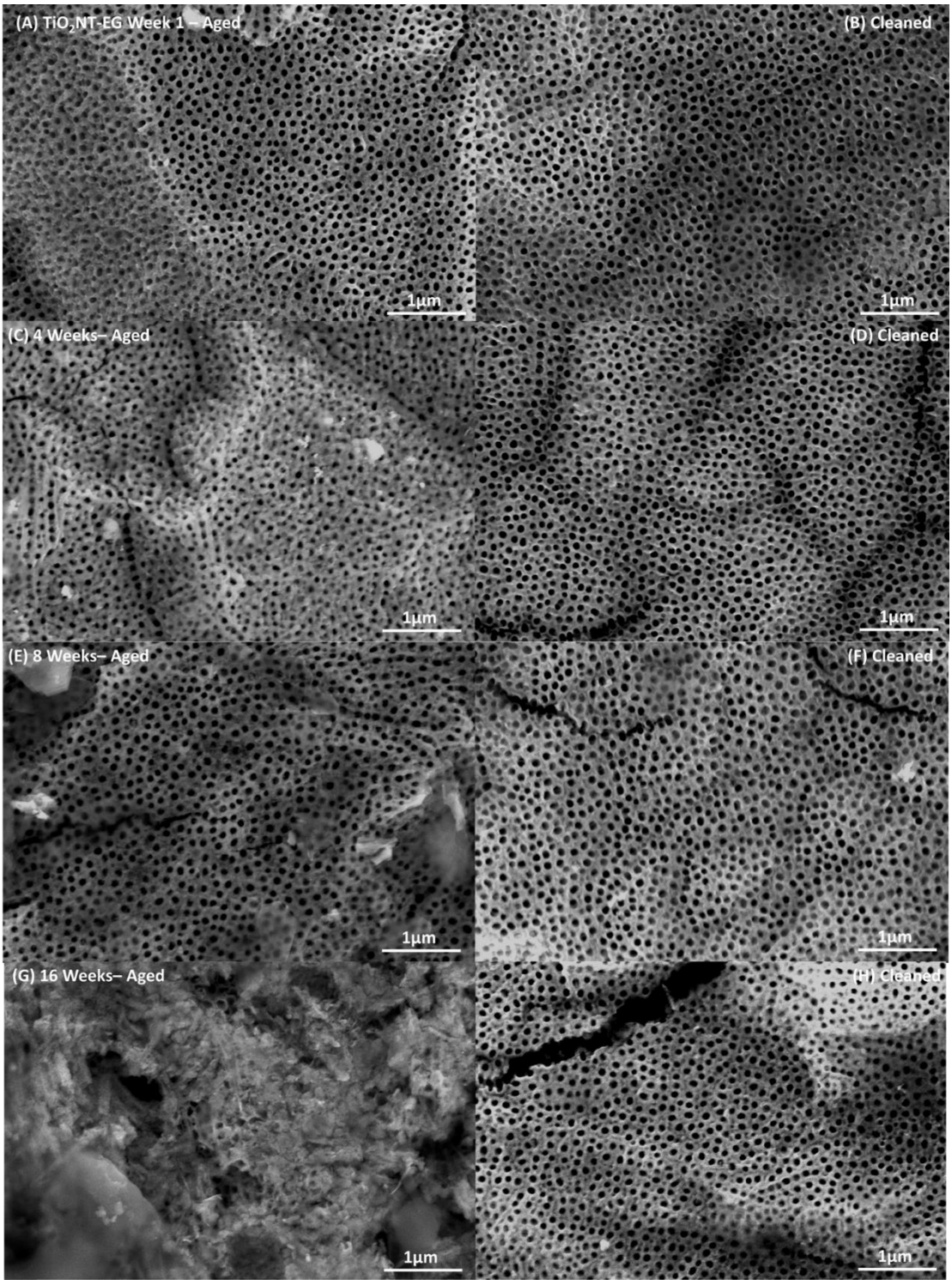
(A) TiO2NT-EG Week 1 – Aged
1µm
(B) Cleaned
1µm
(C) 4 Weeks– Aged
1µm
(D) Cleaned
1µm
(E) 8 Weeks– Aged
1µm
(F) Cleaned
1µm
(G) 16 Weeks– Aged
1µm
(H) Cleaned
1µm

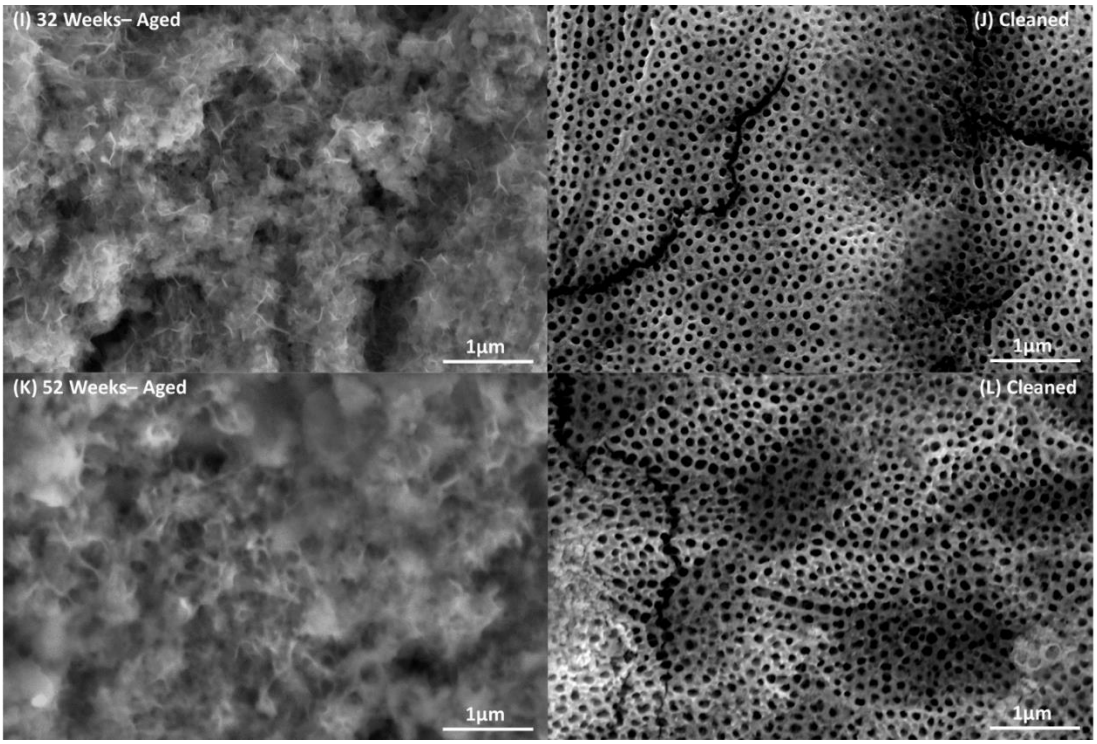

Figure 4. 45 Effect of 0.1M H_2O_2 + 1.2 mW/cm^2 rinse on removal of debris from TiO_2NT-EG. **LHS** – As aged, **RHS** – cleaning. Magnification 50K.

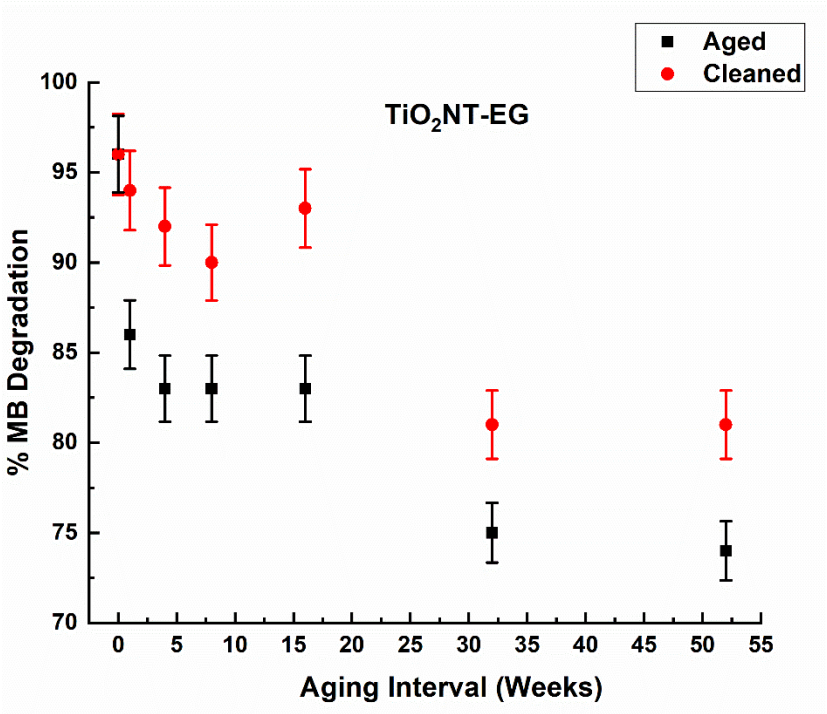

Figure 4. 46 Recovery in MB degradation activity after cleaning with 0.1M H_2O_2 + 1.2 mW/cm^2 UVA. Error bars represent the maximum and minimum error of 3 the photocatalytic activity of 3 samples.

Table 4. 6 Summary of recovery in MB degradation activity of TiO_2NT-EG after 0.1M H_2O_2 + 1.2 mW/cm^2 UVA

Aging Interval (Weeks)	0	1	4	8	16	32	52
Aged (% Degradation)	96	86	83	83	83	75	74
Cleaned (% Degradation)	96	94	92	90	93	81	81

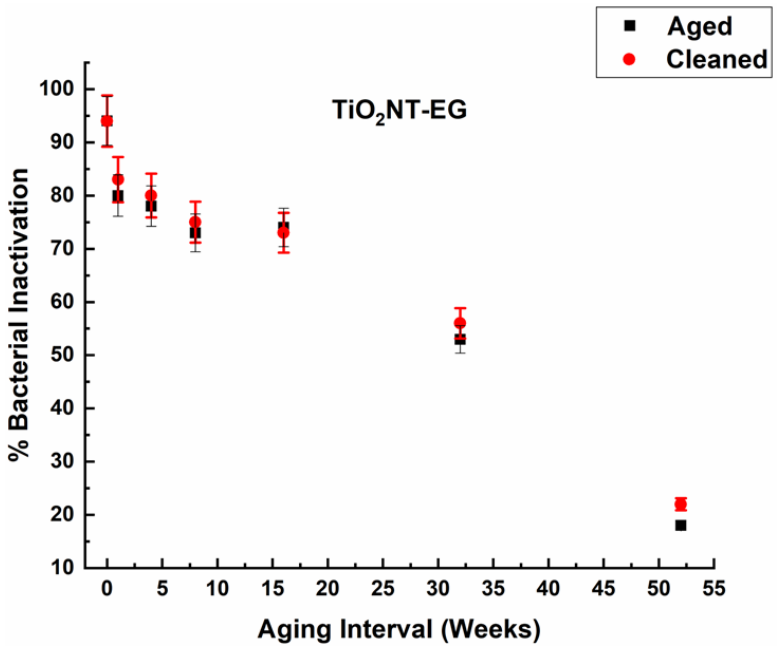

Figure 4. 47 Recovery in antibacterial activity after cleaning with 0.1M H_2O_2 + 1.2 mW/cm^2 UVA. Error bars represent the maximum and minimum error of 3 the photocatalytic activity of 3 samples.

Table 4. 7 Summary of recovery of antibacterial activity of TiO_2NT-EG after 0.1M H_2O_2 + 1.2mW/cm^2 UVA

Aging Interval (Weeks)	0	1	4	8	16	32	52
Aged (% Inactivation)	94	80	78	73	74	53	18
Cleaned (% Inactivation)	94	83	80	75	73	56	22

The morphology of the aged TiO_2NT-Ag coupons and the morphology after cleaning is presented in figure 4.48 a-l. The rinsing regimen was once again very successful with most of the surface being revealed even for the samples aged for 52 weeks. This is because the morphology of the debris settled on the surface was identical to that of TiO_2NT-EG. The peroxide rinse appears to be very effective in removing the fibrous debris. The regeneration of the photocatalyst followed more or less that of the TiO_2NT-EG. The ability of the material to degrade MB before and after cleaning is presented in figure 4.49 and table 4.8. A complete recovery in activity was recorded for the 1st 4 weeks. Near complete recovery was recorded for the timepoints up to 32 weeks. A remarkable recovery was also reported for the final aging interval. Only the 32-week timepoint did not follow the trend recorded for TiO NT-EG. This is attributed to the lower surface coverage recorded for that time interval. This would have allowed the peroxide to have a longer time in contact with the surface, leading to better removal of adsorped degradation products.

The recovery of antibacterial activity was similar to that of TiO_2NT-EG in that it was only marginal. The change in antibacterial activity after cleaning is presented in figure 4.50 and table 4.9. The rationale behind the addition of silver to the material was to have a passive antibacterial effect which did not require photocatalytic activation. The loss of the silver rich deposits from the surface with aging removed this possibility, despite the material at the 52nd week having a higher activity than its TiO_2NT-EG equivalent. The surface appears to be resistant to reactivation with respect to bacterial inactivation. The increase in exposed surface area following cleaning appears to favour the degradation of organic compounds.

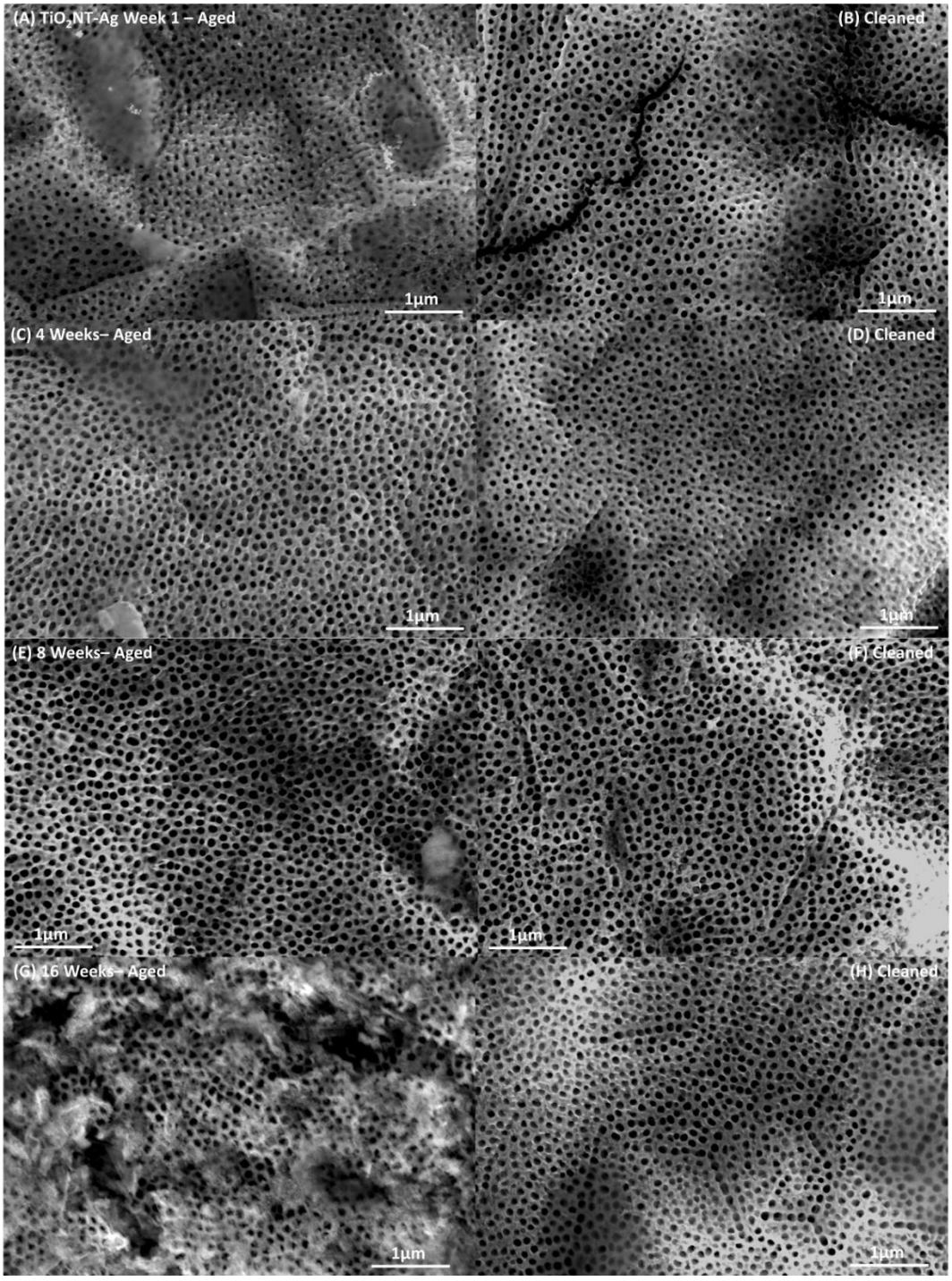
(A) TiO2NT-Ag Week 1 – Aged
(B) Cleaned
(C) 4 Weeks– Aged
(D) Cleaned
(E) 8 Weeks– Aged
(F) Cleaned
(G) 16 Weeks– Aged
(H) Cleaned
1µm

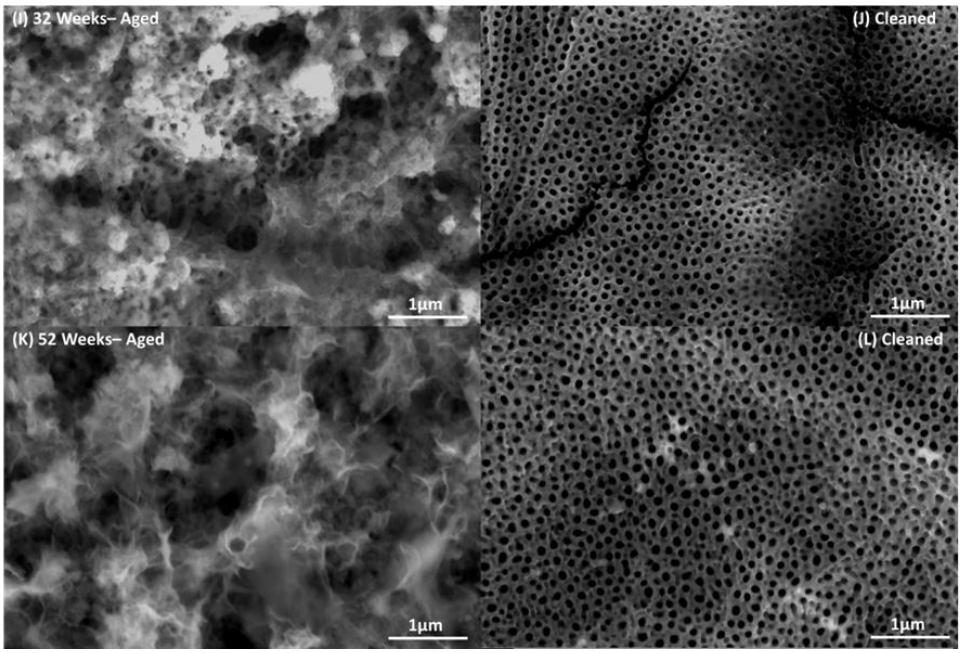

Figure 4. 48 Effect of 0.1 H_2O_2 + 1.2 mW/cm^2 rinse on removal of debris from TiO_2NT-Ag. LHS – As aged, RHS – cleaning. Magnification 50K.

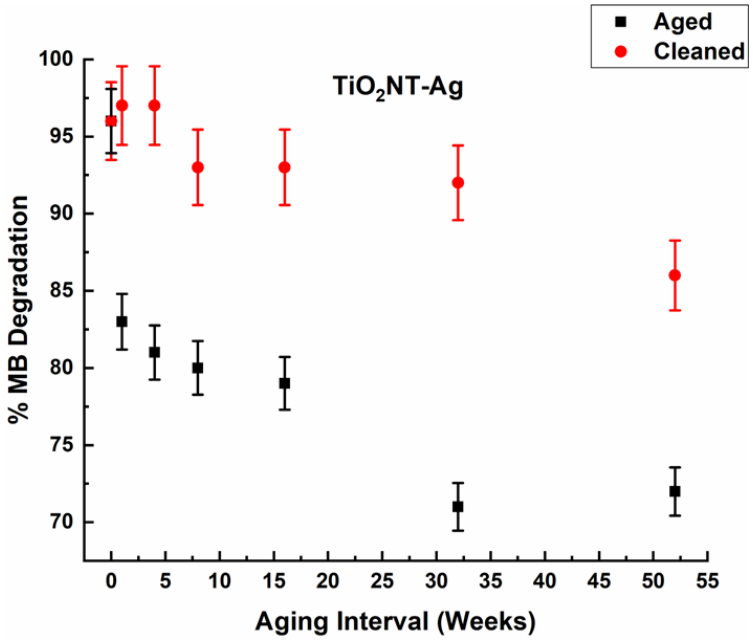

Figure 4. 49 Recovery in MB degradation activity of TiO_2NT-Ag after cleaning with 0.1M H_2O_2 + 1.2 mW/cm^2 UVA. Error bars: Maximum and minimum error of 3 independent readings

Table 4. 8 Summary of MB degradation activity of TiO_2NT-Ag after 0.1M H_2O_2 + 1.2 mW/cm^2 UVA

Aging Interval (Weeks)	0	1	4	8	16	32	52
Aged (% Degradation)	97	83	81	80	79	71	72
Cleaned (% Degradation)	97	97	97	93	93	92	86

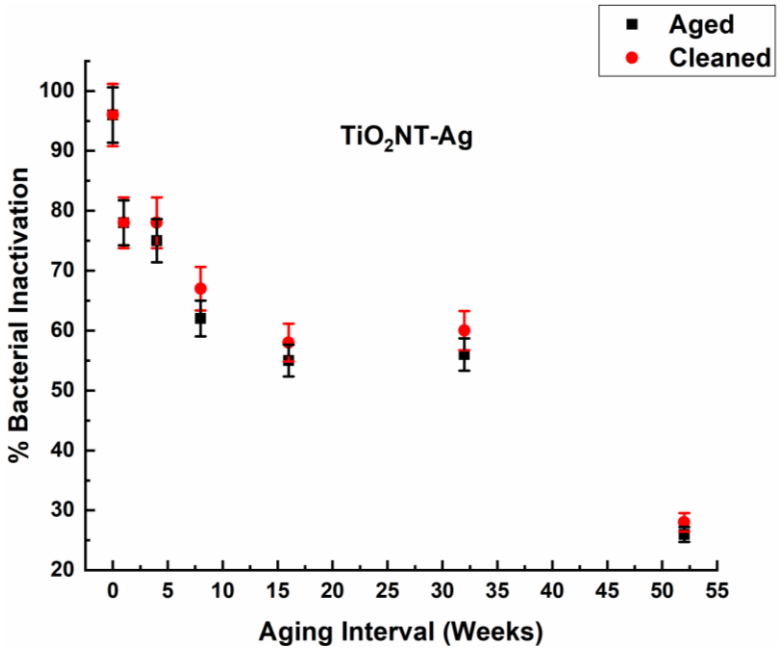

Figure 4. 50 Recovery in antibacterial activity of TiO_2NT-Ag after cleaning with 0.1M H_2O_2 + 1.2 mW/cm^2 UVA. Error bars: Maximum and minimum error of 3 independent readings

Table 4. 9 Summary of recovery in antibacterial activity of TiO_2NT-Ag after 0.1M H_2O_2 + 1.2 mW/cm^2 UVA rinse

Aging Interval (Weeks)	0	1	4	8	16	32	52
Aged (% Inactivation)	96	78	75	62	55	56	26
Cleaned (% Inactivation)	96	78	78	67	58	60	28

The cleaning regimen was less successful for TiO_2 NT-SS than for the other two materials (figure 4.51a-l). The TiO_2NT-SS nanostructure was immediately more susceptible to fouling, with the accumulation of debris being evident after just 1 week of aging. The adhered debris was also more compacted which made its removal by

rinsing more difficult. The rinsing cycle was in part successful as some of the material was lifted off the surface but complete exposure was not achieved even during the earlier aging intervals. In some way the formation of biological layers over the surface aided the cleaning of the surfaces aged for 32 and 52 weeks. The bacterial layer could have adhered to the more compact debris, helping lifting it off the surface, once it was rinsed off with the water.

The recovery of the activity towards MB is shown in figure 4.52 and table 4.10. The result for the 1st week of aging is somewhat ambiguous as the value for the cleaned sample exceeded that of the as produced material. This is likely due to an area of debris which was made more absorbent with the rinse by dispersing it rather than removing it. In this was debris which was previously stacked was spread over the surface allowing it to adsorb the dye even after equilibration was reached. The adsorped MB would contribute to the total of the MB removed. Near complete recovery of the initial activity was achieved until the 4th week, after which the activity of the material had lowered to such an extent that recovery was minimal.

The recovery of the antibacterial activity of the materials was even lower than that of MB. The activity before and after cleaning is presented in figure 4.53 and table 4.11. There was no appreciable recovery following the rinsing cycle.

The loss in activity with aging could only be partially attributed to surface coverage. Had this been the main mode of inactivation, complete or near complete recovery of the material would have been reported in all instances. The addition of H2O2, whilst beneficial, did not prove to be a solution for complete regeneration of the material. Given that at least four routes for deactivation exist, a complete solution using one method is unlikely. The most effective mode of regeneration has been found to be calcination of the material in air. The efficiency of this method is however dependent on the nature of the contaminants on the surface. Compounds which cannot be volatilised will remain adhered to the surface. The thermal regeneration of the material will also preclude its use in places where the ability to heat the materials is not possible.

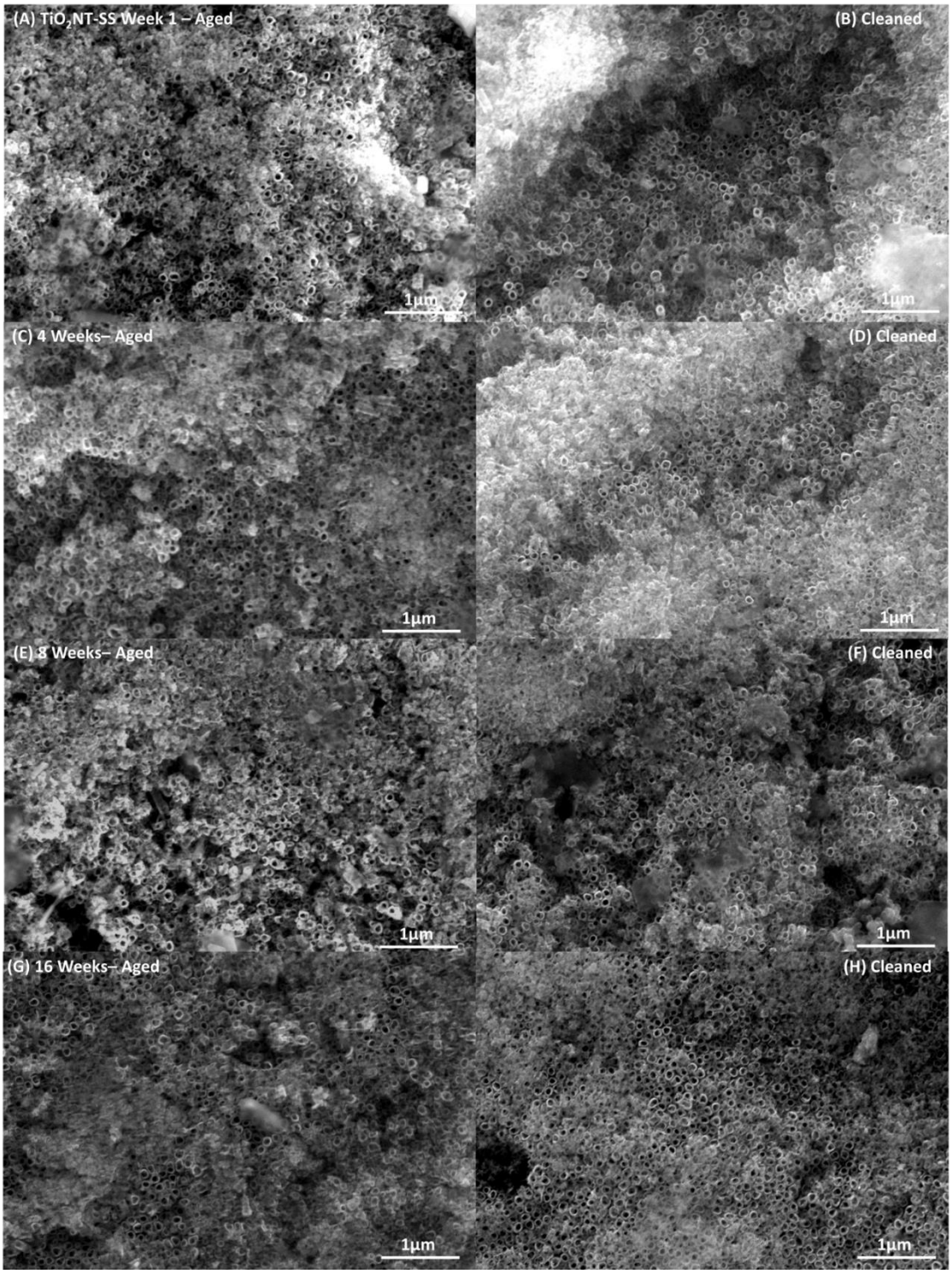
(A) TiO2NT-SS Week 1 – Aged
1µm
(B) Cleaned
1µm
(C) 4 Weeks– Aged
1µm
(D) Cleaned
1µm
(E) 8 Weeks– Aged
1µm
(F) Cleaned
1µm
(G) 16 Weeks– Aged
1µm
(H) Cleaned
1µm

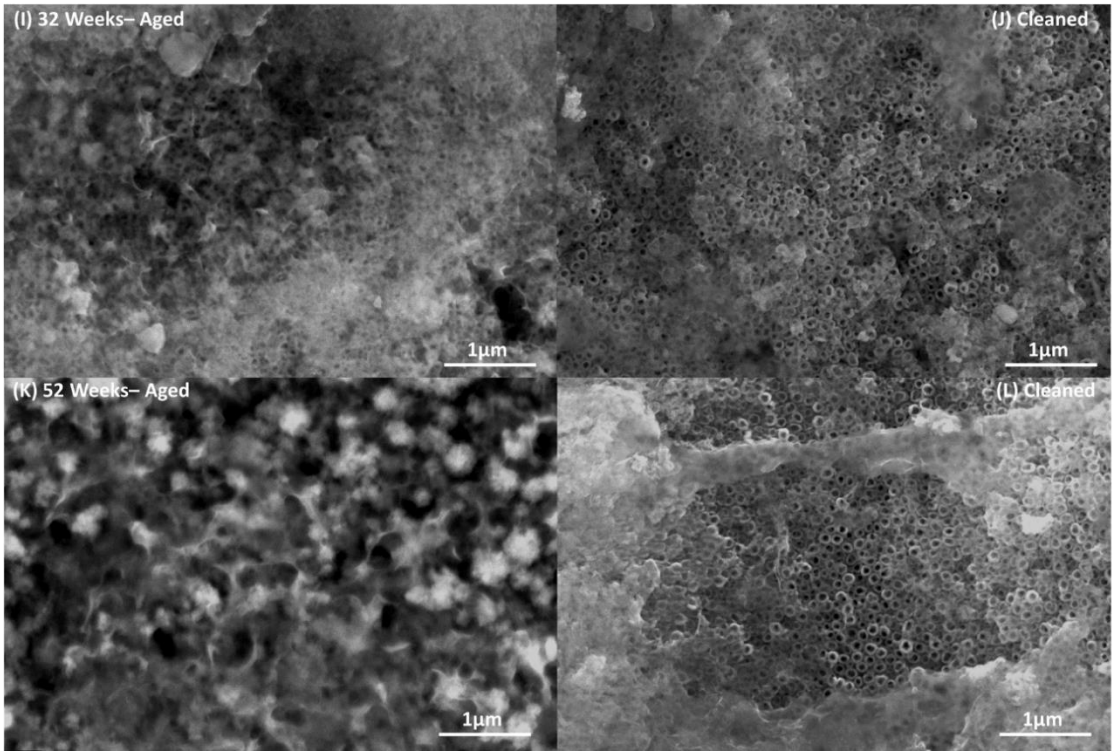

Figure 4. 51 Effect of 0.1 H_2O_2 + 1.2 mW/cm^2 rinse on removal of debris from TiO_2NT-SS. LHS – As aged, RHS – cleaning. Magnification 50K.

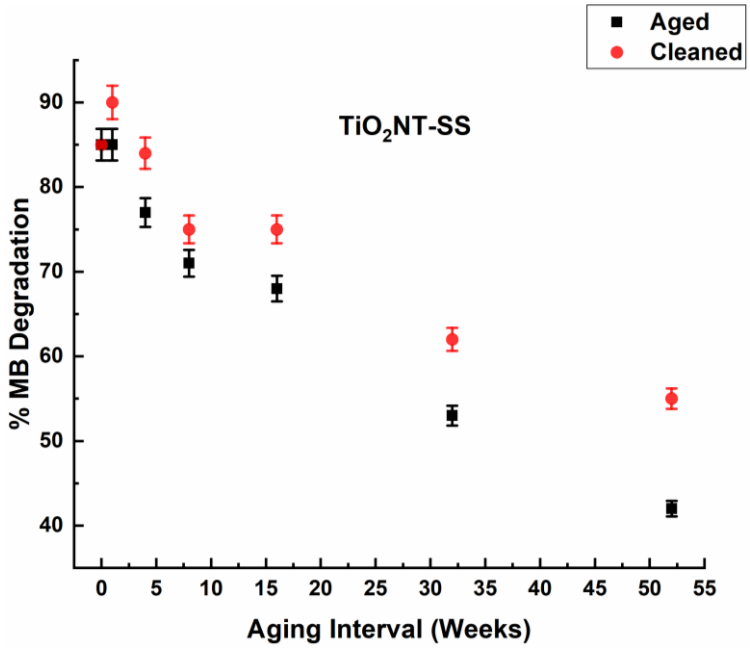

Figure 4.52 Recovery in MB degradation activity of TiO_2NT-SS after cleaning with 0.1M H_2O_2 + 1.2 mW/cm^2 UVA. Error bars represent the maximum and minimum error of 3 the photocatalytic activity of 3 samples.

4.3 Chapter Conclusions

4.3.1 Laboratory Short-Term Aging

- The TiO_2NT-EG and TiO_2NT-AG surfaces being devoid of inter-tube spacing are highly resistant to fouling by insoluble debris. Conversely the more open morphology of TiO_2NT-SS and TiO_2NT-PA caused a high deposition of insoluble material, severely occluding the single nanotubes.
- The mechanical and chemical stability of the TiO_2 ANTA were retained.
- The XRD profiles indicate the formation of a salt layer over the photocatalytic surface. The greater the surface coverage, the higher the intensity of the halite peaks recorded. This was the case for TiO_2NT-SS and TiO_2NT-PA. The debris retained the soluble salts within its structure.
- The XRD profiles also show no evidence of the anatase to rutile transition.
- The optical properties of the surfaces remained mostly unchanged after aging.
- The ability of the materials to degrade MB and their antibacterial activity diminished with aging. However, a remarkably high activity was retained, especially for TiO_2NT-EG and TiO_2NT-AG.

4.3.2 Solar Long-Term Aging

- The morphology of the debris was different than that of the samples aged in the laboratory. The absence of kaolin and cellulose precluded the formation of the compact debris formed on the laboratory aged TiO_2NT-SS and TiO_2NT-PA samples. The solar aged surfaces were covered with a fibrous debris, consistent with the formation of biofilms. The silver in the TiO_2NT-AG delayed the formation of this fibrous layer.
- The halite peak was only detected on the TiO_2NT-SS surface, which was the one with the debris structure similar to that obtained in the laboratory-based aging.

- The anatase-rutile transition was not recorded in the XRD traces.
- The ability of the surfaces to degrade MB after 52 weeks of aging was in general higher that that after 12 weeks. The one exception was TiO_2NT-SS which was 10% lower for the extra 9 months of aging.
- The antibacterial activity of the surfaces aged for 52 weeks was lower than that aged for 12 weeks. The difference in mechanisms for the degradation of MB and inactivation of bacteria plays a huge part in this difference.

4.3.3 Reactivation Strategies

- All 4 reactivation regimes were successful in removing the majority of the debris deposited on the surfaces. The NaOH rinse was less effective than the other treatments but still managed to remove the vast majority of the attached debris.
- The highest recovery in activity towards the degradation of MB was obtained with the 0.1 M H_2O_2 + 1 mW/cm^2 rinse. The lowest recovery was that for the 0.1M NaOH. The NaOH solution did not remove all the debris and this might have impacted the recovery of the material.
- The 0.1M H_2O_2 + 1 mW/cm^2 was chosen to clean the solar aged surfaces. This was successful in removing most of the debris off the TiO_2NT-EG surfaces. The activity with respect to the degradation of MB was nearly wholly recovered up to the 16th week of aging. Lower reactivation efficiencies were recorded for the last two aging intervals. Recovery for the antibacterial activity was however marginal. The debris over TiO_2NT-Ag surfaces was also mostly removed. The activity towards the degradation of MB was nearly completely recovered up to the 32nd week of aging. The recovery of the antibacterial activity was similar to that of TiO_2NT-EG and the final activity was much lower than that of unaged samples. The cleaning action on TiO_2NT-SS was the least effective as the surfaces at each different aging interval retained a significant amount of debris. The activity towards the degradation of MB was wholly recovered until the 4th aging interval. The recovery of the material's antibacterial properties was marginal.

4.4 References

[1] K. A. Thompson, R. S. Summers, and S. M. Cook, "Development and experimental validation of the composition and treatability of a new synthetic bathroom greywater (SynGrey)," Environmental Science: Water Research & Technology, vol. 3, pp. 1120-1131, 2017.

[2] ASTM, "G173-03, Standard Tables for Reference Solar Spectral Irradiances: Direct Normal and Hemispherical on 37 Tilted Surface," ed. West Conshohocken, PA: ASTM International, 2012.

[3] I. O. f. Standardisation, "Fine ceramics (advanced ceramics, advanced technical ceramics) — Determination of photocatalytic activity of surfaces in an aqueous medium by degradation of methylene blue," ed, 2010.

[4] R. Wang, K. Hashimoto, A. Fujishima, M. Chikuni, E. Kojima, A. Kitamura, *et al.*, "Light-induced amphiphilic surfaces," Nature, vol. 388, pp. 431-432, 1997/07/01 1997.

[5] S. Abela, C. Farrugia, R. Xuereb, F. Lia, E. Zammit, A. Rizzo, *et al.*, "Photocatalytic Activity of Titanium Dioxide Nanotubes Following Long-Term Aging," Nanomaterials, vol. 11, p. 2823, 2021.

[6] H. Habazaki, K. Fushimi, K. Shimizu, P. Skeldon, and G. E. Thompson, "Fast migration of fluoride ions in growing anodic titanium oxide," Electrochemistry Communications, vol. 9, pp. 1222-1227, 2007/05/01/ 2007.

[7] S. Cao, W. Huang, S. Zhang, L. Wu, and Y. Song, "A simple strategy to increase the interfacial adhesion between TiO_2 nanotube layer and Ti substrate," Journal of Alloys and Compounds, vol. 772, pp. 173-177, 2019/01/25/ 2019.

[8] S. Berger, S. P. Albu, F. Schmidt-Stein, H. Hildebrand, P. Schmuki, J. S. Hammond, *et al.*, "The origin for tubular growth of TiO_2 nanotubes: A fluoride rich layer between tube-walls," Surface Science, vol. 605, pp. L57-L60, 2011/10/01/ 2011.

[9] J. Olabarrieta, S. Zorita, I. Peña, N. Rioja, O. Monzón, P. Benguria, *et al.*, "Aging of photocatalytic coatings under a water flow: Long run performance and TiO_2 nanoparticles release," Applied Catalysis B: Environmental, vol. 123-124, pp. 182-192, 2012/07/23/ 2012.

[10] G. E. Christidis, "Industrial Clays." vol. 9, ed, 2011, pp. 341–414.

[11] D. G. Schulze, "CLAY MINERALS," in Encyclopedia of Soils in the Environment, D. Hillel, Ed., ed Oxford: Elsevier, 2005, pp. 246-254.

[12] K. Fischer, M. Kühnert, R. Gläser, and A. Schulze, "Photocatalytic degradation and toxicity evaluation of diclofenac by nanotubular titanium dioxide–PES membrane in a static and continuous setup," RSC Advances, vol. 5, pp. 16340-16348, 2015.

[13] P. Roy, S. P. Albu, and P. Schmuki, "TiO_2 nanotubes in dye-sensitized solar cells: Higher efficiencies by well-defined tube tops," Electrochemistry Communications, vol. 12, pp. 949-951, 2010/07/01/ 2010.

[14] D. D. Evanoff Jr. and G. Chumanov, "Synthesis and Optical Properties of Silver Nanoparticles and Arrays," ChemPhysChem, vol. 6, pp. 1221-1231, 2005.

[15] H. Liang, H. Han, F. Wang, Z. Cheng, B. Lin, Y. Pan, *et al.*, "Experimental investigation on spectral splitting of photovoltaic/thermal hybrid system with two-axis sun tracking based on SiO2/TiO_2 interference thin film," Energy Conversion and Management, vol. 188, pp. 230-240, 2019/05/15/ 2019.

[16] X. Zhang, H. Wu, Z. Ke, J. Yang, H. Chen, F. Xue, *et al.*, "A new effective way to degrade methylene blue by introducing negative ions powder into Fe3O4/H2O2 system to accelerate Fe(III)/Fe(II) transformation," Water Science and Technology, vol. 83, pp. 1834-1846, 2021.

[17] M. A. E. Wafi, M. A. Ahmed, H. S. Abdel-Samad, and H. A. A. Medien, "Exceptional removal of methylene blue and p-aminophenol dye over novel TiO_2 /RGO nanocomposites by tandem adsorption-photocatalytic processes," Materials Science for Energy Technologies, vol. 5, pp. 217-231, 2022/01/01/ 2022.

[18] D. Awfa, M. Ateia, M. Fujii, and C. Yoshimura, "Photocatalytic degradation of organic micropollutants: Inhibition mechanisms by different fractions of natural organic matter," Water Research, vol. 174, p. 115643, 2020/05/01/ 2020.

[19] C. S. Turchi and D. F. Ollis, "Mixed reactant photocatalysis: Intermediates and mutual rate inhibition," Journal of Catalysis, vol. 119, pp. 483-496, 1989/10/01/ 1989.

[20] M. Abdullah, G. K. C. Low, and R. W. Matthews, "Effects of common inorganic anions on rates of photocatalytic oxidation of organic carbon over illuminated titanium dioxide," The Journal of Physical Chemistry, vol. 94, pp. 6820-6825, 1990/08/01 1990.

[21] M. Lindner, D. W. Bahnemann, B. Hirthe, and W.-D. Griebler, "Solar Water Detoxification: Novel TiO_2 Powders as Highly Active Photocatalysts," Journal of Solar Energy Engineering, vol. 119, pp. 120-125, 1997.

[22] W. Zhang, T. An, M. Cui, G. Sheng, and J. Fu, "Effects of anions on the photocatalytic and photoelectrocatalytic degradation of reactive dye in a packed-bed reactor," Journal of Chemical Technology & Biotechnology, vol. 80, pp. 223-229, 2005.

[23] C. Guillard, E. Puzenat, H. Lachheb, A. Houas, and J.-M. Herrmann, "Why inorganic salts decrease the photocatalytic efficiency," International Journal of Photoenergy, vol. 7, p. 641208, 1900/01/01 2005.

[24] M. Mavaei, A. Chahardoli, Y. Shokoohinia, A. Khoshroo, and A. Fattahi, "One-step Synthesized Silver Nanoparticles Using Isoimperatorin: Evaluation of Photocatalytic, and Electrochemical Activities," Scientific Reports, vol. 10, p. 1762, 2020/02/04 2020.

[25] A. Ziashahabi, M. Prato, Z. Dang, R. Poursalehi, and N. Naseri, "The effect of silver oxidation on the photocatalytic activity of Ag/ZnO hybrid plasmonic/metal-oxide nanostructures under visible light and in the dark," Scientific Reports, vol. 9, p. 11839, 2019/08/14 2019.

[26] D. He, C. J. Miller, and T. D. Waite, "Fenton-like zero-valent silver nanoparticle-mediated hydroxyl radical production," Journal of Catalysis, vol. 317, pp. 198-205, 2014/08/01/ 2014.

[27] S. W. Karickhoff and G. W. Bailey, "Optical Absorption Spectra of Clay Minerals," Clays and Clay Minerals, vol. 21, pp. 59-70, 1973/02/01 1973.

[28] V. C. Anitha, J. H. Lee, J. Lee, A. N. Banerjee, S. W. Joo, and B. K. Min, "Biofilm formation on a TiO_2 nanotube with controlled pore diameter and surface wettability," Nanotechnology, vol. 26, p. 065102, Feb 13 2015.

[29] S. Salaeh, M. Kovacic, D. Kosir, H. Kusic, U. Lavrencic Stangar, D. D. Dionysiou, *et al.*, "Reuse of TiO_2 -based catalyst for solar driven water treatment; thermal and chemical reactivation," Journal of Photochemistry and Photobiology A: Chemistry, vol. 333, pp. 117-129, 2017/01/15/ 2017.

[30] Z. Chen, Y. Peng, J. Chen, C. Wang, H. Yin, H. Wang, *et al.*, "Performance and Mechanism of Photocatalytic Toluene Degradation and Catalyst Regeneration by Thermal/UV Treatment," Environmental Science & Technology, vol. 54, pp. 14465-14473, 2020/11/17 2020.

[31] C. Liu, S. Tan, and D. Fu, "The research on the deactivation mechanism of TiO_2 nanotube," Desalination and Water Treatment, vol. 57, pp. 28386-28392, 2016/12/13 2016.

[32] L. Ren, W. Huo, G. Li, W. Choi, and T. An, "Photocatalytic mechanisms and photocatalyst deactivation during the degradation of 5-fluorouracil in water," Catalysis Today, vol. 410, pp. 45-55, 2023/02/15/ 2023.

[33] V. G. Gandhi, M. K. Mishra, and P. A. Joshi, "A study on deactivation and regeneration of titanium dioxide during photocatalytic degradation of phthalic acid," Journal of Industrial and Engineering Chemistry, vol. 18, pp. 1902-1907, 2012/11/25/ 2012.

[34] J. Liqiang, X. Baifu, Y. Fulong, W. Baiqi, S. Keying, C. Weimin, *et al.*, "Deactivation and regeneration of ZnO and TiO_2

nanoparticles in the gas phase photocatalytic oxidation of n-C7H16 or SO2," Applied Catalysis A: General, vol. 275, pp. 49-54, 2004/11/08/ 2004.

[35] M. Jonstrup, M. Wärjerstam, M. Murto, and B. Mattiasson, "Immobilisation of TiO_2 for combined photocatalytic-biological azo dye degradation," Water Science and Technology, vol. 62, pp. 525-531, 2010.

[36] J. Schmidt and W. Vogelsberger, "Aqueous Long-Term Solubility of Titania Nanoparticles and Titanium(IV) Hydrolysis in a Sodium Chloride System Studied by Adsorptive Stripping Voltammetry," Journal of Solution Chemistry, vol. 38, pp. 1267-1282, 2009/10/01 2009.

[37] N. Miranda-García, S. Suárez, M. I. Maldonado, S. Malato, and B. Sánchez, "Regeneration approaches for TiO_2 immobilized photocatalyst used in the elimination of emerging contaminants in water," Catalysis Today, vol. 230, pp. 27-34, 2014/07/01/ 2014.

[38] T. S. Natarajan, H. C. Bajaj, and R. J. Tayade, "Preferential adsorption behavior of methylene blue dye onto surface hydroxyl group enriched TiO_2 nanotube and its photocatalytic regeneration," Journal of Colloid and Interface Science, vol. 433, pp. 104-114, 2014/11/01/ 2014

Chapter 5. Upscaling of ANTA and Field Use

In this chapter the focus shifts from laboratory scale experiments and towards field use. An upscaling methodology for the production of larger ANTA surfaces was tested and implemented. The degradation of synthetic greywater was studied and the possibility of inhibition from inorganic species was looked into. The effect of process parameters namely the flow rate and volume of water to be treated on the efficiency of photocatalytic degradation in batch mode was assessed. Finally, the use of solar radiation as a way to inactivate bacteria present in greywater was also investigated.

5.1 Methodology

5.1.1 Upscaling of ANTA for Use in Prototype Reactors

The main challenge in upscaling using electrochemical methods is assuring that the current density on the surfaces is more or less uniform. The main impediment to this when using non-aqueous electrolytes such as ethylene glycol and glycerol is the tendency of the solution to heat up. This excess heat could result in an uncontrolled increase in current which could lead to dielectric breakdown [1]. In the case of dielectric breakdown, the titanium anode would pit rather than sustain the growth-dissolution mechanism that is required for nanotubes to form.

The set-up used for anodising is shown in figure 5.1. A chiller was used to circulate water at 5°C through a looped copper pipe in a closed circuit keeping the water in the cooling bath at low temperature. Two glass anodising baths were then placed in a 300L polyethylene tank. Two air manifolds were attached to the sides of the baths and connected to an air stone to gently agitate the electrolyte when the anodising is under way. Ten 15cm X 15cm Ti plates, 5 anodes and 5 cathodes were racked in a custom-made holder. The plates were previously rinsed in acetone, followed by IPA and finally DI water. The plates were set at a fixed distance of 3cm from each other. To these plates, Ti tabs were spot welded to act as electrical contacts. For clarity only five plates are shown, these were arbitrarily set as the anodes. The remaining slots would hold the cathodes. The plates were arranged in the following order: cathode, anode, anode, cathode, cathode, anode, anode, cathode, cathode, anode. In this way one side of a

specific electrode, cathode or anode, will be facing its counterpart with the opposite polarity. This helps maintain a uniform electric field between the two opposite electrodes.

Fourteen litres of the anodising electrolyte were added, an amount which was enough to have the whole plates submerged but allowing the tabs to remain exposed. The electrolyte was the same as that used for the TiO_2NT-EG and was prepared as per section 3.1.1. To avoid excessive moisture being absorbed by the electrolyte a thin film of mineral oil was spread over the electrolyte. The polyethylene external cooling tank was then carefully filled with water to a level exceeding the liquid level of the electrolyte but low enough to avoid ingress of water in the anodising bath. The water was circulated using a circulation pump to aid in heat dissipation.

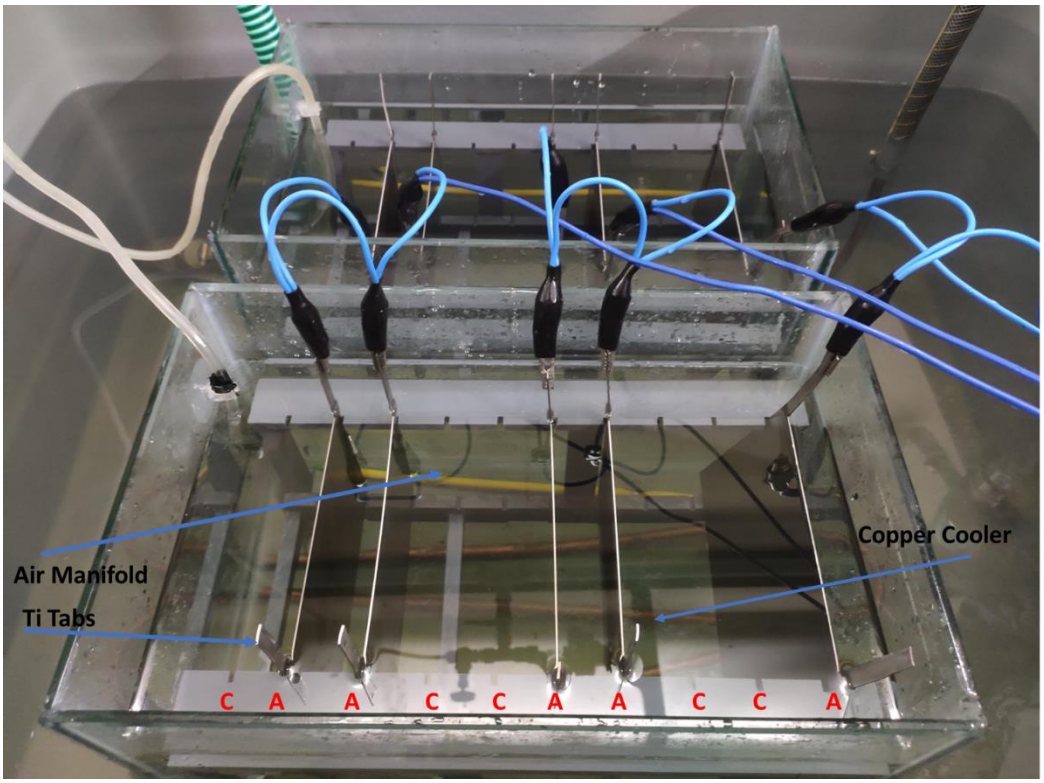

Figure 5. 1 Large-scale anodising set-up showing order of electrodes and cooling system**.**

The anodising process was carried out at 40V for 2 hours. The plates were extracted and rinsed gently with acetone and allowed to air dry. The plates were then heated at 80°C to remove the excess ethanol. The plates were then annealed at 450°C for 2 hours. After allowing the plates to reach room temperature, the plates were cleaned by sonicating for 10 minutes in DI water. The materials thus produced were termed TiO_2 NT-EG 40V. A sample of the platesse after annealing are shown in figure 5.2.

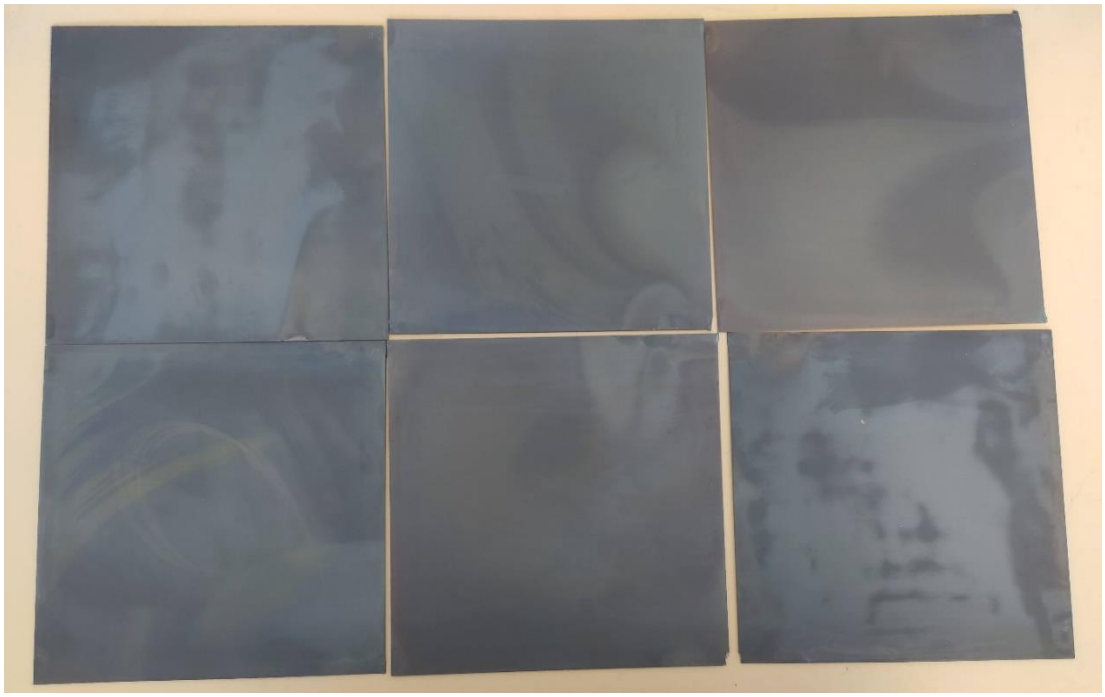

Figure 5. 2 Appearance of 15 cm X 15cm plates after annealing

5.1.2 Assessment of Morphology and Morphological Parameters.

The morphology of the surfaces was assessed by SEM imaging using the same Zeiss Merlin Field Emission SEM described before. The electron high tension was set at 8kV, the working distance was set at 7nm and the probe current was kept at 200 pA. The thickness of the layer was obtained from SEM imaging of a mechanically cracked section of the anodised plate. The layer thickness, tube diameter and tube wall thickness were quantified by image analysis using ImageJ.

5.1.3 Prototype UVA Photocatalytic Reactor

A prototype reactor was constructed by a Econetique, a partner within the Micro WatTs project consortium (figure 5.3). The arrangement of the UVA LED strip lights is presented in figure 5.4. The LED strips were custom made by C-LED SRL. The layout presented in figure 5.4 was derived experimentally, ensuring that the average incident light over the surfaces after passing through the glass was 1.2 ± 0.2 mW/cm^2. The irradiance was measured using an OPTIMUM SRI 2000UV spectrophotometer. For the required irradiance the canopy had to be raised 60 cm above the surface of the photocatalytic tiles.

Two photocatalytic tiles were mounted to the reactor frame. One tile contained 4, 15 cm X 15 cm blank Ti control plates. The other tile housed the TiO_2NT-EG 40V surfaces. The tile was covered with a low iron glass plate. The thickness of the solution circulating over the surfaces was 3mm.

The dosing tank was used to thoroughly mix the solution to be degraded. The contents of the tank could then be divided equally between the two process tanks. The process tanks had a maximum capacity of 5L. The maximum flow rate obtained when the pumps were not throttled was 150 L/h. The minimum flowrate and the minimum volume which could be circulated in the unit were determined to be 100 L/h and 2L respectively.

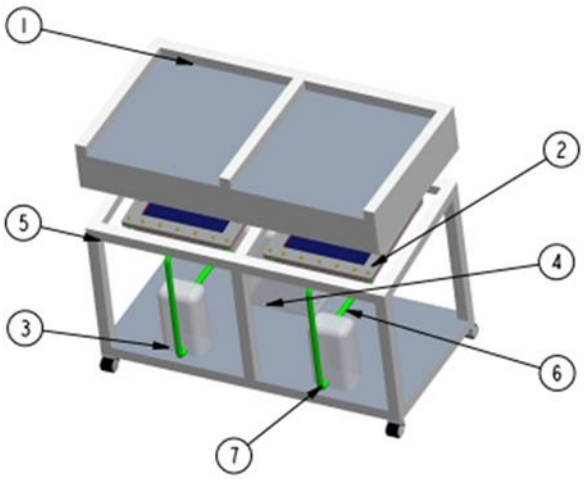

Item	Description
1	UVA Light Canopy
2	Photocatalytic Tile
3	Process Tank
4	Dosing Tank
5	Reactor Frame
6	Return Pipe
7	Supply Pipe

Figure 5. 3 Schematic showing structure and components of prototype UVA reactor.

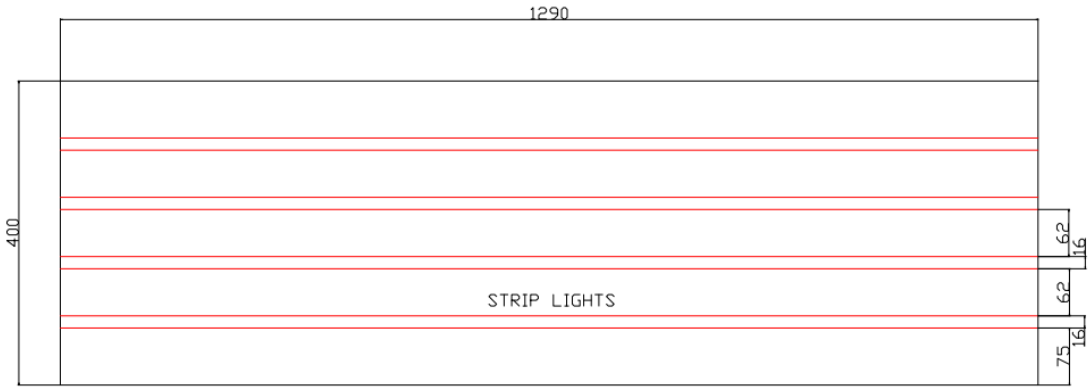

Figure 5. 4 Layout and spacing of UVA strips installed in the canopy**.** All dimensions in mm.

5.1.4 Photocatalytic Efficiency of UVA Photocatalytic Reactor

5.1.4.1 Photocatalytic Degradation of Synthetic Greywater

The degradation of synthetic greywater was determined by measuring the reduction in TOC after an 8-hour treatment cycle. Cellulose and Kaolin were once more omitted from the mixture. To ensure the maximum efficiency of the unit 2L of synthetic greywater were circulated at 100 L/h over the Ti blanks and the ANTA. The TOC value after 1 hour equilibration in the dark and after 8 hours under UVA irradiation was measured using a Shimadzu TOC-L analyser.

The experiment was repeated by using the organic components of the synthetic greywater only i.e., surfactants and yeast extract. The omission of the inorganic constituents of the synthetic greywater was in order to determine whether the inorganic compounds at the concentrations being used had an inhibitive effect on the photocatalytic activity.

5.1.4.2 Photocatalytic Degradation of 22 ppm TOC MB Solution.

To study the effect of different pollutants with the same TOC content as the synthetic greywater, a 22 ppm TOC solution of MB was used. The TOC content of the synthetic greywater was 22ppm and for the purpose of equivalence the MB solution had the same TOC concentration. A 2L solution volume and a 100 L/h flow rate were employed. The absorbance values at 664 nm after a 1-hour equilibration period in the dark and after 8-hours was recorded using a Shimadzu SolidSpec-3700 UV-VIS spectrophotometer. The TOC value after equilibration and at the end of the treatment cycle was measured using the Shimadzu TOC-L analyser.

5.1.4.3 Photocatalytic Degradation of 22 ppm TOC Paracetamol Solution.

The procedure reported in section 5.2.1.2 was repeated by using a 22 ppm TOC paracetamol solution in order to study the effect of molecular structure on degradation. This served as a direct comparison to the results of the 22 ppm MB solution. The absorbance at 243 nm and the TOC value were measured after the equilibration period and at the end of the 8-hour cycle.

5.1.4.4 Effect of Process Parameters on Photocatalytic Activity

The effect of changing flow rate and volume on photocatalytic activity was determined. To obtain a more easily discernible change when the parameters are changed, MB at a concentration of 1.5 X 10^{-5} M was used. The flow rates used were the minimum at 100 L/h and the maximum at 150 L/h. The minimum volume employed was 2L and the maximum 5L. The change in absorbance was measured at 30-minute intervals over a period of 8 hours using a Shimadzu SolidSpec-3700 UV-VIS spectrophotometer. The TOC value after equilibration and at the end of the 8-hour treatment cycle was measured using a Shimadzu TOC-L analyser.

5.1.5 Antibacterial Activity Under Solar Irradiation

5.1.5.1 Prototype Solar Photocatalytic Reactor

The Antibacterial activity of ANTA under Solar irradiation was examined. The experiments were carried out during the months of November and December, where a 6-hour photocatalytic cycle was carried out on three different days. The reactor used was a flat plate batch reactor and was constructed by a third-party forming part of the Micro WatTS project consortium. The unit shared many similarities with the UVA prototype unit. Both units had a section containing the Ti blanks and another the photocatalysts and both had two tanks and pumps with variable flow rates. The main differences are the number of plates of each material, the volume and the flowrates. The schematic shown in figure 5.5 reveals that a total of 48 plates were housed in the unit. The first two windows from the left contained the photocatalysts and the remaining two, the Ti control blanks.

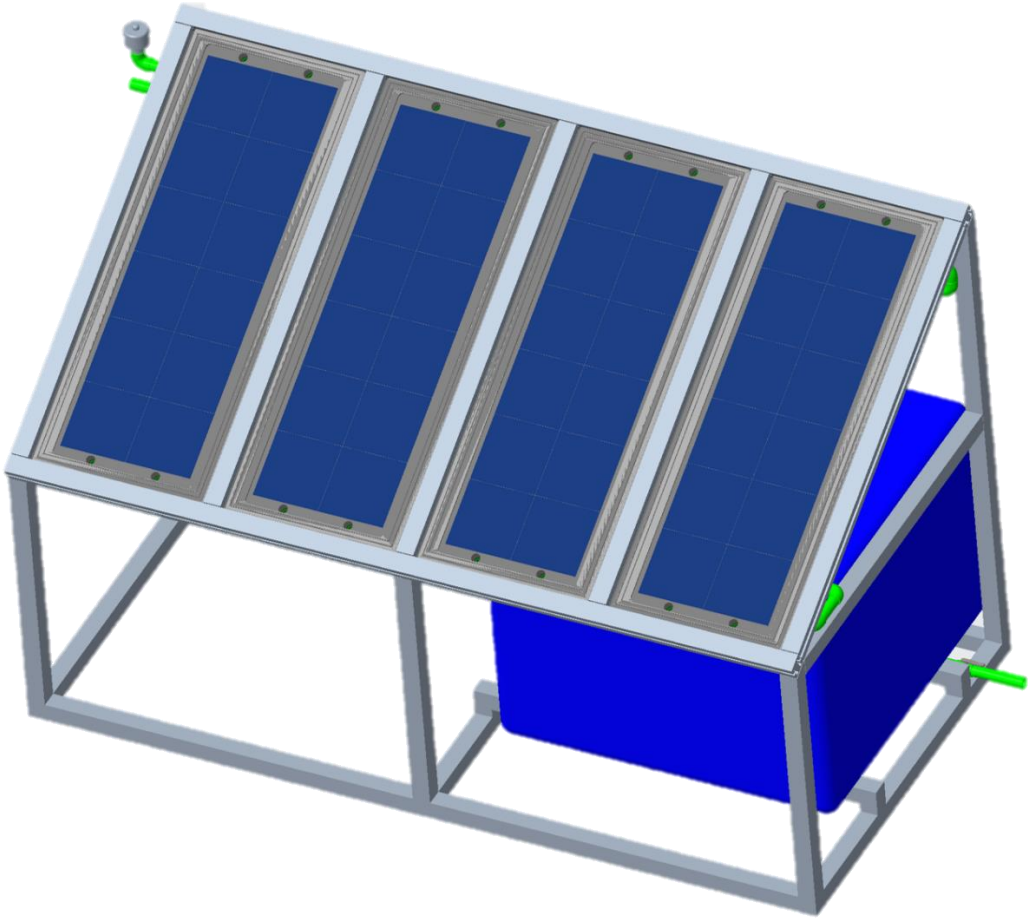

Figure 5. 5 Construction and tile layout of solar greywater reactor

5.1.5.2 Antibacterial Activity of ANTA Under Solar Irradiation

5.1.5.2.1 Preparation of Synthetic Greywater.

The synthetic greywater mixture described by Thompson was implemented as the base to be seeded with bacteria. The seeding was carried out with a BL21 (DE3) strain of *E.coli* which is a mutated non-pathogenic strained. A single colony of BL21 (DE3) was transferred to a 50mL falcon tube containing 30mL of tryptic soy broth (TSB, Merck). The culture was incubated at 37°C at a rotation of 200 RPM for 18 hours. The culture was centrifuged and the supernatant discarded. The pellet precipitated after centrifugation, was re-suspended in 30mL of TSB. The suspension was centrifuged once more, the supernatant discarded and the pellet formed was resuspended in 30mL of TSB. The culture was centrifuged once more and resuspended in 30 mL of TSB. The final suspension served as the bacterial seed for the synthetic greywater. Fifteen millilitres of

the suspension were pipetted in each of the process tanks which were filled with synthetic greywater chemical mixture.

5.1.5.2.2 Bacterial Inactivation Using Solar Radiation

The minimum volume of 15L and flow rate at 150L/h was used during the photocatalytic inactivation cycles. The solution was circulated for 1 hour in both sides of the reactor to fully homogenise the solution and to allow the bacteria to acclimate to the unit. During this equilibration period, the photocatalytic surfaces were covered to omit the effect of light. After the 1 hour of equilibration a 10 ml aliquot was taken from each tank and the covers were removed. Further samples were extracted after 1,3 and 6 hours of irradiation. The temperature of each tank at the single timepoints was measured using a liquid in glass thermometer sterilised with 70% ethanol. The irradiance at each timepoint at several positions on the tiles was recorded using the OPTIMUM SRI 2000UV spectrophotometer. The unit was filled with a 100-ppm peroxide solution overnight to avoid biofilm build-up which was allowed to circulate overnight. The unit was emptied and rinsed twice with softened water.

5.1.5.2.3 Post- Cycle Assessment of Antibacterial activity.

Five, tenfold serial dilutions were prepared from the samples extracted using TSB as the diluent. A 100 µL of each dilution were plated in triplicate on tryptic soy agar (TSA) and incubated at 37°C for 12 hours. The number of colonies on each plate were then counted, omitting the plates which contained less than 20 colonies.

5.2 Results and Discussion

5.2.1 Assessment of Morphology Obtained at 40V applied for 2 Hours

Given that most of the research employing TiO_2 ANTA deals with laboratory scale experiments the need for upscaling for field applications is essential. The upscaling of ANTA is however a recent endeavour and literature is not plentiful. The reason for the lack of upscaling studies has been attributed to the high currents involved which can cause the solution to heat up and possibly cause the dielectric breakdown of the TiO_2 [1]. The main strategies to produce large samples are the direct cooling of the electrolyte, the use of low potentials and short process durations. Linco *et al.* used an 8L electrolyte volume and a carried out the anodising at 40V for 1 hour [2]. Sopha *et al.* maintained the electrolyte temperature at 15°C throughout the duration of the process [1]. Mena *et al.* employed a 40V potential for 1 hour and reported that a potential of 60V resulted in an irregular nanotube structure [3]. Kim *et al.* applied a 60V potential for a maximum of 20 minutes [4]. In a second study Sopha *et al.* managed to apply a potential of 80V for 4hours, however this required the electrolyte to be at 10°C constantly [5].

From the initial testing stages up to the different aging exercises, 25 mm X 25 mm samples were used. Such small surfaces would be economically unfeasible for use in prototype units. In this study upscaling of the anodising served two purposes: the production of 150 mm X 150 mm surfaces and the production of multiple surfaces per anodising cycle. The anodising was performed in baths which could produce five surfaces per cycle, and two such baths were employed each cycle, producing a total of 10 photocatalytic surfaces. Ethylene glycol has a resistivity which is around 40 times greater than that of high purity water [6]. The resistive nature of the glycol electrolyte whilst essential for the growth of long ANTA, its inability to disperse heat makes upscaling of surfaces challenging. Given that the current drawn is proportional to the surface area of the surfaces being anodised, the solution heats up quickly. The increase in temperature increases that rate of reaction, causing a further increase in temperature. The high temperature can disrupt the formation of regular, upright nanotubes [7].

To keep temperatures low, and avoid excessive current densities, the experimental parameters had to be modified. Anodising just one 150 mm by 150 mm at 70V for 1 hour caused the solution to heat up considerably, thus making the parameters unsuitable

for scale up. In order to keep the morphology similar to that obtained on the smaller coupons, a potential of 40V was applied for 2 hours. The lower potential made it possible for the glycol electrolyte to not exceed 30°C when 5, 150mm by 150mm plates were anodised.

The surface morphology of the upscaled ANTA is presented in figure 5.6 a-b. A cross-section of the layer is shown in figure 5.7. The main morphological parameters of the material are compared with those of the TiO_2NT-EG coupons in table 5.1. The material synthesised at the lower voltage will be known hereon as TiO_2NT-EG 40V. The single nanotubes are clearly visible and the titanium oxide and hydroxide is not as obvious as that of the coupon sized TiO_2NT-EG. The tubes are mostly connected together with the exception of areas at the grain boundaries of the metal, where a higher etching rate caused the separation of the tubes. The maximum value of tube diameters is lower at 40V than at 70V. The nanotube diameter is mainly governed by the potential but by adopting a longer anodising time the tube diameters can be increased. In this instance the diameters were deemed suitable as longer durations can separate the tubes further leading to accumulation of debris in the inter-tube spaces. On the other hand, the tube-diameters are more or less identical. The tube wall thicknesses are similar and could be measured more accurately since the tube tops were more defined. The thickness of the layers was also nearly identical to that obtained at 70V, with the longer process time allowing for the continued growth of the tubes. Despite the main morphological parameters being mainly governed by the applied potential, a longer process time can in some cases make up for lower potentials [8].

This work succeeded in producing samples with a combined surface area of 2250 cm^2 in just 2 hours. This exceeds the areas reported by the previously mentioned works, even Sopha's, where the authors were able to produce a surface area of 100 cm^2, when both sides of the titanium substrate are taken into account. In the present study, the value of 2250 cm^2 takes into account only one side of the plates, since one of the sides will not be useable when the surfaces are mounted in the reactor. The current study was successful in upscaling the formation of ANTA without the use of electrochemistry specific equipment such as potentiostats and costly platinum cathodes. This opens the possibility for use of TiO_2 ANTA away from academic environments.

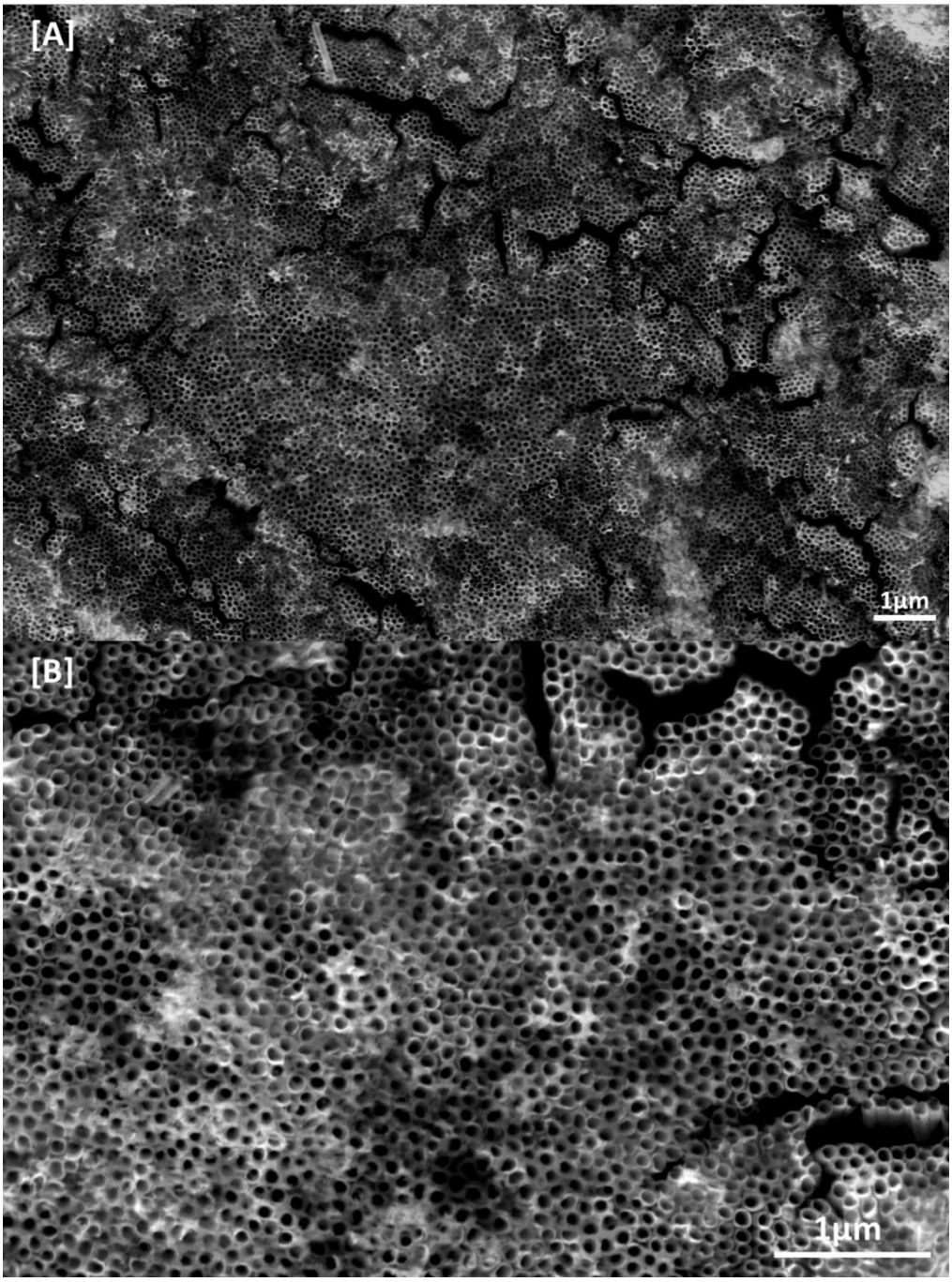

Figure 5. 6 Surface morphology of TiO_2NT-EG 40V A) 20K magnification B) 50K magnification

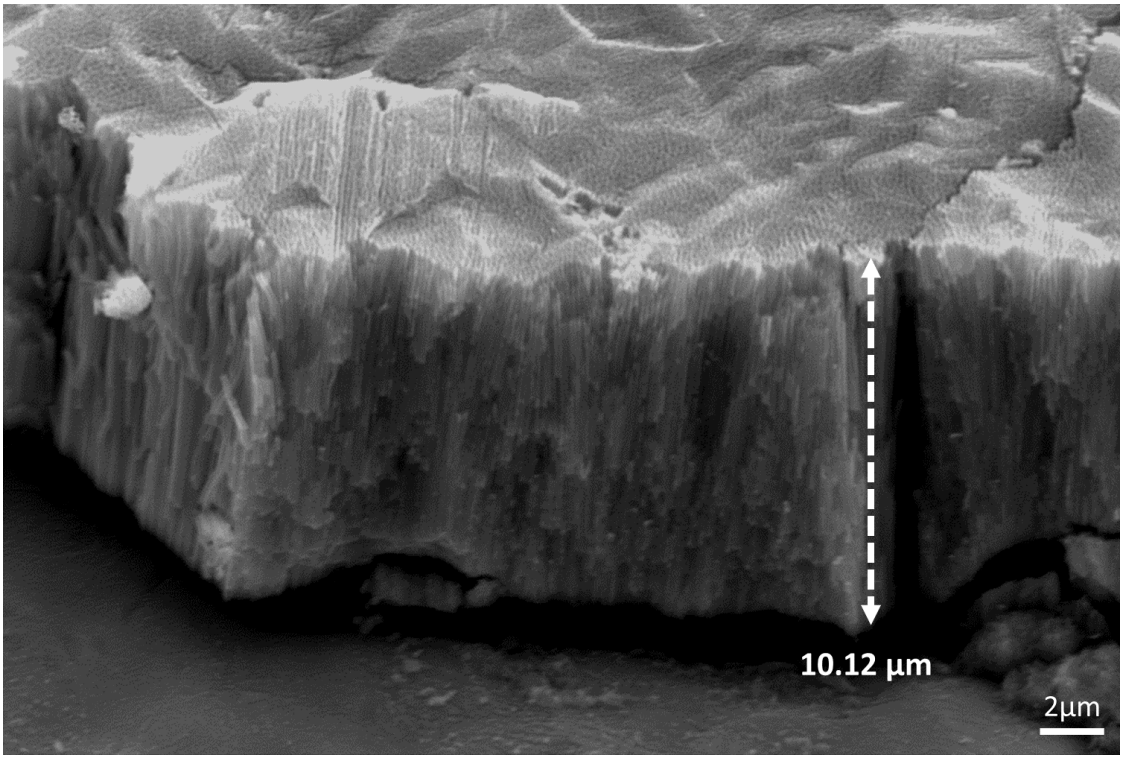

Figure 5. 7 Cross-section view of TiO_2NT-EG 40V. Magnification – 10K

Table 5. 1 Comparison of main morphological parameters of TiO_2NT-EG and TiO_2NT-EG 40V. Errors for tube diameter and wall thickness represents the standards deviation of 50 measurements. The error for layer thickness shows the maximum and minimum error of 10 measurements.

Parameters	Layer Thickness (µm)	Tube Diameter (nm)	Wall Thickness (nm)	Aspect Ratio
70V 1hr	9.99 ± 0.48	85-125 ± 9.3	10.00	79.92 -117.52
40V 2hrs	10.12 ± 0.71	82-106 ± 6.6	9.10-12.71 ± 1.2	95.47 -123.41

5.2.2 Photocatalytic degradation of organic compounds in the Synthetic Greywater Mixture

5.2.2.1 Reduction in TOC Using Optimum Process Parameters

The flat plate reactor configuration was chosen for the simplistic and familiar design which would make commercialisation of photocatalytic units as costs can be kept low. The reactor can be inclined to obtain the maximum irradiance falling over the photocatalysts. This is typically 30°.

The ability of the surfaces to degrade the organic compounds in the greywater mixture was assessed by measuring the TOC value after an 8-hour photocatalytic cycle. To discern between the reduction due to photocatalysis and any reduction from the operation of the unit, a panel containing TiO_2 ANTA surfaces and another housing untreated Ti control plates.

The results presented in figure 5.8 reveal some ambiguity as both materials brought about a significant reduction in the TOC value. The average TOC value of the mixture was 22.4 mg/l. A 30% reduction in TOC was recorded for the blank Ti surfaces. The effect of photocatalytic activity is noticeable, where a 46% reduction in TOC has been reported for TiO_2 NT-EG 40V however another factor must be affecting the TOC value. The surfactants and are resistant to UVA degradation and thus the rate of degradation from photolysis should be nil or extremely low [9]. The extent of photolysis of the organic compounds found in synthetic greywater under quiescent conditions was assessed and the results compiled in figure 5.9. This was done by using 25 mm X 25 mm TiO_2NT-EG 40V coupons immersed in 10mL of the synthetic greywater mixture and irradiated for 8 hours under the canopy.

The churning of the solution within the unit resulted in foaming. The foam, which separates itself from the bulk of the solution, reduces the amount of organic carbon dissolved. When the aliquot is sampled for measuring the TOC value, the foam not extracted with the solution does not contribute to the TOC value. The foaming of the solution describes the reduction in TOC for the Ti surfaces. The foam formation also favoured the photocatalyst, as less organic carbon is available in solution and thus the photocatalytic reaction is more efficient. The TOC value for TiO_2NT-EG 40V is thus considerably lower than that for the untreated Ti.

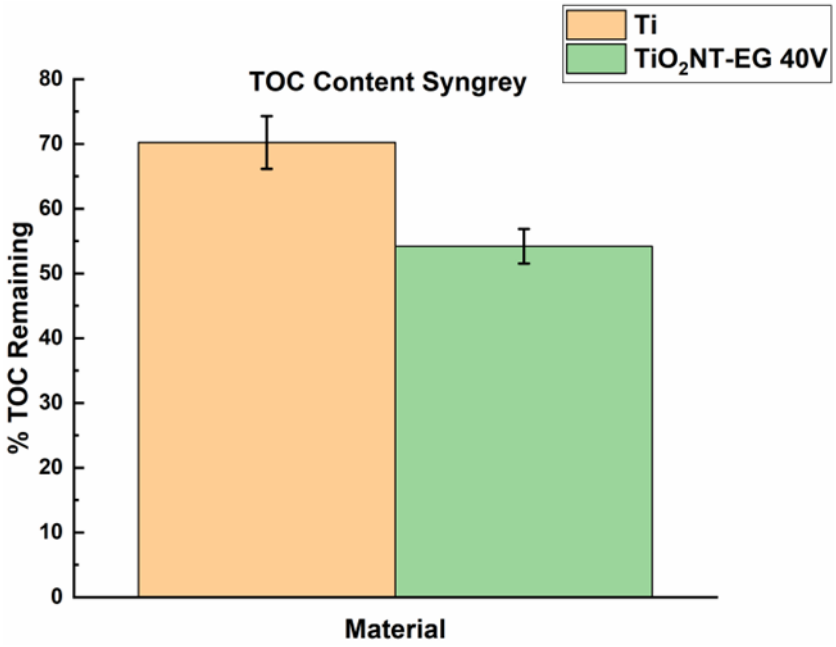

Figure 5. 8 Reduction in TOC content of synthetic greywater mixture after 8-hour photocatalytic cycle. Error bars represent the maximum and minimum error after 3 photocatalytic cycles.

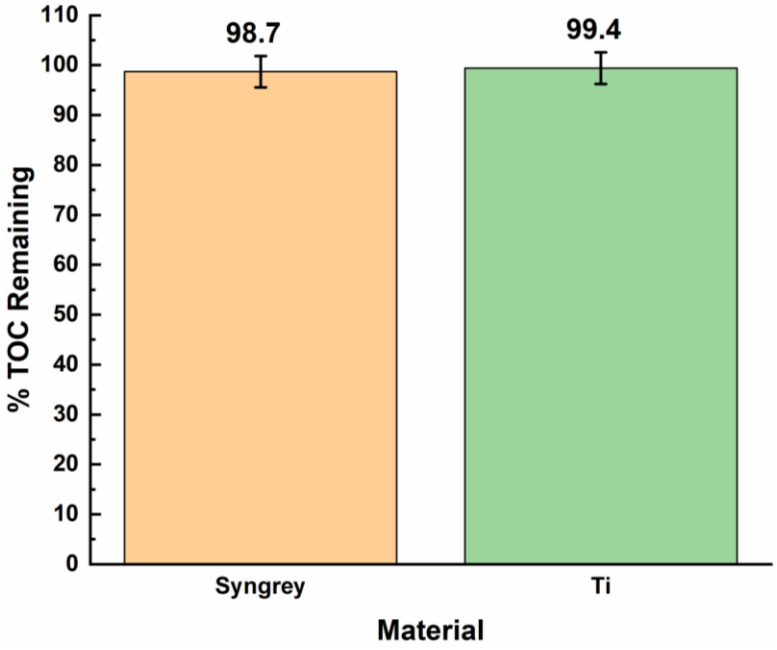

Figure 5. 9 Assessment of possible photolysis of the components of the synthetic greywater mixture. Error bars represent the maximum and minimum error after 3 photocatalytic cycles.

5.2.2.2 Effect of inhibitive species on photocatalytic degradation of organic compounds in synthetic greywater

The effect of the inorganic anions present in Synthetic greywater on the photocatalytic degradation of its organic constituents was assessed. Inorganic anions compete with the organic compounds by adsorbing to the surface preferentially due to their higher mobility and higher charge density, thus hindering the adsorption of the organic species [10, 11]. A solution containing just the surfactants and yeast extract prescribed by the Synthetic greywater composition was used in lieu of the complete formulation. The removal of possible inhibitive species should bolster the efficiency of the unit.

The % TOC remaining is presented in figure 5.10. The loss of organic carbon from foaming is once more evident. For the inactive surface a reduction of 29% was recorded, a reduction not attributed to photolysis. A 42% reduction was recorded for the photocatalytic surface. The results are near identical to those obtained for the complete Synthetic greywater composition. The inhibitive effect was not evident in this study. This indicates that the adsorption of the organic compounds was favoured over that of the anions.

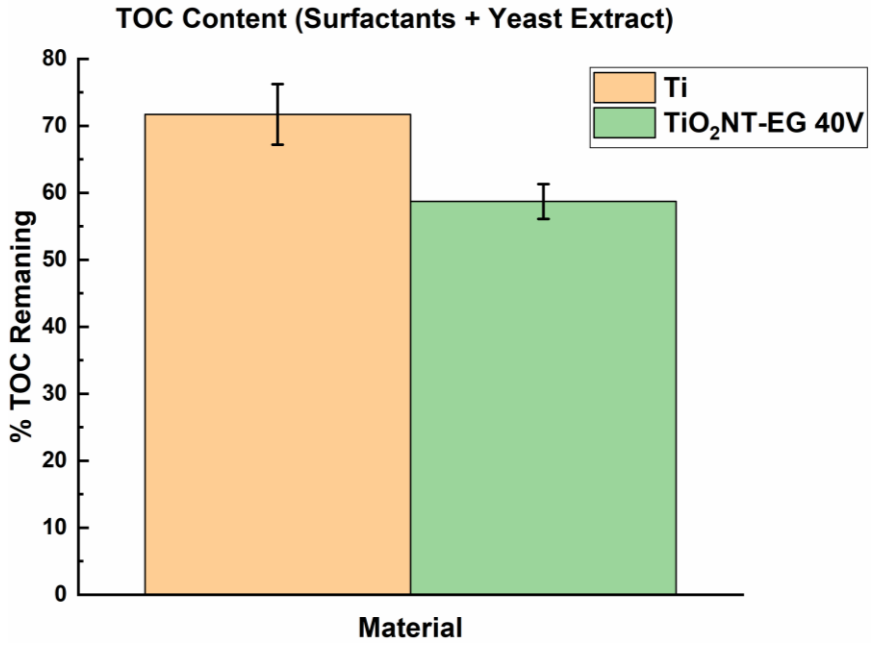

Figure 5. 10 Assessment of possible inhibition by the inorganic species found in the synthetic greywater mixture. Error bars represent the maximum and minimum error after 3 photocatalytic cycles.

5.2.3 Degradation of 22 ppm TOC Single Component Solutions

In order to determine whether the low reduction in TOC of synthetic greywater is due to the complexity and stability of its organic constituents, the 8-hour treatment cycle was repeated but this time using only MB and paracetamol solutions. These solutions also do not foam and thus losses of the TOC content due to this mechanism during processing are kept at a minimum. The TOC content was kept at 22ppm for both pollutants.

5.2.3.1 Degradation of 22 ppm TOC MB Solution

The % degradation of MB in terms of the change in absorbance and TOC is presented in figure 5.11. A slight reduction in both the absorbance value and TOC value were recorded for the Ti blank. The reduction in both values is extremely low and is within the experimental error. This reduction is probably due to some adsorption of the dye whilst it was circulating within the unit. A more remarkable decline in both absorbance and TOC values was however recorded for the photocatalyst. A reduction in absorbance of ≈ 25% and in TOC of ≈ 15% was obtained. The ANTA housed within the flat plate reactor were not extremely efficient in degrading MB. This was despite the fact that the minimum volume and flow rate possible were used to maximise the efficiency of the units. The low volume was employed so that the majority of the total volume would make up the working volume and thus keep the dead volume at a minimum. The use of the lowest flow rate increases the residence time of the molecules over the photocatalytic surface. The solution thickness over the ANTA was also kept at 5mm to reduce the diffusion gradient for the molecules to reach the surface. These results indicate that quiescent conditions tend to increase the rate of photocatalytic degradation.

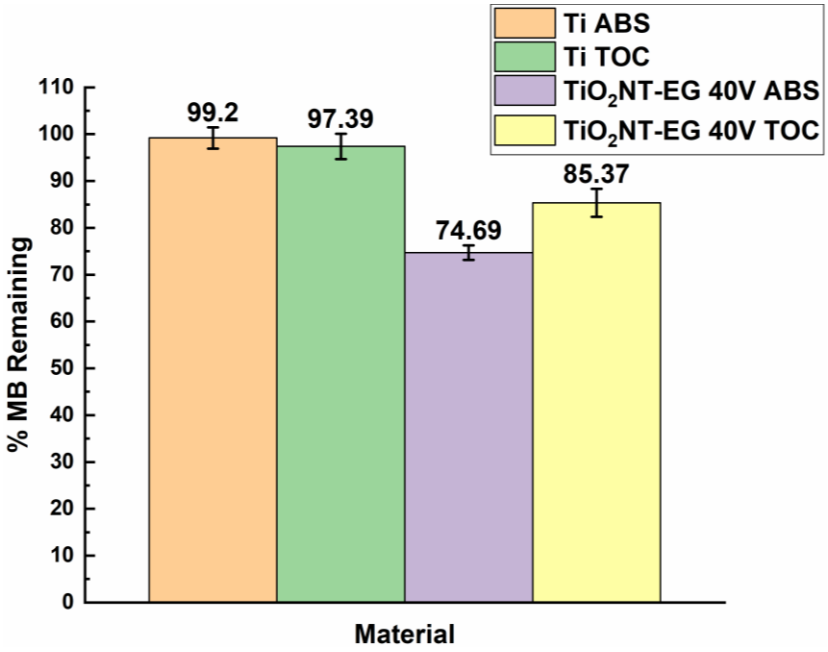

Figure 5. 11 Reduction in absorbance and TOC of 22 ppm MB solution after 8-hour photocatalytic cycle. Error bars represent the maximum and minimum error after 3 photocatalytic cycles.

5.2.3.2 Degradation of 22 ppm TOC Paracetamol Solution

Figure 5.12 presents the % reduction in absorbance and TOC for the 22 ppm TOC paracetamol solution. The activity of the untreated Ti surface was extremely low and is similar to that obtained for the 22 ppm TOC MB solution. The reduction is most likely due to experimental error such as some continued adsorption to the wetted surfaces in the reactor. A ≈ 26% reduction in absorbance and an ≈ 11% reduction in the TOC value was recorded for the photocatalyst. The reduction in TOC is slightly lower than that for MB, indicating that perhaps the methyl groups of the dye molecule are more readily attacked when a flow regimen is employed. This is however an observation and as a definitive conclusion cannot be drawn from the experimental results obtained.

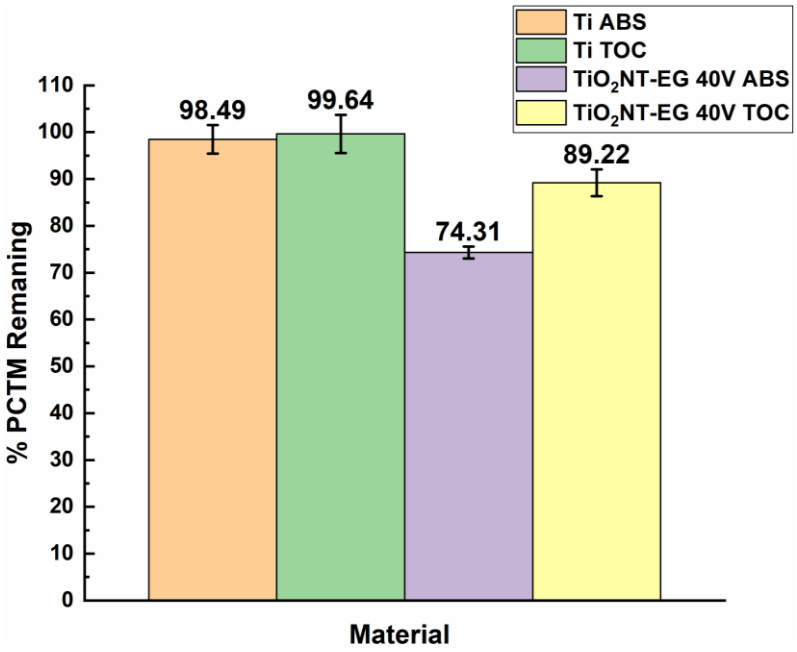

Figure 5. 12 Reduction in absorbance and TOC of 22 ppm paracetamol solution after 8-hour photocatalytic cycle. Error bars represent the maximum and minimum error after 3 photocatalytic cycles.

5.2.4 Effect of Operational Parameters on Unit Efficiency

The prototype unit allows the flow rate and exposed volume to be varied. These two parameters can be adjusted to maximise the productivity of the unit i.e., the degradation efficiency for the degradation of pollutants. These two parameters are the easiest to change, as is the assessment, of their effect. The surface area of the photocatalytic surfaces used in the unit were fixed. By changing the flow rate and volume, the productivity afforded by a larger surface area can be approached if not matched. The increase in surface area of the catalyst will affect the size of the unit, making its adoption in modern dwellings difficult.

To be in a better position to compare the activity with different operating conditions, the degradation of a $1X10^{-5}$M MB solution was assessed. The degradation rate of the 22 ppm TOC MB solution was not particularly high and therefore the changes in activity with the variation of operational parameters might be difficult to quantify [12]. The higher the concentration, the lower available photocatalyst surface per molecule. The catalyst load can be easily increased in reactors which use slurries or powders but not so much for reactors using supported catalysts [13]. The more dilute solution will be degraded more thoroughly and any significant modification to the operational parameters should have a clear effect of the degradation rate.

5.2.4.1 Efficiency of Unit at Lowest Flow Rate (100 L/h) and Volume (2L)

The extent of degradation of the MB solution and the resulting rate constant are presented in figure 5.13 a-b. Around 95% of the MB molecules were degraded after 8 hours of photocatalytic treatment. The rate constant at k = 0.00583 min^{-1}. This is around 2.5 times lower than that measured previously onof the 25 mm X 25 mm coupons TiO_2NT-EG 25mm by 25mm coupons (k = 0.01425 min^{-1}). The absorbance and TOC values after treatment are compared in figure 5.14. There is basically no reduction in both absorbance and TOC for the Ti blank. The degradation of MB in terms of the reduction of the absorbance is complete as the solution was fully decolourised. A reduction in TOC value of ≈ 47% after the 8-hour treatment cycle was obtained. This is considerably lower than that (56.8 %) which was also achieved in just 4 hours by the TiO_2NT-EG 25 mm X 25 mm coupons. (56.8 %), which was also achieved in just 4 hours.

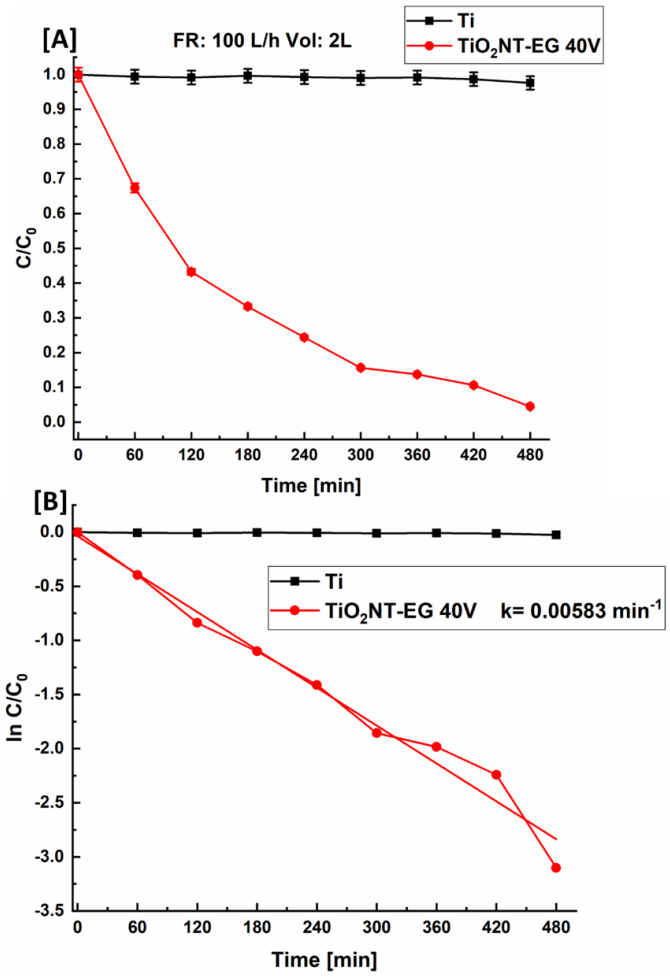

Figure 5. 13 A) Reduction in absorbance over 8-hour cycle B) Rate constant for the reaction at 100 L/h and 2 L volume. C = absorbance at time *t*, C_0 = absorbance of untreated solution

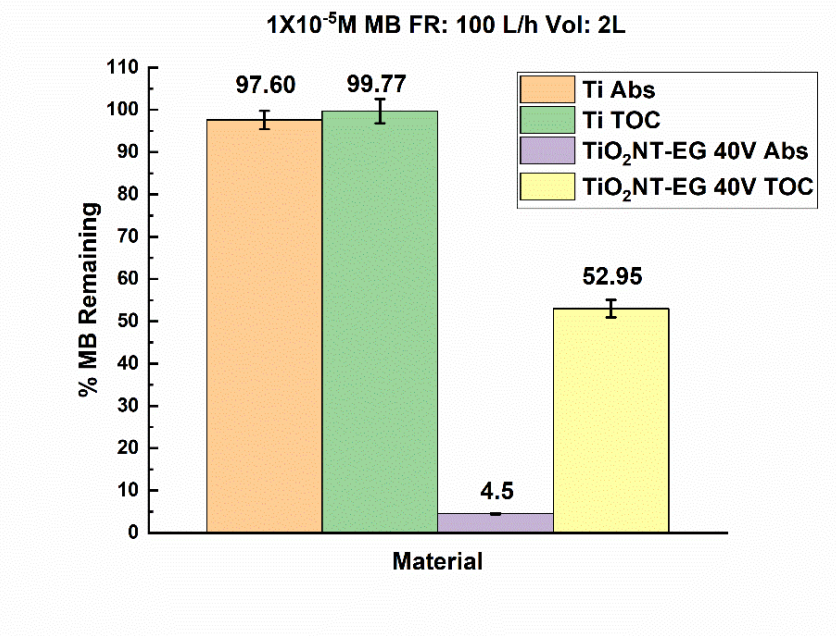

Figure 5. 14 % MB remaining after 8-hour photocatalytic cycle expressed as absorbance and TOC. Flow rate 100 L/h – Volume 2L. Error bars represent the maximum and minimum error after 3 photocatalytic cycles.

5.2.4.2 Efficiency of Unit at Highest Flow Rate (150 L/h) and Lowest Volume (2L)

The selection of lowest volume and flow rate should provide the highest productivity of the unit. A low flow rate increases the residence time over the UVA irradiated surface which increases the likelihood of the pollutant to be degraded. A larger flow rate and volume will decrease the residence time of the solution, which will reduce the efficiency of the process. By quantifying the decline in productivity, the suitability of a unit can be determined. If for example the bacterial load of greywater is sufficiently decreased for direct use or short-term storage, reducing the bacterial load further might not be essential. By increasing, the volume and or the flow rate the amount of water treated would be higher.

The activity of the ANTA using a faster flow rate is presented in figure 5.15. The reduction in absorbance value throughout the 8-hour photocatalytic cycle at ≈ 98% is slightly higher that that at 100L/h. The resulting rate constant at 0.00817 min^{-1} is around 30% higher than that obtained at the lower flow rate. This can be attributed to the removal of mass transfer limitations [14]. The higher flow rate can also remove remnants of degraded molecules where they are replaced by unaltered ones. This however did not enhance the rate of mineralisation of the dye as at the faster flow rate it is around 6% less than that at 100 L/h. This indicates that the low retention time of the

molecules on the surface decreased the extent of the modification of the molecule [15]. The rate of degradation as expressed by the change in absorbance can be high as the destruction of the chromophore is all that is required. For the TOC to decrease the molecules need to be oxidised all the way to CO_2. The % reduction in absorbance and TOC are summarised in figure 5.16.

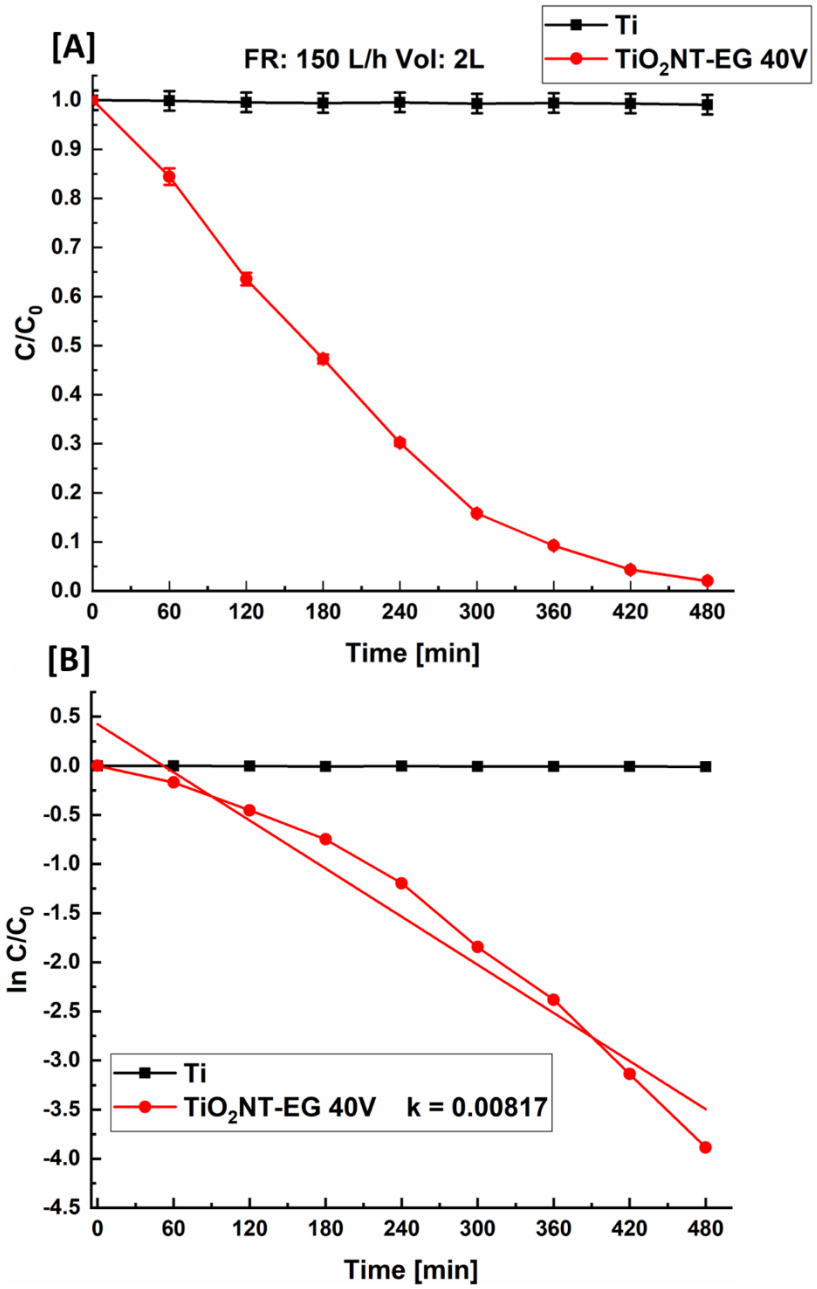

Figure 5. 15 A) Reduction in absorbance over 8-hour cycle B) Rate constant for the reaction at 150 L/h and 2 L volume. C = absorbance at time *t*, C_0 = absorbance of untreated solution

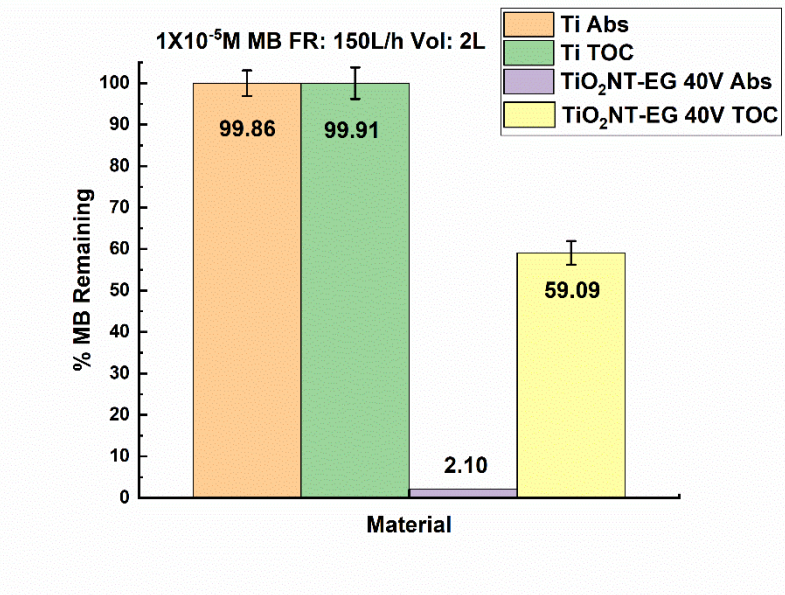

Figure 5. 16 % MB remaining after 8-hour photocatalytic cycle expressed as absorbance and TOC. Flow rate 150 L/h – Volume 2L. Error bars represent the maximum and minimum error of 3 photocatalytic cycles.

The effect of increasing the volume to the maximum capacity of 5L on the absorbance of the solution is presented in figure 5.17 a-b. The reduction in absorbance after the 8-hour cycle is ≈ 73%, which is significantly lower than when the flow rate was increased. This also reflected in the lowering of the rate constant to 0.00268 min-1. The reduction in TOC was also marginal at ≈ 10% (figure 5.18). The increase in solution volume increases the number of molecules and thus decreases the available photocatalyst surface area for reaction.

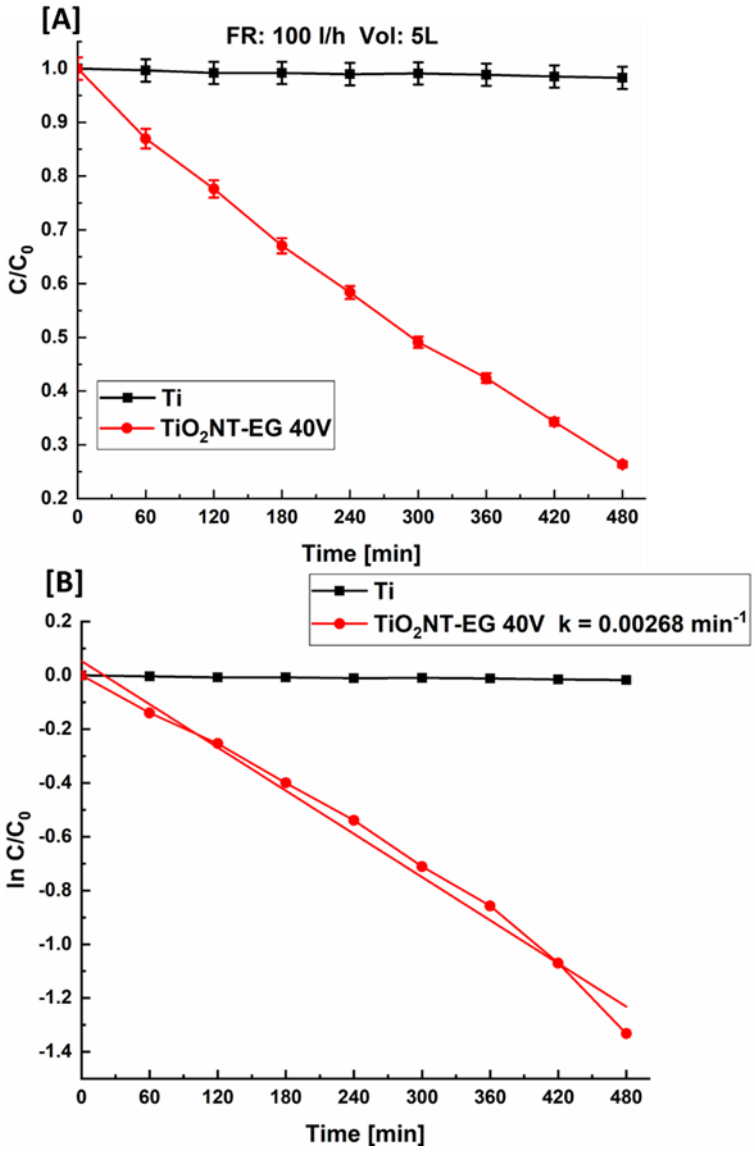

Figure 5. 17 A) Reduction in absorbance over 8-hour cycle B) Rate constant for the reaction at 100 L/h and 5 L volume. C = absorbance at time *t*, C_0 = absorbance of untreated solution

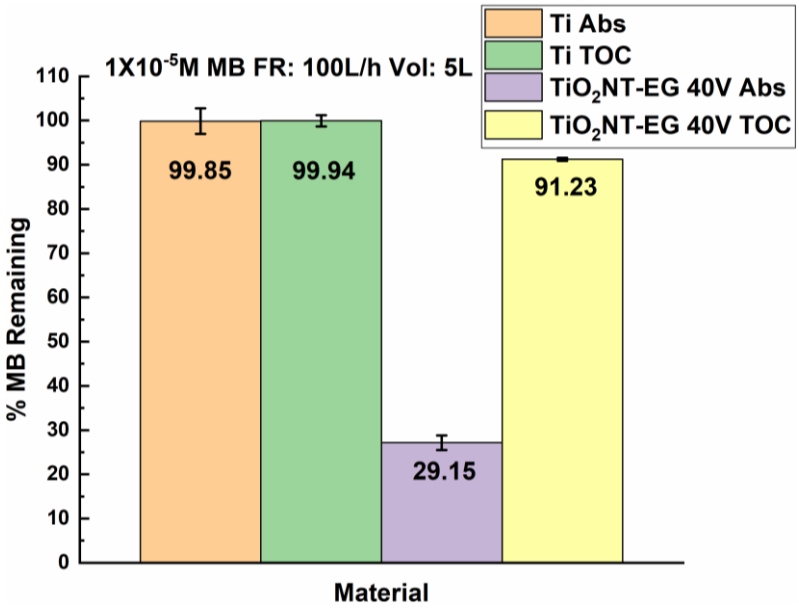

Figure 5. 18 % MB remaining after 8-hour photocatalytic cycle expressed as absorbance and TOC. Flow rate 100 L/h – Volume 5L. Error bars represent the maximum and minimum error of 3 photocatalytic cycles.

The results in this section highlight the importance of a high photocatalyst load. The tests carried out under quiescent conditions utilised a 6.25 cm^2 photocatalyst surface area for 10 ml of solution. Thus 0.625 cm^2 of activated surface per ml of solution was available. In the initial test at the lowest flow rate and that involving the subsequent increase in flow rate, 900 cm^2 of ANTA surface were used with 2l of solution. This resulted in 0.45 cm^2 of ANTA surface per mL being available for reaction. The reduction of mass transfer limitations afforded by the increased flow rate could not make up for the lower catalyst load. The catalyst concentration was reduced even further when 5L of solution were used, where just 0.18 cm^2 ANTA surface per ml was available. Whilst the morphology of theTiO_2NT-EG 40V ANTA might have not been identical and the absence of flow increased the retention time, these factors are outweighed by the higher photocatalyst to solution ratio. The rate constant is compared to the surface area to solution volume ratio in figure 5.19.

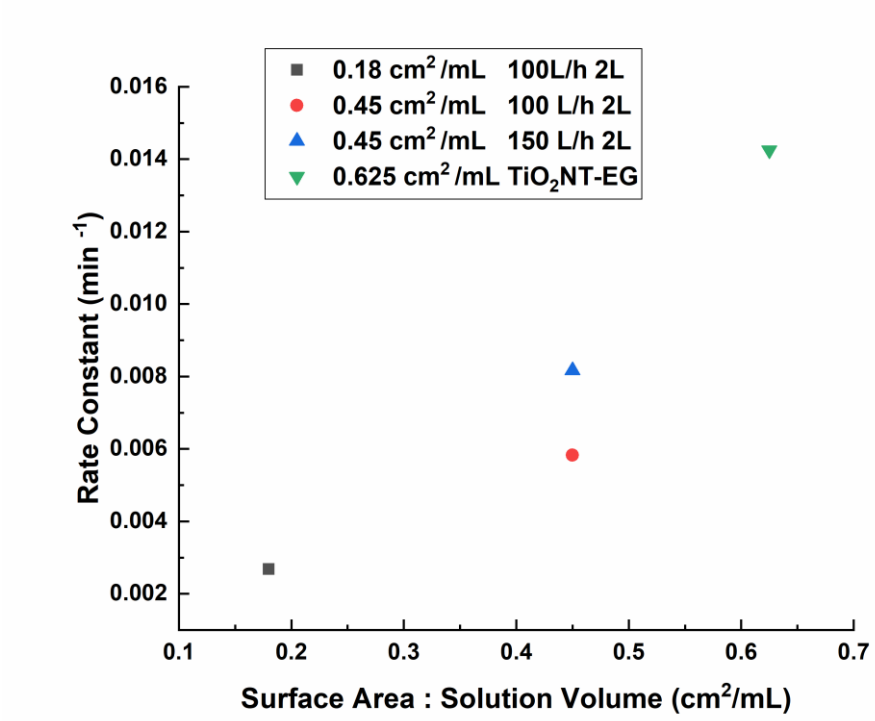

Figure 5. 19 Comparison of rate constant with the surface area to solution volume ratio

5.2.5 Bacterial Inactivation Under Solar Radiation

The potential of using the plentiful sunlight available in Malta increases the eco-friendly aspect of photocatalytic surfaces. A solar greywater photocatalytic reactor was designed to study the potential for inactivation of bacteria by harnessing UV from solar radiation. The unit was tested in the months of November and December, where the temperate climate, reduces the possibility of thermal inactivation of the bacteria. It also acts as a way to measure the activity of the unit under low solar irradiance. By eliminating heat as an inactivation mechanism, the mechanical and photocatalytic inactivation of the bacteria can be discerned. The effect of mechanical damage through the operation of the unit will be determined by using Ti blanks.

The change in bacterial concentration on three different days over a 6-hour irradiation period is shown in figures 5.20 a-c. The water temperature and irradiance measured at each sampling interval for the ANTA section of the reactor is compiled in table 5.2. The results indicate that on the three different days there was no effective antibacterial

activity being shown by the photocatalytic surfaces. This was in spite of using the lowest possible volume and the lowest flow rate of 150 L/h. The starting concentration in the range of 10^6 CFU/mL was not reduced significantly and at the most the final value reached 10^5 CFU/mL. Whilst there is a clear trend that the ANTA provide a higher antibacterial effect, this is still not remarkably higher than that of the Ti blanks. It is also unlikely that any loss in bacterial activity is due to the solution temperature as these were way below 40°C The British Standard Institution has published some guidelines for the safe bacterial levels for non-potable applications after treatment of greywater. Standard BS 8525:2010 Greywater Systems- Part 1: Code of Practice identifies an *E.Coli* content of 250 CFU/100mL as the upper limit for use in toilet flushing, gardening and laundry [16]. This low level of bacterial content was not achieved in any of the experimental runs carried out. One parameter which could have led to the low antibacterial activity was the low irradiance recorded during the months of November and December. The choice of these months was however essential as the lowest efficiency of the unit had to be determined. Whilst higher activities are expected in summer, the unit should not have a seasonal useability. Another parameter is the photocatalyst to solution ratio. With a surface area of 5400 cm^2 and a 15L volume, the available photocatalyst surface area is 0.36 cm2/mL. This ratio is even lower than that of the UVA prototype unit (0.45 cm^2/mL). The surface area of the ANTA governs the overall size of the flat plate reactor. The system must be sized such that there is an excess of photocatalyst when compared to the solution volume. The volume of water treated is vital if photocatalytic reactors housing TiO_2 ANTA are to be commercialised. Whilst using such units solely for reducing water wastage is commendable, the economics in terms of lower potable water consumption need to be factored in.

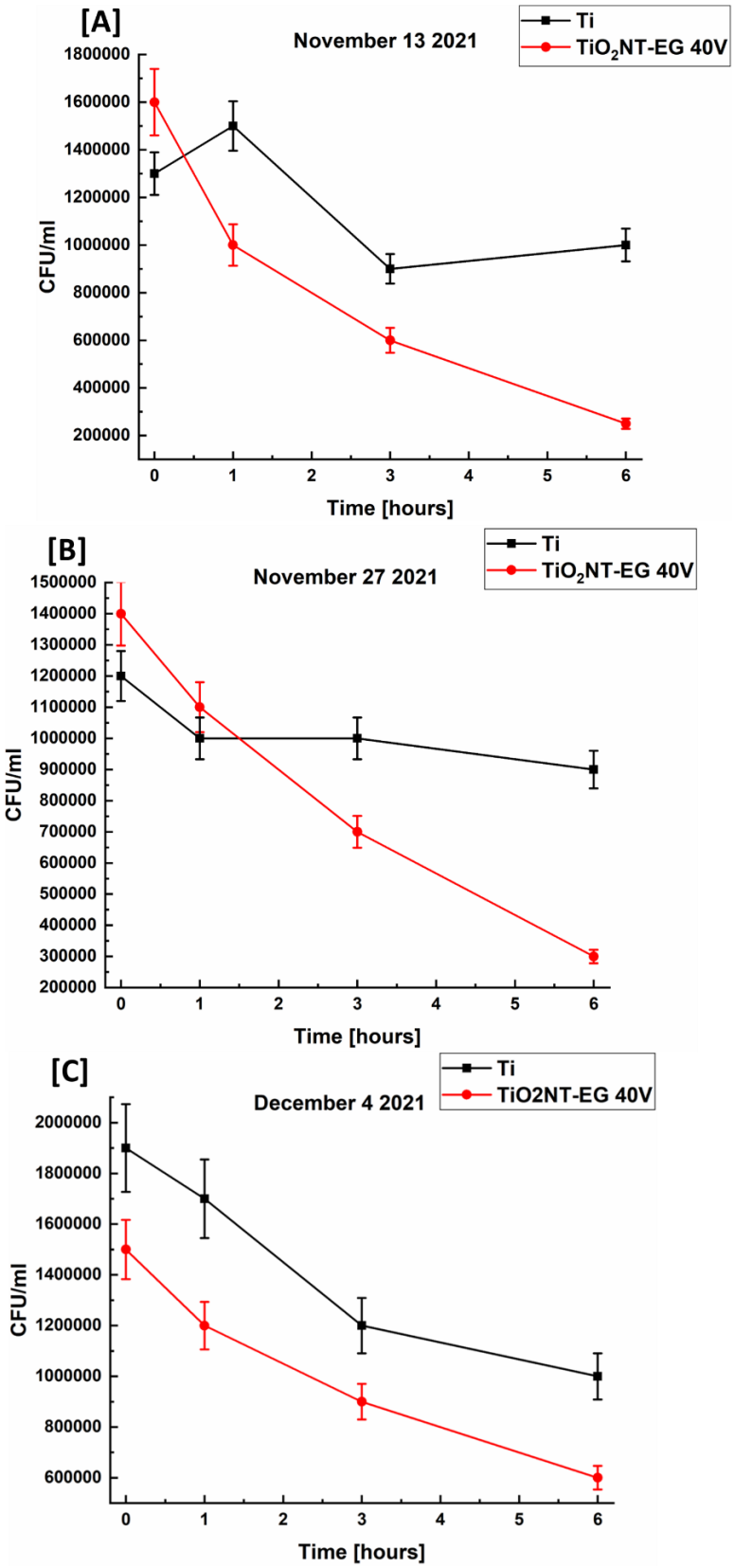

Figure 5. 20 Bacterial reduction after 6-hour irradiation cycle on different days. Error bars: minimum and maximum error based on plating sample at each timepoint in triplicate.

Table 5. 2 Summary of climatic conditions recorded during the solar photocatalytic antibacterial tests

13-11-2021			
Time	**Water Temperature(°C)**	**Global Irradiance (mW/cm^2)**	**UV Irradiance (mW/cm^2)**
0	16.9	9.81	0.82
1	18.7	10.96	0.91
3	25.2	39.97	2.6
6	23.1	15.89	0.95
28-11-2021			
Time	**Water Temperature(°C)**	**Global Irradiance (mW/cm^2)**	**UV Irradiance (mW/cm^2)**
0	16.2	10.17	0.61
1	17.6	10.75	0.54
3	24.7	33.21	1.80
6	22.8	16.15	0.19
04-12-2021			
Time	**Water Temperature(°C)**	**Global Irradiance (mW/cm^2)**	**UV Irradiance (mW/cm^2)**
0	13.2	10.65	0.64
1	17.1	11.56	0.69
3	23.8	37.20	2.30
6	22.4	13.95	0.60

5.3 Chapter Conclusions

- By employing a 40V potential for 2 hours well defined, upright ANTA layers with a high thickness can be obtained. This using aA simple setup where cooling water is circulated around the anodising bath and mixing the solution electrolyte by sparging bubbling with air was sufficient to avoid excessive electrolyte temperatures.

- The anions present in the synthetic greywater mixture did not adversely affect the photocatalytic activity of the surfaces. Thus, ANTA should be able to degrade greywater.

- The efficiency of the system falls when higher concentrations of pollutants are employed. The higher the number of molecules in solution, this because the lower the amount of available photocatalyst per unit volume of pollutant.

- A sufficiently high retention time is required for effective photocatalytic degradation of pollutants to take place. Lower flow rates ensure a longer retention time of the molecules over the surface. Whilst high flow rates can reduce mass transfer limitations due to agitation, the retention time is also decreased, thus negatively impacting the efficiency of the system.

- The solution volume must be such that there is a high photocatalytic surface area available per mL of solution. Large volumes in essence decrease the concentration of the photocatalyst, and ANTA being supported, the concentration is fixed according to the size of the photocatalyst surfaces.

- Mineralisation of organic compounds was not completely achieved, mainly due to low available surface area and the retention time not being enough for complete oxidation of the molecules. Degradation by-products obtained through incomplete oxidation can be toxic and in complex water matrices difficult to identifyty.

- The antibacterial activity of the units using solar radiation was not enough to render the effluent safe for reuse. Whilst the climatic parameters might not have extracted the best performance from the surfaces, high irradiance values year-round are not possible.

- A flat plane reactor containing ANTA might not be suitable as a standalone solution for greywater treatment. The reactor can be used to bolster the oxidising ability

of compounds such as hydrogen peroxide or sodium hypochlorite. This combination of photocatalysis and oxidants can help degrade recalcitrant molecules and microbial species. The addition of an oxidant can keep the size of the unit contained.

5.4 References

[1] H. Sopha, M. Baudys, M. Krbal, R. Zazpe, J. Prikryl, J. Krysa, *et al.*, "Scaling up anodic TiO_2 nanotube layers for gas phase photocatalysis," Electrochemistry Communications, vol. 97, pp. 91-95, 2018/12/01/ 2018.

[2] J. Lincho, J. Gomes, M. Kobylanski, B. Bajorowicz, A. Zaleska-Medynska, and R. C. Martins, "TiO_2 nanotube catalysts for parabens mixture degradation by photocatalysis and ozone-based technologies," Process Safety and Environmental Protection, vol. 152, pp. 601-613, 2021/08/01/ 2021.

[3] E. Mena, M. J. Martín de Vidales, S. Mesones, and J. Marugán, "Influence of anodization mode on the morphology and photocatalytic activity of TiO_2 -NTs array large size electrodes," Catalysis Today, vol. 313, pp. 33-39, 2018/09/01/ 2018.

[4] H.-i. Kim, D. Kim, W. Kim, Y.-C. Ha, S.-J. Sim, S. Kim, *et al.*, "Anodic TiO_2 nanotube layer directly formed on the inner surface of Ti pipe for a tubular photocatalytic reactor," Applied Catalysis A: General, vol. 521, pp. 174-181, 2016/07/05/ 2016.

[5] H. Sopha, M. Baudys, L. Hromadko, M. Lhotka, D. Pavlinak, J. Krysa, *et al.*, "Scaling up anodic TiO_2 nanotube layers – Influence of the nanotube layer thickness on the photocatalytic degradation of hexane and benzene," Applied Materials Today, vol. 29, p. 101567, 2022/12/01/ 2022.

[6] G. L. Song and D. H. StJohn, "11 - Corrosion of magnesium (Mg) alloys in engine coolants," in Corrosion of Magnesium Alloys, G.-l. Song, Ed., ed: Woodhead Publishing, 2011, pp. 426-454.

[7] L. Mohan, C. Dennis, N. Padmapriya, C. Anandan, and N. Rajendran, "Effect of Electrolyte Temperature and Anodization Time on Formation of TiO_2 Nanotubes for Biomedical Applications," Materials Today Communications, vol. 23, p. 101103, 2020/06/01/ 2020.

[8] K. Indira, U. K. Mudali, T. Nishimura, and N. Rajendran, "A Review on TiO_2 Nanotubes: Influence of Anodization Parameters, Formation Mechanism, Properties, Corrosion Behavior, and Biomedical Applications," Journal of Bio- and Tribo-Corrosion, vol. 1, p. 28, 2015/10/07 2015.

[9] E. Miłosek, L. Kuźmicka, and J. Karpińska, "Direct and forced photodegradation of sodium dodecyl sulfate and tetraoctylammonium bromide," Toxicological & Environmental Chemistry, vol. 96, pp. 27-40, 2014/01/02 2014.

[10] H. Y. Chen, O. Zahraa, and M. Bouchy, "Inhibition of the adsorption and photocatalytic degradation of an organic contaminant in an aqueous suspension of TiO_2 by inorganic ions," Journal of Photochemistry and Photobiology A: Chemistry, vol. 108, pp. 37-44, 1997/07/31/ 1997.

[11] C. Hu, T. Yuchao, L. Lanyu, H. Zhengping, W. Yizhong, and T. Hongxiao, "Effects of inorganic anions on photoactivity of various photocatalysts under different conditions," Journal of Chemical Technology & Biotechnology, vol. 79, pp. 247-252, 2004.

[12] S. M. Tichapondwa, J. P. Newman, and O. Kubheka, "Effect of TiO_2 phase on the photocatalytic degradation of methylene blue dye," Physics and Chemistry of the Earth, Parts A/B/C, vol. 118-119, p. 102900, 2020/10/01/ 2020.

[13] B. Neppolian, H. C. Choi, S. Sakthivel, B. Arabindoo, and V. Murugesan, "Solar/UV-induced photocatalytic degradation of three commercial textile dyes," Journal of Hazardous Materials, vol. 89, pp. 303-317, 2002/01/28/ 2002.

[14] C.-H. Wu and J.-M. Chern, "Kinetics of Photocatalytic Decomposition of Methylene Blue," Industrial & Engineering Chemistry Research, vol. 45, pp. 6450-6457, 2006/09/01 2006.

[15] K. Natarajan, T. S. Natarajan, H. C. Bajaj, and R. J. Tayade, "Photocatalytic reactor based on UV-LED/TiO_2 coated quartz tube for degradation of dyes," Chemical Engineering Journal, vol. 178, pp. 40-49, 2011/12/15/ 2011.

[16] T. B. S. Institution, "Greywater systems –Part 1: Code of practice," ed. London: The British Standard Institution 2010

6.Summary of Thesis Conclusions

- The high potential employed in the synthesis of TiO_2NT-EG and TiO_2NT-Ag contributed to the high thickness and nanotube diameters which translated to the highest overall photocatalytic activities.
- The overall order of reactivity is: TiO_2NT-Ag > TiO_2NT-EG > TiO_2NT-SS > TiO_2NT-PA.
- The ethylene glycol electrolyte could be used for at least 10 anodising cycles without any significant loss in photocatalytic activity.
- The photocatalytic activity towards the degradation of MB and *E.Coli* diminished with aging. A remarkably high photocatalytic activity was retained for TiO_2NT-EG and TiO_2NT-AG.
- The highly active anatase phase was stable despite 1-year of exposure.
- By using a 0.1M H_2O_2 solution under UVA light at 365nm and 1.2mW/cm^2 surface debris can be effectively removed. The MB degradation photocatalytic activity was sufficiently recovered, whereas recovery of the antibacterial activity was marginal.
- The TiO_2NT-EG surfaces provided a facile synthetic method coupled with a high photocatalytic activity. The inclusion of silver did not increase the activity to any great extent. The TiO_2NT-EG surfaces are viable for upscaling.
- The ANTA synthesis was successfully upscaled by reducing the applied potential from 70V used for the synthesis of TiO_2NT-EG to 40V. By lowering the potential and keeping the temperature of the anodising solution low, 10, 15 cm X 15 cm surfaces were produced.
- The efficiency of a reactor housing ANTA falls with higher contaminant concentrations. The higher concentrations reduce the effective photocatalyst loading.
- A suitably high retention time is required for effective photocatalytic degradation rates. This can be increased by reducing flow rates and treating low solution volumes.
- Mineralisation of organic compounds was not completely achieved, mainly due to an unfavourable photocatalyst to solution ratio.

- The antibacterial activity of the units using solar radiation was not enough to reduce the bacterial load to a value which would make the greywater safe for reuse.

7. Suggestions for Future Work

Units relying solely on photocatalysis for treating complex matrices such as greywater might not be suitable as a standalone solution. The surface area required for treatment of a significant volume of water might make the units unfeasibly large. Strategies aimed at bolstering the activity of the materials in order to overcome a low photocatalyst to solution ratio should be the focus of future research endeavours. These strategies should however keep cost in mind.

The unfavourable ratio could be offset by the introduction of an easily available, safe and low-cost oxidising agent. The addition of hydrogen peroxide might be useful in bolstering the activity. The combination of photocatalysis and oxidising agent could improve the efficiency of the unit whilst keeping the size of the unit contained. Research should be undertaken in finding a concentration of hydrogen peroxide which increases the reaction rate but does not act as a scavenger for the photogenerated ROSs.

The treatment efficiency would benefit from the enhancement of the visible light activity of the nanotube arrays. In this study the TiO_2NT-EG nanotube arrays have been found to be extremely resistant to fouling and easily up scalable, thus, enhancing their visible light activity is worthwhile. The addition of dopant species in the anodising bath might be a cost-effective way to enhance visible light activity. Similarly, self-doping by applying a cathodic polarisation cycle after anodising can introduce defects and increase the prevalence of Ti^{3+} both of which can extend the visible light activity. The research would entail finding the proper process parameters which would introduce the required dopants. The materials can then be aged to determine whether the doping effect wanes with use.

Photocatalysis can be used as part of a sequence of processes. An initial treatment can reduce the contaminant load allowing for the more recalcitrant species to be degraded by photocatalysis. Electrocoagulation can be a suitable first treatment to reduce the COD load and also to precipitate out colloidal particles and oils to reduce fouling of the surface. The study would include monitoring any changes in pH and how these affect the photocatalytic activity. The direction of pH change (acidic/basic) can be adjusted by using different electrode materials. Similarly, the minimum current density that needs to be applied should be determined. This will avoid applying excessive currents which

would consume the electrodes prematurely and also possibly alter the pH of the greywater.

Future research should be carried out with a specific application in mind. One such approach is determining the needs required for the treatment of the greywater generated in a dwelling housing a certain number of individuals. Variations in the greywater loads can be implemented to determine the maximum productivity of the unit, especially when large amounts of greywater are being generated. The results obtained should help identify the most suitable way to treat a particular greywater stream. This would eventually help in customising the greywater reactor for the needs of a particular dwelling. A safety margin, to cater for higher greywater strengths should also be determined.

Annex A.

In this work a modified version of BS ISO 10678:2010 “Determination of photocatalytic activity of surfaces in an aqueous medium by degradation of methylene blue” was used. The testing methodology was altered to use a volume lower than the 35 mL stipulated in the standard. This decision was taken after testing using the 35 mL volume produced relatively low degradation rates. This is due to lower surface area afforded by supported photocatalysts. The tests were repeated using 10- and 20-mL solution volumes. The 10 mL volume provided the higher activity which would make changes in activity due to aging more easily discernible. The aim of the project was also to produce functional units, whereby the solution thickness and process parameters such as treated volume and flow rate could be optimised to maximise the amount of water treated. As such, the use of larger volumes in the initial phases of the project was not critical to the final outcome.

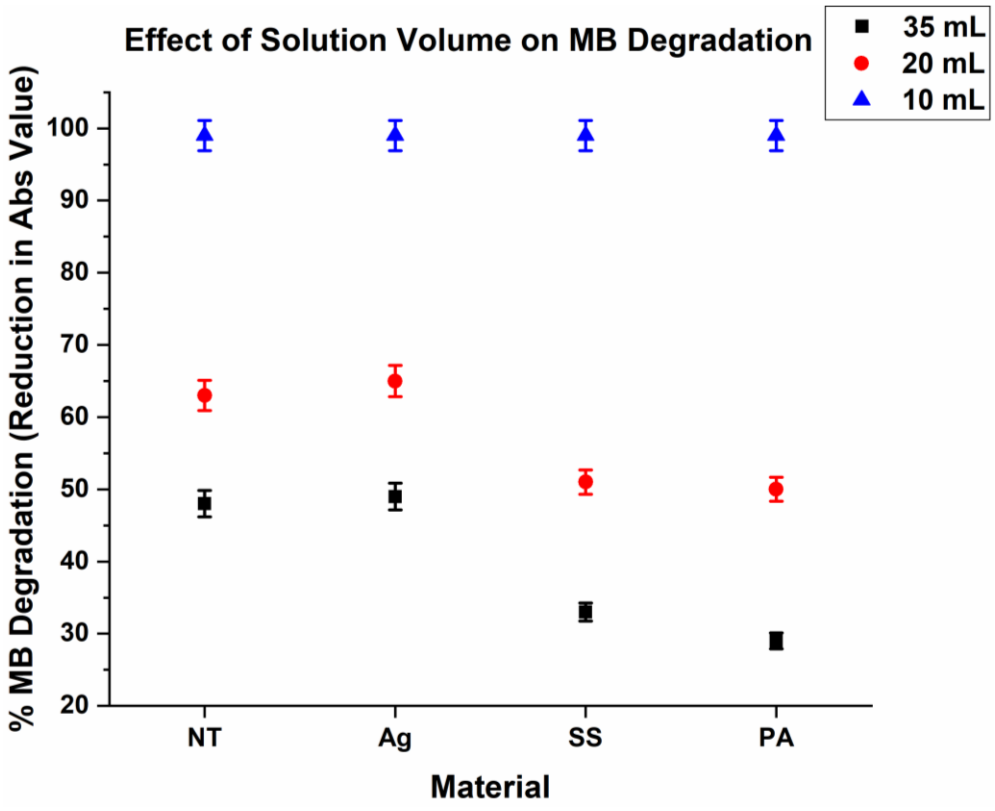

Figure A. 1 Effect of Solution Volume on Reduction of Absorbance Value of MB. Error bars computed from the maximum and minimum error of 3 independent measurements.